Interlaminar Deformation at a Hole in Laminated Composites: A Detailed Experimental Investigation Using Moiré Interferometry

David H. Mollenhauer

Dissertation submitted to the Faculty of the Virginia Polytechnic Institute and State University in partial fulfillment of the requirements for the degree of

Doctor of Philosophy
in
Engineering Mechanics

Daniel Post, Co-Chairman
Kenneth L. Reifsnider, Co-Chairman
Werner E. Kohler
Ronald D. Kriz
James R. McCoy

August 20, 1997
Blacksburg, Virginia

Interlaminar Deformation at a Hole in Laminated Composites: A Detailed Experimental Investigation Using Moiré Interferometry

David H. Mollenhauer

(**ABSTRACT**)

The deformation on cylindrical surfaces of holes in tensile-loaded laminated composite specimens was measured using new moiré interferometry techniques. These new techniques were developed and evaluated using a 7075-T6 aluminum control specimen. Grating replication techniques were developed for replicating high quality diffraction gratings onto the cylindrical surfaces of holes. Replicas of the cylindrical specimen gratings (undeformed and deformed) were fabricated onto circular steel sectors. Narrow angular regions of these sector gratings were directly evaluated in a moiré interferometer. This moiré interferometry approach eliminated potential sources of error associated with other moiré interferometry approaches.

Two composite tensile specimens, fabricated from IM7/5250-4 pre-preg with ply lay-ups of $[0°_4/90°_4]_{3s}$ and $[+30°_2/–30°_2/90°_4]_{3s}$, were examined using the newly developed moiré interferometry techniques. Circumferential and thickness direction displacement fringe patterns (each 3° wide) were assembled into 90°-wide mosaics around the hole periphery for both composite specimens. Distributions of strain were calculated with high confidence on a sub-ply basis at select angular locations. Measured strain behavior was complex and displayed ply-by-ply trends. Large ply-related variations in the circumferential strain were observed at certain angular locations around the periphery of the holes in both composites. Extremely large ply-by-ply variations of the shear strain were also documented in both composites. Peak values of shear strain approached 30 times the applied far-field axial strain. Post-loaded viscoelastic shearing strains were recorded that were associated with the regions of large load-induced shearing strains. Large ply-grouping-related variations in the thickness direction strain were observed in the $[+30°_2/–30°_2/90°_4]_{3s}$ specimen. An important large-scale trend was observed where the thickness direction strain tended to be more tensile near the outside faces of the laminate than near the mid-ply region. The measured strains were compared with the three-dimensional analysis technique known as Spline Variational Elastic Laminate Technology (SVELT), resulting in a very close match and corroborating the usefulness of SVELT.

Acknowledgements

The author was supported financially through the Palace Knight program of the United States Air Force. The support and efforts of Elizabeth Ferguson, Lu Voronyak, and the staff of the Palace Knight program are gratefully appreciated.

The assistance from Air Force personnel at Wright Laboratory has been invaluable in this research effort. The insightful discussions with Dr. Nick Pagano and Jeff Schaff are sincerely acknowledged. Administrative assistance given by Karen Kettler, Jason Price, Dr. Jim McCoy, and Roger Griswold was highly valuable. The mentoring from Dr. Jim McCoy and Roger Griswold is also appreciated.

Technical assistance from personnel at the University of Dayton Research Institute is greatly appreciated. Thanks to Dr. Ran Kim, John Camping, Ron Cornwell, and Brian Rice for specimen lay-up, fabrication, and testing. Technical discussions with John Camping about fixture design and machining were invaluable and are appreciated. Special thanks go to Dr. Endel Iarve for his insightful comments and for providing numerical data for comparison with experimental results obtained in this research.

Contributions to this research by the faculty and staff of the Department of Engineering Science and Mechanics (ESM) of Virginia Polytechnic Institute and State University is appreciated. Thanks to Shelia Collins for her administrative support. Thanks also to the staff of the ESM machine shop for their assistance with machine tools and materials. The discussions with Dr. David Dillard about surface wrinkling phenomena were very helpful. The generosity of Professor C.W. Smith by allowing the author the use of his laboratory and computer facilities is gratefully appreciated.

The guidance from the author's dissertation committee is acknowledged. Many technical contributions to this work were made through discussions with Dr. Daniel Post, Dr. Kenneth Reifsnider, Dr. Ronald Kriz, Dr. Werner Kohler, and Dr. Jim McCoy.

The advice and comments from Dr. André Lavoie on the preparation of the electronic version of this dissertation have been invaluable. Thanks go to Charles Randow for providing software and special machining capabilities. Special thanks go to Eric Finlayson for being a great friend, for his assistance with darkroom photography, for many hours of technical discussions, and for putting up with monopolization of his computer.

The support from the author's parents through this endeavor has been generous. Thanks especially to the author's father for his anecdotal and technical advice.

Special thanks go to the author's lovely wife, Jennifer. She has patiently been supportive throughout this graduate degree. Many long hours of discussion on technical ideas, grammatical issues, and figure layout design are gratefully appreciated.

Table of Contents

List of Figures

List of Tables

Chapter 1: Introduction and Review of Literature

1.1 Overview of the Problem and Research Focus

1.1.1 Focus of Research

The goal of this project was to provide significant experimental observations of the behavior of tensile-loaded laminated composites with holes. Specifically, the research focused on the use of moiré interferometry to gather information about interlaminar deformation due to tensile loading on the cylindrical walls of an open hole in a laminated composite. An additional goal was to evaluate a new numerical modeling technique developed elsewhere by comparison with the experimental results

The research focused first on development of experimental techniques and their evaluation. The requisite moiré interferometry techniques were developed to measure displacements on the hole surface and specimen face under tensile loading using an isotropic control specimen. This isotropic, homogeneous tensile specimen was modeled using an approximate two-dimensional elasticity solution. The experimental and analytical results were compared to verify the newly developed experimental techniques. Two laminated composite specimen configurations were then chosen, and tensile members with open holes were produced. Sub-ply level variations in displacement were measured on the cylindrical surfaces of the holes from these composite specimens, which had two different stacking sequences. Distributions of strain at angular locations around the periphery of the holes were calculated from the recorded displacement fringe patterns. The experimental strain results were compared with strain results from the relatively new three-dimensional modeling technique known as Spline Variational Elastic Laminate Technology (SVELT).

Much of the research builds upon the excellent research accomplishments of Boeman (1991). Several contributions introduced in this research advanced the techniques presented by Boeman. These include new approaches to the diffraction grating replication process. Also included in the contributions from this research was a new procedure for using moiré interferometry to evaluate singly curved diffraction gratings. This new procedure completely eliminates uncertainties present in other methods.

1.1.2 Background

Throughout history, structural engineers have had to contend with the stress concentrating effect of open or filled holes in structural plates and shells. Engineers and mathematicians have been attempting to model this problem for more than a century. Kirsch (1898) determined the in-plane stress distribution in an infinite isotropic plate with an open hole. Two-dimensional solutions for this problem are easily implemented and can be found in almost any elasticity book. Solutions for plates with finite dimensions are not as readily obtained or implemented, but are still available (Howland, 1930; Savin, 1969). In general, the problem of an open hole in a thin homogeneous, isotropic plate subject to in-plane loading is adequately modeled using two-dimensional analyses. The actual behavior, however, in plates that are nonhomogeneous or manufactured from anisotropic materials is poorly approximated by these isotropic two-dimensional analyses. Infinite orthotropic plates with open holes were modeled by Green and Zerna (1954) while investigating stress concentrations in wood. Savin (1969) and Lekhnitskii (1968) also produced infinite orthotropic plate solutions as well as infinite anisotropic plate models.

Fiber-reinforced, laminated, composite materials are now routinely used in the manufacture of structural plate and shell components. Plates manufactured with these materials can be modeled using a two-dimensional theory known as classical laminate theory (CLT) (Jones, 1975). Composite plates with holes have also been modeled using various two-dimensional analyses (Green and Zerna, 1954; Savin, 1969; Greszczuk, 1972; Lekhnitskii, 1968; Rowlands, *et al.*, 1973). Analyses on composites with multiple layers and multiple fiber orientations typically smear the layer properties through the thickness to produce an equivalent, one-layer orthotropic or anisotropic plate. These approaches with smeared properties can accurately represent the global behavior of a composite plate or shell, but they do not adequately model the complex, three-dimensional stress behavior in regions near traction-free edges.

Free-edge effects can be caused by mismatches in the Poisson's ratios of neighboring plies (Pagano, 1974). They can also occur because of differences in the axial-to-shear strain coupling behavior in neighboring plies (Pipes and Pagano, 1970). The study of this free-edge phenomenon has been intense over the past few decades. Most of the studies have focused on the edge effects in simple, straight-edged composites loaded uniaxially. Various types of stress analyses were performed, including approximate elasticity solutions (Pipes and Pagano, 1974), finite difference analyses (Altus, *et al.*, 1980; Pipes and Pagano, 1970), finite element method (FEM) (Dong and Goetschel, 1982; Herakovich, *et al.*, 1985; Wang and

Crossman, 1977; Whitcomb, *et al*., 1982), boundary-layer theory (Wang and Choi, 1982a; Wang and Choi, 1982b), higher-order plate theory analysis (Pagano, 1974), and variational methods (Kassapoglou and Lagace, 1986; Kassapoglou and Lagace, 1987; Pagano, 1978). Attesting to the complexity of the problem, results of these analyses sometimes did not agree well, even to the extent of predicting conflicting signs of interlaminar stresses as well as conflicting magnitudes. Free-edge effects on straight edges were also examined experimentally. Experimental investigations have used geometric moiré (Oplinger, *et al*., 1974; Pipes and Daniel, 1971) and moiré interferometry (Guo, *et al.*, 1992; Hale and Adams, 1996; Herakovich, *et al.*, 1985; Perry and McKelvie, 1993b) to quantify strains on the faces and edges of composites. Researchers have also examined the modes of failure (Herakovich, 1981; Pagano and Pipes, 1973) and onset of delamination (Perry and McKelvie, 1993b; Kim and Soni, 1984) for comparison with theory.

Analytical efforts have attempted to investigate the edge effect phenomenon in models of composites with holes. As with the straight free-edge case, various analytical techniques have been employed. These include the finite element method (Barboni, *et al.,* 1995; Carlsson, 1983; Lucking, *et al.,* 1984; Rybicki and Schmueser, 1978; Thompson and Griffin, 1990; Raju and Crews, 1982; Nishioka and Atluri, 1982), boundary value methods (Folias, 1992; Ye and Yang, 1988; Yen and Hwu, 1993), and variational approaches (Saeger, 1989). Experimental efforts on this subject have also taken several approaches. Most have been associated with two-dimensional analyses or analyses that neglect composite edge effects. Of these, several authors explored the stress and strain behavior around holes using optical methods (such as geometric moiré, diffraction moiré, and photoelasticity) and/or strain gages (Asundi and Yang, 1993; Rowlands, *et al.,* 1973; Serabian, 1991; Tan and Kim, 1990). Lekhnitskii or Savin anisotropic two-dimensional stress analyses in conjunction with mechanical testing have also been used to examine and predict laminate strength (Lo, *et al.,* 1983; El-Zein and Reifsnider, 1990; Whitney, *et al.,* 1984). One author used strain gage data from the face of the composite in conjunction with failure observation for comparison with three-dimensional finite element results (Carlsson, 1983). Two purely experimental investigations using optical methods and strain gages examined the stress and strain distributions on the faces of composites and on the curved free-edge surface inside the hole (Boeman, 1991; Daniel, *et al*., 1974). The consideration of nonlinear behavior was discussed in Daniel *et al*. (1974) and Serabian (1991).

A novel numerical approach called SVELT, based on a cubic spline approximation of displacements and interlaminar stress components, has been recently applied to model laminated composites containing open holes (Iarve and Soni, 1993b; Iarve, *et al.,* 1994; Iarve, 1996). Pullman and Schaff (Pullman and Schaff, 1996) have shown that for a cross-ply laminate, the SVELT model requires four times fewer degrees of freedom than the finite element method. SVELT results have been compared with experimental results by moiré interferometry and shown to accurately calculate in-plane strains on the surface of a relatively complex 28-ply composite (Schaff, *et al.*, 1996).

1.1.3 Motivation

SVELT is a relatively new method for modeling laminated composites with holes, and it requires validation. There are several methods for validating a new modeling technique. First, results can be compared with other results from generally accepted modeling techniques. The second method involves comparisons with experimental observations. Experimental comparisons involve either direct numerical comparisons or phenomenological comparisons. Comparing hard numbers like strain or displacement with an appropriate experimental technique (e.g., strain gages or moiré interferometry) can directly show how well a model performs. Phenomenological observation of such things as ply cracking or delaminations can also be used to corroborate the predictive capabilities of a model.

The techniques developed in this research were designed to eliminate uncertainties that existed with other methods. The new methods were intended for the measurement of displacement and strain variations on the cylindrical surface of a hole with improved quantitative accuracy. These measurements and the accompanying phenomenological observations are aimed at specifically providing information for validation of the SVELT modeling method as well as providing evidence for further model development.

1.2 Review of Literature

1.2.1 Interlaminar Stresses in Straight-Edged Composites

The principal cause for the existence of interlaminar stresses in composite materials is a mismatch in material properties between neighboring plies. Laminated plate theory requires that a symmetric laminate deform under a state of plane stress. For this to be true in composites with layers of different materials, tractions would be required on edges that should be traction free (Pipes and Pagano, 1970). Two simple types of laminates can be used as examples to describe the main characteristics of three-dimensional interlaminar stresses. These are angle-ply laminates with plies oriented at either $+\theta°$ or $-\theta°$ and cross-ply laminates with plies oriented at 0° and 90°. Schematics of laminates of these types are shown in Figure 1.1 with an assigned coordinate system that will be used throughout this document.

There are two types of material property mismatches that are significant to tensile loading configurations. The Poisson's ratio, defined as the negative of the ratio of transverse strain to axial strain, varies with ply angle (Equation 1.1a). The coefficient of mutual influence (Lekhnitskii, 1963), defined as the ratio of the in-plane shear strain to axial strain, also varies with ply angle (Equation 1.1b). Consequently, these material properties can change precipitously at ply interfaces.

$$\text{(a)} \quad \nu_{xy} = -\frac{\varepsilon_y}{\varepsilon_x} \qquad \text{(b)} \quad \eta_{xy,x} = \frac{\gamma_{xy}}{\varepsilon_x} \tag{1.1}$$

A schematic of an angle-ply laminate loaded in tension is drawn in Figure 1.2. A free-body diagram of a unit length of one layer of an angle-ply laminate indicates an unbalanced force problem similar to the cross-ply situation. Plate theory only accounts for an in-plane shear stress, τ_{xy}. This stress will create a global moment that must be compensated by an interlaminar shear stress distribution, $\tau_{xz}(y)$. Whitney *et al*. (1984) calls this type of edge effect the First Mode Mechanism. These interlaminar stresses have been shown, as will be discussed later, to be of significant magnitude only in the boundary region near the traction-free edge.

Figure 1.3 shows a schematic of a cross-ply laminate loaded in tension. A cross-section along AA′ is shown in Figure 1.3 and illustrates how individual laminae would deform transversely if the laminae were free from neighboring ply constraints. Two free-body diagrams of the shaded part of the top ply are also shown. One free-body diagram is unbalanced as predicted by plane stress plate theory. Plate theory only predicts in-plane stresses; and since no traction was applied to the free-edge, the resulting free-body diagram is not in equilibrium. Figure 1.3 also shows a balanced free-body diagram that assumes the existence of two other components of stress. The distribution of interlaminar shear stress $\tau_{yz}(y)$ equilibrates the forces generated by σ_y in the y-direction. However, the interlaminar normal stress $\sigma_z(y)$ is needed to counteract a moment induced by $\tau_{yz}(y)$. The $\sigma_z(y)$ distribution must balance forces in the z-direction by itself and therefore must have regions of both compressive and tensile values. Whitney *et al*. (1984) labels this type of edge effect the Second Mode Mechanism. As with the previous example, this interlaminar shear stress is significant only in the boundary region near the traction free edge.

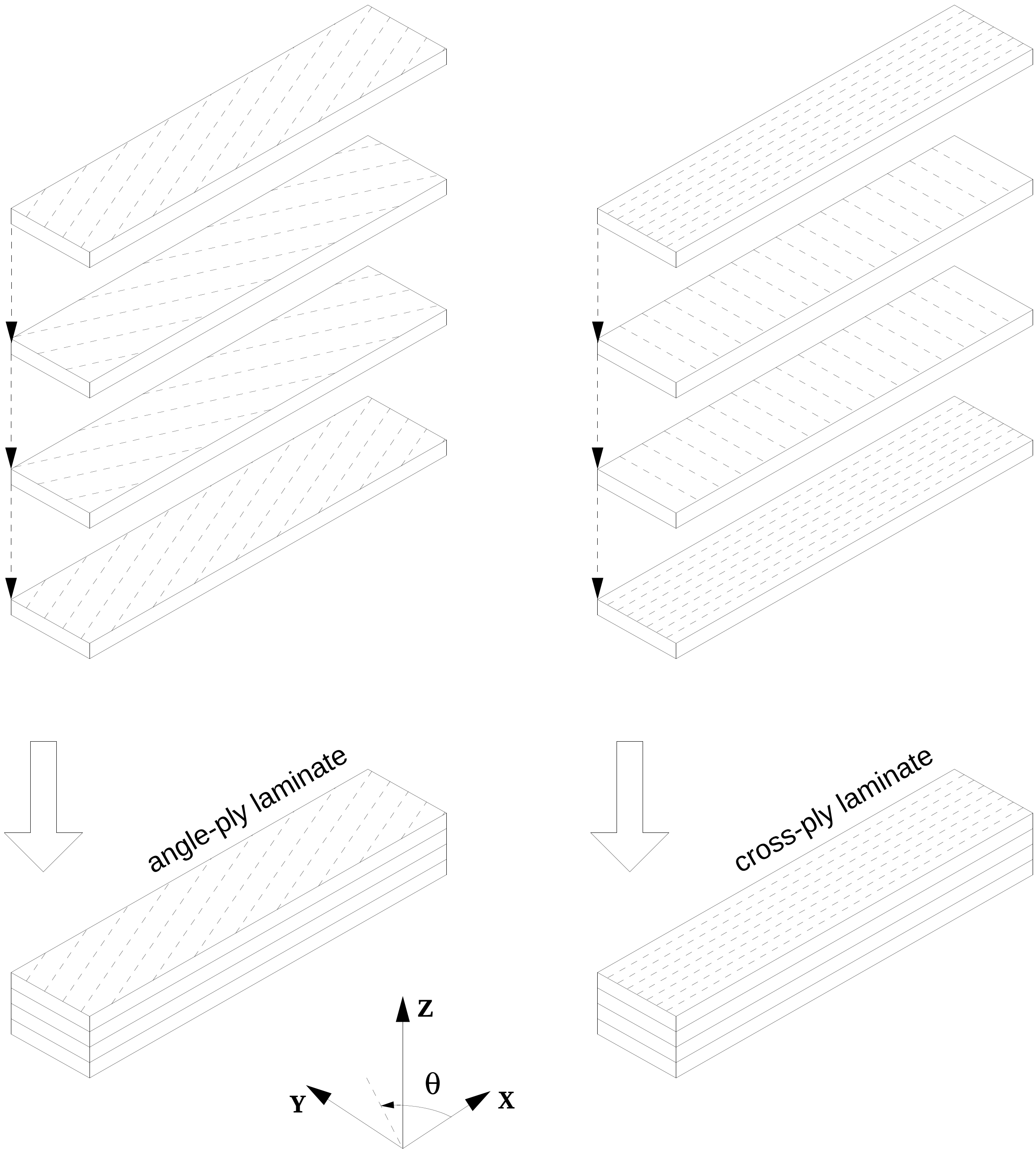

Figure 1.1: Schematic of an angle-ply and a cross-ply laminate (dotted lines represent fiber directions).

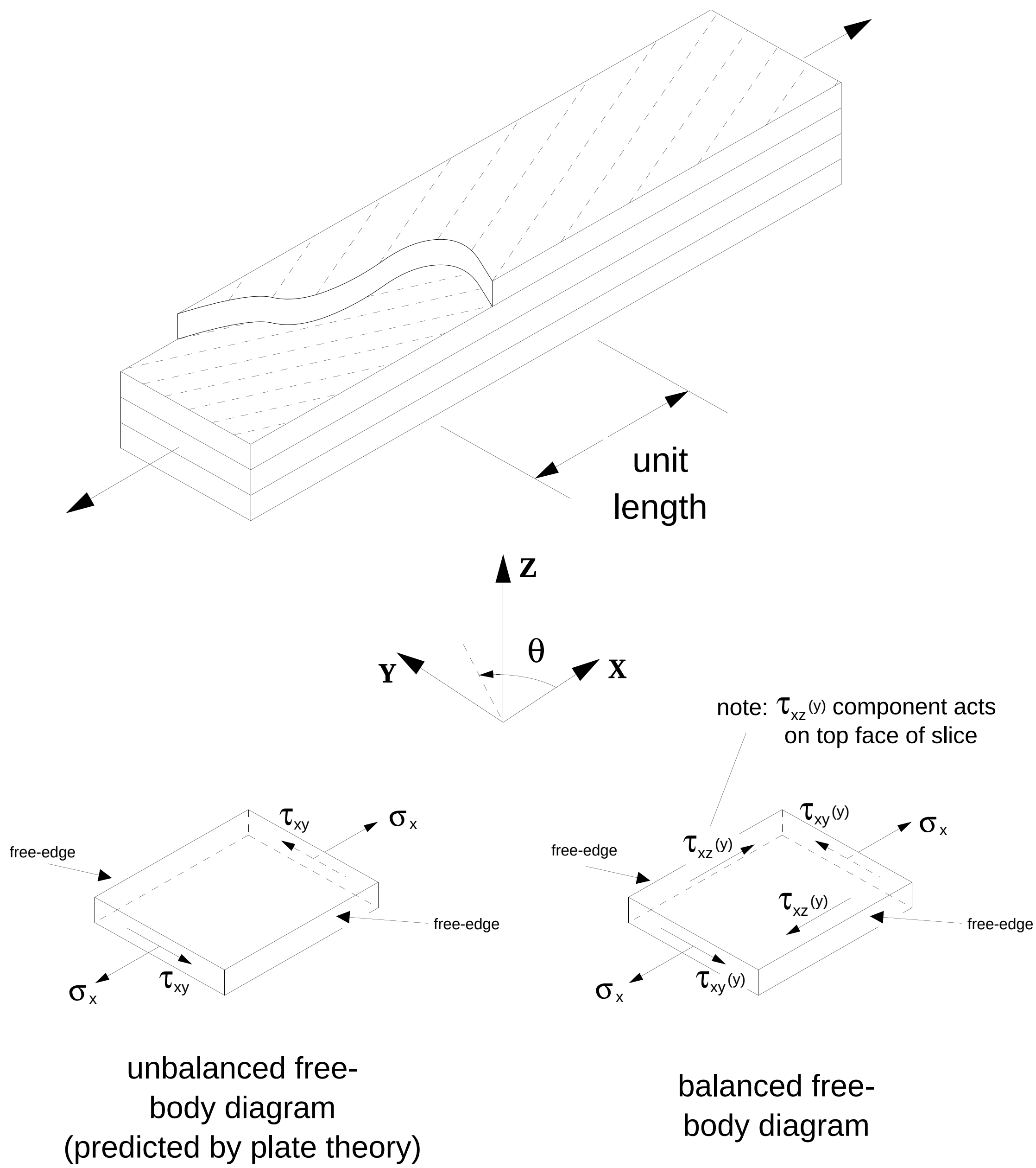

Figure 1.2: Schematic of an angle-ply laminate under load with two free-body diagrams of a unit length of the bottom ply.

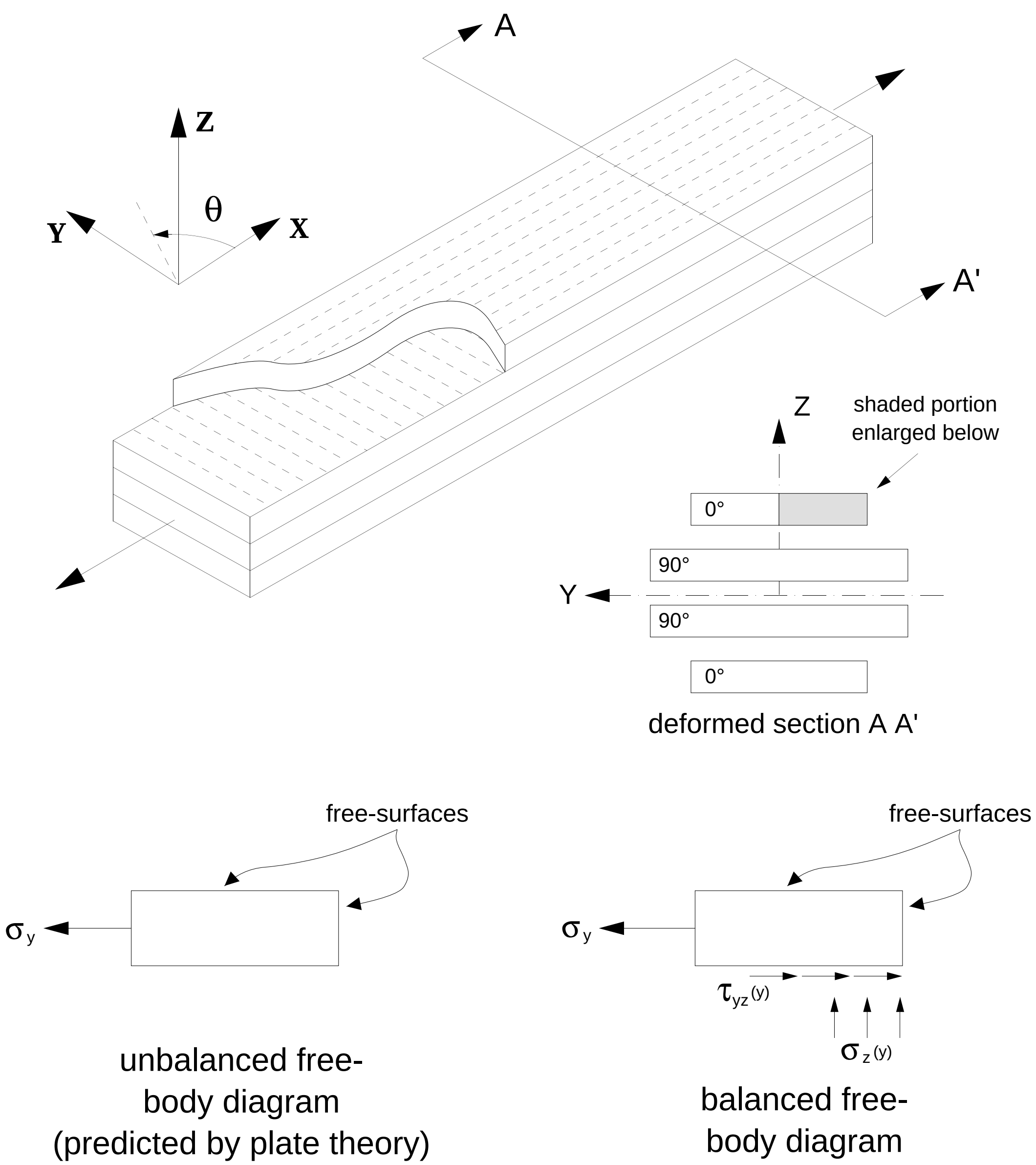

Figure 1.3: Schematic of a cross-ply laminate under load, a deformed cross-section, and two free-body diagrams.

Angle-Ply Laminates

One of the first attempts to model a composite laminate and include free-edge effects was conducted by Pipes and Pagano (1970). An exact elasticity formulation was developed for a four-layer, symmetric angle-ply laminated composite under "uniform axial extension." The phrase "uniform axial extension" refers to the class of problems where ε_x is constant and all stress components are independent of the axial coordinate, x. The governing set of equations was solved using the finite-difference method. A $[+45°/-45°]_s$ laminate of typical graphite/epoxy construction was modeled. This model predicted a rapid increase in τ_{xz} near the free edge that indicated possible singular behavior. The model also predicted a slight decrease in the axial stress, σ_x, and a decrease of in-plane shear stress, τ_{xy}, to zero at the free edge. Interestingly enough, however, the model showed the existence of the three other components of stress. CLT does not predict any σ_y for this laminate, and intuition would expect that due to the matched ν_{xy} of each layer that σ_y should be zero throughout. As a result of the predicted σ_y, though, τ_{yz} and σ_z also must exist as suggested by the discussion in the previous section. σ_y and τ_{yz} approach zero at the free edge, as is necessary to satisfy the traction-free edge condition. The magnitudes of σ_y, σ_z, and τ_{yz} relative to σ_x are quite small, whereas the magnitude of τ_{xy} is nearly half as large as σ_x. The shear component, τ_{xz}, possibly approaches infinity at the free edge.

A very important and useful result from the work accomplished by Pipes and Pagano (1970) is that the stress components induced by the free edge rapidly decay with distance from the free edge. The CLT solution is recovered at a small distance from the free edge. The region of deviation from CLT (called the boundary layer) was found to be independent of laminate width and was determined to be approximately one laminate thickness.

The functional form of the axial displacement distribution proposed by Pipes and Pagano (1970) was experimentally verified by Pipes and Daniel (1971). Geometric moiré (Dally and Riley, 1965; Durelli and Parks, 1970) was used on the face of a tensile-loaded $[+25°_4/-25°_4]_s$ laminate by Pipes and Daniel (1971). The predicted axial displacements matched the moiré results quite well. Also, the moiré results supported the finding that the boundary layer region was approximately equal to one laminate thickness.

Pipes and Pagano revisited the problem of edge effects in angle-ply laminates by constructing an approximate elasticity solution (Pipes and Pagano, 1974). A tractable solution process was derived by making two of the three insignificant components of stress (σ_y and σ_z) identically zero. This approximation results in a violation of equilibrium in the y- and z-directions. The compatibility equations, however, are satisfied. Comparison with their previous numerically solved exact elasticity solution (Pipes and Pagano, 1970) along the ±45° interface yielded a very close match for τ_{xz}. Analyses by the new solution technique verified that the boundary-layer is approximately equal to the laminate thickness. The authors reported that changes in ply orientation effect the distribution of stresses within the boundary-layer, but do not greatly effect the boundary-layer extent.

A comparison of experimentally and analytically obtained surface and edge displacements was made by Oplinger *et al.* (1974). A "layered plate" model was developed for angle-ply laminates. It consisted of fiber layers and matrix layers. For verification, geometric moiré was used to measure the displacements on the face and the edges of several different tensile-loaded $[+\theta/-\theta]_s$ type laminates of boron/epoxy and graphite/epoxy construction. Comparisons of axial displacements on the faces of $[+10°_4/-10°_4]_s$ laminates of both material systems yielded close correlation between experiment and analysis. For laminates with larger θ values, the match was not as close. Edge data comparison for the $[+20°_4/-20°_4]_s$ boron/epoxy laminate yielded a close match when the theoretical data was scaled by a constant multiplier. The authors claim that attention should be focused on the roll of nonlinear response and viscoelastic relaxation to explain differences in their model results and experimental results.

Altus *et al.* (1980) used a modified finite difference scheme to analyze symmetric ±10°, ±20°, and ±30° graphite/epoxy laminates. Results were presented for the ±30° case along the interface. Unfortunately, confident comparisons with results from Pipes and Pagano (1970; 1974) are impossible since their model involved ±45° laminates. Similar trends should exist, however. Altus *et al.* (1980) showed that τ_{xz} became very large as the free edge was approached. Similar results were also presented by Pipes and Pagano (1970). The predicted distribution of τ_{yz} was completely different from the Pipes and Pagano (1970) model. The variation of σ_z was nearly the same as the Pipes and Pagano (1970) model, except that the Altus *et al.* (1980) model predicted a rapid shift from tension to compression very near the free edge.

Wang and Crossman (1977) developed a finite element model for several composite laminate stacking sequences. Included in the examination was a symmetric ±45° laminate that the authors compared with the Pipes and Pagano (1970) finite difference results. Along the ±45° interface, a relatively close match was seen for τ_{xz} and $\tau_{yz,}$ except that τ_{yz} was not found to approach zero as is necessary to satisfy the traction-free edge condition. Axial stress and τ_{xy} did not match well in the boundary-layer where again the traction-free edge condition was not satisfied by the τ_{xy} component. The distribution of σ_z was found to be almost exactly the opposite (with respect to sign) as that reported in the Pipes and Pagano (1970) paper. Note that in Wang and Crossman's (1977) paper, σ_z was plotted with the incorrect sign as reported in Whitcomb *et al.* (1982).

Pagano (1978) used a variational theorem devised by Reissner (1950) to develop a solution method for stress fields in composite laminates. A set of requirements was enforced by the model. These are that generally all six stress components are present, that traction and displacement continuity conditions at ply interfaces must be satisfied, and that "layer equilibrium" must be satisfied. Layer equilibrium means that force and moment resultants acting on the free edges of a layer and the interfacial stresses must lead to vanishing force and moment resultants. In-plane stresses were assumed to vary linearly with z through a given layer. In practice, the author often sub-divided each ply into several layers to improve solution accuracy. The results for a $[\pm 45°]_s$ laminate were compared with the Wang and Crossman (1977) FEM results. The stress components, σ_x and τ_{xy} , within the center of the +45° ply were found to agree quite well. At the interface between the ±45° plies, τ_{xz} was found to agree very well.

The reliability of using FEM for calculating free-edge stresses was examined by Whitcomb *et al.* (1982). In this paper, the authors examined two analytically solvable problems that contained stress discontinuities or singularities. They convincingly show that, for these two model problems, the FEM predicts the correct values of stress except in a boundary region near the stress discontinuity or singularity. This boundary region is generally restricted to the two elements nearest the stress singularity or discontinuity. Whitcomb *et al.* (1982) further present results from a refined FE model of a $[\pm 45°]_s$ laminate. They found that the σ_y, τ_{yz}, and τ_{xy} components of stress violated the traction-free edge condition. This was attributed to the nonsymmetric nature of the stress tensor at a singularity (Whitcomb *et al.*, 1982).

An approach using Lekhnitskii's stress potentials and eigenfunction expansion was examined by Wang and Choi (1982a; 1982b). With this solution methodology, it was shown that in the general case of a mismatch in ν_{xy} and/or $\eta_{xy,x}$ of neighboring plies a singularity exists. These singularities in laminated composites were found to be much weaker than singularities associated with elastic cracking problems. Wang and Choi (1982a; 1982b) compared their interfacial results with interfacial stresses obtained with the Pipes and Pagano (1970) model and the Wang and Crossman (1977) model. Close correlation exists between the Wang and Choi (1982a; 1982b) model and the Wang and Crossman (1977) model except for the τ_{yz} component (note: the σ_z component of stress from Wang and Crossman should be inverted). All models predict similar distributions of τ_{xz}.

Herakovich *et al.* (1985) used moiré interferometry to optimize a finite element model for an angle-ply laminate. The axial displacements were measured along the free edge of various $[+\theta_2/-\theta_2]_s$ laminates. The shear strain, γ_{xz}, was calculated from the displacement patterns and compared with FEM results with various node spacing and element types. It was determined that the most realistic and trouble-free model was constructed of a four-node isoparametric, rectangular element grid. Also documented was the finite nature of the shear strain concentration which indicates that a real composite does not possess the type of singularity found in a mathematically perfect model. Considerable variation in shear strain along the edge of the tested composites was also found and was attributed to nonuniformities in the composite materials. This observation has been strengthened by the recent work performed by Hale and Adams (1996) who document large variations in shear strain with slight in-plane fiber misalignments of a ply.

Kassapoglou and Lagace (1987) produced a closed form solution for analysis of uniaxially loaded angle-ply and cross-ply laminates that uses the Force Balance Method and the minimization of complementary energy. For the angle-ply solution, the authors make use of the fact that CLT predicts a zero σ_y for each ply. They imposed this condition throughout the laminate and come to the conclusion that σ_z and τ_{yz} must also be zero. The σ_z=0 result was indicated in a previous paper where the authors employed the Force Balance Method (1986). Interfacial results of τ_{xz}, τ_{xy}, and σ_x for a [±45°]s laminate were compared with a finite difference solution (Pipes and Pagano, 1970), a finite element model (Wang and Crossman, 1977), and an eigenfunction expansion solution (Wang and Choi, 1982b). All predictions of τ_{xz} match well. Differences were found in the predicted distributions of τ_{xy} and σ_x. The two models (Pipes and Pagano, 1970; Kassapoglou and Lagace, 1987) where τ_{xy} satisfies the traction-free boundary condition are similar, while the two models (Wang and Crossman, 1977; Wang and Choi, 1982b) which violate the traction-free edge condition are nearly identical.

Wang and Choi (1982a) have indicated that a singularity exists at the interface between ±45° plies at the free edge. Whitcomb *et al.* (1982) have concluded that the stress tensor is not symmetric and the traction-free condition does not need to be fulfilled at the singularity. Kassapoglou and Lagace (1987) note that Wang and Choi's (1982a) predicted singularity strength is weak and is only significant over a distance on the order of a fiber diameter. The question that arises at this point is, who is right? Does the traction-free edge condition hold at the singularity? Clearly the imposition of this boundary condition effects the stress results as mentioned in the previous paragraph. A conclusive answer in the literature to this question has eluded the author.

Several of the references discussed above have indicated that σ_y, σ_z, and τ_{yz} are insignificant compared with the other three components of stress in angle-ply laminates. Jones (1975) states that the presence of a mismatch in $\eta_{xy,x}$ and none in ν_{xy} produces only τ_{xz}. That is, an angle-ply laminate will not produce σ_y, τ_{yz}, or σ_z but only τ_{xz}. Kassapoglou and Lagace (1987) used the CLT results of σ_y=0 to produce a model that showed σ_z and τ_{yz} were also zero. Pipes and Pagano (1974) created an approximate elasticity solution that was based on setting two of these three insignificant stress quantities to zero. They found, however, that the resulting stress state violated equilibrium in the y- and z- directions.

The moiré interferometry results of Guo *et al*. (1992), at the interface between ±45° layers in a quasi-isotropic laminate, show that σ_z probably does not vary across the interface. In this case, there exists a nearly constant and relatively large σ_z across the ±45° group of plies due to the nature of the tested $[90°_2/0°_2/+45°_2/-45°_2]_{3s}$ laminate instead of the small σ_z predicted for an angle-ply laminate. Whitcomb *et al*. (1982) predicted the distribution of σ_z across the ±45° interface on the free edge and show a variation. While these example laminates are not identical, the variable nature of σ_z predicted in the $[\pm 45°]_s$ laminate near the interface on the free edge should also be present in the $[90°_2/0°_2/+45°_2/-45°_2]_{3s}$ laminate. One thing to note, however, is that the predicted magnitudes of σ_z in a $[\pm 45°]_s$ laminate are about an order of magnitude less than the applied stress and may require enhanced moiré interferometry techniques to resolve them.

$[0°/90°]_s$ and $[\pm\alpha/\pm\beta]_s$ Type Laminates

Pagano and Pipes (1970) proposed a distribution of σ_z necessary to balance the moment caused by τ_{yz} in laminates with ν_{xy} mismatches. In particular they examined a $[\pm 15°/\pm 45°]_s$ laminate and a $[\pm 45°/\pm 15°]_s$ laminate. Evidence from Foye and Baker (1970) showed that the tensile fatigue strength of these two laminate configurations was markedly different, a result not predictable with CLT. In their paper, Pagano and Pipes demonstrate with successive free-body diagrams (similar to those in Figure 1.3) that σ_z will be entirely tensile along the free edge for the $[\pm 15°/\pm 45°]_s$ laminate, thus promoting delamination, while σ_z will be entirely compressive along the free edge for the $[\pm 45°/\pm 15°]_s$.

Pagano (1974) modified a higher order plate theory proposed by Whitney and Sun (1973) to calculate the interlaminar normal stress along the central plane of a $[0°/90°]_s$ laminate. A thickness stretch deformation factor was added to the assumed displacement form of the Whitney and Sun (1973) model which already contained shear deformation components. The predicted distribution of σ_z along the mid-plane of a $[0°/90°]_s$ laminate was compared with a finite difference elasticity solution developed by Pipes (1972). Both methods calculate similar σ_z distributions which show that σ_z could be singular at the free edge. The prediction also showed that the boundary-layer is approximately a laminate thickness in width.

The finite element solution of Wang and Crossman (1977) for a $[0°/90°]_s$ laminate was compared by Pagano (1978) to his Reissner's variational model (both of these methods were discussed in the previous section). Comparisons were made between σ_z distributions along the central plane and the distributions of σ_z and τ_{yz} along the 0°/90° interface. Excellent agreement was found, except when the variational model was not refined enough and where the finite element model failed to meet the traction-free edge condition with τ_{yz}.

Kassapoglou and Lagace's (1987) minimum complimentary energy model was also applied to a $[0°/90°]_s$ laminate. As for the angle-ply laminate, they observed the CLT solution and found that the τ_{xy} component of stress was identically zero for this type of laminate. Formulation of their model with this information produce an identically zero τ_{xz}. The authors only present the σ_z component of stress varying at the $[0°/90°]_s$ interface; and, unfortunately, they mistakenly compare this with the Pagano (1974) and Pipes (1972) solutions at the mid-plane. Nevertheless, the comparison shows a relatively close match and any differences are similar to those shown in the Wang and Crossman (1977) paper for the same situation with a $[\pm 45°/0°/90°]_s$ laminate.

Comments on the Straight Free-Edge Problem

There are several important observations to note about the literature examined on the straight free-edge problem. There is little disagreement over the predicted distributions of the primary interlaminar stress components arising from the free edge in first and second mode problems (i.e., τ_{xz} for angle-ply laminates and σ_z for cross-ply laminates). The presented information for free-edge stresses in a $[0°/90°]_s$ laminate is primarily concerned with σ_z (probably due to this component's importance in determining delamination potential), and little is published about the other components. Specifically, only one mention of τ_{xz} was made [identically zero (Kassapoglou and Lagace, 1987)], a few papers discuss τ_{yz} (close agreement was demonstrated), and none of the papers reviewed mentioned anything about the distributions of σ_x, σ_y, and τ_{xy}. For angle-ply laminates, the research community seemed to be preoccupied with the importance of the σ_z distribution as well, even though is was shown to be small in all cases (except for possible singular behavior at the free edge). Little agreement was had for any of the insignificant components of stress arising from the free-edge effect (σ_z, σ_y, and τ_{yz}). Some have even claimed that only τ_{xz} arises from these types of laminates (Jones, 1975). There was much disagreement in the predicted effects of the free edge on the primary stress components, σ_x and τ_{xy}, depending on whether the traction-free edge condition was fulfilled or not fulfilled.

The most important things to glean from the previous discussion are as follows:

(1) Mode one problems primarily produce a large τ_{xz} distribution at the edge while mode two problems primarily produce a large σ_z and τ_{yz} distribution near the edge.

(2) The boundary-layer was shown to be generally around one laminate thickness in width.

(3) The singular nature of the interface between plies in mode one problems is probably a mathematical artifact as indicated in the Herakovich *et al*. (1985) paper and indicated by the Guo *et al*. (1992) data.

(4) Regardless of how the traction-free edge was handled, the variations of τ_{xz} in an angle-ply laminate were consistently reproduced. However, there was a significant difference in the distributions of σ_x and τ_{xy}, depending on the assumptions and approximations regarding the traction-free edge.

1.2.2 Plates with Open Holes

Mathematical Modeling

In 1898, Kirsch (1898) published an elasticity solution for an infinite isotropic plate with a hole loaded uniaxially. His solution is familiar to most students of elasticity. It is expressed as follows:

$$
\begin{aligned}
\sigma_r &= \tfrac{1}{2}p(1-\frac{a^2}{r^2}) + \tfrac{1}{2}p(1-\frac{a^2}{r^2})(1-\frac{3a^2}{r^2})\cos(2\theta) \\
\sigma_u &= \tfrac{1}{2}p(1+\frac{a^2}{r^2}) - \tfrac{1}{2}p(1+\frac{3a^4}{r^4})\cos(2\theta) \\
\tau_{ru} &= -\tfrac{1}{2}p(1-\frac{a^2}{r^2})(1+\frac{3a^2}{r^2})\sin(2\theta)
\end{aligned}
\tag{1.2}
$$

where r is the radius, θ is the angle measured from the axial centerline, p is the far-field load, and a is the radius of the hole. Infinite plate solutions are applicable to plates with hole-diameter to specimen-width ratios of less than 1/10. An elasticity series solution for uniaxially loaded finite width plates with holes was developed by Howland (1930). The procedure proved to be algebraically involved but quite successful.

Several researchers have examined infinite orthotropic and anisotropic plates with holes (Green and Zerna, 1954; Lekhnitskii, 1968; Savin, 1969). Green and Zerna (1954) produced an analytical model of an infinite orthotropic plate (modeling a wooden panel) with a stress concentration. Lekhnitskii (1968) and Savin (1969) used complex variable techniques to produce models of infinite orthotropic and anisotropic plates with open holes.

Other researchers have used two-dimensional solutions for composite strength predictions. Greszczuk (1972) employed a Green and Zerna (1954)-type solution to calculate the stress distribution around a hole in an orthotropic plate. He used a Hencky-Von Mises distortion energy failure criteria and found that the strength of composite plates is less sensitive to stress concentrations than isotropic plates. Whitney and Nuismer (1974) used an axial stress distribution of an isotropic infinite plate to predict the strength of a composite laminate. They proposed two simple stress failure criteria. The "point stress criteria" assumes failure occurs when the axial stress at some distance from the hole edge equals the unnotched failure stress. The "average stress criteria" assumes failure occurs when the average axial stress over some distance from the hole edge equals the unnotched failure stress. Whitney *et al*. (1984) refined the process by using a Lekhnitskii-type analysis to calculate the axial stress distribution for use in their average stress and point stress failure criteria. Lo *et al*. (1983) used a Savin (1969)-type solution to predict stresses around holes. They employed several failure criteria (maximum stress, maximum strain, and tensor polynomial) to predict progressive damage and failure of a composite laminate with a hole. El Zein and Reifsnider (1990) used an average of the Tsai-Wu failure criteria over some distance from the hole in conjunction with a Lekhnitskii stress solution to predict failure for off-axis unidirectional laminates (i.e., lay-ups such as [$+\theta°$]).

Three-dimensional finite element models of 14 laminated composites were analyzed by Rybicki and Schmueser (1978). One quarter of the top half of each laminate was modeled using three layers of elements. Several of the ply lay-ups contained ($+\theta°/-\theta°/-\theta°/+\theta°$) ply groupings. Rybicki and Schmueser combined the $\pm\theta°$ plies into a single ply assigned with the effective orthotropic properties of the ($+\theta°/-\theta°/-\theta°/+\theta°$) ply grouping. This was done in an attempt to reduce the FE model size. Unfortunately, this approach is drastically limiting. It probably predicts the interlaminar normal strains caused by the second mode type of mismatch (i.e., mismatch in ν_{xy}) between the ($+\theta°/-\theta°/-\theta°/+\theta°$) grouping and the other grouping of plies (typically $0°_2$ or $90°_2$) with reasonabe accuracy. It cannot, however, resolve any of the stresses induced by the first mode mismatch ($\eta_{xy,x}$) between the $+\theta°$ and $-\theta°$ plies.

Nishioka and Atluri (1982) presented a finite element analysis that contained special elements around the boundaries of the hole. Using a modified complimentary energy principle, the authors developed three-dimensional analytical stress solutions in the region near a hole boundary. These solutions were embedded into an assumed-stress hybrid element. Built into the special hole element were the following properties:

- the traction-free edge condition around the hole is automatically satisfied
- the z-direction stresses are continuous across ply boundaries
- the in-plane stresses are allowed to be discontinuous across a ply boundary.

The remainder of the laminate (away from the hole boundary-layer) was modeled using standard plane stress elements. A Lagrange multiplier technique was then applied to match the stress conditions between the special elements and the regular plate elements.

A large, sub-structured finite element model of a laminated composite was constructed by Carlsson (1983). A 28-ply $[\pm45°/0°_2/\pm45°/90°/0°_3/\pm45°/0°_2]_s$ graphite/epoxy laminate was modeled. Three 20-node elements were used through a ply thickness. Extensive sub-structuring was used to reduce the necessary computer requirements. Unfortunately, Carlsson (1983) employed incorrect symmetry conditions and modeled only one eighth of the laminate (i.e., one quarter of the top half of the laminate). The reason this is a problem is demonstrated in Figure 1.4. Any of the angle-plies, when symmetrized, become equivalent to the chevron arrangement shown in Figure 1.4. Clearly the finite element model does not correspond to the desired lay-up and will produce incorrect results, especially near the two planes of symmetry (x=0 and y=0). In spite of this problem, Carlsson (1983) obtained fairly close correlation between the FE model and two strain gages measuring axial strain near the hole.

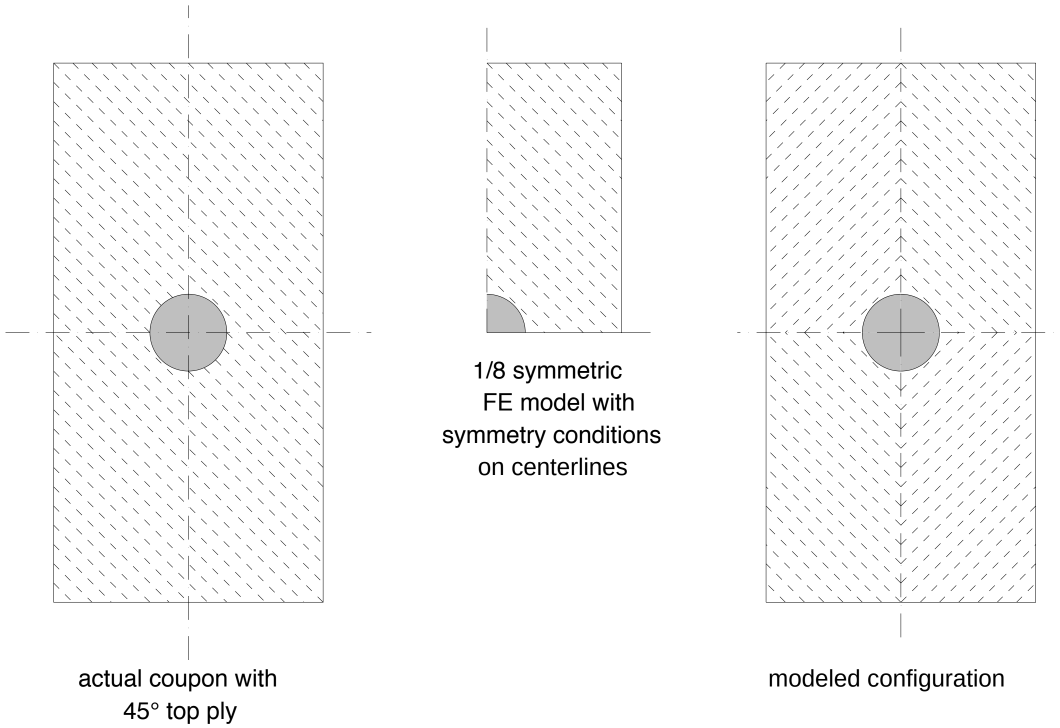

Figure 1.4: Schematic of incorrectly modeled symmetry conditions.

An exploration of the effect of varying the hole radius to laminate thickness ratio (R/t) on the interlaminar stresses in a $[0°/90°]_s$ laminate was reported by Lucking *et al*. (1984). They used a three-dimensional finite element approach with extensive use of "zooming" to reduce the necessary computer resources while enhancing the predicted interlaminar stress accuracy. This method coarsely modeled the entire laminate. A new, more refined FE model was constructed with the outside boundary located at a specified radius from the hole edge. Interpolated displacements obtained from the coarse model were then prescribed at the new boundary. The entire process was repeated once more to produce a very highly refined model of the boundary-layer around the hole. Generally, Lucking *et al*. (1984) found that the magnitudes of σ_z and $\tau_{\theta z}$ increased with increasing R/t ratios.

Two other notable finite element efforts are those of Thompson and Griffin (1990) and Barboni *et al*. (1995). Thompson and Griffin (1990) employed a "global/local" technique nearly identical to Lucking *et al*. (1984). They investigated several different $[0°/90°]_s$-type laminates with varying thicknesses and hole sizes.

They concluded that the magnitudes of interlaminar stresses grow with hole size up to some "critical" hole diameter and then begin to decline again for larger holes. Barboni *et al*. (1995) used a multilayer higher-order finite element formulation on a $[90°/0°]_s$ laminate and a $[-45/+45]_s$ laminate. They compared the results from the $[90°/0°]_s$ laminate with the Nishioka and Atluri (1982) model discussed previously, with a stress-based model by Ko and Lin (1992), and with the Rybicki and Schmueser (1978) model also discussed previously. Very close agreement in σ_θ distribution around the hole at the 90°/0° interface was seen between the Nishioka and Atluri (1982) model, the Ko and Lin (1992) model, and the Barboni *et al*. (1995) model. The comparison of σ_z predicted by all four models at the mid-plane around the hole showed little agreement in the predicted values. Unfortunately, Barboni *et al*. (1995) used incorrect symmetry conditions for the $[-45/+45]_s$ laminate. They modeled only half of the top half of the laminate and created a chevron type of arrangement similar to Carlsson's (1983). When compared with the predicted values of σ_θ at the laminate mid-plane from Nishioka and Atluri (1982), however, the match was close.

An approach similar to Nishioka and Atluri (1982) was presented by Yen and Hwu (1993). They built on Reiss and Locke's (1961) work that showed that a three-dimensional elasticity problem can be broken into two problems, each of two dimensions. They claim that the interior problem can be treated as a generalized plane stress problem and that the boundary-layer problem can be modeled as a generalized plane deformation (strain) problem. In Yen and Hwu's (1993) study, they used CLT to solve the interior problem and a finite element solution for the boundary-layer problem. A comparison of σ_z and $\tau_{\theta z}$ with Lucking *et al*. (1984) showed very close agreement

Two other boundary-layer approaches were examined by Folias (1992) and Ye and Yang (1988). Folias obtained a local asymptotic solution valid in the boundary-layer around an open hole in a laminated composite. The method shows that a singularity exists between any two plies at the hole edge that have a property mismatch. Other observations about the reported singularity are that it varies with angular location around the hole, that the singularity strength is smaller than in the isotropic laminated plate (laminated with isotropic materials of differing properties), and that the singularity depends on the material properties and orientations of the two respective laminae. Folias (1992) noted that macroscopic models do not account for the microscopic singularities present when fibers intersect the free edge at large angles and that these singularities will be large compared with those calculated with macroscopic models.

Ye and Yang (1988) solved the free-edge problem in a laminate with an arbitrary curved edge by superimposing an interior CLT solution with an asymptotic boundary-layer solution. Their boundary-layer solution was separated into a series of discrete problems around the perimeter of the curved free edge. Each of these solutions used the Kassapoglou and Lagace (1986) solution for interlaminar stresses as if each location were a straight free edge. The straight free edge problem modeled at each of the points around the curve corresponds to a straight free edged laminate with plies oriented exactly the same way as the curved edge composite's plies were oriented to the local tangent.

Initial development of a method using independent polynomial spline approximations of displacement and interlaminar stress components to analyze the three-dimensional stress state around a hole began with research presented by Bogdanovich and Iarve (1983). In this paper, the authors demonstrated a method for analyzing thick composite beams under dynamic bending using piece-wise polynomial approximation. Several two-dimensional and three-dimensional formulations using polynomial spline approximations for analysis of composite plates were published (Bogdanovich and Yarve, 1988; 1989; Bogdanovich and Iarve, 1992). Iarve and Soni (1993a) presented a three-dimensional spline approximation solution for laminated composites with holes. The Cartesian coordinates used by the authors proved to require a very large number of degrees of freedom to give satisfactory results. A curvilinear transformation (also based on spline approximations) applied to this problem resulted in a model capable of analyzing practical composites containing holes (Iarve and Soni, 1993a; Iarve and Soni, 1993b). Finally, Iarve (1996) presented a comparison of the SVELT model with a closed form asymptotic solution, and it was demonstrated that a close match existed between the two modeling techniques. A detailed comparison of SVELT and FEM was performed by Pullman and Schaff (1996). They analyzed isotropic, orthotropic, and cross-ply plates with holes and found that the results of both models agreed quite well. FEM, however, required three to five times the number of degrees of freedom necessary to produce converged results at the edge of the hole. Recent developments with the SVELT modeling effort indicate that the required number of degrees of freedom may be reduced by a factor of four (Iarve, 1997).

Experimental Efforts

Rowlands *et al*. (1973) examined glass/epoxy [0°/+45°/-45°/0°/90°/0°/-45°/+45°/0°] laminates containing holes with geometric moiré, strain gages, and photoelastic coatings for comparison with a two-dimensional finite element analysis and a Lekhnitskii (1968)-type solution. Five large, but thin, laminates were produced (66 cm by 25 cm by 2.2 mm with 2.54 cm holes). The large size facilitated greater accuracy of measurements with the experimental techniques. Geometric moiré was tried with transmitted light on one specimen and with reflected light on another specimen and was found to work well in either configuration. Strain gages were extensively applied over the face of all composites and on the inside faces of the holes. A 1 mm-thick birefringent coating was applied to the face of all specimens. Comparisons between the analytical and experimental results in the linear range were quite close. The authors concluded that strain gages remain highly effective for use on composites, that photoelasticity had to be carefully used due to the anisotropy of the composite, and that moiré analysis was extremely effective with composites.

Continuing this work, Daniel *et al*. (1974) examined the effect of the stacking sequence and material choice on the behavior of composite materials with holes. Three material systems were studied (glass fiber-, boron fiber-, and graphite fiber-reinforced epoxy). Ten basic stacking arrangements of 0°, 90°, and ±45° plies were included in the study. Strain gages, birefringent coatings, and geometric moiré were used. The testing of [0°/+45/-45°/0°/90/0°/-45/+45°/0°] laminates of all three material systems revealed that the glass/epoxy behaved nonlinearly well before failure. The boron/epoxy showed strain redistribution near the hole boundary just before failure, and the graphite/epoxy material displayed nearly linear behavior to failure. In general, the authors noted that the strength-reduction factor varied with lay-up and was highest in lay-ups that contained strong tensile σ_z and/or large $\tau_{\theta z}$.

Tan and Kim (1990) used strain gages to measure strain concentrations in composites with holes. They developed a procedure to decouple nonlinear and damage effects on the strain concentration from the linear contributions. They first examined the quality of the drilled hole visually and with x-rays (after a bit of load had been applied and removed). If no damage was found, the strain distribution across the face was measured at many loads, and the linear contribution to strain concentration was calculated. Finally, they discussed how to determine whether any variations at higher load were due to nonlinear material behavior or due to damage (or both). The authors claim that a careful procedure such as the one described must be applied whether strain gages, moiré, or photoelasticity are being used.

The creep behavior of graphite/epoxy laminates with holes was examined by Tuttle and Graesser (1990) with moiré interferometry. Their ten-hour, room temperature tests showed that fiber-dominated laminates showed no viscoelastic behavior while matrix-dominated specimens exhibited viscoelastic effects. A numerical/digital method was developed to calculate strain distribution from the moiré fringe patterns over the whole field of view.

An experimental program was conducted by Schaff *et al*. (1996) in an attempt to examine the accuracy of the SVELT modeling technique. Tensile-loaded, 28-ply IM7/5250-4 laminates were examined with phase-shifting moiré interferometry, modeled with SVELT, and examined with x-rays. Comparisons between the SVELT and moiré strain results showed very close agreement. Initial damage results demonstrated that SVELT could routinely predict the general location of damage by using a simple transverse stress failure criteria. A deficiency that was expressed, however, was that to date there has been no verification of the SVELT solution for thermal stresses in the vicinity of the hole, and that the inclusion of thermal deformation alters the stress state around the drilled hole in the loaded composite.

As stated before, much of the experimental research contained in this document builds on the pioneering efforts of Boeman (1991). Boeman examined the interlaminar deformations in composite laminates with holes using moiré interferometry. The experimental technique was utilized directly on the curved, free surface of the hole and was able to record sub-ply variations in the circumferential-direction and z-direction displacement fields. Details of his research are discussed in a following section.

1.3 Techniques Used in This Study

1.3.1 Analytical Techniques

Finite Width, Isotropic Strip with a Hole

Howland's (1930) solution expresses a stress function, χ, as a series of individual stress functions that all satisfy the biharmonic equation ($\nabla^4\chi=0$), where

$$\chi \equiv \chi_0' + \chi_0 + \chi_1 + \chi_2 + \ldots \tag{1.3}$$

This series has the following properties:

χ_0' forces χ to have the proper stresses at infinity, but none at the strip edges,

χ_0 forces χ to satisfy the traction-free boundary conditions at the hole edge, thus giving the infinite plate solution.

χ_1 forces χ to satisfy the traction-free boundary conditions at the strip edges, but adds stress at the hole edge,

χ_2 forces χ to satisfy the boundary conditions at the hole edge, but adds stress at the strip edge,

and so on. Each new term adds stresses to one of the traction-free edges, but each iteration decreases the magnitude of the added stresses. Howland presents a method that allows the calculation of χ_{2r+1} and χ_{2r+2} from χ_{2r}. The series can be truncated at any point where the desired boundary condition is exactly satisfied and the other boundary condition is satisfactorily met.

A solution based on Howland's (1930) work was implemented in the present research using the computer program Mathematica. The results were used to verify the moiré interferometry techniques developed for this research program. The model was constructed to exactly match the control specimen which was fabricated from 7075-T6 aluminum. The series solution was truncated such that the boundary conditions at the hole would be exactly satisfied, but those at the straight free edge would only be approximately satisfied. In practice, however, the series was carried out far enough that the straight free-edge boundary conditions were satisfied over an acceptable area. Convergence of the model was verified out to at least a specimen width from the center of the hole in the axial direction.

Spline Variational Elastic Laminate Technology

The analysis package SVELT is a computer program developed with the methodology described in Iarve (1996). It is based on independent spline approximations of the displacement components u, v, and w for a given ply as shown in Equation 1.4.

$$
\begin{aligned}
u(\rho,\phi,z) &= \sum_i \sum_j \sum_k U_{ijk}\left[R_i(\rho)\right]\left[\Phi_j(\phi)\right]\left[Z_k(z)\right] \\
v(\rho,\phi,z) &= \sum_i \sum_j \sum_k \mathbf{V}_{ijk}\left[R_i(\rho)\right]\left[\Phi_j(\phi)\right]\left[Z_k(z)\right] \\
w(\rho,\phi,z) &= \sum_i \sum_j \sum_k W_{ijk}\left[R_i(\rho)\right]\left[\Phi_j(\phi)\right]\left[Z_k(z)\right]
\end{aligned}
\tag{1.4}
$$

The generalized curvilinear coordinates are ρ and ϕ which are mapped into the x–direction and y-direction. U_{ijk}, V_{ijk}, and W_{ijk} are the unknown spline coefficients. $R_i(\rho)$, $\Phi_j(\phi)$, and $Z_k(z)$ are the basic sets of spline functions for each coordinate. Expressions for interlaminar tractions are constructed with similar expressions. A system of equations is constructed with the displacement equations, the interlaminar tractions, and the prescribed tractions using the principle of minimum potential energy. After the displacement boundary conditions have been enforced, the spline coefficients can be solved from the remaining set of equations. Continuous functions for displacements are found throughout homogeneous regions. The strain-displacement relations and the constitutive relations can be used at any point in the homogeneous region to determine stress and strain.

Conventional finite elements produce field discontinuities at the boundaries of every element. SVELT maintains continuity throughout a homogenous ply while allowing strain discontinuity at ply interfaces in order to achieve interlaminar traction continuity.

1.3.2 Experimental Techniques

Overview of Moiré Interferometry

Moiré interferometry is an optical interferometry technique that is capable of measuring in-plane displacements with high sensitivity (Post *et al.*, 1994). It can be described in terms analogous to an experimental technique known as geometric moiré (Dally and Riley, 1965). This analogy does not fully explain the physics of moiré interferometry, but it is useful since the governing equations for determining displacements using the two techniques are identical. A rigorous explanation of the physics and principles of moiré interferometry can be found in the literature (Dai, *et al.*, 1990; Post *et al.*, 1994).

In geometric moiré, a ruled bar and space grating of relatively low frequency (two to four lines per mm) is molded onto the surface of a flat specimen. A bar and space grating of identical frequency and orientation (called the reference grating) is superimposed over the specimen grating. If the specimen is deformed, then the molded specimen grating is also deformed. A fringe pattern is produced by the physical interference between the light and dark grating lines of the deformed specimen grating and the undeformed reference grating. This fringe pattern is a contour map of in-plane displacements in a direction perpendicular to the reference grating lines. Fringe patterns can be recorded, and the displacement at any point can be determined by using Equation 1.5.

$$U(x,y) = \frac{1}{f} N(x,y) \tag{1.5}$$

where U is the displacement perpendicular to the reference grating lines, f is the frequency of the reference grating, and N is the fringe order at the point of interest. The contours in a fringe pattern are typically assigned integer values. These values are called the fringe orders. Fringe orders values can be assigned based on *apriori* knowledge of the strain, or they can be determined experimentally (Post *et al.*, 1994).

In moiré interferometry, a grating is also formed on the surface of the specimen. However, instead of evaluating the specimen grating with a real reference grating as in geometric moiré, a virtual reference grating is created when two beams of coherent laser light illuminate the specimen at such an angle as to produce interference lines of frequency f (f=2400 lines/mm for this study). The undeformed virtual reference grating and the deformed grating on the specimen interact and produce a contour pattern of in-plane displacements perpendicular to the virtual reference grating lines. A schematic of a moiré setup is shown in Figure 1.5 with a fringe pattern from a small region on the cylindrical surface of a hole in a composite laminate.

The process of forming a grating on the specimen (a process called "replication") is shown schematically in Figure 1.6. The specimen grating is usually a cross-line grating, meaning that it has two sets of mutually perpendicular grating lines, allowing for the measurement of displacements in two orthogonal directions. This is accomplished by aligning the virtual reference grating with one set of lines, recording the fringe pattern image, and using a virtual reference grating that is rotated 90° to examine the displacements in the other direction.

Displacements are related to the two images (x-displacement fringe pattern and y-displacement fringe pattern) by expressions similar to that of Equation 1.5.

$$\begin{aligned} U_x(x,y) &= \frac{1}{f} N_x(x,y) \\ U_y(x,y) &= \frac{1}{f} N_y(x,y) \end{aligned} \tag{1.6}$$

where U_x and U_y are the displacements in the x- and y- directions and N_x and N_y are the fringe orders from the x- and y- displacement fringe patterns. The strains can then be expressed using Equation (1.6) and the classical definitions of linear strain:

$$\begin{aligned} \varepsilon_x &= \frac{\partial U_x}{\partial x} = \frac{1}{f}\left[\frac{\partial N_x}{\partial x}\right] \\ \varepsilon_y &= \frac{\partial U_y}{\partial y} = \frac{1}{f}\left[\frac{\partial N_y}{\partial y}\right] \\ \gamma_{xy} &= \frac{\partial U_y}{\partial x} + \frac{\partial U_x}{\partial y} = \frac{1}{f}\left[\frac{\partial N_y}{\partial x} + \frac{\partial N_x}{\partial y}\right] \end{aligned} \tag{1.7}$$

where ε_x and ε_y are the normal strains and γ_{xy} is the shear strain.

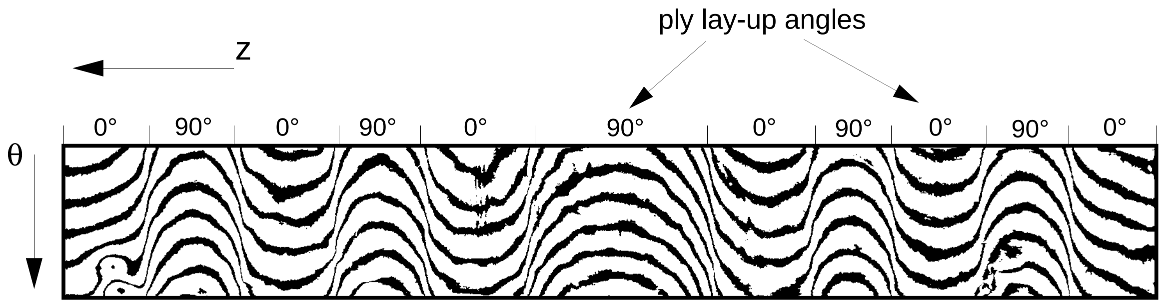

This fringe pattern is the theta-direction displacement fringe pattern from one angular location on the periphery of a hole in a composite (note the obvious influence of the ply boundaries)

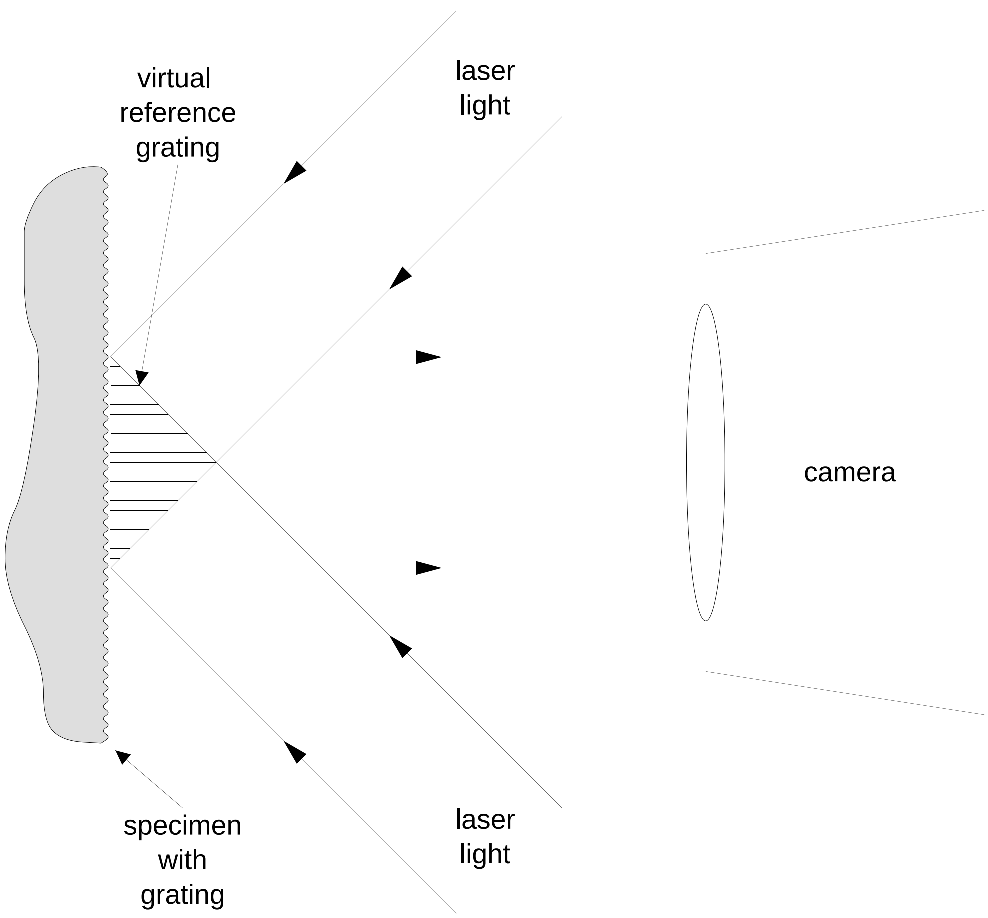

Figure 1.5: Schematic diagram of moiré interferometry with a representative fringe pattern.

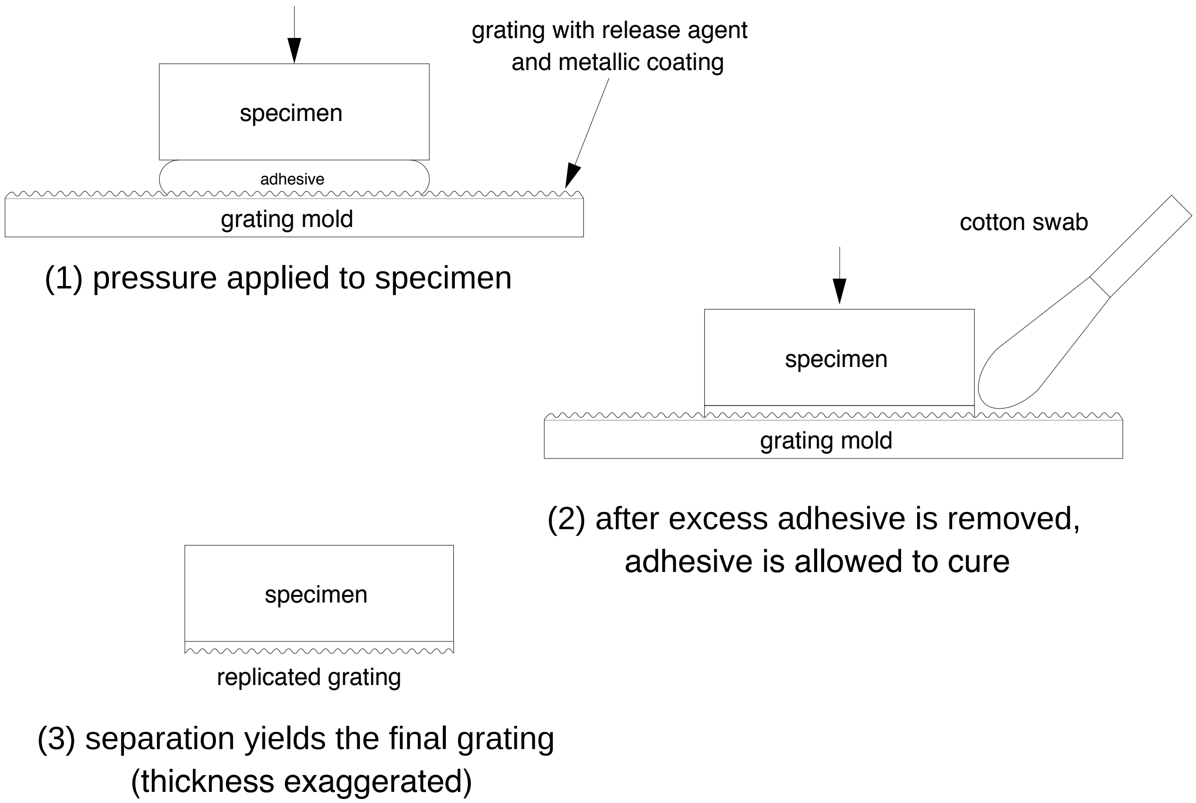

Figure 1.6: Schematic of the grating replication process.

Although the fringe order N_i is commonly determined visually from the fringe image (in integer increments), it is apparent from Equations 1.6 and 1.7 that if the incremental values of N_i between whole number fringe orders could be determined accurately, the resolution of calculated displacements and strains could be improved. The human eye can visually determine fractional fringe orders to some degree. Several digital techniques have been described in the literature to enhance the accuracy of fringe analysis. These techniques include Fourier transform analysis (Bone *et al.*, 1986), phase-shifting analysis (Creath, 1988; Hariharan *et al.*, 1987; Huntley, 1989; Lassahn *et al.*, 1994; Perry and McKelvie, 1993b), and optical/digital fringe multiplication (Han, 1992; Han, 1993). For a comparison of phase-shifting techniques with Fourier analysis, the excellent paper by Perry and McKelvie (1993a) should be consulted.

Discussion of Boeman's Research

Boeman (1991) examined the interlaminar deformation on the free edge of holes in composite laminates loaded in compression. His method of applying moiré interferometry to a curved surface began by first replicating a diffraction grating to a spring steel shim 0.051 mm (0.002 inches) thick. The combined grating and shim were attached to a circular sector (grating side out) with foam-core double-stick tape such that the final radius of the sector with the tape and shim was approximately 12.7 mm (0.5 inches). The curved grating assembly was then inserted into the 25.4 mm (1.0 inch) diameter hole of the unloaded composite specimen and a replica was formed onto the free edge of the hole over an arc somewhat greater than 90°. A miniature interferometer was constructed to interrogate the curved grating within the hole while the specimen was under load. The miniature interferometer proved to be awkward, and a method following an example from McKelvie and Walker (1978) was employed subsequently.

McKelvie and Walker (1978) made a replica of a specimen diffraction grating while the specimen was under load, and then analyzed the deformed replica in an interferometer on an optical table. Boeman used the same apparatus as was used to replicate a grating onto the hole (the circular sector, double-stick tape, and a clean steel shim) to make a replica of the curved grating while the specimen was under load. The replica of the deformed diffraction grating on the steel shim was then flattened out by attaching it to a powerful magnet. This assembly was examined in an interferometer on an optical table. Several advantages of this technique were listed. These include elimination of vibration problems and the ability to examine large angular areas of the hole at once. One difficulty that was noted was that when any shim with a grating on it is bent around an arc, the grating surface experiences a normal strain proportional to the thickness of the shim and grating. If the grating (original and/or deformed replica) was not of uniform thickness over the whole shim, then a variable strain would be added to the measured deformations. Boeman detailed several methods of compensating for this. One of these was the suggestion of insuring a uniformly thin grating.

Boeman discussed several conclusions and made several suggestions about the future of this research. A few of these are listed below.

(1) The axial strain on a straight free edge is constant across the thickness of the specimen (moiré examinations of straight free edges were also conducted).

(2) The circumferential strain along the cylindrical surface of the hole (analogous to axial strain in comment #1 above) was not necessarily constant through the thickness of the specimen.

(3) Shear strains at the interface between plies can change very rapidly with angular location. Thus, establishing the angular location of a measurement is critical.

(4) The measured responses exhibited large variations, indicating high material variability.

(5) Improved replication techniques for replicating uniformly thin gratings on steel shims should be sought.

Moiré Interferometry Techniques Applied to This Research

The investigation into measuring interlaminar deformations was built on the knowledge gained by Boeman (1991). Specifically, steel shims were again used to create a curved grating. Much effort was expended in attempting to insure a uniformly thin grating on these shims. The techniques developed for transferring the grating to the unloaded specimens and from the loaded tensile specimens where new and required careful validation. Thus, an isotropic control specimen was examined and the experimental results were compared with an accepted elasticity technique (Howland, 1930). Several new techniques were explored for gathering moiré data from the deformed replicas. One of these will be described in Chapter 2 along with detailed descriptions of the experimental replication techniques developed for this research.

Analyses of the fringe patterns obtained in this research were accomplished in several ways. The finite-increment method (Boeman, 1991; Post *et al.,* 1994) was used for manual strain determination. Where the finite-increment method could not be used, fringe vectors (Post *et al.,* 1994) were employed for manual analysis (this is often referred to as the tangent method). Digital phase shifting of the type discussed in Lassahn *et al*. (1994) was used in conjunction with numerical differentiation to obtain strain data in a few instances.

Chapter 2: Experimental Procedures

2.1 Overview

Three tensile specimens with 25.4 mm (1.0 inch) diameter holes were examined in this research. An aluminum tensile specimen was used to aid in the development of the necessary moiré interferometry techniques. Results from this specimen were used to validate the interferometry techniques developed in this research. Two composite specimens were then examined with the newly developed techniques.

A general description of the methods used in this research to extract displacement information from the cylindrical surfaces of holes is as follows in the next paragraph. A detailed description follows in the subsequent sections, and a step-by-step listing of the grating replication procedures are contained within Appendix A.

The first step involves replicating a diffraction grating onto the specimen. The next step records the specimen deformation by replicating a copy of the deformed specimen diffraction grating while the specimen is under load. Later, each replica of the deformed diffraction grating is viewed in a moiré interferometer and the fringe pattern is recorded. Finally, displacements and strains are extracted from the fringe patterns.

2.2 Grating Replication

2.2.1 Replicating a Diffraction Grating onto a Steel Shim

A cross-line diffraction grating (1200 lines/mm) was replicated to a 0.102 mm (0.004 inch) steel shim that was 12.7 mm (0.5 inch) wide. A 12.7 mm (0.5 inch) thick steel gage block was used as a pressure plate as shown in Figure 2.1. The resulting grating covered the width of the shim for a length of approximately 35 mm (1.38 inches). The casting resin, Envirotex Lite, was used as the replicating agent. Upon separation, excess adhesive on the back of the shim and adhesive flashing on the side of the shim were removed with sandpaper. A film of Kodak Photo Flo and water was sprayed onto the grating and allowed to dry. The shim/grating was then placed into a vacuum deposition chamber, and a thin coating of aluminum was deposited over the grating.

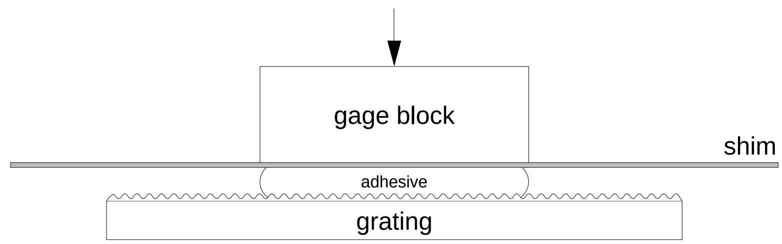

pressure applied to gage block

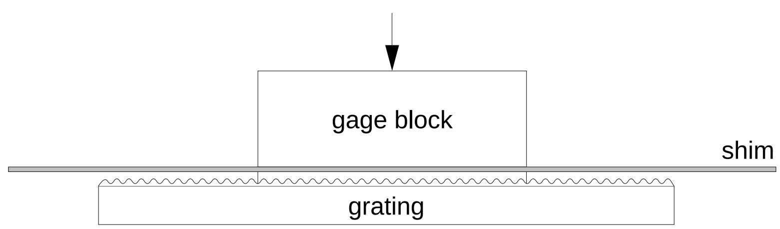

after excess adhesive is removed,
adhesive is allowed to cure

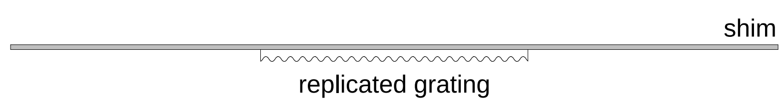

separation yields the final grating
(thickness exaggerated)

Figure 2.1: Schematic of the process for replicating a diffraction grating onto a steel shim.

Initial efforts to produce a uniformly thin grating were fairly successful. Gratings with 0.001 mm average thickness were routinely produced. Unfortunately, these had thickness variations of approximately ±0.001 mm. Some areas on these gratings were damaged by excessive thinness. Finally, less applied force resulted in slightly thicker gratings (approximately 0.004 mm) with approximately ±0.002 mm thickness variations. The thickness variations were measured with a digital micrometer stage, and the thickness was found to vary most significantly along the length of the shim.

2.2.2 Replicating a Diffraction Grating onto a Steel Sector

A cross-line diffraction grating was replicated onto a precisely machined steel sector (25.4 mm diameter). This was accomplished by wrapping the shim and grating combination, discussed in the previous section, around a steel sector with the grating side facing the sector. Figure 2.2 shows a schematic of the replication procedure. The steel sector was attached to a translation stage; and after a small amount of adhesive was poured onto the grating on the shim, the sector was pushed into the shim/grating combination. A rubber band was used to apply pressure to the shim, forcing it to conform to the sector. The epoxy resin, PC-10C, from Measurements Group, Inc., was used as the replicating agent. Excess adhesive was removed using fine grit sandpaper. A solution of Kodak Photo Flo and water was sprayed onto the grating and allowed to dry. A thin coating of aluminum was deposited over the grating.

2.2.3 Replicating a Diffraction Grating onto a Steel Plate

A cross-line diffraction grating was replicated onto a precisely machined flat steel plate (50.8 mm square and 12.7 mm thick). The flat plate was designed to mate-up with the steel sector to produce a continuous grating area over the flat plate and sector faces as illustrated in Figure 2.3. A bolt hole used to attach the sector and a guide pin hole used to align the sector had to be cleared of adhesive after the replication process by drilling and reaming. The epoxy resin, PC-10C, was used as the replicating agent. A solution of Kodak Photo Flo and water was sprayed onto the grating and allowed to dry. A thin coating of aluminum was deposited over the grating.

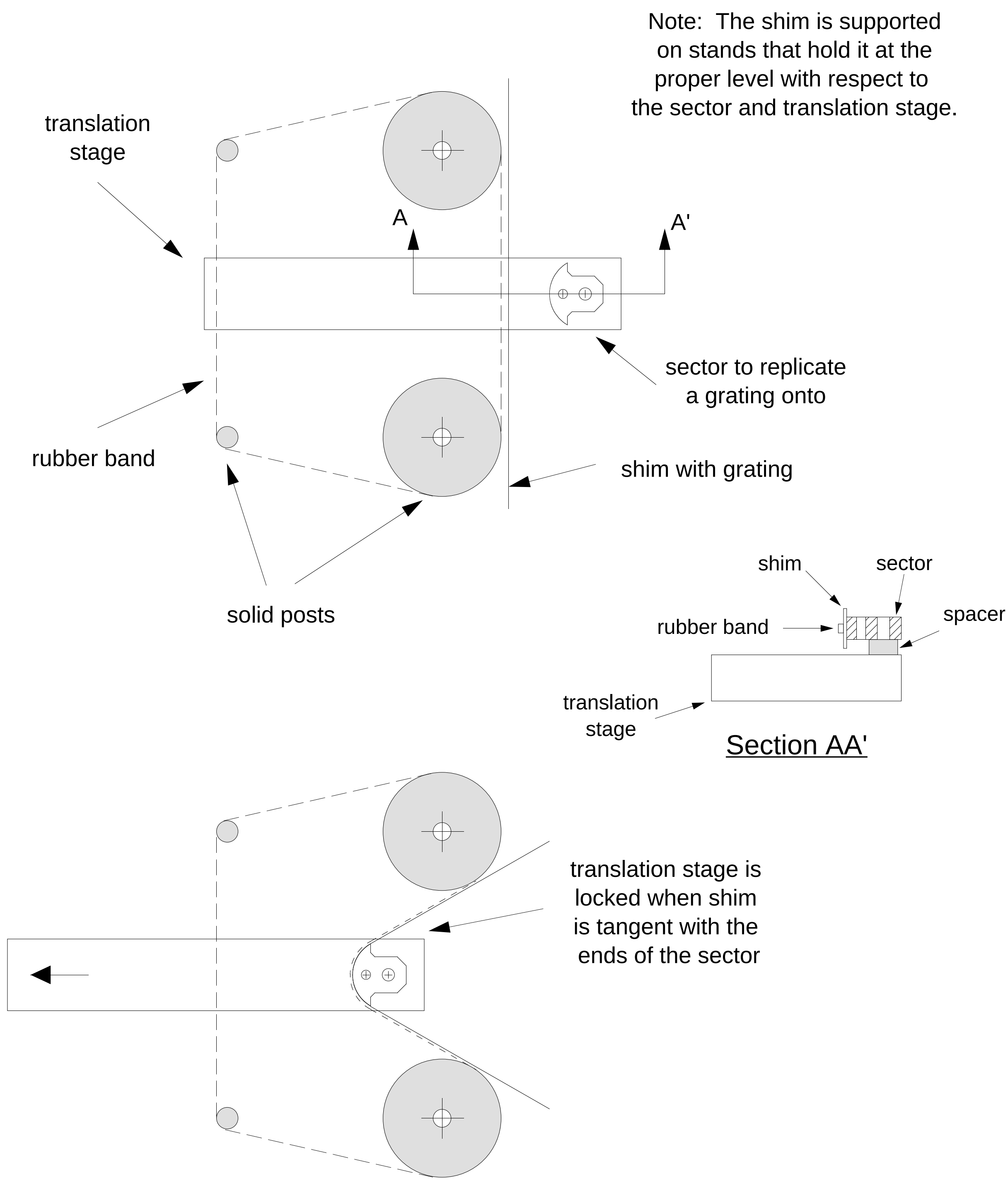

Figure 2.2: Schematic of the process for replicating a diffraction grating to a steel sector.

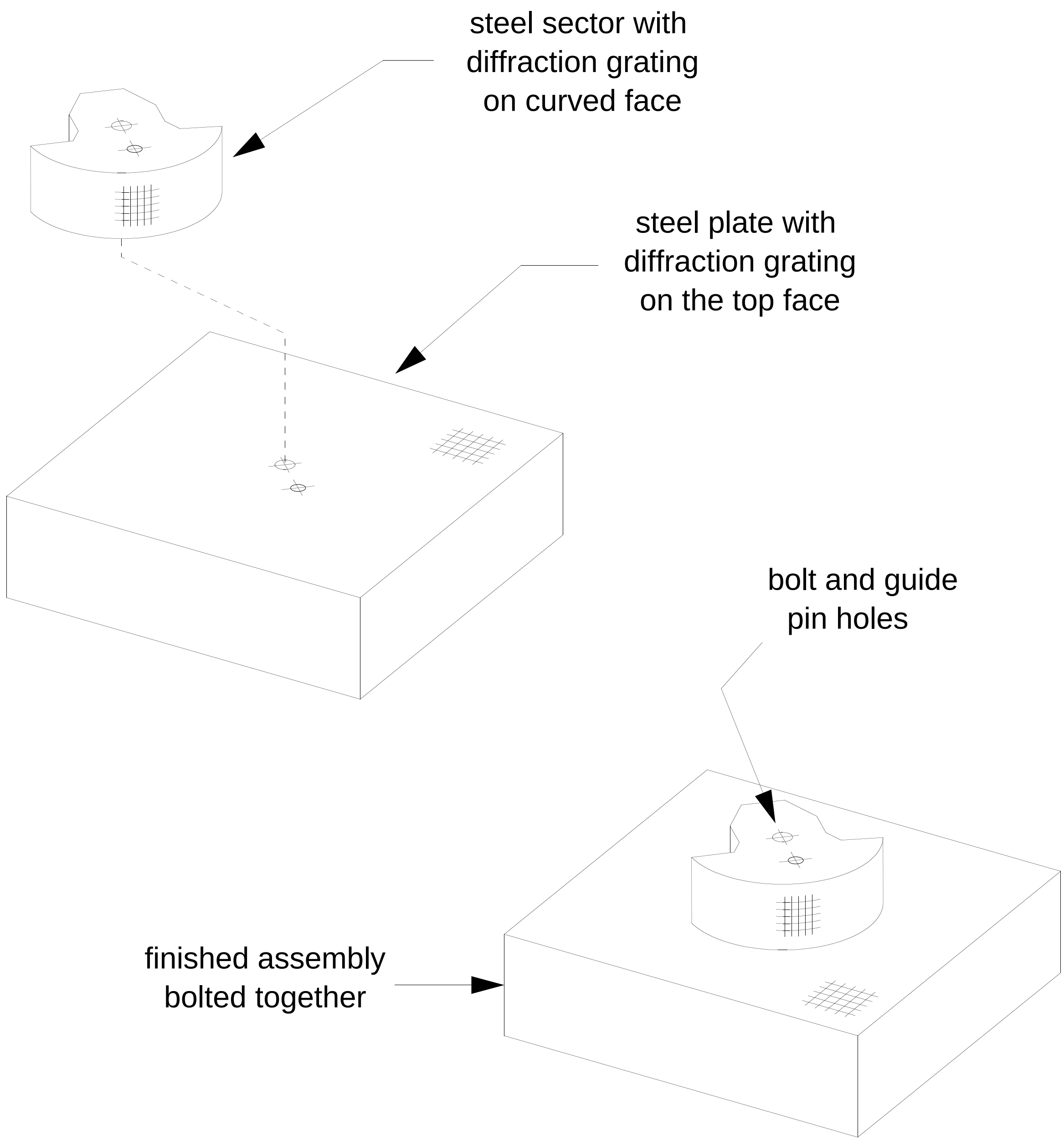

Figure 2.3: Schematic of a circular steel replication sector, a square steel replication plate, and the assembly of a sector and a plate.

2.2.4 Replicating a Diffraction Grating onto the Specimen

The sector and plate combination were used to replicate a cross-line diffraction grating onto the specimen as shown schematically in Figure 2.4. The resulting grating covered a 50.8 mm (2.0 inch) square on one face of the specimen surrounding the hole and approximately 110° on the cylindrical surface of the hole. PC-10C was again used as the replicating agent.

In the actual replication process, the sector and plate with gratings were first bolted together into an aluminum frame. The frame was designed to align the specimen with respect to the sector and plate combination. It was also designed to apply in-plane and out-of-plane pressure to the specimen, squeezing out excess adhesive and creating a thin grating. Figure 2.5 shows a series of photographs of a sector and plate combination (without grating) attached to the alignment frame with and without a translucent plastic demonstration specimen.

After the sector and plate had been attached to the frame, uncured PC-10C adhesive was poured around the plate with extra adhesive pooled in front of the sector face. The specimen was carefully lowered onto the pool of adhesive. This was done such that the sector grating was not scraped by the edges of the hole. This replication step was accomplished with the specimen oriented horizontally. When an adequate amount of adhesive had been squeezed into the gap between the specimen and sector, the specimen was gently pushed against the sector. Slight pressure was applied in-plane in the axial direction (by hand) and in the transverse direction (using the pressure application screws). The out-of-plane pressure plate was attached and slight force was applied. Alternating between in-plane and out-of-plane adjustments, the force was gradually increased until a reasonably thin grating was attained.

Excess adhesive was carefully cleaned with cotton swabs for about 45 minutes. The sector, plate, and frame were designed to allow access to all edges where adhesive spew would occur. When the adhesive had cured, the in-plane pressure was removed. The bolt attaching the sector to the plate was then removed. After removing the out-of-plane pressure, the specimen (with the sector attached) was separated from the plate by applying out-of-plane pressure to the specimen. The adhesion of the sector to the specimen was sufficient to allow the separation between plate and specimen without the separation of the sector from the specimen. The sector was separated from the specimen by clamping the sector in a vise and gently tapping the specimen until separation occurred.

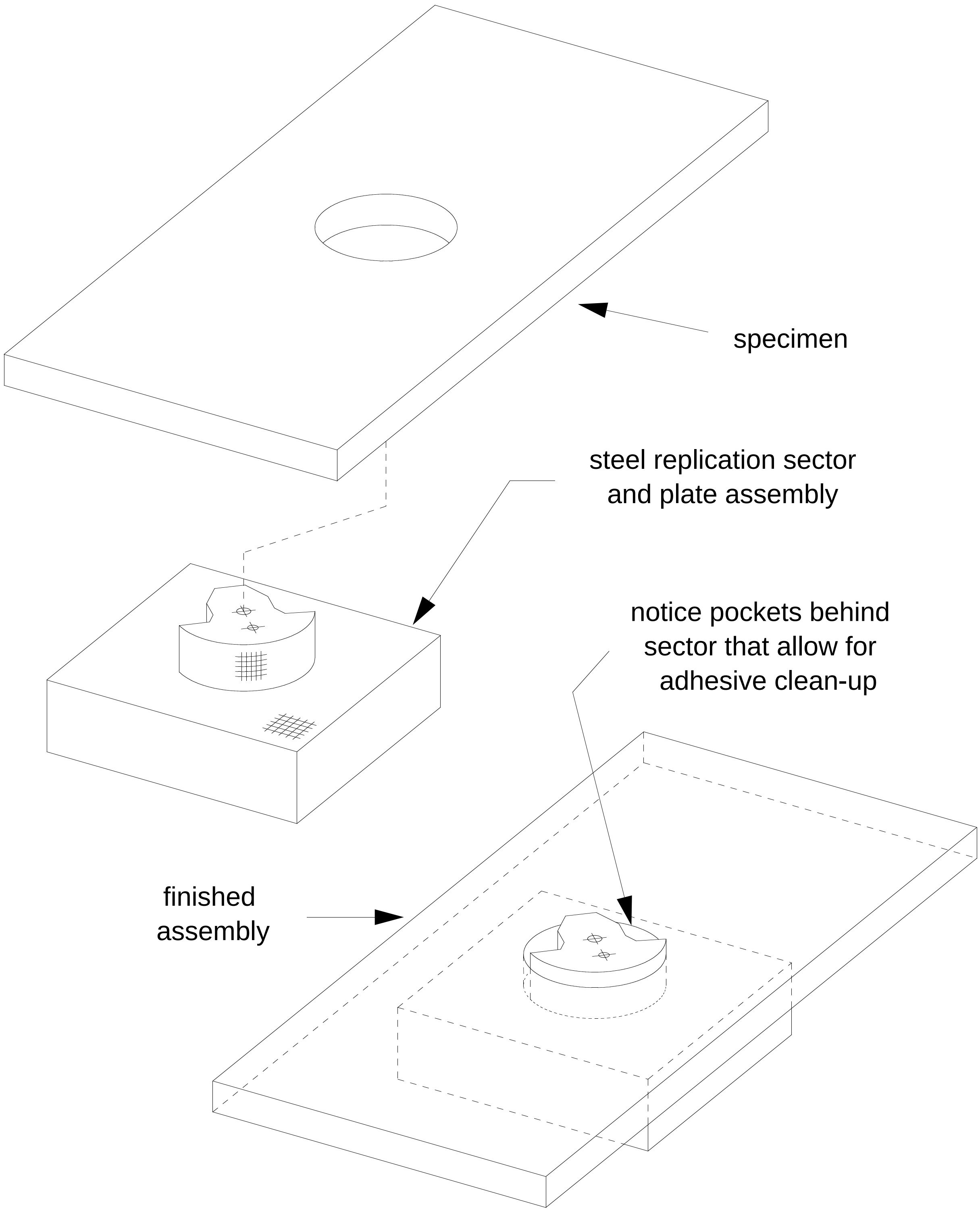

Figure 2.4: Schematic of the process for replicating a grating onto (or from) a tensile specimen with a hole.

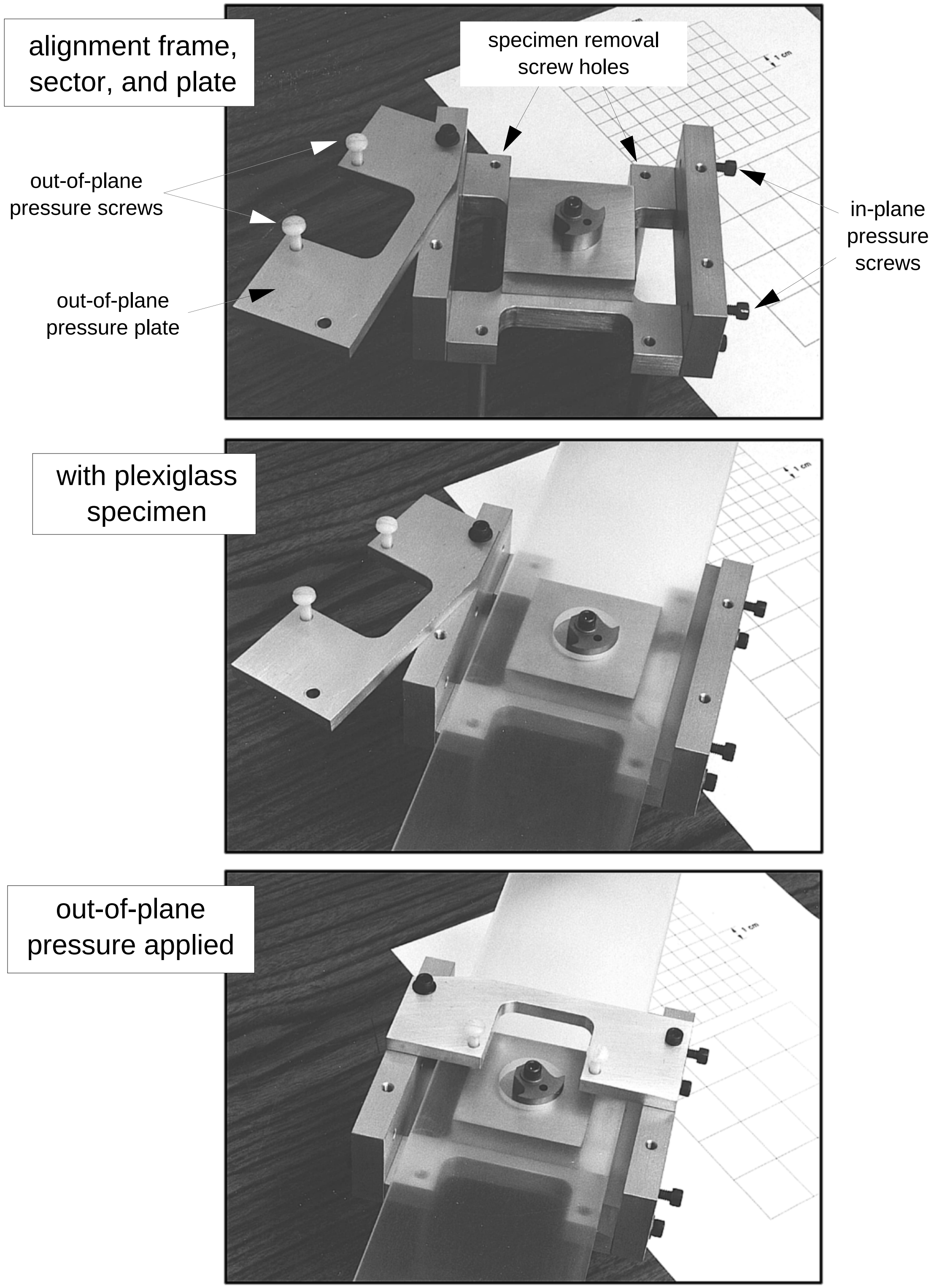

Figure 2.5: Photographs of the aluminum alignment frame with a replication sector, a replication plate, and a plexiglass specimen attached.

Fiducial marks placed on the sector and plate (by scratching the gratings with a razor blade) before replication were intended to aid in determining geometric location on the specimen in subsequently replicated gratings. Unfortunately it was found that marking the sector with sufficient accuracy was extremely difficult. To alleviate this problem, additional fiducial marks were placed at the 0° location directly on the specimen gratings.

2.2.5 Replicating a Diffraction Grating from a Deformed Specimen

Replicas of the specimen gratings (loaded or unloaded) were produced using techniques similar to those described in Section 2.2.4. First, a cleaned and primed plate and sector combination (with no grating) were bolted into the aluminum alignment frame. General Electric Corporation's RTV-615 silicon rubber was used as a replicating agent. This resin was chosen because it will not adhere to most surfaces unless the surface is primed. Therefore, the adhesion can be selectively chosen such that it does not adhere to the specimen grating, while it adheres to the replication plate and sector. The sector and plate were primed with General Electric's SS4155 primer. RTV-615 has a cure time of approximately 48 to 72 hours. It was felt that this cure time was too long to maintain a specimen under load. The ratio of curing agent to resin was altered to the maximum recommended 20% curing agent. Cure times were reduced to approximately 8 to 18 hours.

Uncured RTV-615 was poured onto the plate with extra liquid silicone rubber pooled in front of the sector face. The same plate, sector, and frame assembly were carefully positioned against the specimen (which was oriented vertically in a testing machine frame). When an adequate amount of silicon rubber had been forced through the hole around the sector, the assembly was settled against the side of the hole. After positioning the assembly against the specimen and pushing the sector against the side of the hole, slight out-of-plane pressure was applied. Alternating between in-plane and out-of-plane adjustments, the pressure was gradually increased until a reasonably thin grating was attained. Excess liquid was carefully cleaned with cotton swabs for about two hours.

In a manner similar to that described in Section 2.2.4, the bolt that attached the sector to the plate was removed. Out-of-plane pressure applied to the specimen forced the separation of the plate and aluminum alignment frame from the specimen. Unfortunately, the adhesion of the sector to the specimen was insufficient to prevent the sector from also being separated at the same moment. The sector grating was typically ruined in this process. The RTV-615 generally seeped under the sector, bonding it to the plate. A solution was found that required the underside of the sector to be coated with aluminum in the vacuum chamber, coated with Photo Flo, and coated again with aluminum before being primed and assembled into the aluminum frame. When this solution was implemented, separation of the plate was routine. The sector was then separated by attaching a bolt through its central bolt hole and applying continuous, fingertip pressure to the end of the bolt until separation occurred.

2.2.6 Coating Silicon Rubber Gratings with Reflective Material

A diffraction grating used in moiré interferometry is typically coated with a reflective material to improve diffraction efficiency. Several difficulties were encountered when attempting to vacuum deposit aluminum onto the RTV-615 gratings produced as described in Section 2.2.5. When attempting to coat the gratings with aluminum, it was found that the aluminum reacted slightly with the silicon rubber. Instead of creating a bright and highly reflective surface, the coating turned slightly dark. It was also found that if the coating of aluminum was thick (almost opaque), a wrinkle pattern appeared as shown in Figure 2.6. It was also found that the wrinkling occurred in another General Electric silicon rubber resin, RTV-664.

Similar wrinkling phenomena has been observed before by Plassa (1969) and others. The wrinkling observed by Plassa occurred due to a coefficient of thermal mismatch between the substrate material and the coating material. The CTE mismatch was such that when the temperature was lowered, the coating was placed in biaxial compression. Unfortunately, this appears to be an inadequate explanation for the occurrence of wrinkling in the present study. The CTE mismatch between metals and RTV-615 is such that the coating would be placed in biaxial compression if the system temperature had been elevated during vacuum deposition. This is only true if the RTV-615 substrate were monolithic. In the present research, however, the RTV-615 formed a very thin layer over a steel (or glass) substrate. Glass substrates were examined because of the availability of large quantities of RTV-615 gratings on glass substrates. The combination of glass, RTV–615, and a thin aluminum layer would serve to place the RTV-615 and aluminum layers into biaxial tension if the temperature had been elevated by the vacuum deposition process. This phenomenon was also observed with gold coatings.

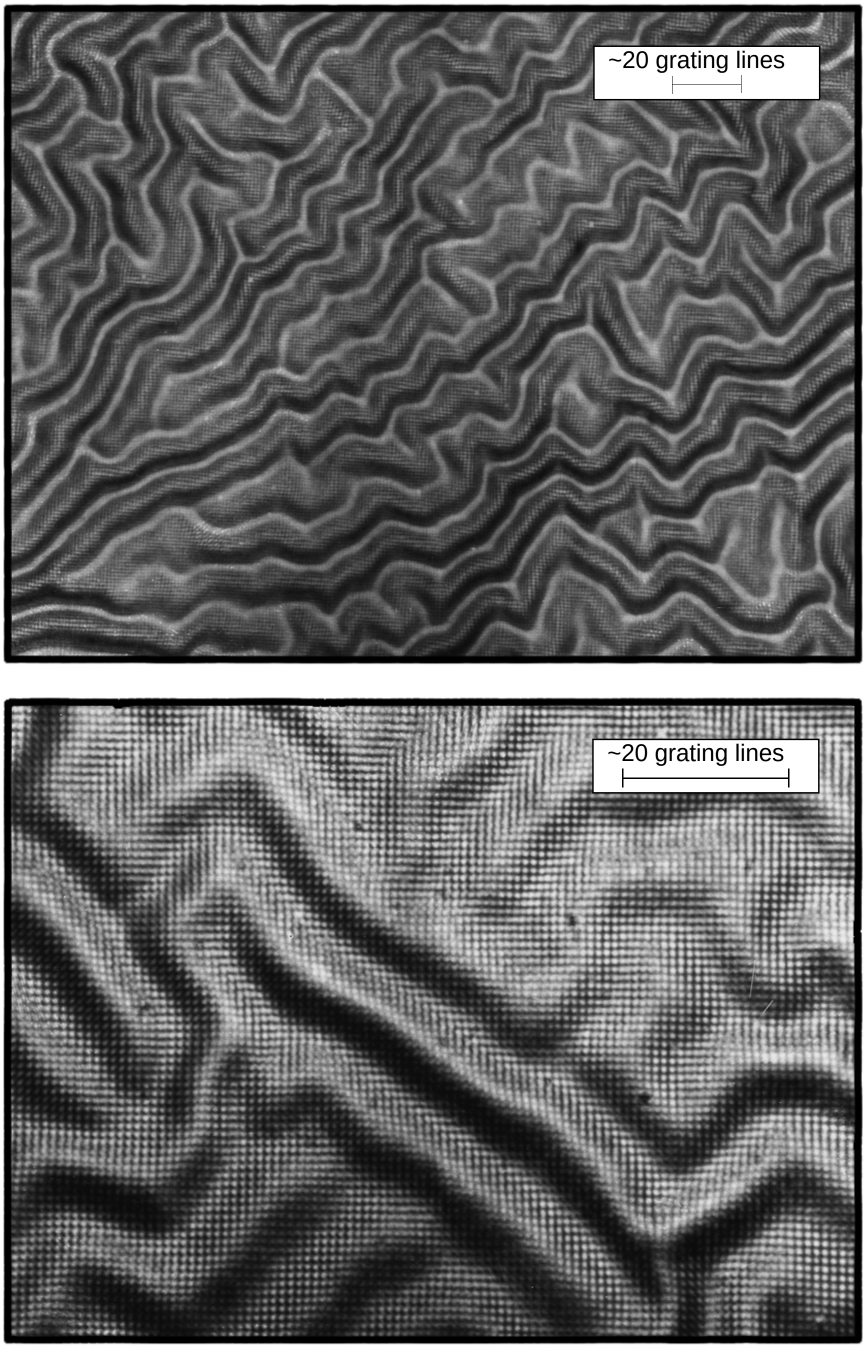

Figure 2.6: Micrographs of the wrinkling phenomenon which occurred on silicon rubber diffraction gratings opaquely coated with aluminum or gold.

It was found that the severity of the wrinkling phenomenon was directly related to the thickness of the applied metallic coating. The thicker the coating, the more pronounced the wrinkling. This trend is identical to the trend mentioned in Plassa (1969). However, the wrinkling did not always occur immediately upon removal from the vacuum chamber (and the presumed cooling that would result). One observed case occurred two weeks after the coating process. If the problem was caused by a CTE mismatch, it would be expected that the wrinkling would occur immediately (assuming that viscoelastic or time dependant phenomena are not in operation).

Post (1996) suggested that the wrinkling could be caused by out-gassing from the RTV-615 resin. It was found that the wrinkling phenomenon was less likely to occur in older and/or post-cured samples of RTV-615 gratings. This observation supports Post's hypothesis, but no further examination of this problem has been conducted.

As a result of the problems encountered with vacuum deposition of metallic coatings onto silicon rubber gratings, three actions were taken. First, the silicon rubber gratings were post-cured at 100°C for 24 hours. Care was taken to verify that the information recorded on the gratings was not altered by the post-curing process. Second, gold was used as the coating material to avoid reactions with the silicon rubber. Finally, an extremely thin coating was applied to the surface of the grating. This enhanced the surface reflectivity enough to allow for photographic recording of the resulting fringe patterns as discussed in the next few sections.

2.3 Moiré Interferometry with Curved Sector Gratings

2.3.1 Undesired Additions to the ε_θ Strain Component

Boeman (1991) noted that when any shim with a grating on it is bent around an arc, the grating surface experiences a normal strain in the θ–direction. This strain is proportional to the radial distance of the grating surface from the neutral axis of bending. If the grating was of constant thickness, an unknown constant value of ε_θ would be added to the cylindrical specimen grating during the replication process. If the grating was not of uniform thickness over the whole shim, then an unknown variable ε_θ would be added to the cylindrical specimen grating during the replication process.

When a beam bends into an arc (or is flattened from an arc), the ε_θ strain (or axial strain) experienced at any point in the beam is a function of the radius of curvature of the arc and the distance from the neutral axis of the beam as shown in Figure 2.7. For a steel shim of thickness $\mathbf{t_s}$ with a grating of thickness $\mathbf{t_g}$, the circumferential strain at the grating surface caused by bending a flat shim into an arc of radius **r** is given by Equation 2.1. This equation assumes that the neutral axis of the beam is always at the mid-plane of the steel shim.

$$\varepsilon_\theta = \frac{(\frac{1}{2}t_s + t_g)}{r} \tag{2.1}$$

The difference in the circumferential strain at the grating surface for two different grating thicknesses, $\mathbf{t_{g1}}$ and $\mathbf{t_{g2}}$, is given by Equation 2.2.

$$\Delta\varepsilon_\theta = \frac{(t_{g2} - t_{g1})}{r} \tag{2.2}$$

For the present research, where **r** was 12.7 mm (0.5 inches), the variation in circumferential strain was calculated to be 78 $\mu\varepsilon$ for every 0.001 mm (0.000039 inches) difference in the grating thickness. The gratings used in this research had approximately ±0.002 mm variations in thickness, corresponding to ±156 $\mu\varepsilon$ variation in circumferential strain.

One method for extracting displacement information from the cylindrical surface of the hole was implemented by Boeman (1991). He produced a replica of the deformed cylindrical specimen grating on a steel shim, and he examined this grating in a moiré interferometer while the shim was forced flat by a magnet. This method would incur unknown additions to the circumferential strain from this step as well as the original step of replicating a grating onto the specimen. A method for correcting the unknown additions to the circumferential strain would be to correlate the measured circumferential strain near the top edge of the hole with strain data measured from the flat face of the specimen. This idea was the impetus for using the flat steel replication plate discussed in Section 2.2. The data from the flat face would not experience unknown variations due to differences in grating thickness. The circumferential strain data could be adjusted to match the flat surface data. Unfortunately, this method would only correct for constant additions to the circumferential strain or additions due to grating thickness variations in the circumferential direction. Any variation in the grating thickness in the z-direction would be neglected.

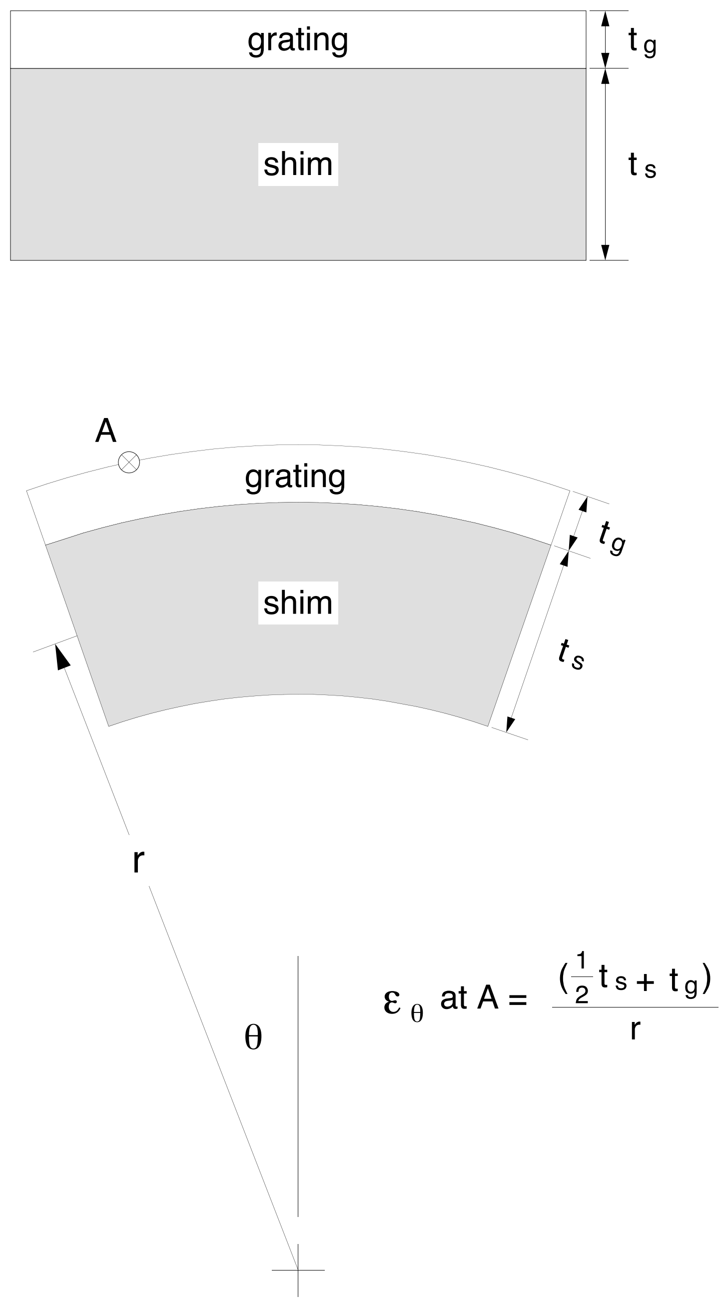

Figure 2.7: Strain at the grating surface caused by bending a steel shim into a circular arc of radius r (thicknesses exaggerated).

A more serious difficulty with the shim analysis method would be localized grating thickness variations due to the deformation of the specimen. If the specimen experienced large radial deformation variations, the grating replication process would accurately replicate these radial deformation features as well as replicating the deformed grating lines. Upon flattening, the variations in grating thickness would correspond to variations in circumferential strain that are not related to the actual circumferential deformation. As a result of the uncertainties involved with the thickness of the gratings replicated to a steel shim, another method for extracting fringe data from the curved sector gratings was sought. The method described below completely eliminated this uncertainty and the uncertainty of initial shim grating thickness variations.

2.3.2 Discrete Sections from Circular Sector Gratings

The method used in the present study to extract displacement information from the curved steel sector replicas of the deformed specimen gratings involved examining narrow, discrete angular sections in the interferometer. Figure 2.8 shows a schematic of the process. The curved nature of the grating surface causes the output light to diverge at a sharp angle. It was found that by using a highly corrected, large aperture camera lens 4° to 5° of the curved sector could be imaged. The resulting fringe pattern appeared as a long and narrow rectangle, with the long axis corresponding to the z-direction and the narrow axis corresponding to the θ–direction. An example of a fringe pattern recorded using this method is shown in Figure 1.5. If a poor quality or simple lens was used, the image was drastically distorted in both axes. The Nikon 135 mm f2.4 lens used in this research produced sharp focus with no visible distortion. Focussing proved difficult, however, in the sense that slight errors in focus resulted in large changes in the apparent width of the rectangle that was imaged. This would cause the apparent magnification in the θ–direction to be different from the magnification in the z-direction.

To account for the possibility of slight focusing mistakes, a rotation stage was constructed to precisely rotate the curved sector. After an image was recorded, the sector was rotated a known amount (3° for example) and another image was recorded. These two images could then be compared and common features noted. The distance from the edge of the imaged rectangle to a common feature was measured for each image. The difference between these values corresponded to the magnified length of an arc of 3° length on the actual sector. In this manner, the geometric scale in the θ–direction was determined.

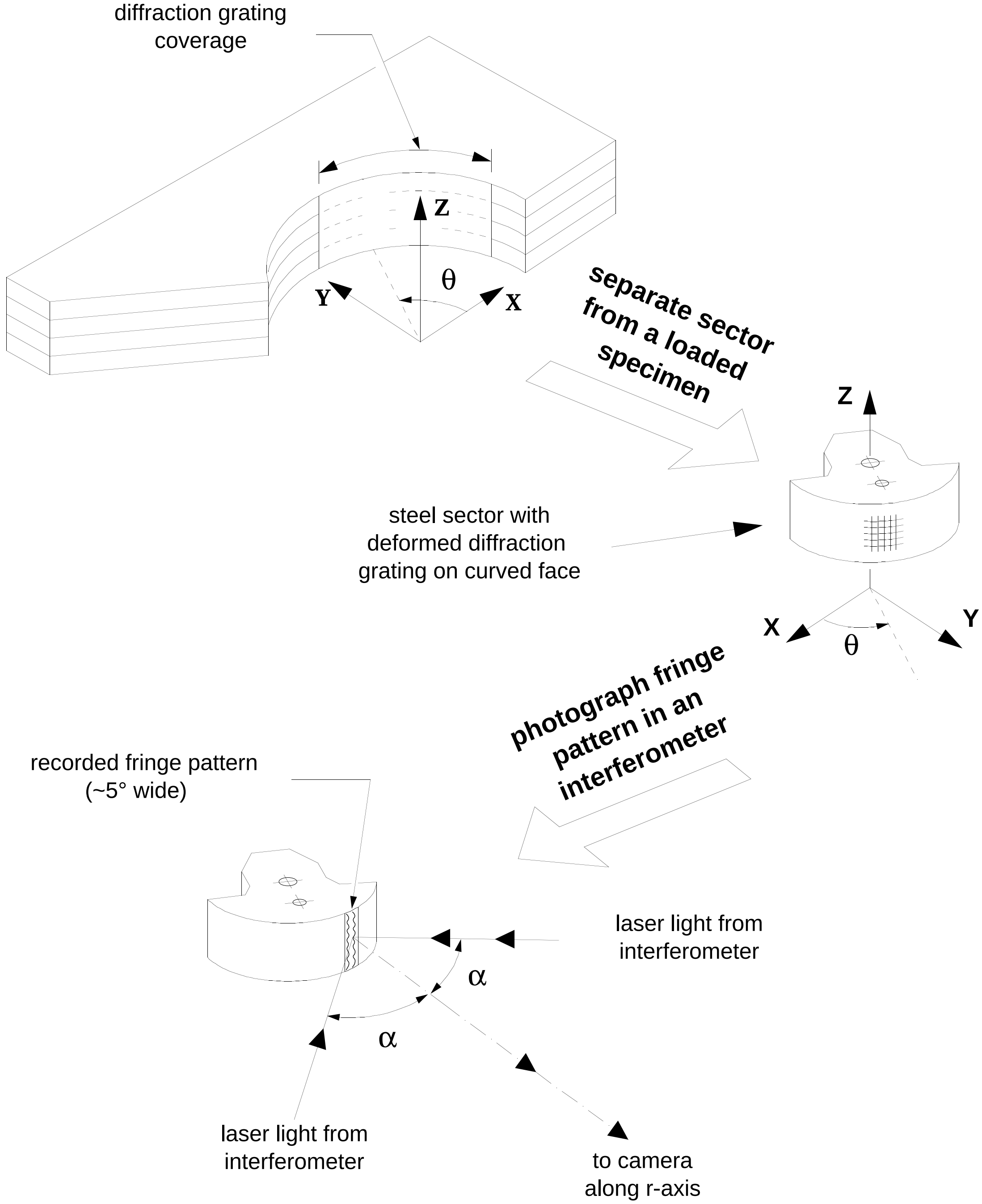

Figure 2.8: Schematic of the discrete angular section method for recording fringe patterns from a curved sector grating.

The main advantage of recording fringe patterns in a discrete manner from the curved sector gratings is that it completely eliminates the difficulties associated with the grating thickness on the steel shims. The interferometer can be tuned to produce a null image at a particular angular location using the original sector that was used to replicate a grating onto the specimen. When the null image is obtained, any circumferential strain induced by variations in the original shim grating thickness are automatically corrected with a carrier of extension. The curved sector grating replicated from the deformed specimen can then be inserted into the interferometer and the fringe image recorded. If the initial pattern contained significant numbers of fringes, it can also be recorded and analyzed. The null image information can then be subtracted from the deformed information.

A disadvantage with the discrete angular location method is that an out-of-plane rotation of the diffraction grating with respect to the interferometer will result in the addition of a false compressive strain. The magnitude of this strain is given in Equation 2.3.

$$\varepsilon = -\frac{\psi^2}{2} \tag{2.3}$$

The false additional strain is ε, and ψ is the angle of rotation about an axis parallel with the grating lines being evaluated. In the discrete angular location method of analyzing diffraction gratings on curved surfaces, every degree of geometric location difference from the center of the location being analyzed corresponds with a degree of out-of-plane rotation. However, the effects of this on calculated strain are negligible for two reasons. First, the circumferential gage lengths in this research were generally between 1° and 2°. Second, the false compressive strain error from a curved surface corresponds with the integration of errors caused by the varying out-of-plane rotations across the gage length. Integration over a 1° gage length yields a –13 $\mu\varepsilon$ error, and integration over a 2° gage length yields a –50 $\mu\varepsilon$ error. The error caused by the out-of-plane rotation effect would have a systematic dependance on the strain analysis gage length. Variations in the strain error would be small since the gage lengths used at a given angular location were relatively consistent. In the present research, these errors were corrected through interferometer tuning as discussed in the previous paragraph.

The following step-by-step procedure outlines essentially how all experiments were conducted.

(1) The original curved sector grating was obtained (or a curved sector grating produced from the undeformed specimen). This sector will be referred to as the "null" sector.

(2) A sector grating produced from a deformed specimen was obtained. This sector will be referred to as the "deformed" sector.

(3) The null sector was placed into the interferometer and rotated to the desired angular location.

(4) The best possible null field was tuned in the z-direction fringe pattern and in the θ–direction fringe pattern. In every case, the null fields were sufficiently sparse that they were not photographed.

(5) The null sector was replaced with the deformed sector. This sector was rotated to the same angular location as in Step 3.

(6) The rigid body rotation (about the r-axis) was adjusted to eliminate most rigid body rotations.

(7) The z-direction and θ–direction fringe patterns were then photographed.

(8) The deformed sector was replaced with the null sector, a new desired angular location was chosen, and Steps 3 through 8 were repeated until all desired angular locations had been examined.

As mentioned in Step 4 above, the null field fringe patterns encountered in this research were sufficiently sparse to be neglected. In every case, these null fields contained less than a half of a fringe across a 5° field of view (1.11 mm), and often the fringe patterns contained less than one quarter of a fringe. A change of a half a fringe order in a 1.11 mm field of view corresponds with a strain of approximately 185 $\mu\varepsilon$. In the present research, strain errors caused by neglecting the null field fringe patterns are believed to be less than 60 $\mu\varepsilon$.

The discrete angular section method for recording fringe information from a cylindrical sector grating proved to be simple and robust. The procedures are very similar to a typical moiré interferometry test in which a null field is first obtained and then a deformed fringe pattern is recorded. Advantages, other than compensating for unknown strain additions, include the ability to conduct moiré interferometric evaluations of the sector gratings at the convenience of the researcher. Different combinations of carriers of rotation and/or extension can be used to enhance the fringe patterns if desired. The rotation stage used to establish θ–direction magnification also allows the curved sectors to be rotated to precise angular locations that can be correlated with geometric locations on the actual tensile specimens. Fringe patterns can be recorded with different media (photography, video, CCD), and phase-shifting analysis can easily be employed.

2.4 Specific Experiments Conducted

Specific information about the three tensile specimens examined in this research and the experiments conducted on them are contained in the following sections.

2.4.1 Aluminum Tensile Specimen Testing

An aluminum tensile specimen with a hole was examined using the techniques described in the previous sections. The specimen was produced from 7075-T6 aluminum. Properties of 7075-T6 are listed in Table 2.1.

Table 2.1: Properties of 7075-T6 aluminum plate.

$E_{tension}$ GPa (Msi)	$E_{compression}$ GPa (Msi)	ν	σ_{yield} MPa (Ksi)
71.0 (10.3)	72.4 (10.5)	0.33	503.0 (73.0)

The specimen was 61 cm (24.0 inches) long, 73.7 mm (2.90 inches) wide, and 6.6 mm (0.26 inches) thick with a 25.4 mm (1.00 inch) diameter hole located at the specimen center.

A cross-line diffraction grating was replicated onto the specimen as described in Section 2.2.4. The grating consisted of a 50.8 mm (2.0 inch) square grating on the flat face of the specimen, surrounding the hole. The replication also produced a grating of approximately 110° of arc on the cylindrical surface of the hole, spanning approximately –10° to 100°. Fiducial marks that had been placed on the original sector grating were transferred to the grating on the cylindrical surface of the hole. The marks were placed at 0°, 30°, 45°, 60°, 85°, 90°, and 95°. Slight misalignments during the replication process caused these locations to be shifted by approximately –2° to –2°, 28°, 43°, 58°, 83°, 88°, and 93°. The misalignment magnitude was determined by placing a fiducial mark at 0° directly onto the specimen cylindrical surface grating.

Three replicas were made of the specimen grating following the procedure outlined in Section 2.2.5. One replica was made at zero load, before any load had been applied to the specimen. The other replicas were formed when the specimen was loaded to 27.56 MPa (4,000 psi) and 82.68 Mpa (12,000 psi), respectively. The aluminum specimen was loaded in tension with 9.5 mm (0.375 inch) pins inserted into holes drilled at each end of the specimen. Load was applied by a Tinius Olsen, screw-driven load frame. The load was maintained for approximately 18 hours while the RTV-615 silicon rubber resin cured.

Copper, instead of gold, was vacuum deposited on the replicated gratings. At this point in the testing program, the wrinkling phenomenon discussed in Section 2.2.6 had not been encountered. Fortuitously, the coating of copper applied was very thin and did not wrinkle. After several months of exposure to room air, however, the copper coating on these gratings degraded dramatically by corrosion and peeling.

Moiré interferometric fringe patterns from the flat face grating replicated at 27.56 MPa were photographically recorded. The distribution of axial strain along the transverse centerline was determined from these patterns using the finite-increment method discussed in Appendix B.

Moiré interferometric fringe patterns from all curved sector gratings were recorded at several angular locations. These angular locations were 3°, 28°, 43°, 58°, 83°, and 88°. The replicated gratings were damaged at the 0° and 90° locations. The 3° and 83° locations were the regions closest to 0° and 90° of sufficient quality for analysis. Phase shifting analysis of the type described in Lassahn *et al*. (1994) was performed on digital images recorded at 3°, 28°, 43°, 58°, and 83°.

2.4.2 Composite Tensile Specimen Testing

Two composite ply lay-ups were examined in this research. Three tensile test specimens of each lay-up were fabricated from IM7/5250-4. IM7 is a carbon fiber and 5250-4 resin is a blend of bismalimide and cyanate ester. The properties of a typical lamina of IM7/5250-4 are given in Table 2.2.

Table 2.2: Properties of an IM7/5250-4 lamina.

$\mathbf{E_1}$	152.7 GPa (22.15 Msi)
$\mathbf{E_2}$ & $\mathbf{E_3}$	8.96 GPa (1.30 Msi)
$\mathbf{G_{12}}$ & $\mathbf{G_{13}}$	5.93 GPa (0.860 Msi)
$\mathbf{G_{23}}$	3.28 GPa (0.476 Msi)
ν_{12} & ν_{13}	0.321
ν_{23}	0.449
α_1	$0.61\text{x}10^{-6}$/°C ($0.34\text{x}10^{-6}$/°F)
α_2 & α_3	$25.2\text{x}10^{-6}$/°C ($14.0\text{x}10^{-6}$/°F)
0° Max. Tensile	2.70 GPa (391 Ksi)
0° Max. Compressive	-2.09 GPa (-303 Ksi)
90° Max. Tensile	51.2 MPa (7.42 Ksi)
90° Max. Compressive	-285.4 MPa (-41.4 Ksi)
Max. Shear	87.6 MPa (12.7 Ksi)

All laminates were fabricated at the United States Air Force's Materials Directorate of Wright Laboratory by personnel from the University of Dayton Research Institute (UDRI). Extreme care was taken to insure that the plies were accurately placed. Examination of the surface plies of all composite specimens indicated that these plies were within 0.5° of the specified top ply angles. The specimens were 61 cm (24.0 inches) long and 73.7 mm (2.90 inches) wide with a 25.4 mm (1.00 inch) diameter hole located at the specimen center.

Photographs of the cylindrical surfaces of two specimens of each of the composite lay-ups were recorded. These were evaluated for ply waviness or other irregularities. The best specimen of each lay-up was chosen to be further examined using the moiré interferometry techniques described in previous sections. The lesser quality specimens of each lay-up were set aside for later use. The third, nonphotographed specimens of each lay-up were tested in an attempt to determine the first acoustical emission event and the failure load.

Strain gages were applied to each of the moiré specimens as discussed in the following sections. Both specimens were tabbed with fiberglass for gripping, but the available gripping apparatus induced significant amounts of bending in the specimens. Instead of gripping, the moiré specimens were loaded in tension with 12.7 mm (0.5 inch) diameter pins through holes drilled at each end of the two specimens.

As with the aluminum specimen, a cross-line diffraction grating was replicated onto each composite specimen using the methods described in Section 2.2.4. The gratings consisted of a 50.8 mm (2.0 inch) square grating on the flat face of each specimen, surrounding the hole. The replication also produced gratings of approximately 110° of arc on the cylindrical surface of the holes, spanning approximately –10° to 100°.

$[0°_4/90°_4]_{3s}$ Laminate

The $[0°_4/90°_4]_{3s}$ specimens were 6.35 mm (0.249 inches) thick. The specimen tested for first ply failure load and ultimate failure load showed an initial acoustic emission event at 66.6 MPa (9,600 psi). The maximum load capacity of the available testing machine was reached before specimen failure. Significant damage had occurred, and the ultimate failure strength is believed to be slightly higher than the maximum applied load of 444 MPa (64,400 psi). These tests were performed at Wright Laboratory by UDRI personnel. Four strain gages were bonded onto the moiré interferometry test specimen. These were located 152 mm (6.0 inches) from the center of the hole. Two gages were bonded onto the front and two on the back of the specimen, 12.7 mm (0.5 inches) from each edge. One gage failed during testing. These gages were used to monitor far-field strain and evaluate the level of bending in the specimen.

Several replicas of the $[0°_4/90°_4]_{3s}$ specimen grating were made while the specimen was under 50 MPa (7,250 psi) applied far-field stress. The first attempt using RTV-615 did not succeed. The resin did not cure properly over portions of the grating. A second attempt, using RTV-664, produced a grating that had poor diffraction efficiency. RTV-664 contains particles, and it is believed that the particulate size is similar to the diffraction grating pitch. A third attempt successfully replicated the loaded specimen grating using RTV-615. A very thin coating of gold was applied after post-curing and no wrinkling was observed. Each replication attempt held the specimen under load for approximately 18 hours, and the attempts were made on successive days.

Immediately after the three days of loaded grating replication (54 hours under load), a replica of the specimen grating was made at zero load (this sector will be referred to as the "first post-load" sector). This was intended to record any permanent or viscoelastic deformation of the composite caused by the applied load. To examine whether the observed viscoelastic deformation was truly permanent, another replica of the specimen grating was made at zero load eight months later (this sector will be referred to as the "second post-load" sector). After this final specimen replica was made, x-ray photographs of the specimen were produced. These images, recorded at Wright Laboratory, showed no damage in the vicinity of the hole.

Fringe patterns for U_θ and U_z were recorded from the loaded sector grating at 3° intervals from 9° to 90° following the procedures outlined in Section 2.3.3. The specimen grating was damaged in the 0° region. The patterns were photographically recorded on Kodak Technical Pan film (35mm film format). The fringe pattern for each angular location spanned slightly less than 5°. All of the photographically recorded fringe patterns were digitally scanned into a computer. Common features in neighboring images were used to establish the magnification in the θ-direction, and the known thickness of the specimen was used to determine the magnification in the z-direction. The digital images were then scaled in the θ-direction so that the magnification factor was identical in both directions.

Detailed analyses of ε_θ and $\gamma_{\theta z}$ were performed at the 45°, 60°, 66°, 75°, 84°, and 90° locations. These analyses were performed within the image processing computer program Adobe Photoshop. The data points chosen for analysis were based on the ply boundary locations at the angular location of interest. The plies of the $[0°_4/90°_4]_{3s}$ composite were noticeably wavy. Ply boundary locations were determined from the original photographs of the periphery of the hole before the specimen grating had been applied. Figure 2.9 shows the locations of analyzed data points within a typical ply. Data points were concentrated toward ply boundaries. Analyses of the fringe patterns for ε_θ were accomplished using the finite-increment method as discussed in Appendix B. The gage-length of each measurement was typically between 1° and 2° of arc (0.22 mm to 0.44 mm) depending on the location of fringe centers. Analyses of the fringe patterns for $\gamma_{\theta z}$ were accomplished using the tangent method also discussed in Appendix B. The analyses for $\gamma_{\theta z}$ used only the U_θ displacement patterns. The contributions of the U_z fringe patterns to $\gamma_{\theta z}$ were trivial and were not included in the analyses. Analyses of the U_z fringe patterns for ε_z were not performed because of the sparseness of the U_z fringe patterns.

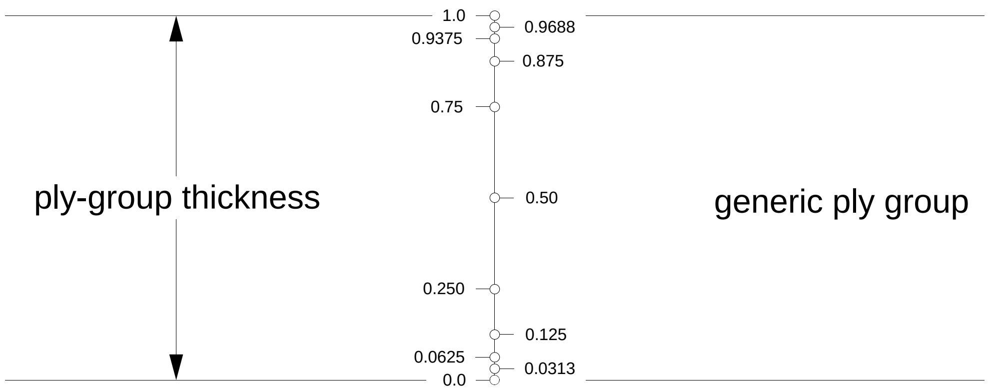

$[0_4/90_4]_{3s}$ laminate.

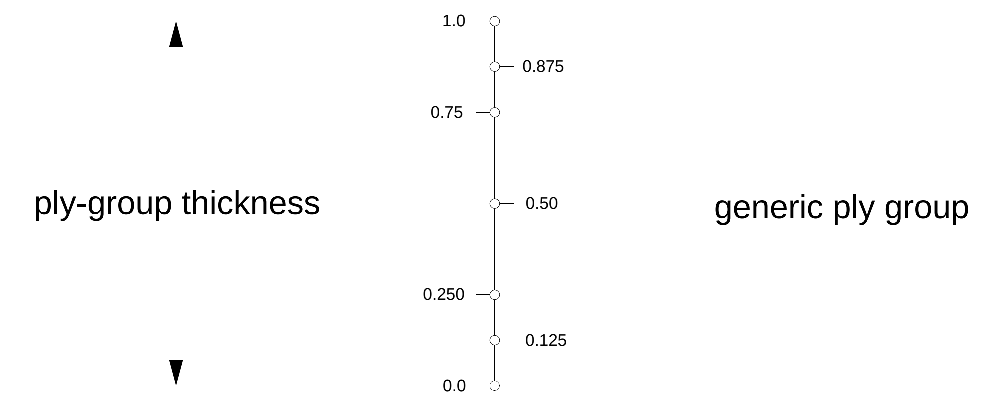

$[+30_2/-30_2/90_4]_{3s}$ laminate.

Figure 2.9: Data point locations for both laminates expressed as fractions of a ply-group thickness.

Fringe patterns for U_θ and U_z were photographically recorded from the first post-load sector at 30°, 39°, 45°, 60°, 75°, 78°, 81°, 84°, and 90°. A carrier of extension was added to the U_θ fringe patterns, and carriers of extension and rotation were added to the U_z fringe patterns. The second post-load sector was examined visually in the interferometer for signs of remaining plastic deformation. Fringe patterns for U_θ and U_z were photographically recorded for the 45°, 60°, 78°, and 84° angular locations.

$[+30°_2/-30°_2/90°_4]_{3s}$ Laminate

The $[+30°_2/-30°_2/90°_4]_{3s}$ specimens were 6.18 mm (0.243 inches) thick. The specimen tested for first ply failure load and ultimate failure load showed an initial acoustic emission event at 68.9 MPa (10,000 psi). The ultimate failure strength was 291 MPa (42,200 psi). These tests were also performed at Wright Laboratory by UDRI personnel. Four strain gages were bonded onto the moiré interferometry test specimen. These were located 127 mm (5.0 inches) from the center of the hole. Two gages were bonded onto the front and two on the back of the specimen. These gages were located 12.7 mm (0.5 inches) from each edge.

One replica of the $[+30°_2/-30°_2/90°_4]_{3s}$ specimen grating was produced while the specimen was in the testing machine frame, but no load had been applied. This grating was to be used as a null sector grating. Two replicas of the specimen grating were produced while the specimen was under 50 MPa (7,250 psi)-applied far-field stress. The first attempt, using RTV-664 silicon rubber, was successful, although the grating had poor diffraction efficiency. When a coating of vacuum deposited gold was applied, the grating was ruined due to the wrinkling phenomenon discussed previously. A second replication attempt several days later, using RTV-615 silicon rubber, succeeded. A very thin coating of gold was applied after post-curing, and no wrinkling was observed. The two loaded replicating events held the specimen under 50 MPa for approximately 36 hours.

Immediately after the second replication attempt, a replica of the specimen grating was made at zero load. This was again an attempt to quantify any plastic or viscoelastic deformation that had occurred in the composite during the 36 hours of loading. To verify whether the observed viscoelastic deformation was permanent, another replica of the specimen grating at zero load was made approximately eight months later. After this final specimen replica was made, x-ray photographs of the specimen were produced. These images, recorded at Wright Laboratory, showed no damage in the vicinity of the hole.

Fringe patterns for U_θ and U_z were recorded from the loaded sector grating at 3° intervals from 0° to 90° following the procedures outlined in Section 2.3.3. Fringe patterns were also recorded for U_z at 3° intervals from 60° to 90° with a carrier of rotation added to the U_z fringe pattern. The patterns were photographically recorded on Kodak Technical Pan film (35mm film format). The fringe pattern for each angular location spanned slightly less than 5°. All of the photographically recorded fringe patterns were digitally scanned into a computer. Common features in neighboring images were used to establish the magnification in the θ-direction, and the known thickness of the specimen was used to determine the magnification in the z-direction. The digital images were then scaled in the θ-direction so that the magnification factor was identical in both directions.

Detailed analyses of ε_θ and $\gamma_{\theta z}$ were performed at the 15°, 45°, 60°, 66°, 75°, 84°, and 90° locations. Detailed analyses of ε_z were performed at the 60°, 66°, 75°, 84°, and 90° locations. These analyses were performed within Adobe Photoshop. The data points chosen for analysis were based on the ply boundary locations at the angular location of interest. Figure 2.9 shows the locations of analyzed data points within a typical ply. The plies of the $[+30°_2/-30°_2/90°_4]_{3s}$ composite were not as wavy as the $[0°_4/90°_4]_{3s}$ composite. Ply boundary locations were determined from the original photographs of the periphery of the hole before the specimen grating had been applied. Analyses of the fringe patterns for ε_θ were accomplished using the finite-increment method as discussed in Appendix B. The gage-length of each measurement was typically between 1° and 2° of arc (0.22 mm to 0.44 mm) depending on the location of fringe centers. Analyses of the fringe patterns for ε_z and $\gamma_{\theta z}$ were accomplished using the tangent method also discussed in Appendix B. The analyses for $\gamma_{\theta z}$ used only the U_θ displacement patterns. The contribution of the U_z fringe patterns to $\gamma_{\theta z}$ were trivial and were not included in the analyses.

A series of digital images of fringe patterns for U_θ and U_z were recorded for the 56°, 58°, 60°, 62°, and 64° locations from the loaded and zero load sector gratings. Phase-shifting analysis of the type discussed in Lassahn *et al*. (1994) was performed on the recorded digital images. The resulting digital data sets of U_θ and U_z were manipulated and differentiated to produce digital data sets containing ε_θ, ε_z, and $\gamma_{\theta z}$. Strains were averaged over approximately 1° in the θ-direction. Null fringe pattern information was subtracted from the load information, eliminating any errors caused by out-of-plane rotation effects or shim grating thickness variations.

Fringe patterns for U_θ and U_z were photographically recorded from the first post-load sector at 60°, 69°, 72°, 75°, 78°, 81°, 84°, 87° and 90°. A carrier of extension was added to the U_θ fringe patterns, and carriers of extension and rotation were added to the U_z fringe patterns. A series of digital images were captured of a portion of the U_θ and U_z fringe patterns at 87°. Detailed phase-shifting analysis was performed on these images. The second post-load sector was examined visually in the interferometer for signs of remaining plastic deformation. Fringe patterns for U_θ and U_z were photographically recorded for the 69°, 81°, 84°, 87°, and 90° angular locations.

Chapter 3: Results and Discussion

3.1 Aluminum Test Results and Discussion

The fringe patterns resulting from the interrogation of the flat face gratings from the aluminum specimen were of relatively poor quality. Superior fringe patterns could have been obtained using typical moiré interferometry techniques. The moiré results for axial strain (ε_x) on the flat surface of the specimen at the transverse centerline are shown in Figure 3.1. These data are compared with analytical results obtained using the Howland (1930) solution as discussed in Section 1.3.1. Moiré measurements extend to approximately 25.4 mm (1.0 inch) from the hole center, since the square steel replication plate had dimensions of 50.8 mm (2.0 inches). The match between the analytical solution and moiré is very close, with no indication of side-to-side bending. At the outer extent of the moiré data, the comparison is not as close. The measured results show more tensile strain than predicted by Howland's solution. It is believed that the out-of-plane pressure application screws caused the tensile increase in these areas. As a result of this observation, pressure distribution plates were applied under the screw tips in subsequent procedures to alleviate point force loading.

Fringe pattern results for U_θ at 58° and 27.56 MPa (4,000 psi) and U_θ at 83° and 82.68 Mpa (12,000 psi) are shown in Figure 3.2. Also included in this figure are the corresponding null images. All images contained a carrier of extension. The long dimension in these images corresponds to the z-direction (6.6 mm in length), and the short dimension corresponds to the θ-direction (cut within Adobe Photoshop to approximately 3°). The long scratch-like grating damage visible in each of these images are the fiducial marks placed at 58° and 83°, respectively. The distortion visible at the bottom end of the loaded fringe images results from the RTV-615 silicon rubber peeling away from the steel sector substrate. This location corresponds with the side of the sector that bolts to the steel replication plate. While producing a replica of the specimen grating, the separation of the replication plate from the specimen and sector causes the silicon rubber grating to tear at the joint between the replication sector and replication plate. Occasionally this peeled an inconsequential portion of the silicon rubber grating away from the sector face.

The moiré results from both applied loads for ε_θ, ε_z, and $\gamma_{\theta z}$ at 3°, 28°, 43°, 58°, and 83° are plotted in Figure 3.3. The strain values were calculated by averaging the strain results, obtained by phase-shifting, over a 1° by 3 mm (0.12 inch) region at the angular location of interest. These data are also compared with analytical results obtained using the Howland (1930) solution. The Howland solution is a

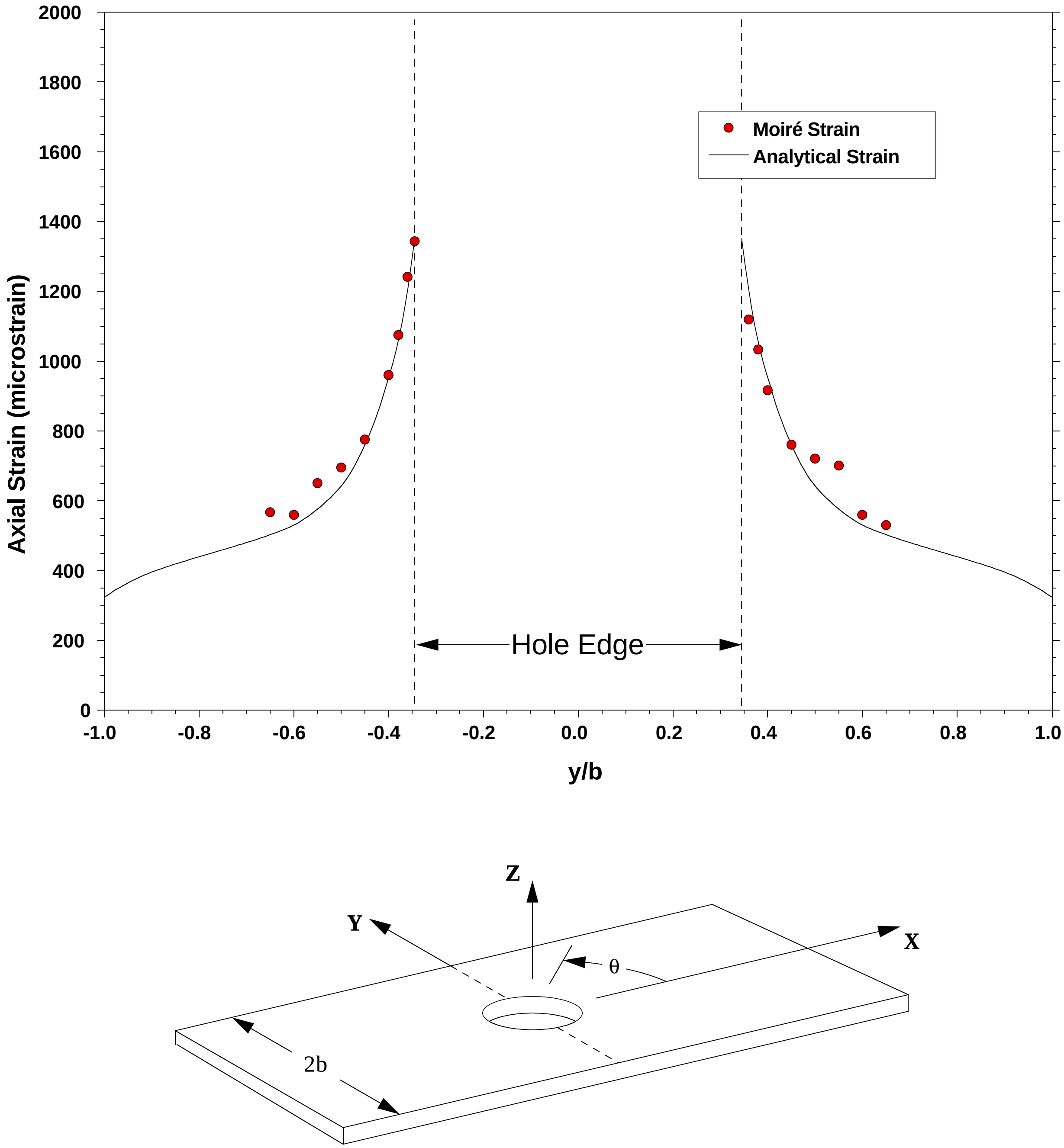

Figure 3.1: Axial strain comparison along the line x=0 for the tensile-loaded aluminum control specimen at 27.56 MPa (4,000 psi).

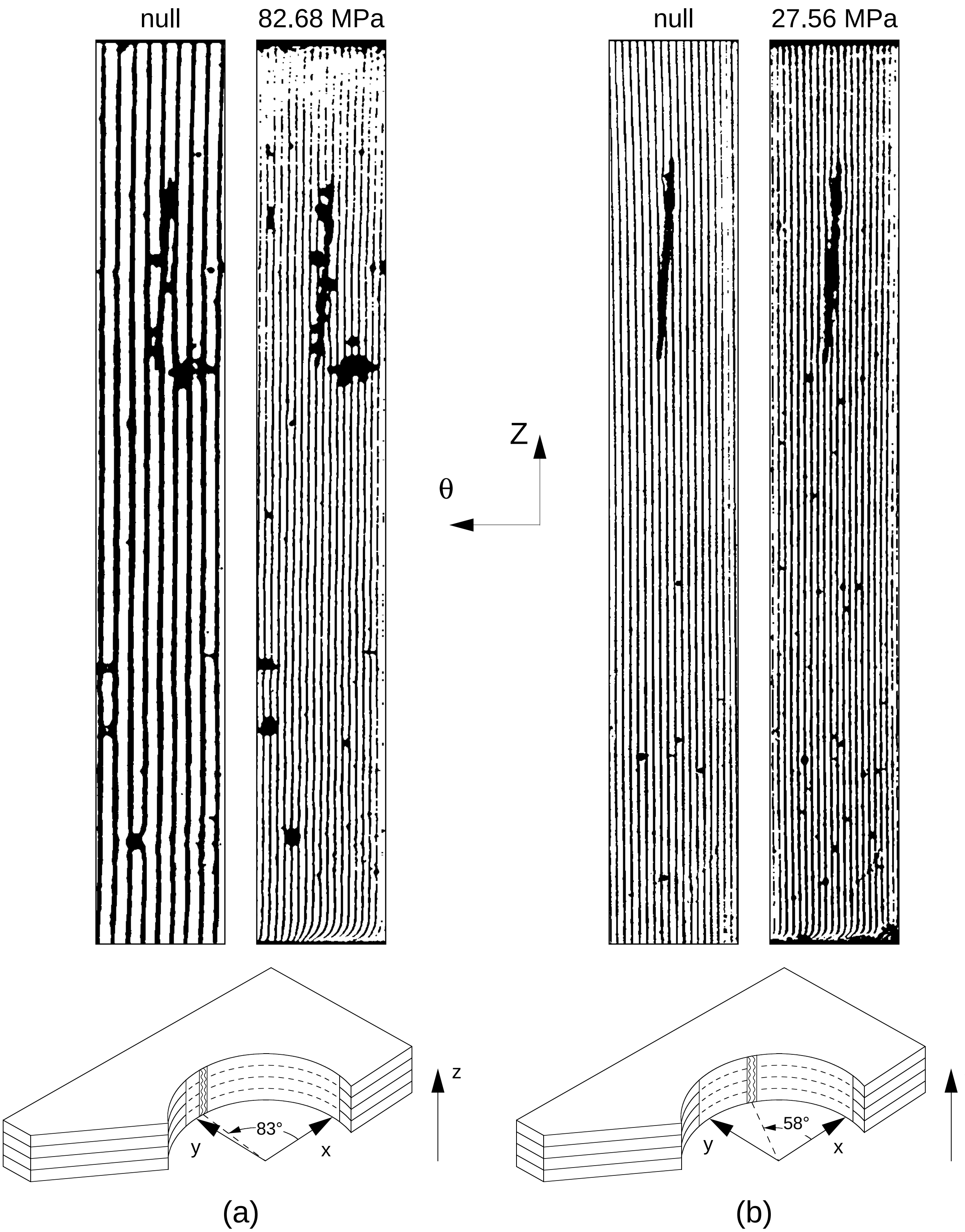

Figure 3.2: U_θ fringe patterns from the null and load sector gratings from the aluminum specimen at (a) 83° loaded to 82.68 MPa and at (b) 58° loaded to 27.56 MPa (note: all patterns contain carriers of extension).

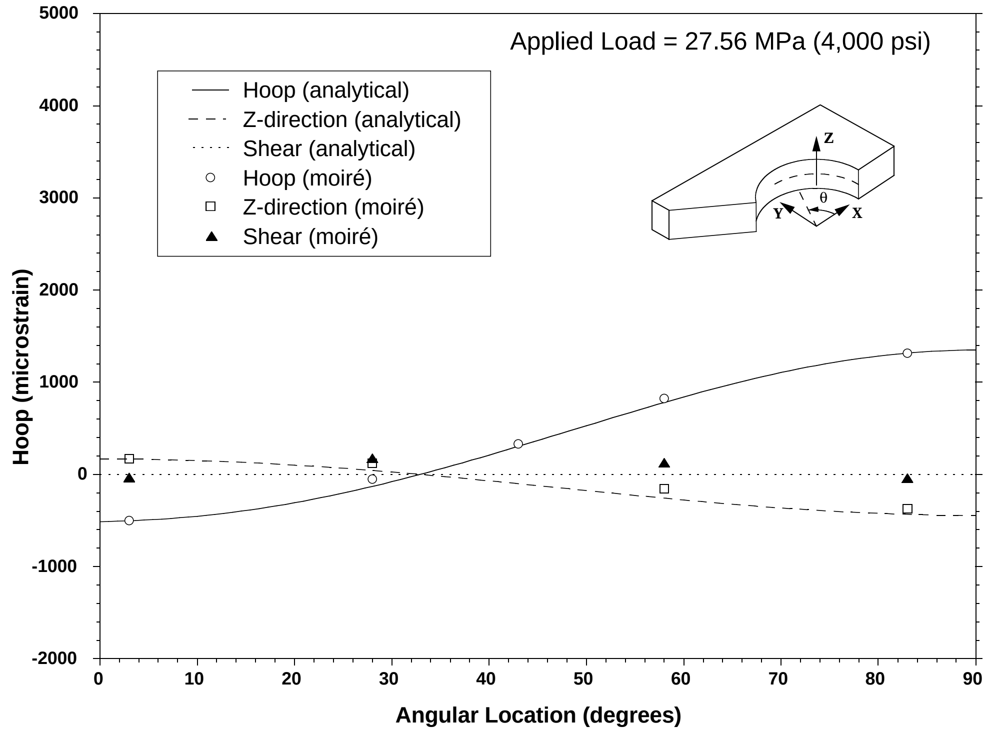

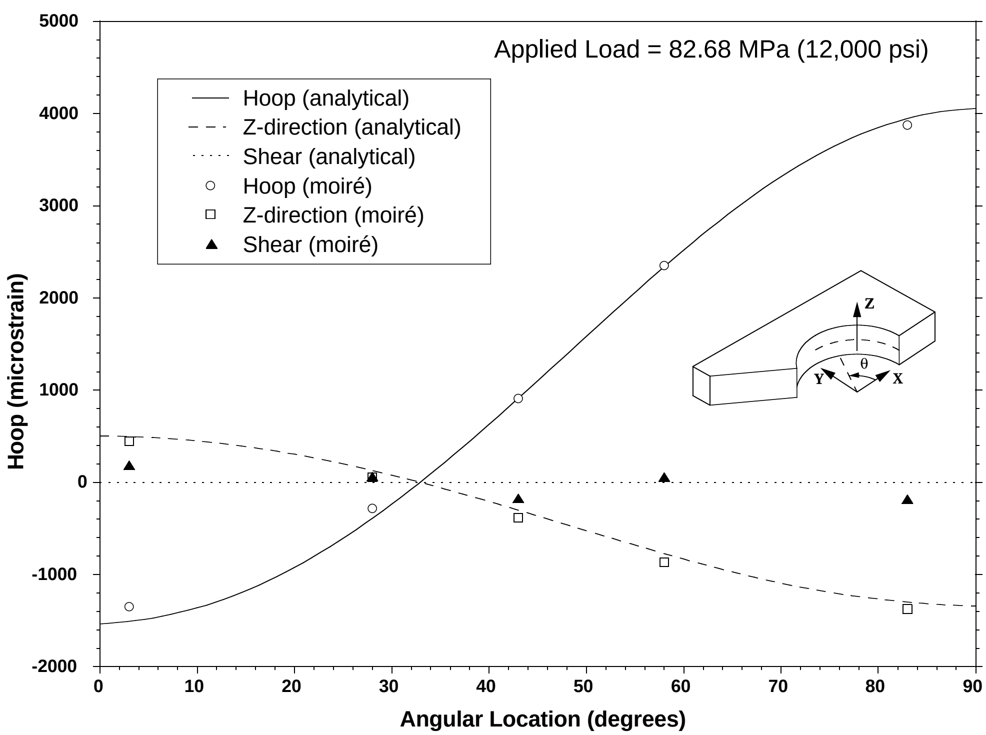

Figure 3.3: Strain comparison around the periphery of the hole for the tensile-loaded aluminum control specimen at 27.56 and 82.68 MPa.

two-dimensional solution. The shear is, therefore, predicted to be identically zero, and ε_z is simply a Poisson's effect of ε_θ. The match between moiré and analytical ε_θ and ε_z is very close at both loads. The average percent difference (compared with the maximum ε_θ) for ε_z was 4.5% for the 27.56 MPa load and 1.9% for the 82.68 Mpa load. The average percent difference (compared with the maximum ε_θ) for ε_θ was 2.4% for the 27.56 MPa load and 1.7% for the 82.68 Mpa load. The match between the analytical and moiré interferometry results for $\gamma_{\theta z}$ was not quite as close as for the other components of strain. The average percent difference (compared with the maximum ε_θ) for $\gamma_{\theta z}$ was 6.9% and for the 27.56 MPa load and 3.3% for the 82.68 Mpa load.

The comparison between moiré and analytical strain results has demonstrated that the grating replication and analysis techniques described in Chapter 2 work for specimens with relatively smooth gradients in strain. The aluminum specimen, however, did not contain regions of high strain gradients as expected in a multi-layer composite material system.

3.2 Results from Loaded Composites

Fringe patterns from the replicas of the flat face gratings were not recorded or analyzed. The quality of the fringe patterns obtainable from the steel replication gratings was considered inferior to those obtainable using standard moiré interferometry techniques. Also, since the discrete sector method was being implemented to examine the sector gratings, the flat face information was not required to correct for undesired additions to ε_θ resulting from shim grating thickness variations.

3.2.1 $[0°_4/90°_4]_{3s}$ Laminate

The discrete nature of the moiré measurements described in Section 2.3.3 make a continuous display of fringe patterns around the cylindrical surface of the hole impossible. It is possible, however, to create a mosaic of fringe images from each of the photographed angular locations. Figures 3.4 and 3.5 show mosaics of the U_θ and U_z fringe patterns for the $[0°_4/90°_4]_{3s}$ specimen, respectively. In these figures, each rectangular fringe pattern is a 3° slice from the approximately 5° fringe pattern recorded at the specified angular locations around the periphery of the hole. Slight rigid body rotation differences of the loaded sector grating about the r-axis may result in slight differences in the appearance of neighboring fringe patterns. Attempts were made during testing to tune the rotation to produce symmetrical fringe

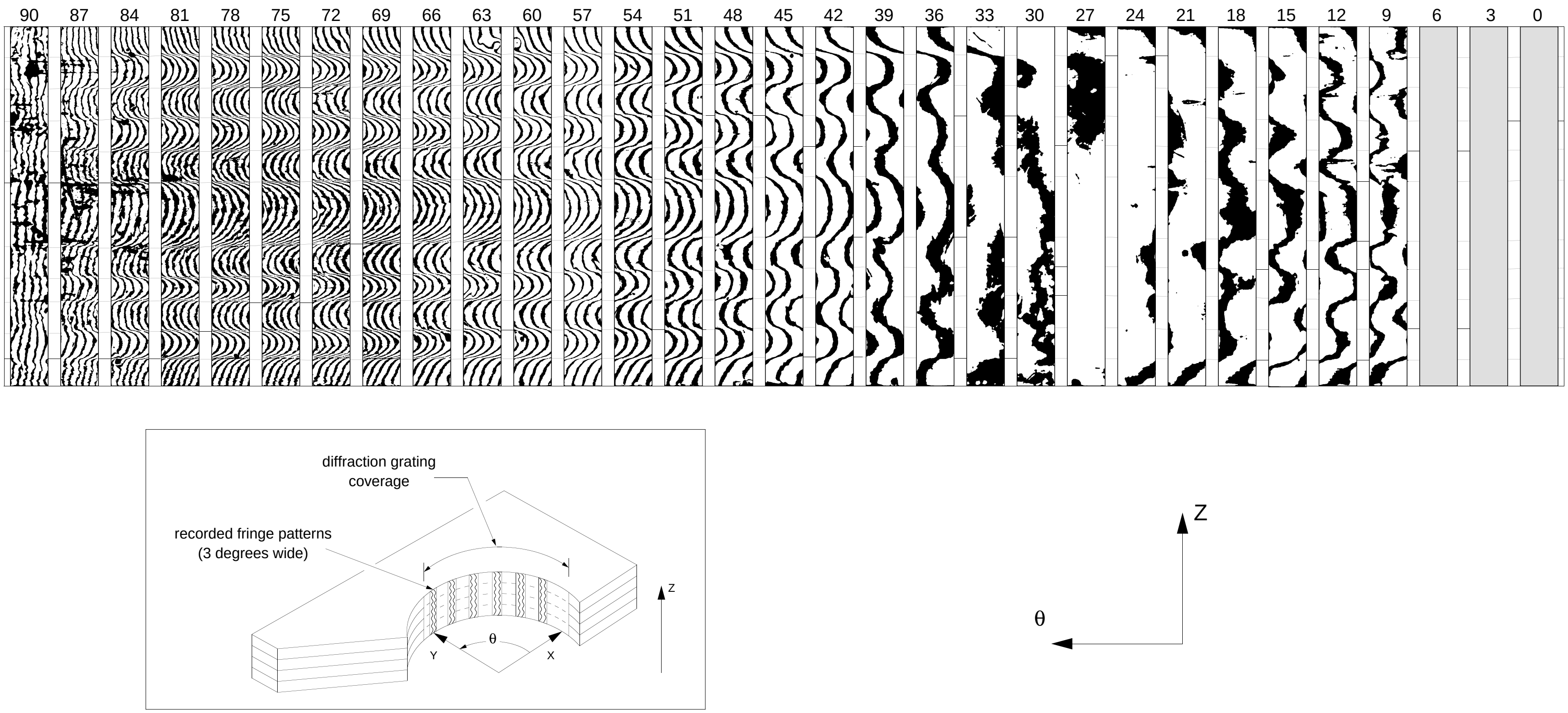

Figure 3.4: Mosaic of U_θ fringe patterns from the $[0_4/90_4]_{3s}$ laminate loaded at 50 MPa. Each fringe pattern is 3° wide, and the horizontal lines between fringe patterns are the approximate ply boundaries.

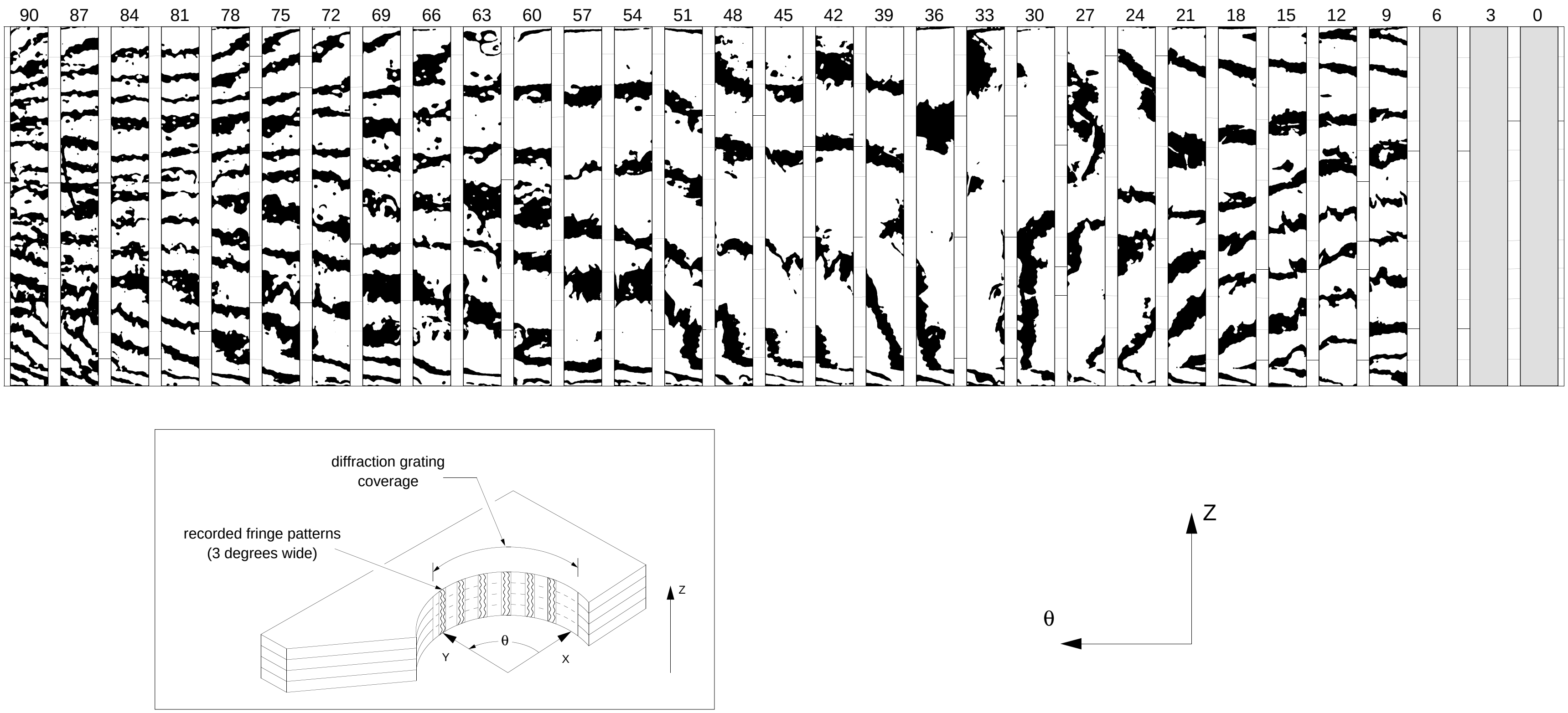

Figure 3.5: Mosaic of U_z fringe patterns from the $[0_4/90_4]_{3s}$ laminate loaded at 50 MPa. Each fringe pattern is 3° wide, and the horizontal lines between fringe patterns are the approximate ply boundaries.

patterns at each angular location. Horizontal lines between each fringe pattern in these figures correspond to the approximate locations of the actual ply boundaries. These were determined from the initial photographs of the hole periphery before a grating had been applied.

The regions of the grating from 0° to 6° were damaged, and the photographs of these areas do not appear on the mosaics in Figures 3.4 and 3.5. Visible from 81° to 90° and again from 9° to 12° is minor grating damage which occurred during initial grating replication. The fringe patterns in these mosaic images show that the grating was generally replicated without damage from the top face to the bottom face of the laminate.

To the author's knowledge, results of the type shown in Figure 3.4 have never been published in the literature before. Boeman's (1991) work included a continuous fringe pattern from a quadrant of the cylindrical surface of a hole in a composite material. His efforts, however, contained the effects of unknown additions to the circumferential strain caused by variations in the shim grating thickness. The U_θ fringe pattern mosaic presented in Figure 3.4 does not contain unknown additions caused by shim grating thickness variations. In fact, the estimated error caused from the neglection of the null fringe patterns is believed to be below 60 $\mu\varepsilon$.

The fringe pattern mosaics presented in Figures 3.4 and 3.5 are extremely useful. Complete fringe information over an entire quadrant could allow a researcher to detect interesting or unusual changes in behavior from point to point. Once interesting locations have been identified, these areas can be examined in detail.

ε_θ for the $[0°_4/90°_4]_{3s}$ Laminate

Results of the detailed fringe analyses of the U_θ fringe patterns for ε_θ at 90°, 84°, 75°, 66°, 60°, and 45° are presented in Figures 3.6-3.11, respectively. The circumferential strain, ε_θ, is determined from the distance between fringes in the circumferential direction, i.e., the vertical direction in the figures. Despite the undulation of fringes, the variation of vertical separation is not great. Within these figures and subsequent similar figures, the vertical dotted lines represent the idealized ply boundaries. The filled triangles represent the approximate ply boundaries on the actual specimen. The numbers across the top of these charts represent the lay-up angle of the particular ply. All graphs are plotted on the same scale. The actual ply boundaries are, in some cases, significantly displaced from the idealized ply boundaries. This is especially true at the 90°, 84°, and 75° locations. A wave in the plies near the transverse centerline of the composite was visible on both sides of the hole and on both straight edges of the composite.

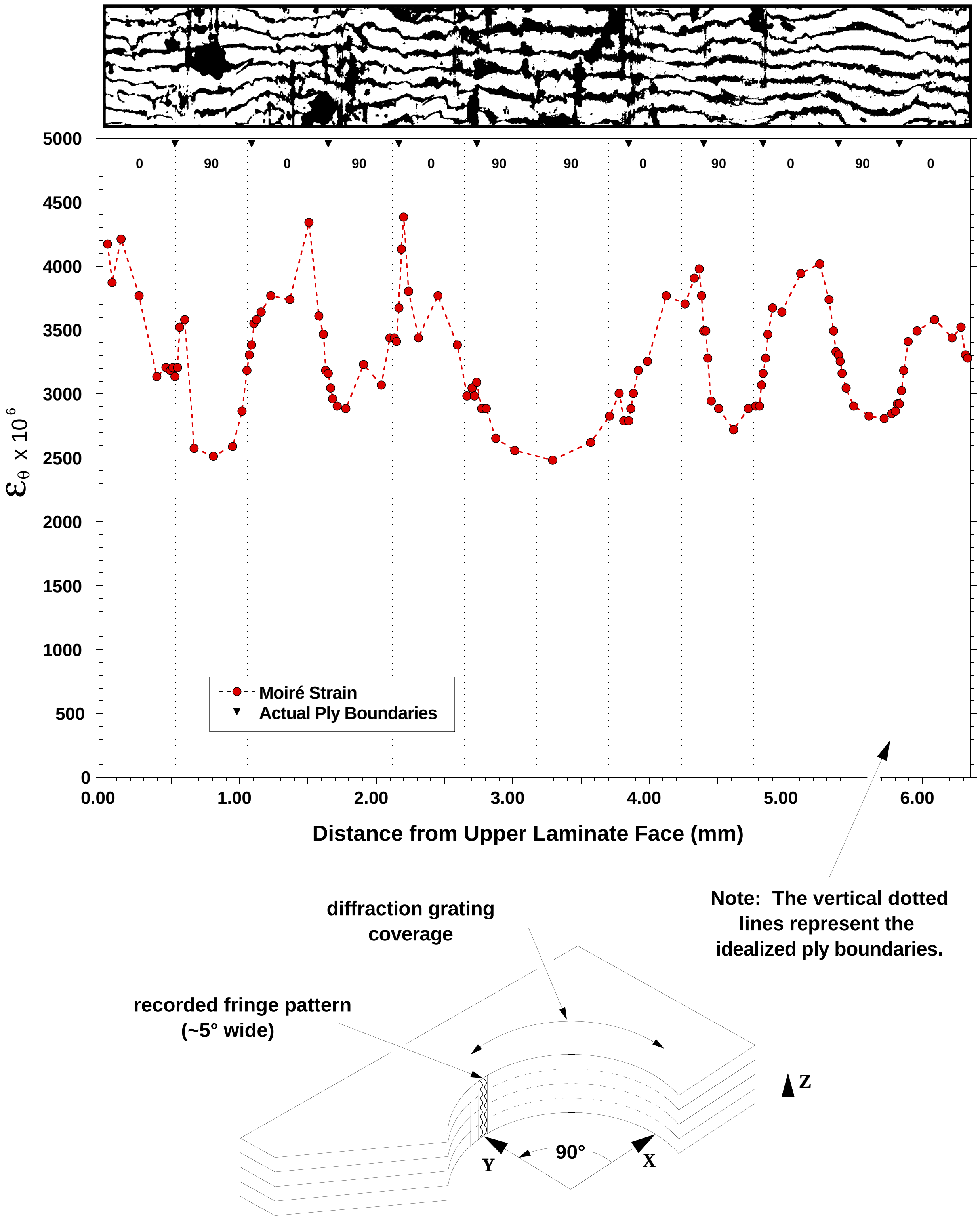

Figure 3.6: Circumferential strain variation at 90° for the $[0_4/90_4]_{3s}$ laminate.

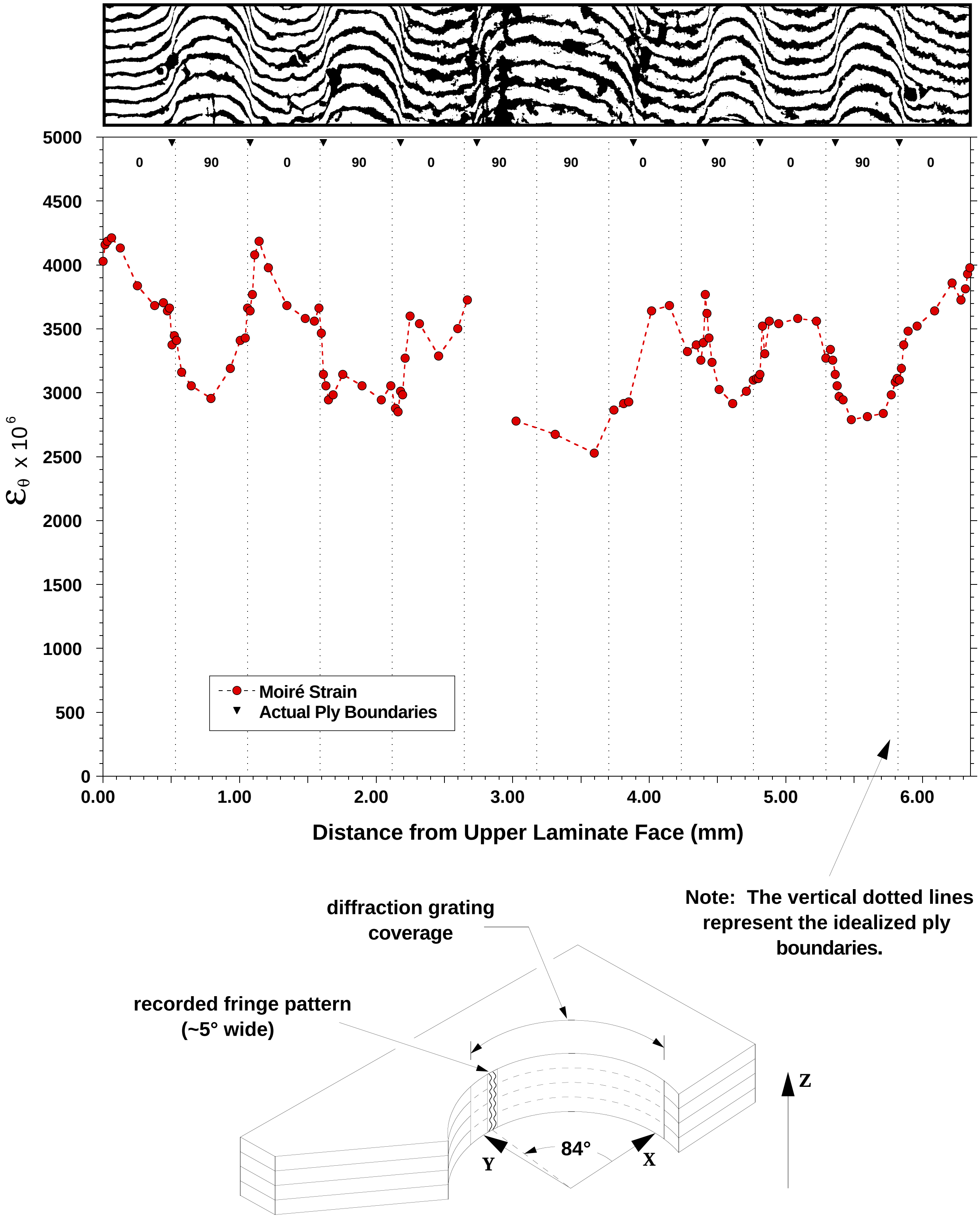

Figure 3.7: Circumferential strain variation at 84° for the $[0_4/90_4]_{3s}$ laminate.

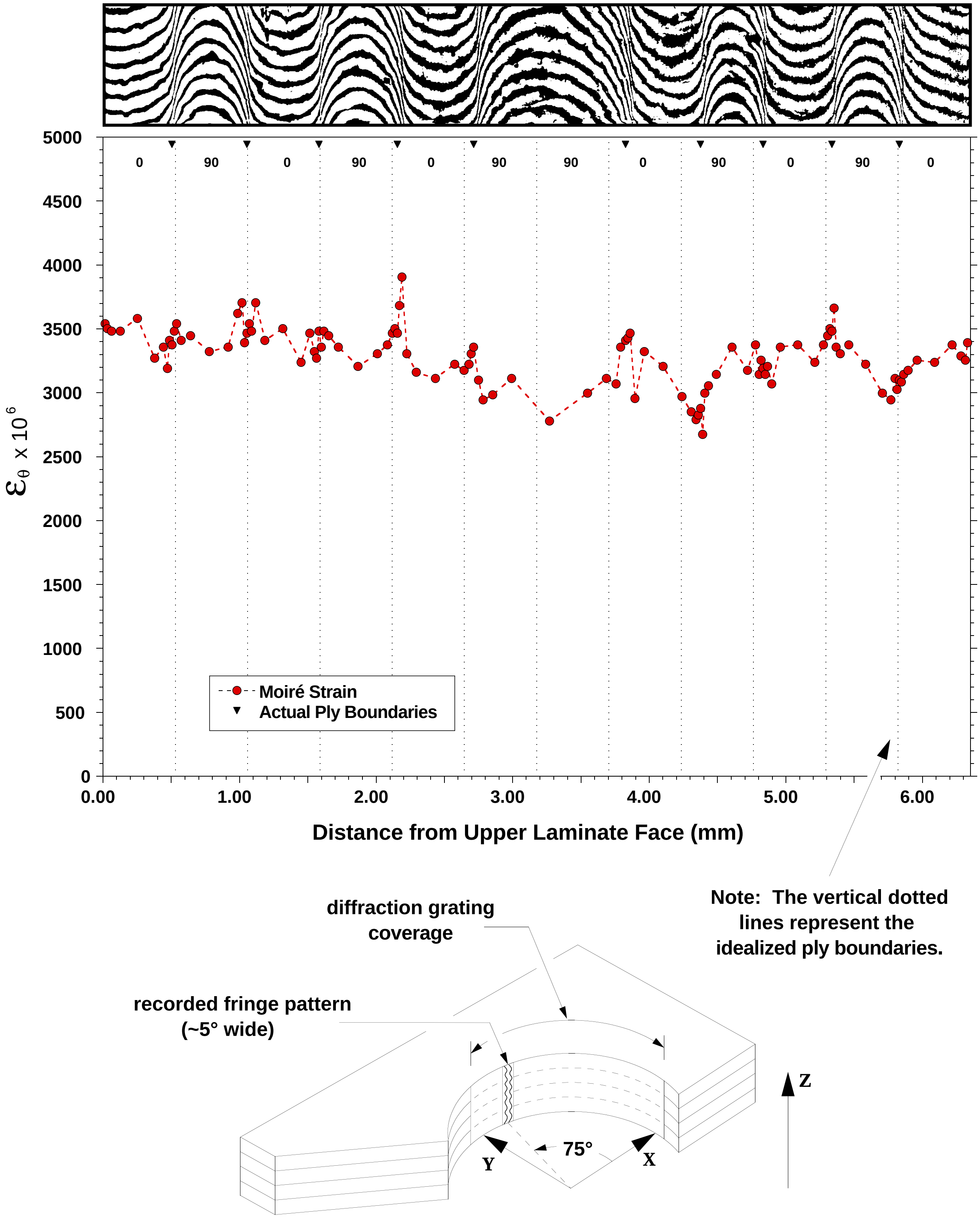

Figure 3.8: Circumferential strain variation at 75° for the $[0_4/90_4]_{3s}$ laminate.

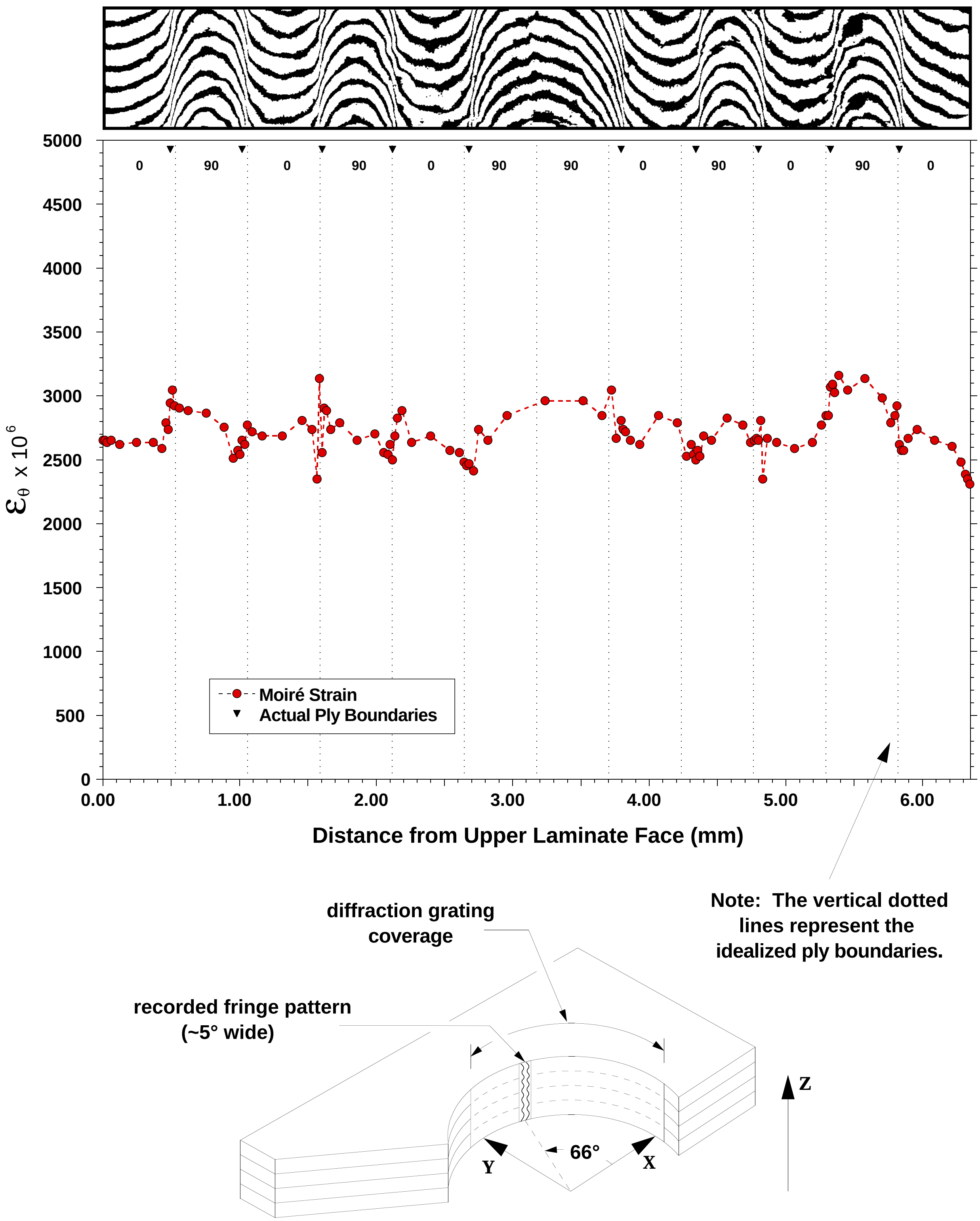

Figure 3.9: Circumferential strain variation at 66° for the $[0_4/90_4]_{3s}$ laminate.

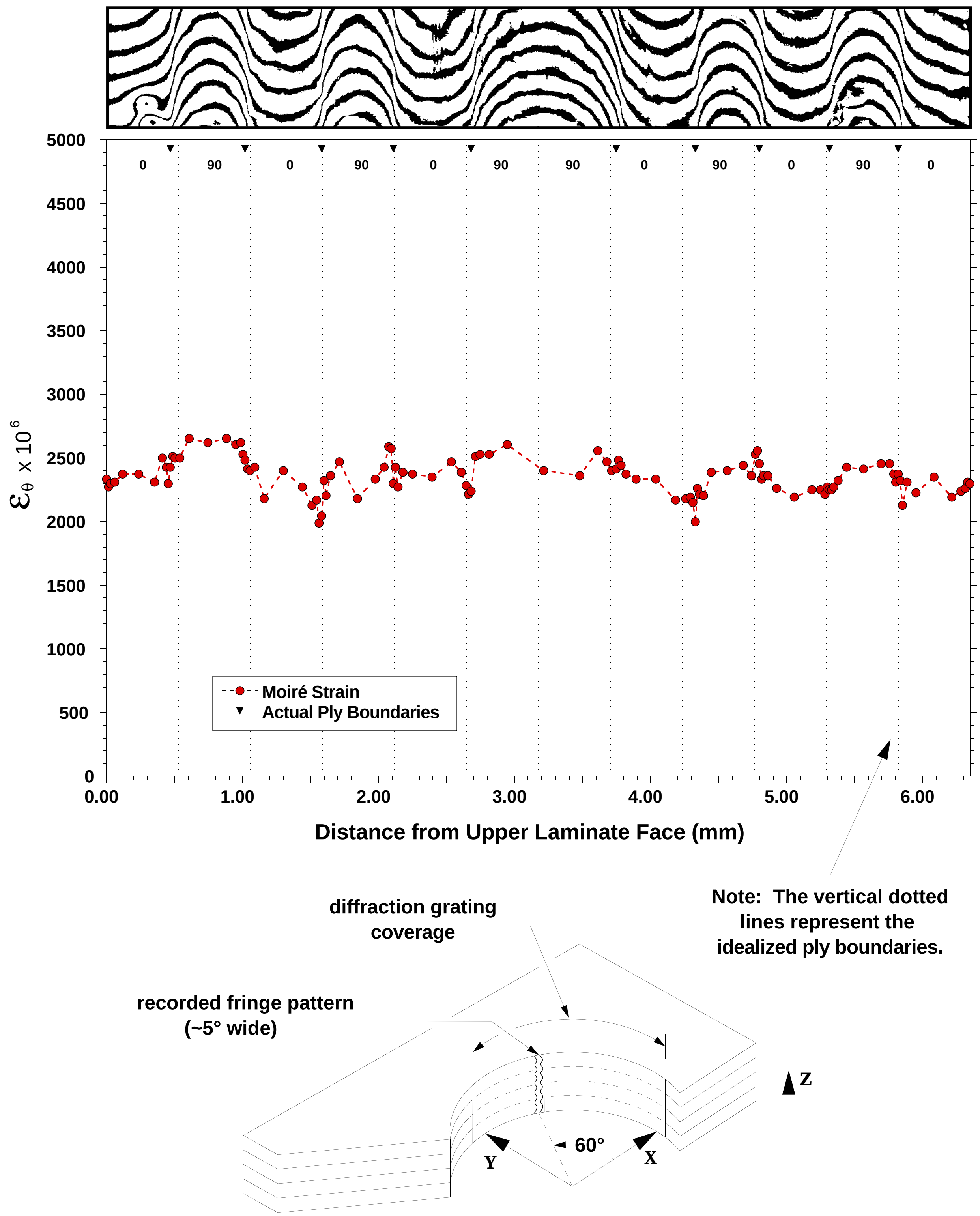

Figure 3.10: Circumferential strain variation at 60° for the $[0_4/90_4]_{3s}$ laminate.

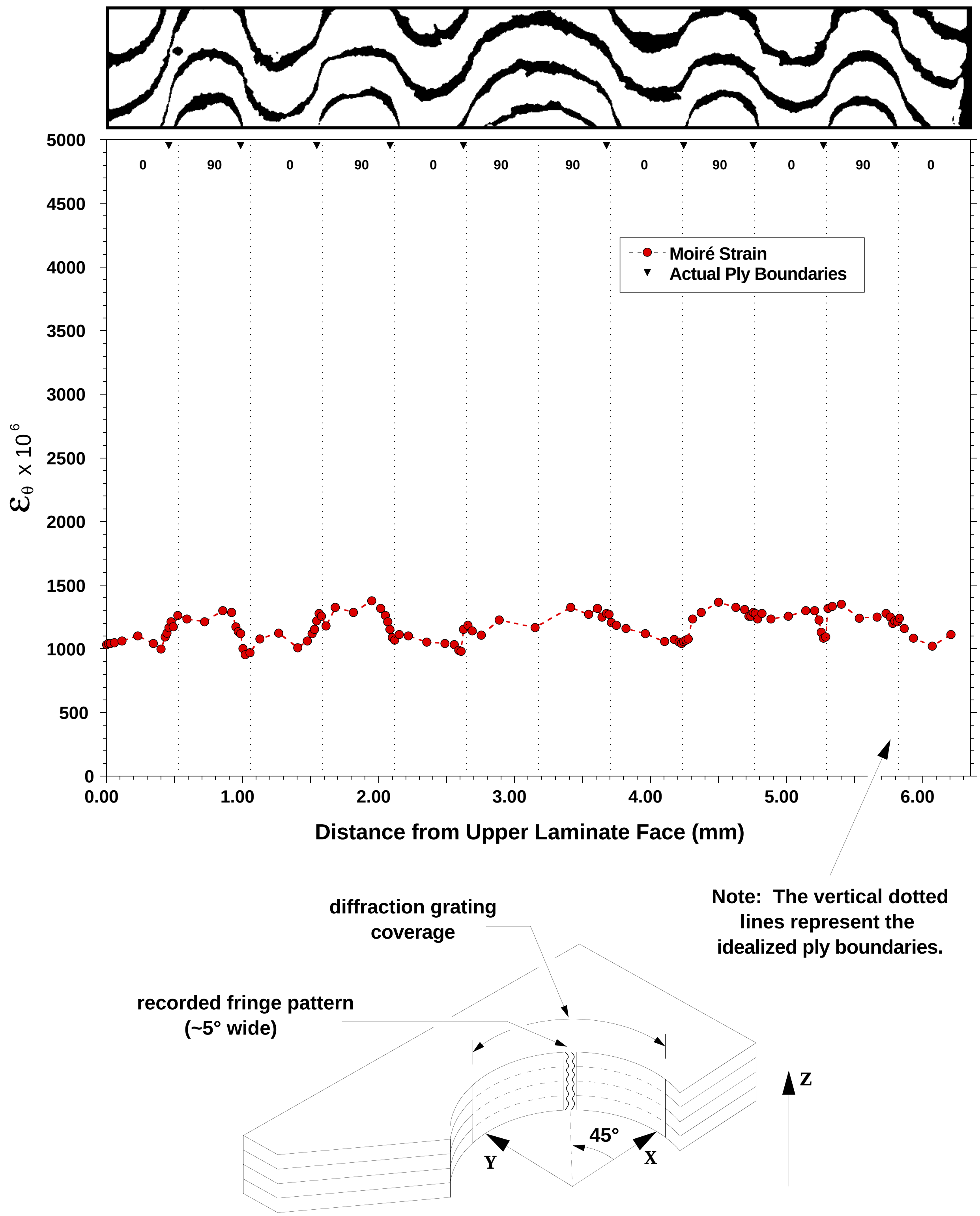

Figure 3.11: Circumferential strain variation at 45° for the $[0_4/90_4]_{3s}$ laminate.

There is significant noise present in the plots of ε_θ in Figures 3.6-3.11. Details of possible sources of noise are discussed in a later section. A discussion of the accuracy of the strain calculated using the finite-increment method is included in Appendix B, which conservatively concludes that analysis errors are less than 250 $\mu\varepsilon$. It is important to note that sub-ply variations of strain on the cylindrical surface of a hole in a composite have not been found in the literature at this level of detail. The graphs of strain presented here and in later sections have not been smoothed or averaged (except over the analysis gage length). Anomalies are, perhaps, represented more than the ideal strain behavior. To blunt the effects of anomalies, it is possible to the average results from both sides of the mid-plane.

Despite the noise, there are clear trends in some of the distributions of ε_θ. At the 90° and 84° locations, it is clear that ε_θ is more tensile in the 0° plies than in the 90° plies. The 75° and 66° results do not show any noticeable trends. The distribution of strain at 60° and 45° barely show the trend that ε_θ is slightly more tensile in the 90° plies than in the 0° plies. This trend is exactly the opposite of what is visible at 90° and 84°.

The measured circumferential strain values are quite large. At the 90° location, the strain in the 0° plies is approximately six times as high as the measured far-field axial strain of 660 $\mu\varepsilon$.

$\gamma_{\theta z}$ for the $[0°_4/90°_4]_{3s}$ Laminate

Results of the detailed fringe analyses of the U_θ fringe patterns for $\gamma_{\theta z}$ at 84°, 75°, 66°, 60°, and 45° are shown in Figures 3.12-3.16, respectively. The noise level appears to be less than in the ε_θ case, until the graph scale is considered. All plots in Figures 3.12-3.16 share the same scale which has a range nine times as large as the scale in Figures 3.6-3.11. A discussion of the accuracy of the strain calculated using the tangent method is contained in Appendix B, which concludes that analysis errors are typically less than 250 $\mu\varepsilon$. $\gamma_{\theta z}$ is determined by $\Delta N_\theta/\Delta z$, which varies strongly in the undulating fringe display. The variation of $\Delta N_z/\Delta\theta$ is negligible in the companion fringe pattern and was not considered in the calculation of $\gamma_{\theta z}$.

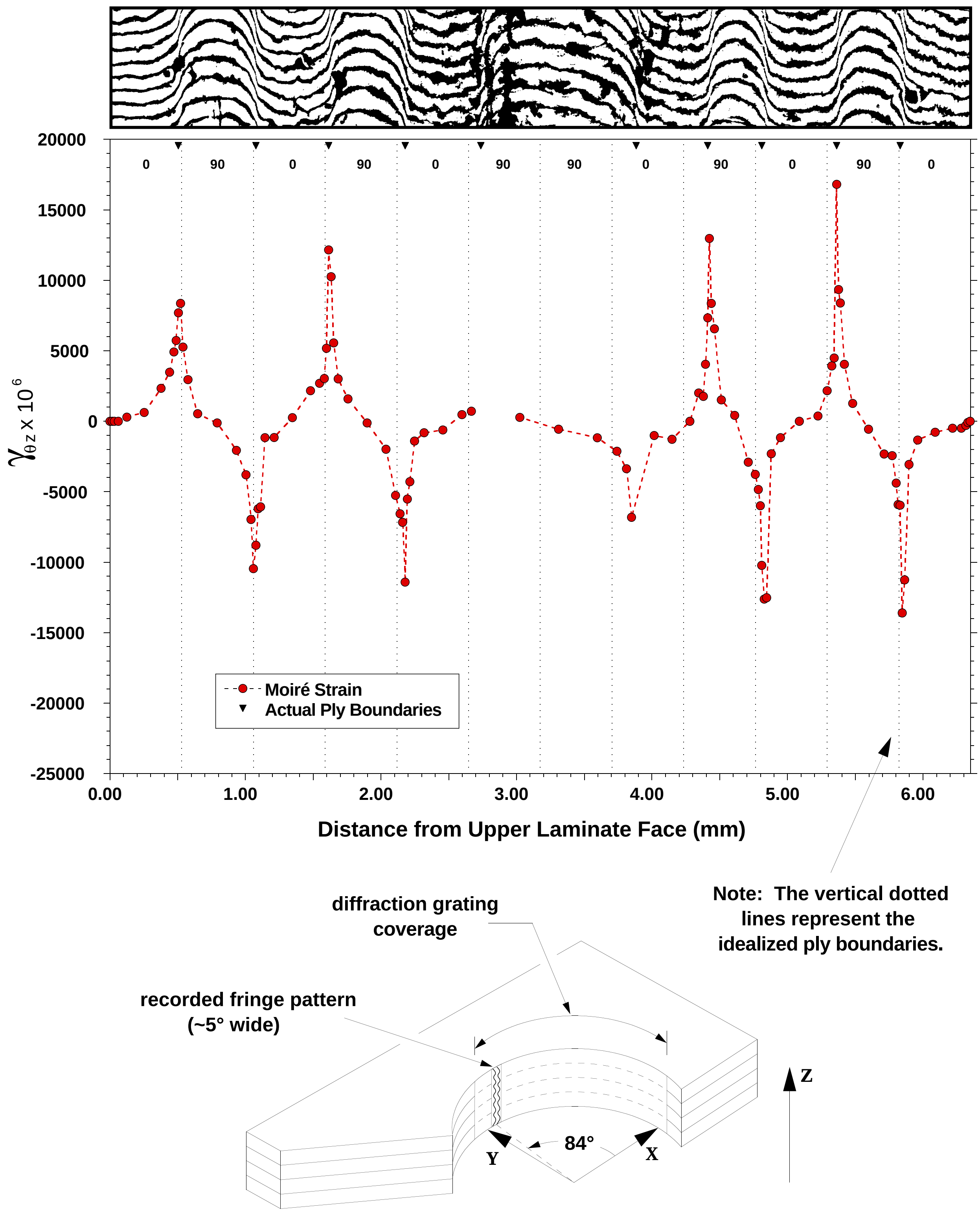

Figure 3.12: Theta-Z shear strain variation at 84° for the $[0_4/90_4]_{3s}$ laminate (note: shear strain calculated from U_θ pattern only).

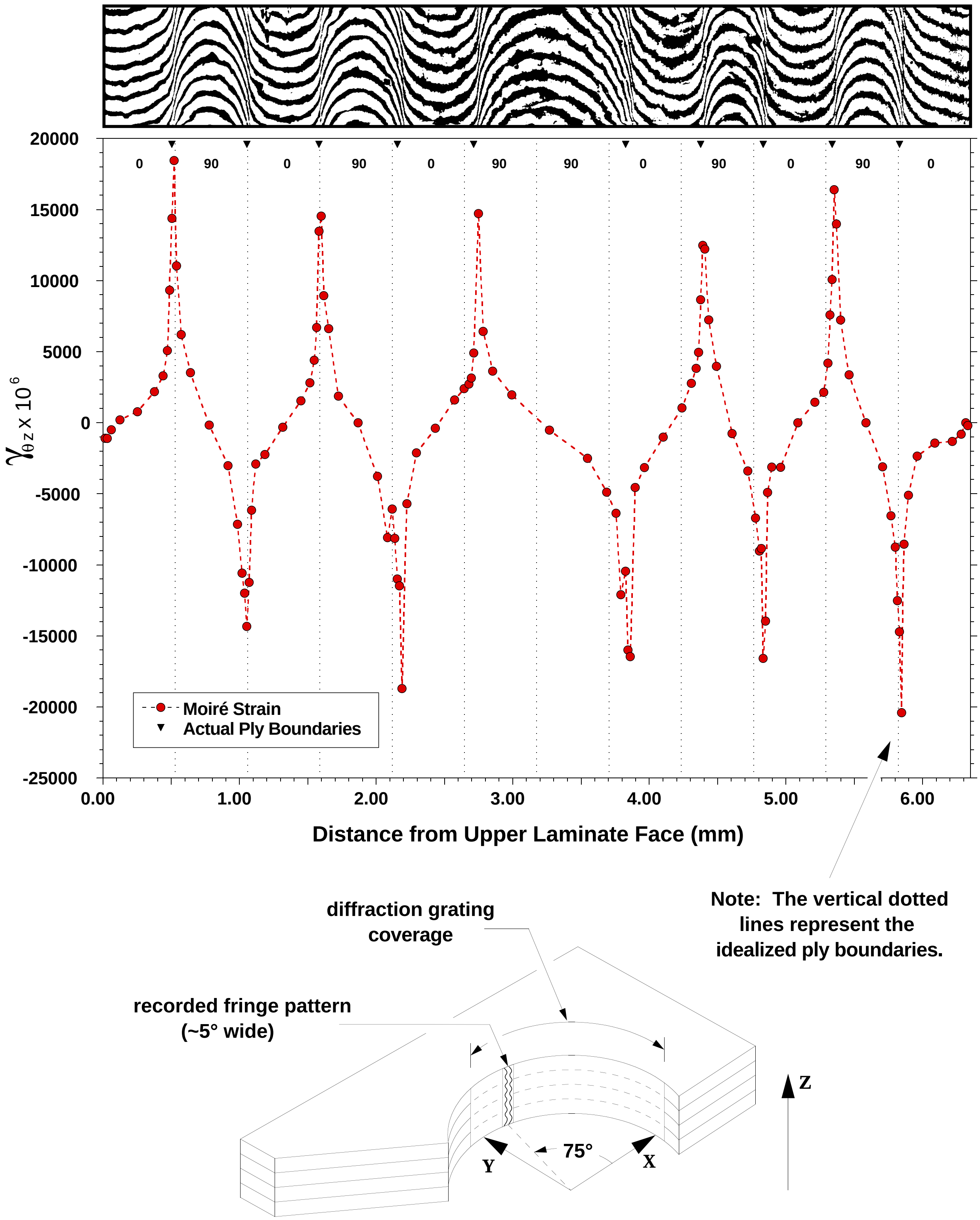

Figure 3.13: Theta-Z shear strain variation at 75° for the $[0_4/90_4]_{3s}$ laminate (note: shear strain calculated from U_θ pattern only).

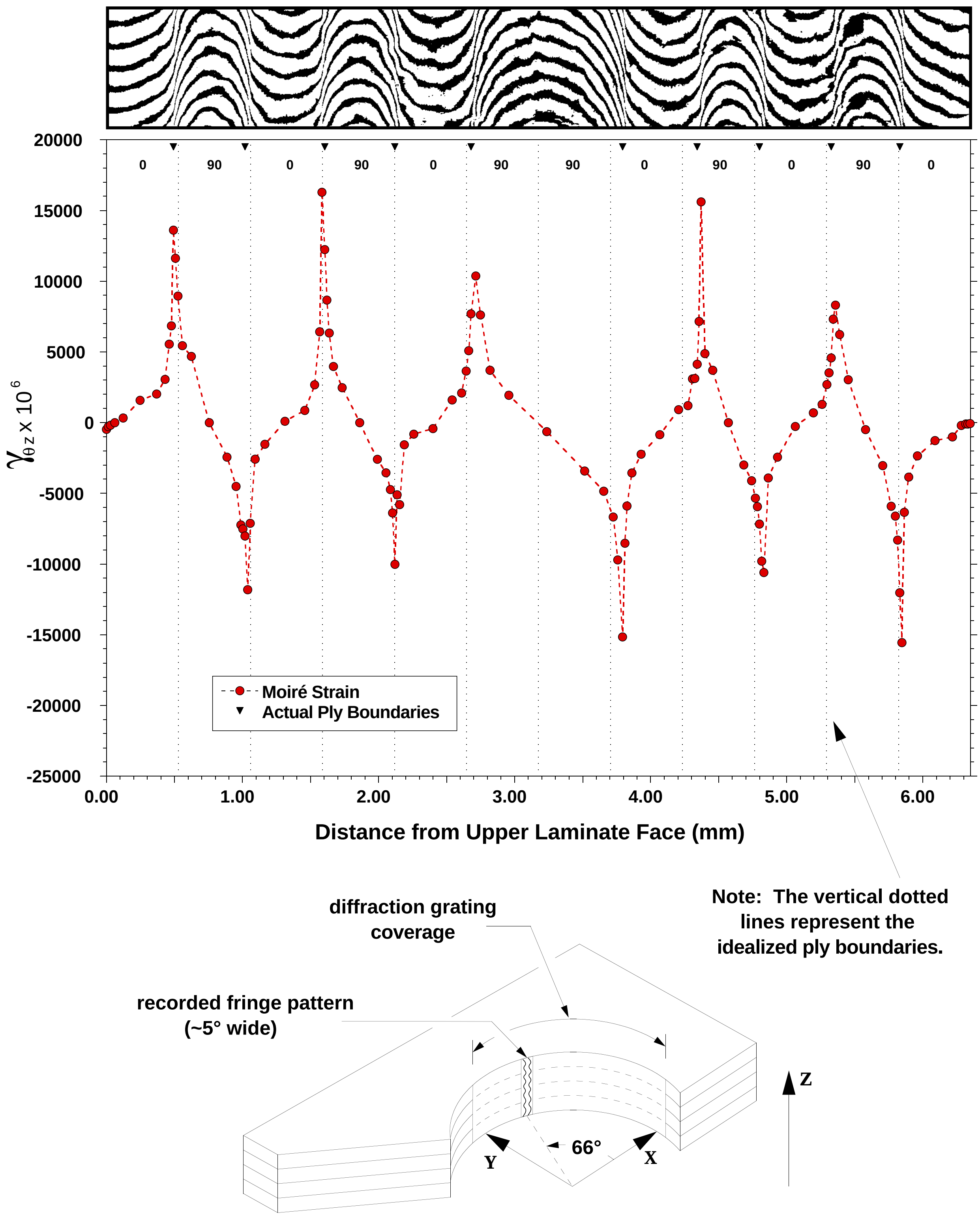

Figure 3.14: Theta-Z shear strain variation at 66° for the $[0_4/90_4]_{3s}$ laminate (note: shear strain calculated from U_θ pattern only).

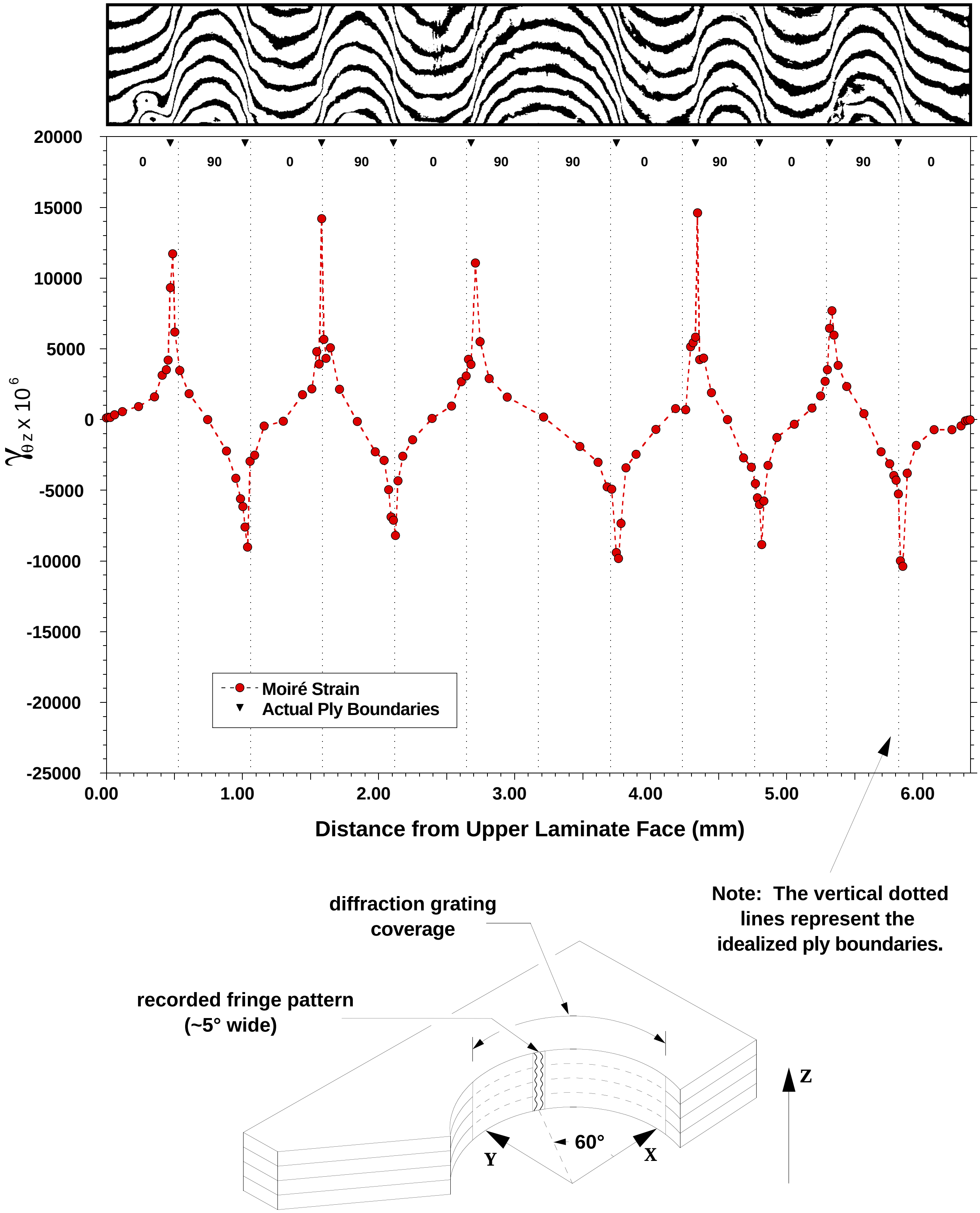

Figure 3.15: Theta-Z shear strain variation at 60° for the $[0_4/90_4]_{3s}$ laminate (note: shear strain calculated from U_θ pattern only).

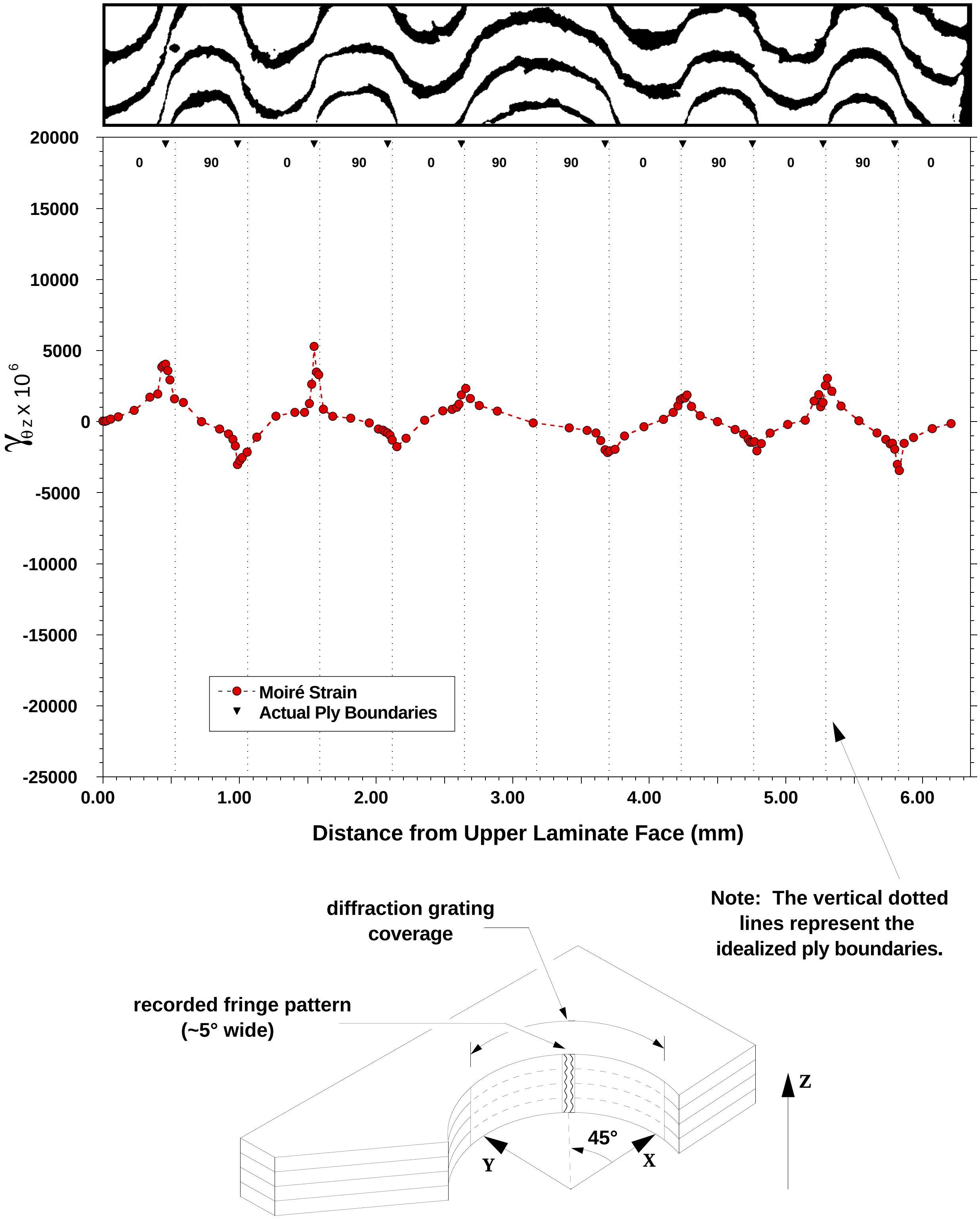

Figure 3.16: Theta-Z shear strain variation at 45° for the $[0_4/90_4]_{3s}$ laminate (note: shear strain calculated from U_θ pattern only).

Peak positive and negative values of shear occur at the interfaces between plies of differing lay-up angle. Maximum calculated values of $\gamma_{\theta z}$ approach 20,000 $\mu\varepsilon$ (2% strain) at some locations, approximately 30 times as high as the measured far-field axial strain. In the 84° plot (Figure 3.12), the third positive peak from the left is not apparent on the figure. This is due to the lack of reliable fringe data in the region of the ply interface. No strain was calculated in this region. The signs of the maxima and minima at ply interfaces remain consistent between the angular locations. The peaks at the right sides of Figures 3.12-3.15 are displaced from the idealized ply boundaries. This is again due to the ply waviness observed in this particular specimen.

These results are amazingly detailed. At many of the angular locations in Figures 3.12-3.16, it is clear from the distribution of $\gamma_{\theta z}$ that the strain rapidly increases in a very narrow region near the ply interfaces. The correlation of the peak strain values with the actual ply boundary locations is fantastically close. The measured shear strain is approximately zero at the mid-plane and at the laminate surfaces at each angular location, as expected.

3.2.2 $[+30°_2/-30°_2/90°_4]_{3s}$ Laminate

Mosaics of the U_θ and U_z fringe patterns for the $[+30°_2/-30°_2/90°_4]_{3s}$ specimen are shown in Figures 3.17 and 3.18, respectively. Figure 3.19 contains a mosaic of the U_z fringe patterns with an applied carrier of rotation from the 60° to 90° locations. The 60° to 66° locations shared a similar carrier of rotation. The 72° to 90° location shared a similar carrier of rotation that was different from the carrier applied to the 60° through 66° region. In these figures, each rectangular fringe pattern is a 3° slice from the approximately 5° fringe pattern recorded at the specified angular locations around the periphery of the hole. As mentioned in Section 3.2.1, slight discrepancies between neighboring fringe patterns can be attributed to small rigid body rotation differences of the loaded sector grating about the r-axis. Horizontal lines between each fringe pattern in these figures correspond to the approximate locations of the actual ply boundaries.

The top edge of the mosaics in Figures 3.17 and 3.18 show that a narrow region of grating was chipped during the initial process of replicating a grating onto the specimen. The bottom edge, from 78° to 90°, shows considerable grating damage that occurred when too much pressure was applied during the loaded specimen replication process. Visible also in these mosaic images are other areas of minor damage. Nevertheless, extensive data are available.

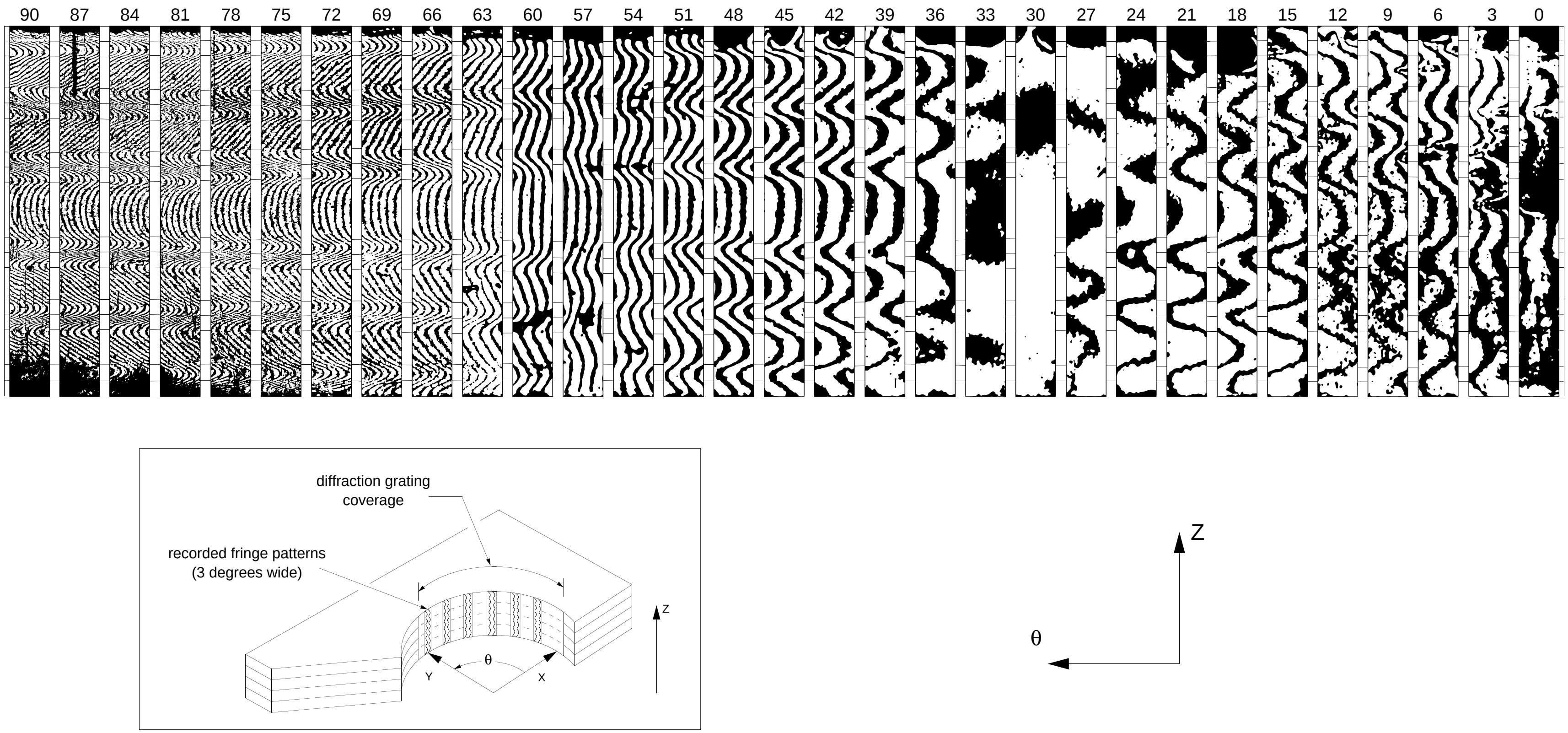

Figure 3.17: Mosaic of U_θ fringe patterns from the $[+30_2/-30_2/90_4]_{3s}$ laminate loaded at 50 MPa. Each fringe pattern is 3° wide, and the horizontal lines between fringe patterns are the approximate ply boundaries.

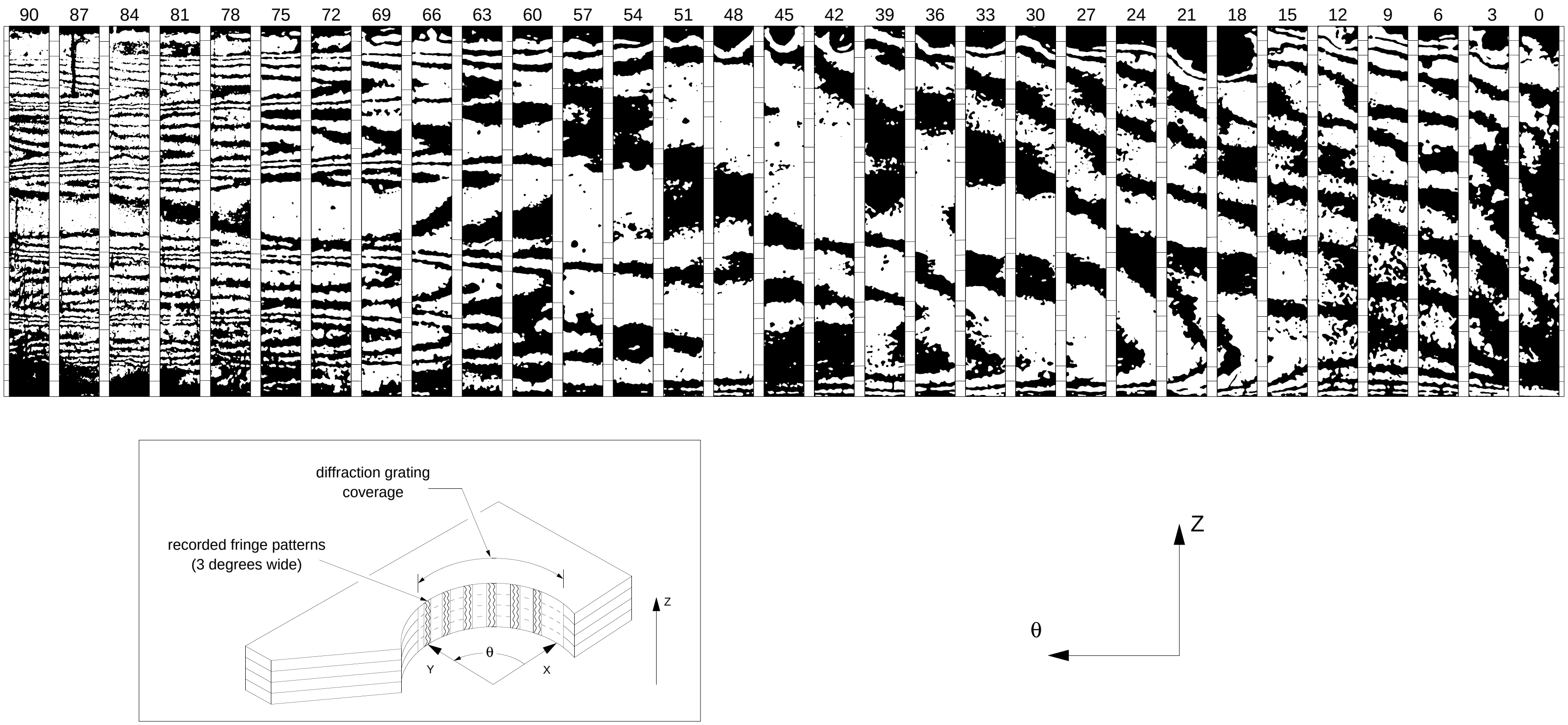

Figure 3.18: Mosaic of U_z fringe patterns from the $[+30_2/-30_2/90_4]_{3S}$ laminate loaded at 50 MPa. Each fringe pattern is 3° wide, and the horizontal lines between fringe patterns are the approximate ply boundaries.

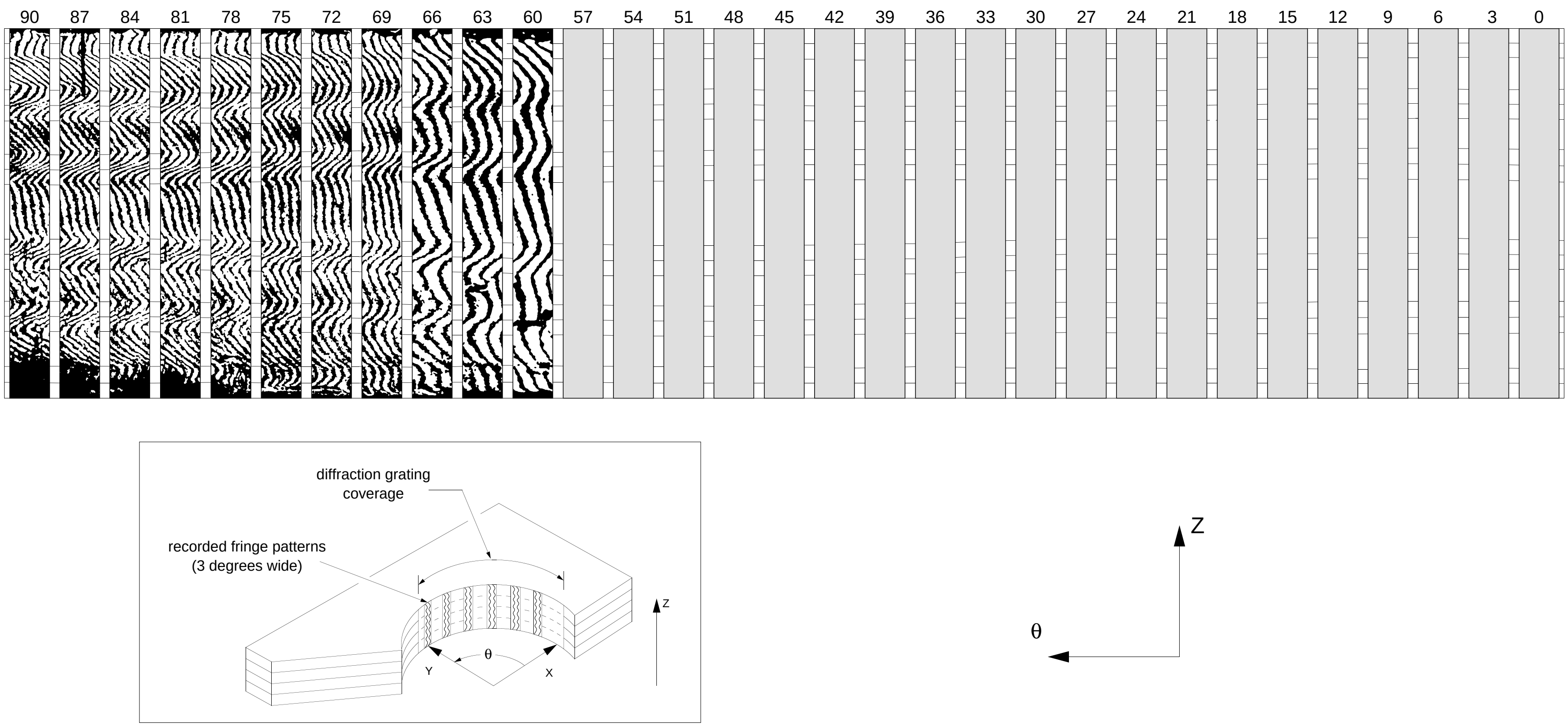

Figure 3.19: Mosaic of U_z fringe patterns from the $[+30_2/-30_2/90_4]_{3S}$ laminate loaded at 50 MPa. Each fringe pattern is 3° wide, and the horizontal lines between fringe patterns are the approximate ply boundaries. (note: each fringe pattern contains a carrier of rotation)

The nature of the fringe patterns presented in Figures 3.17 and 3.18 are noticeably different from those presented in Figures 3.4 and 3.5. The U_θ fringe pattern for the $[+30°_2/-30°_2/90°_4]_{3s}$ specimen is more complex than the U_θ mosaic for the $[0°_4/90°_4]_{3s}$ specimen. One interesting feature visible in this mosaic image occurs in the region around 60° in Figure 3.17. Examination of the mid-ply region for angular locations greater than 60° shows that the central fringes are cupped toward the right. For angular locations less than 60°, these central fringes appear cupped toward the left. Section 3.3.1 will discuss this phenomenon. Also visible in the U_θ pattern in Figure 3.17 is that the fringes in the 90° plies (the broader ply groupings) are angled and nearly straight at the higher angular locations. This is an indication of relatively large levels of shear strain occurring throughout the ply grouping, rather than just at the boundaries as in the $[0°_4/90°_4]_{3s}$ specimen. The U_z fringe pattern for the $[+30°_2/-30°_2/90°_4]_{3s}$ specimen, presented in Figure 3.18, shows zones of concentrated fringes that are associated with the +30°/-30° interfaces. No such concentration of fringes are found in the U_z fringe pattern from the $[0°_4/90°_4]_{3s}$ specimen shown in Figure 3.5.

ε_θ for the $[+30°_2/-30°_2/90°_4]_{3s}$ Laminate

Results of the detailed fringe analyses of the U_θ fringe patterns for ε_θ at 90°, 84°, 75°, 66°, 60°, 45°, and 15° are presented in Figures 3.20-3.26, respectively. All figures are plotted on the same scale, except Figure 3.26 where the range is the opposite of the range plotted in Figures 3.20-3.25. The actual ply boundary locations were generally close to the idealized locations. Distributions of ε_θ at 90° and 84° are noisy and show no consistent ply-related trends. An especially large peak is visible in Figure 3.20 at the interface between the second ±30° ply interface from the upper laminate face. At the 45° and 15° locations, the distribution of ε_θ also did not show any consistent ply-related trends.

The 75°, 66°, and 60° distributions of ε_θ do, however, show consistent, ply-related trends. Figure 3.22 shows a distribution that contains maxima occurring either in the -30° plies or at the interfaces between the -30° and 90° plies. The minima tend to occur within the +30° plies. Figures 3.23 and 3.24 also show distinct ply-related patterns of maxima and minima. The maxima are relatively sharp and are generally located in the middle of the -30° plies. The minima are generally broad in shape and appear to be centered on the interfaces between the +30° and 90° plies.

The measured circumferential strain values are quite large. At the 90° location, the strain in places exceeds 3.7 times the measured far-field axial strain of 1070 $\mu\varepsilon$.

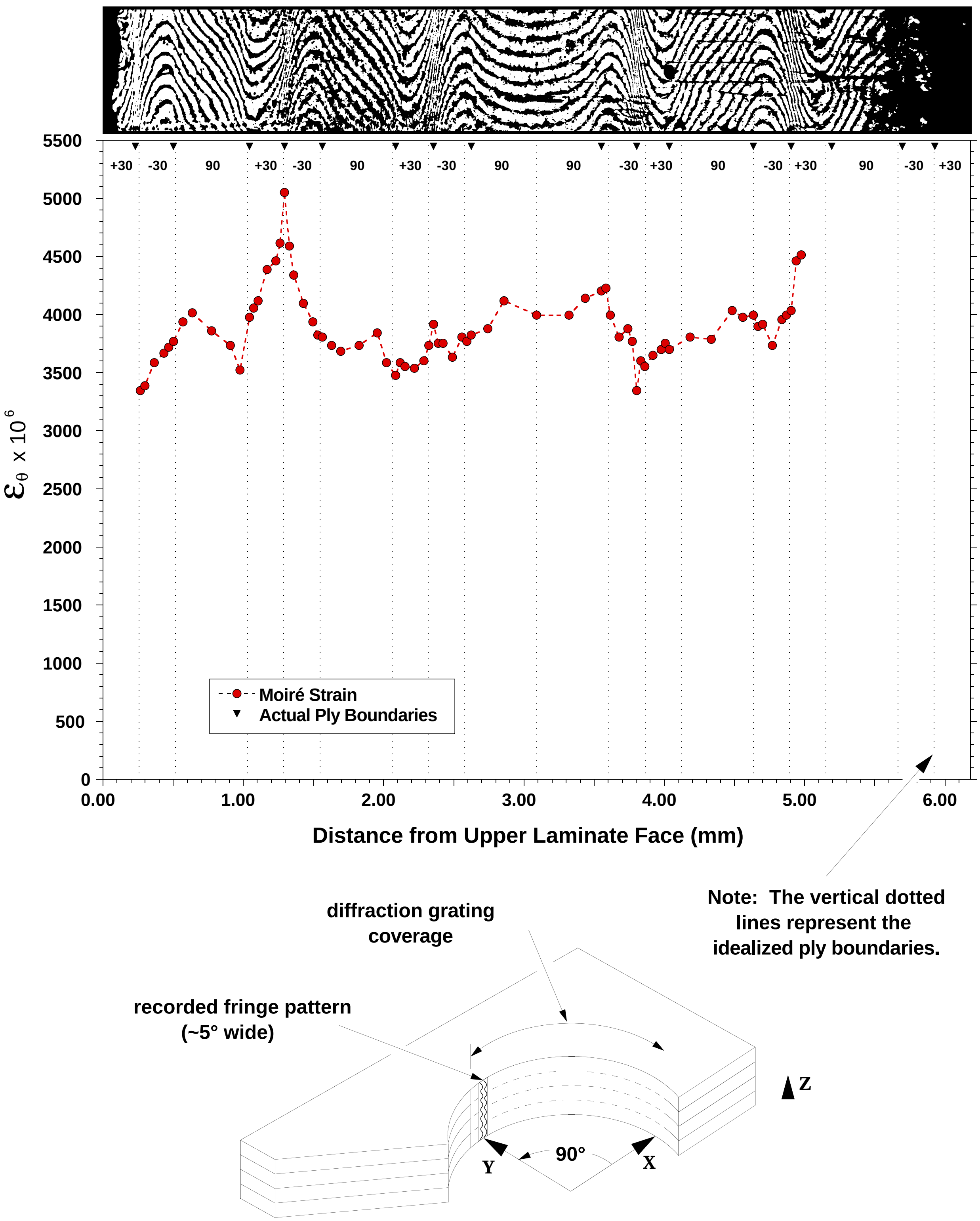

Figure 3.20: Circumferential strain variation at 90° for the $[+30_2/-30_2/90_4]_{3s}$ laminate.

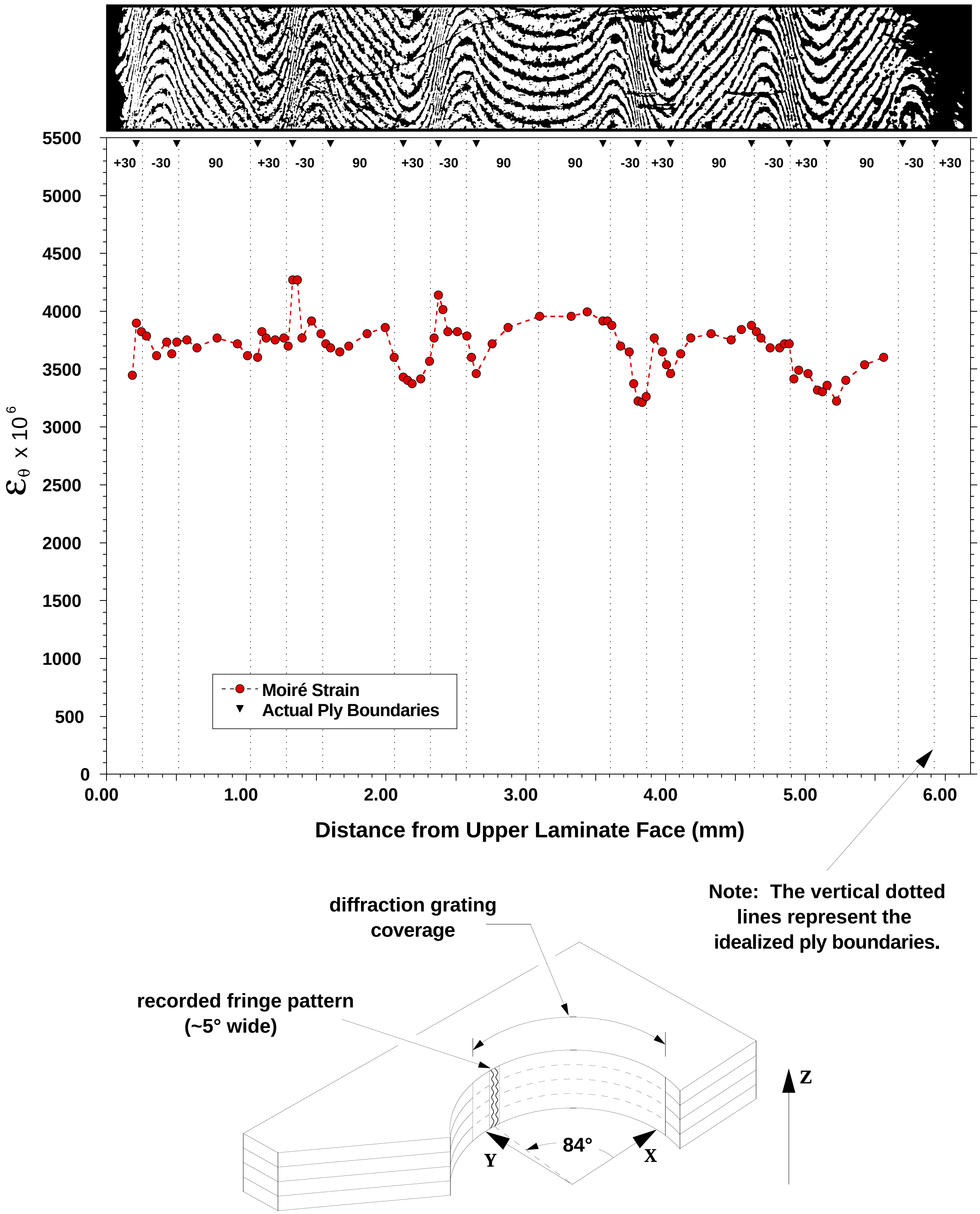

Figure 3.21: Circumferential strain variation at 84° for the $[+30_2/-30_2/90_4]_{3s}$ laminate.

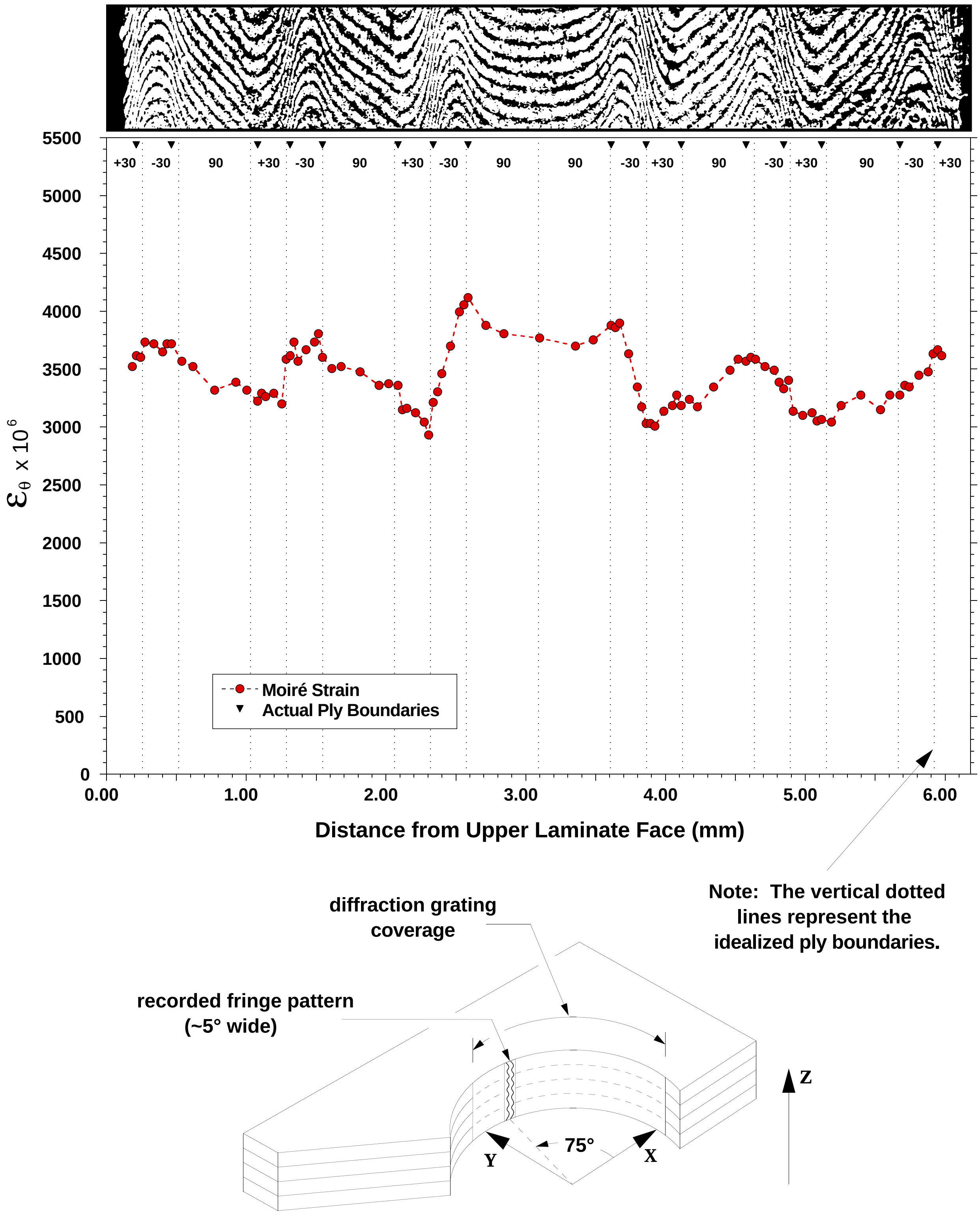

Figure 3.22: Circumferential strain variation at 75° for the $[+30_2/-30_2/90_4]_{3s}$ laminate.

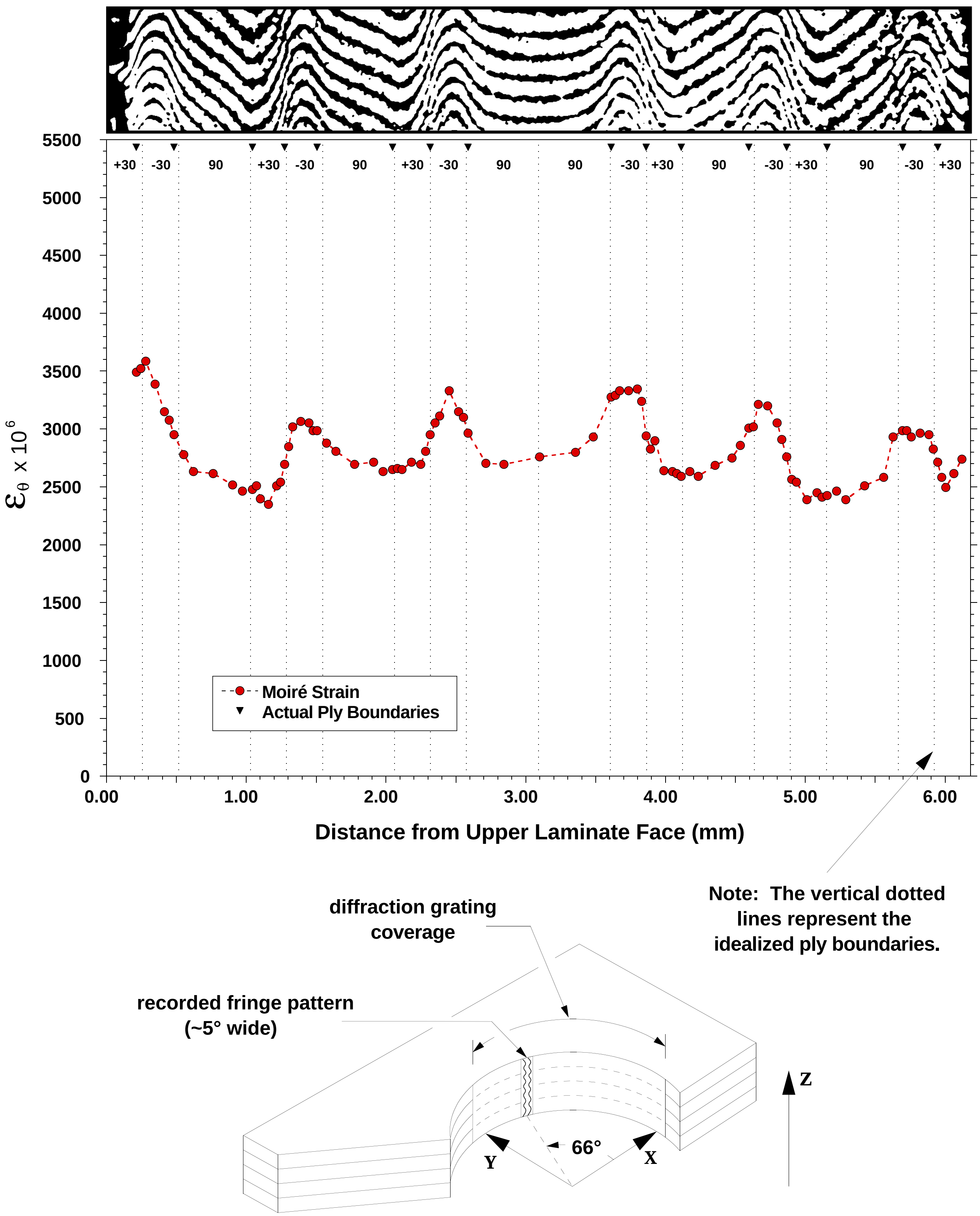

Figure 3.23: Circumferential strain variation at 66° for the $[+30_2/-30_2/90_4]_{3s}$ laminate.

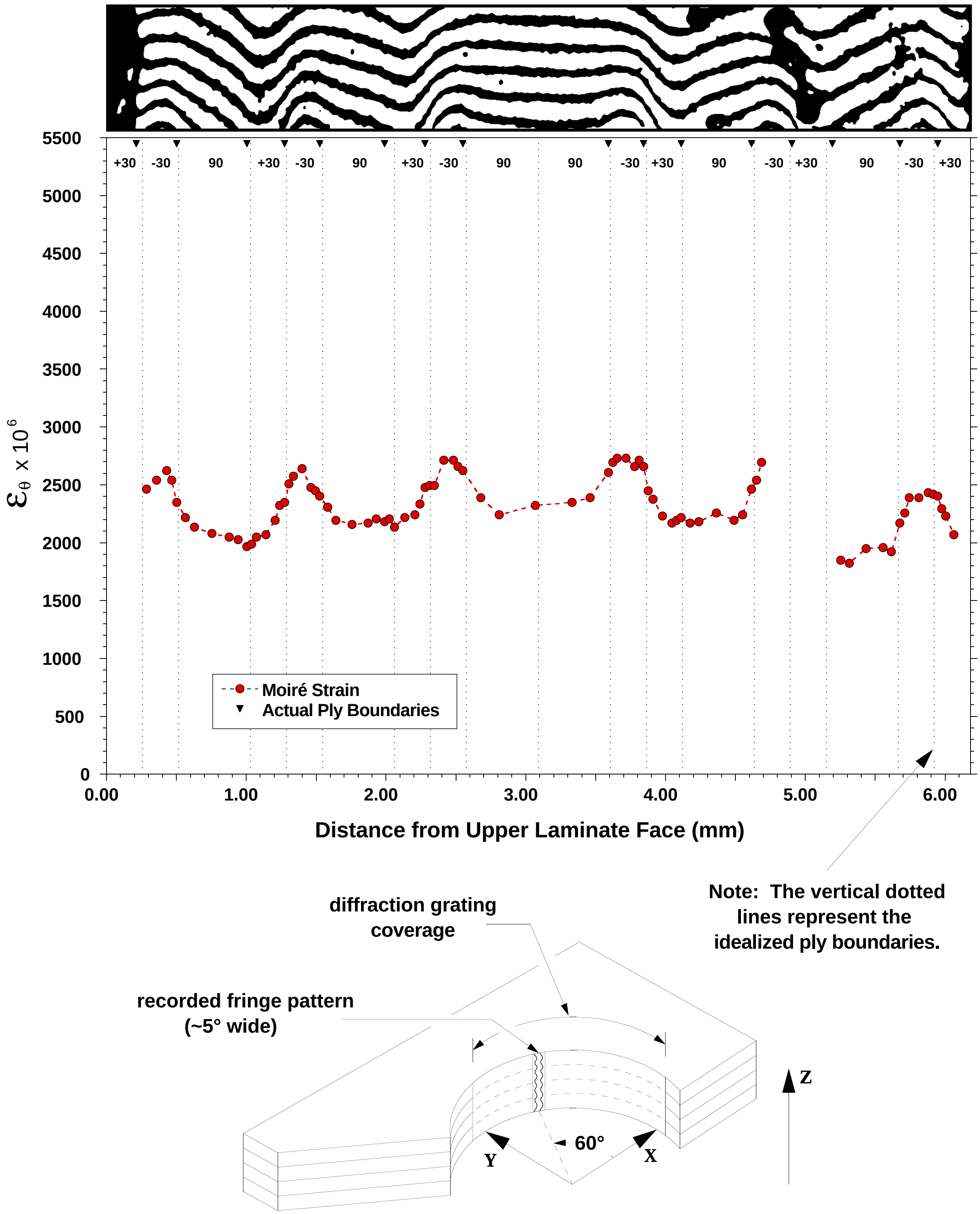

Figure 3.24: Circumferential strain variation at 60° for the $[+30_2/\text{-}30_2/90_4]_{3s}$ laminate.

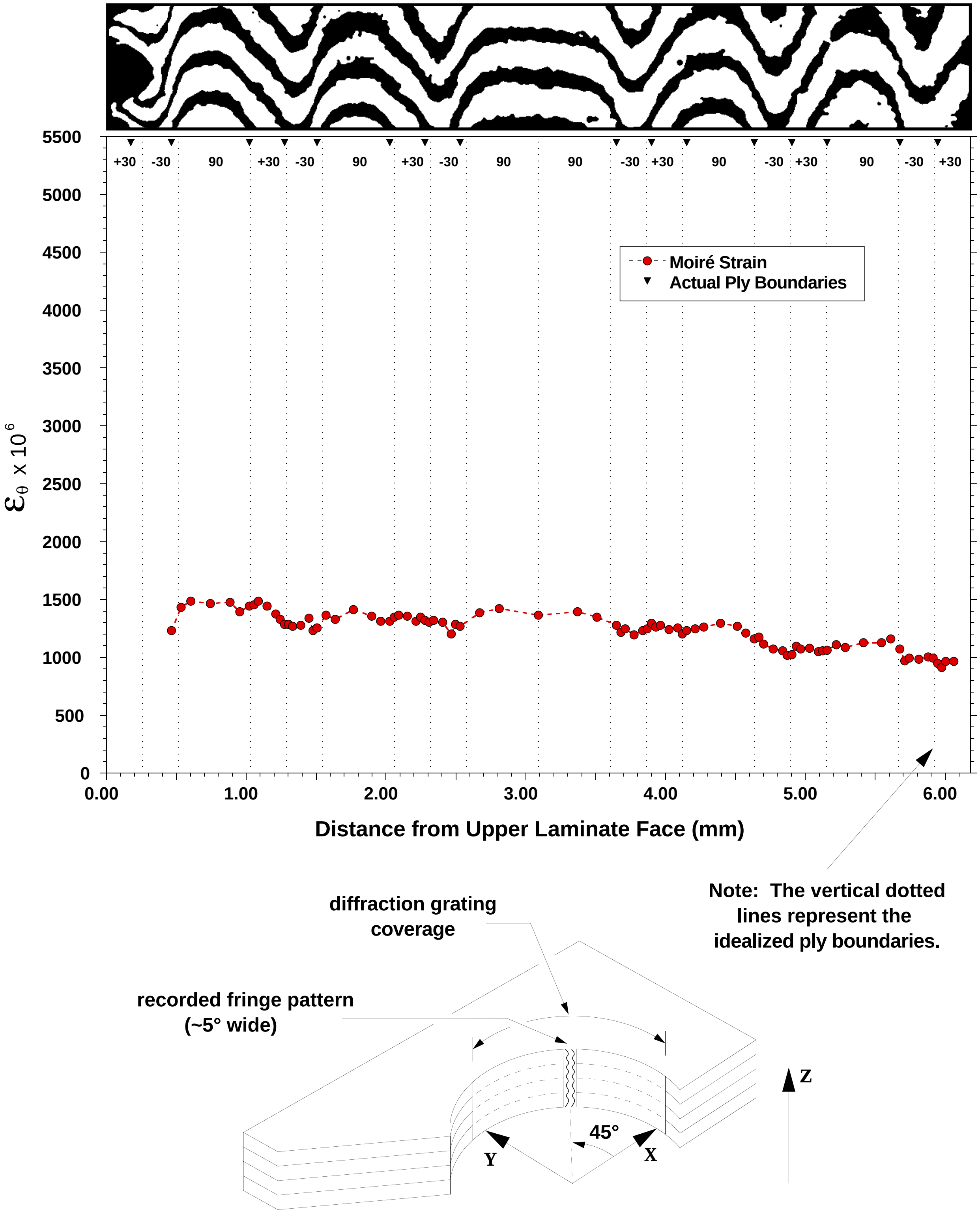

Figure 3.25: Circumferential strain variation at 45° for the $[+30_2/-30_2/90_4]_{3s}$ laminate.

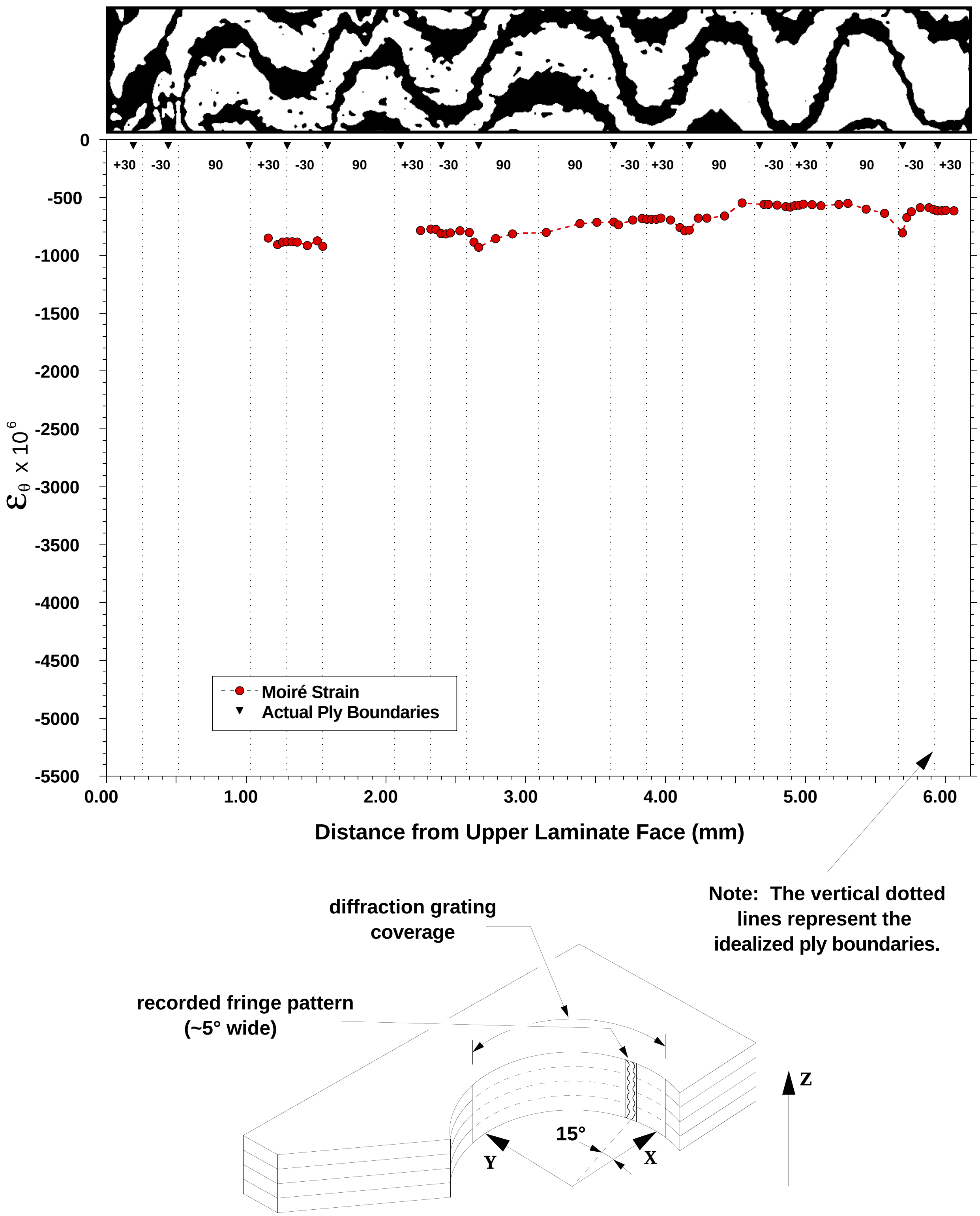

Figure 3.26: Circumferential strain variation at 15° for the $[+30_2/-30_2/90_4]_{3s}$ laminate.

$\gamma_{\theta z}$ for the $[+30°_2/-30°_2/90°_4]_{3s}$ Laminate

Results of the detailed fringe analyses of the U_θ fringe patterns for $\gamma_{\theta z}$ at 90°, 84°, 75°, 66°, 60°, 45°, and 15° are shown in Figures 3.27-3.33. The plots in Figures 3.27-3.29 share the same scale. A common scale is also shared by the graphs in Figures 3.30-3.33. All descriptions of the distributions of $\gamma_{\theta z}$ will be in reference to the left halves of Figures 3.27-3.33. The distributions of $\gamma_{\theta z}$ in the right halves of these figures are approximately the negative mirror images of the left-half distributions.

As in the shear strain plots for the $[0°_4/90°_4]_{3s}$ specimen, the graphs of $\gamma_{\theta z}$ for the $[+30°_2/-30°_2/90°_4]_{3s}$ specimen show small details. The largest peaks of $\gamma_{\theta z}$ found in Figures 3.27-3.33 are generally broader than those found at equivalent angular locations in the $[0°_4/90°_4]_{3s}$ specimen. Also the 90° ply groupings experience relatively large values of $\gamma_{\theta z}$ throughout the ply grouping, as opposed to the generally lower levels of strain found in the ply groupings of the $[0°_4/90°_4]_{3s}$ specimen. The measured shear strain is approximately zero at the mid-plane, as expected. Because of grating damage near the laminate surfaces, it was not possible to determine whether the shear approaches zero at the laminate surfaces.

Peak positive shear values occur at the interfaces between the +30° and -30° plies for the 90°, 84°, 75°, 66°, and 60° (Figures 3.27-3.31) angular locations. Maximum calculated values of $\gamma_{\theta z}$ exceed 30,000 $\mu\varepsilon$ (3.0% strain) at some locations, 28 times as large as the measured far-field axial strain. These peaks are sharp in all cases except at the 60° location. Descending from these peak interfacial values, $\gamma_{\theta z}$ reaches minimum values at the interfaces between the +30°/90° plies and the –30°/90° plies. A slight rise in $\gamma_{\theta z}$ is typically apparent within the 90° plies.

Sharp positive peaks in $\gamma_{\theta z}$ occur at the interfaces between the -30° and 90° plies at the 45° angular location. Broader negative peaks occur either at the interface between the +30° and -30° plies or within the +30° plies. Negative peaks occur at the interfaces between the -30° and 90° plies in Figure 3.33 (15° angular location). Broader positive peaks occur at the 90° and +30° interfaces.

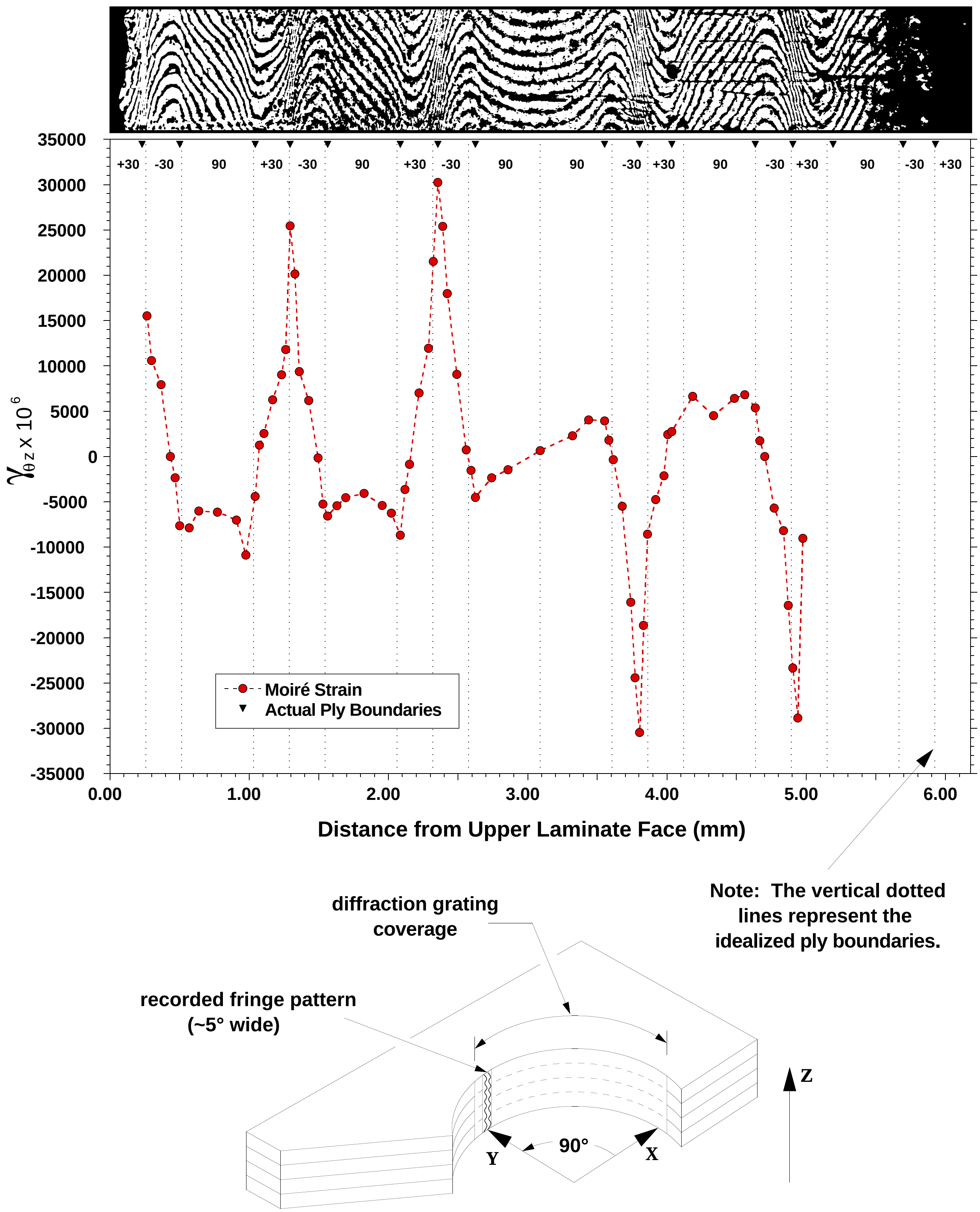

Figure 3.27: Theta-Z shear strain variation at 90° for the $[+30_2/-30_2/90_4]_{3s}$ laminate (note: shear strain calculated from U_θ pattern only).

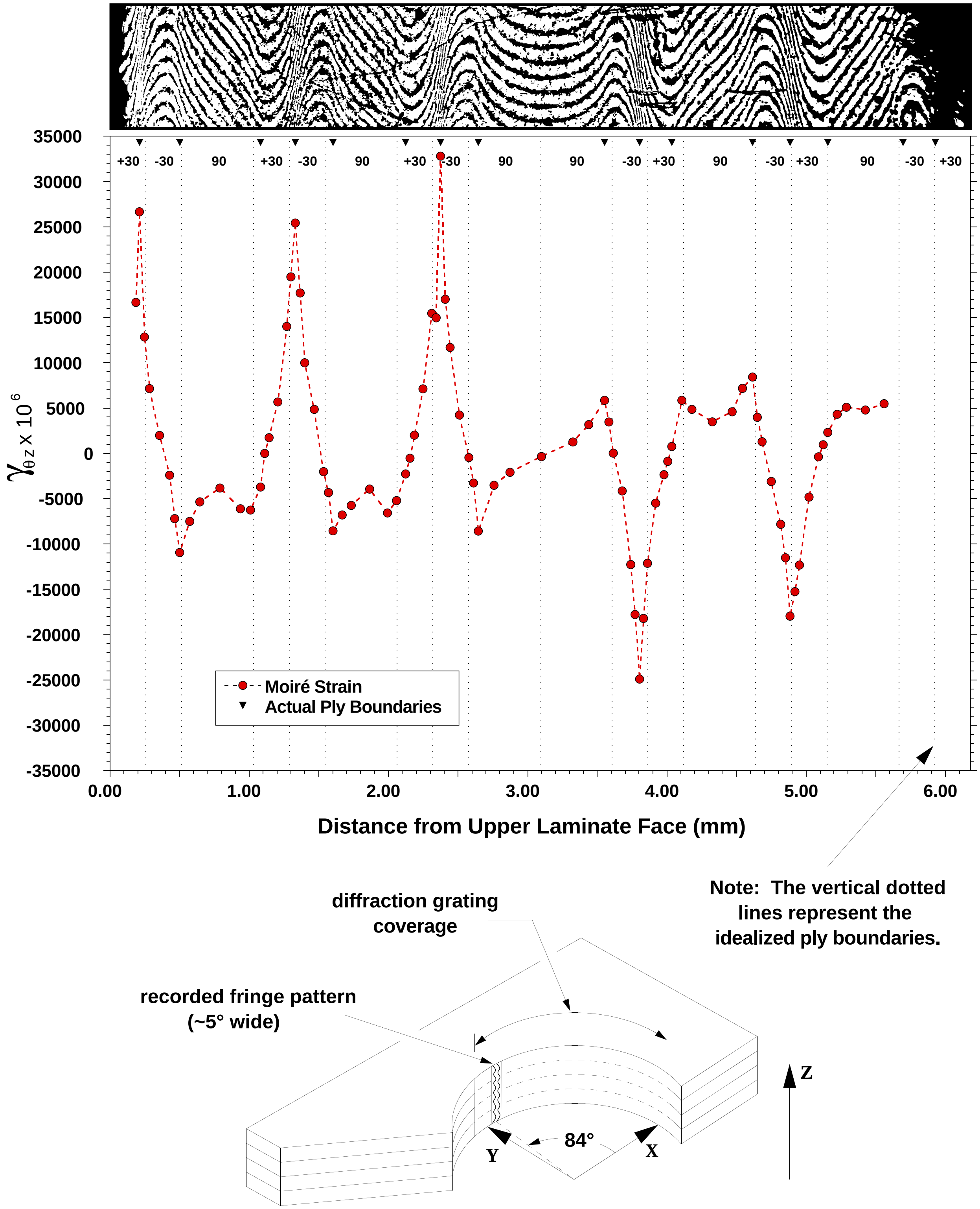

Figure 3.28: Theta-Z shear strain variation at 84° for the $[+30_2/-30_2/90_4]_{3s}$ laminate (note: shear strain calculated from U_θ pattern only).

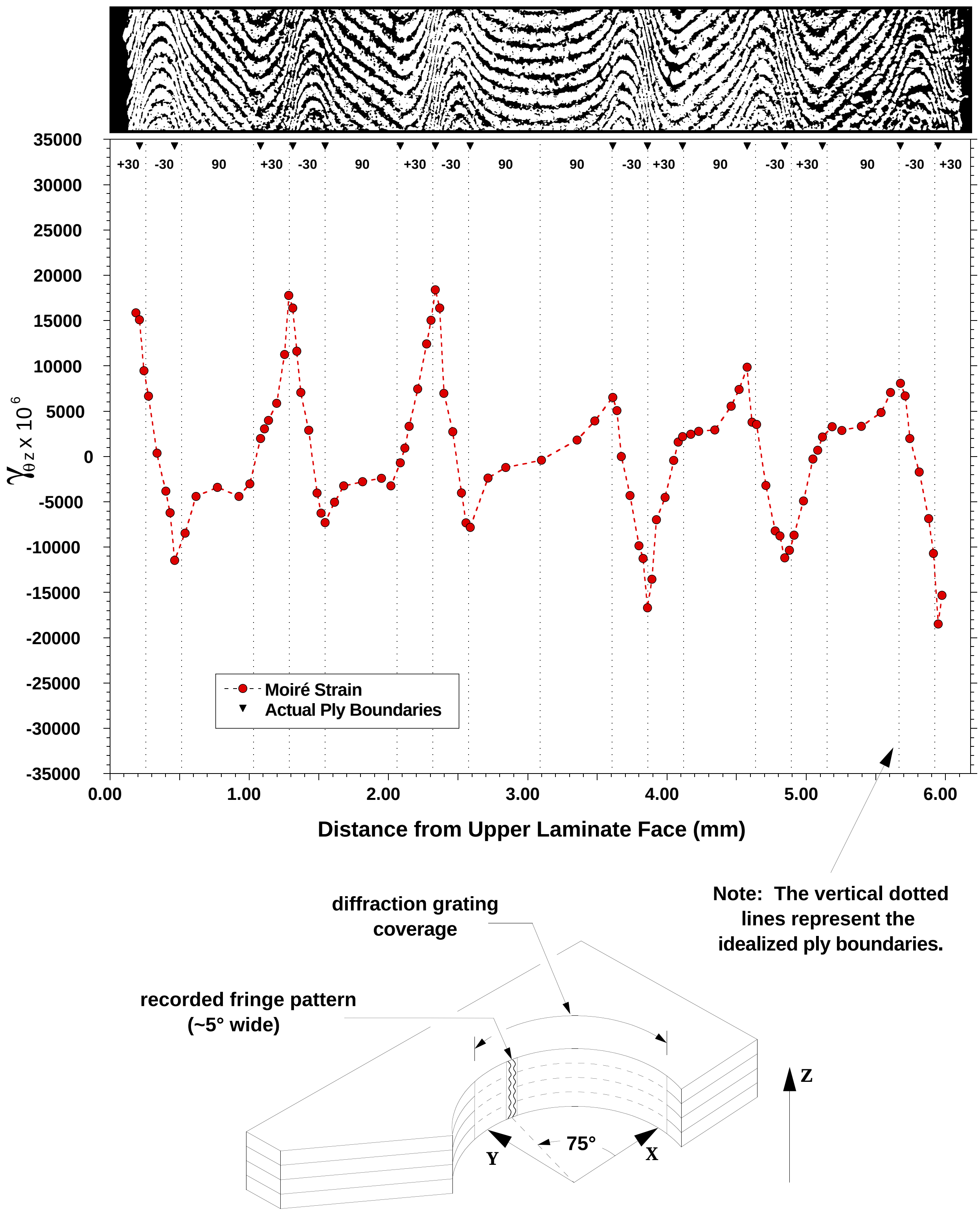

Figure 3.29: Theta-Z shear strain variation at 75° for the $[+30_2/-30_2/90_4]_{3s}$ laminate (note: shear strain calculated from U_θ pattern only).

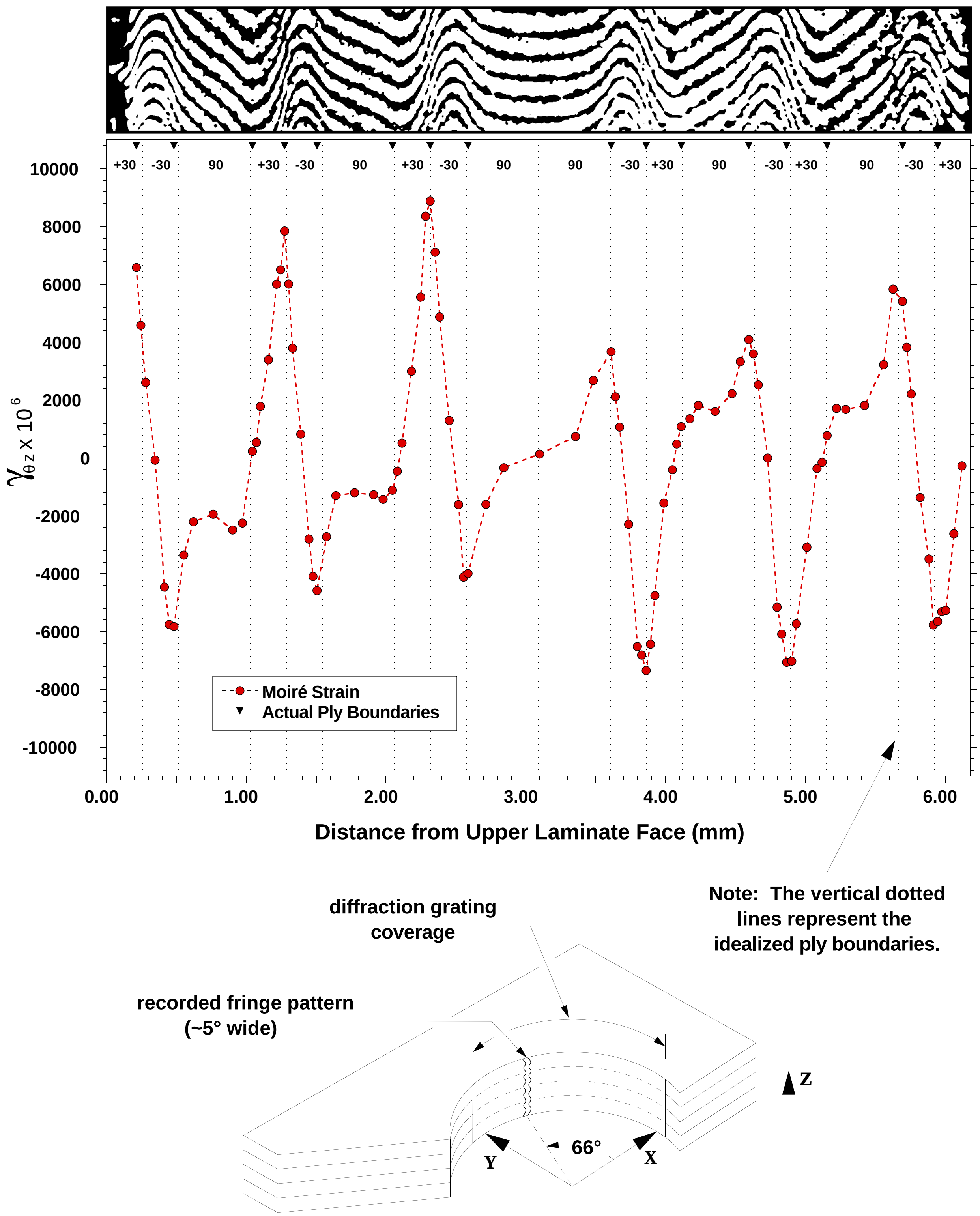

Figure 3.30: Theta-Z shear strain variation at 66° for the $[+30_2/-30_2/90_4]_{3s}$ laminate (note: shear strain calculated from U_θ pattern only).

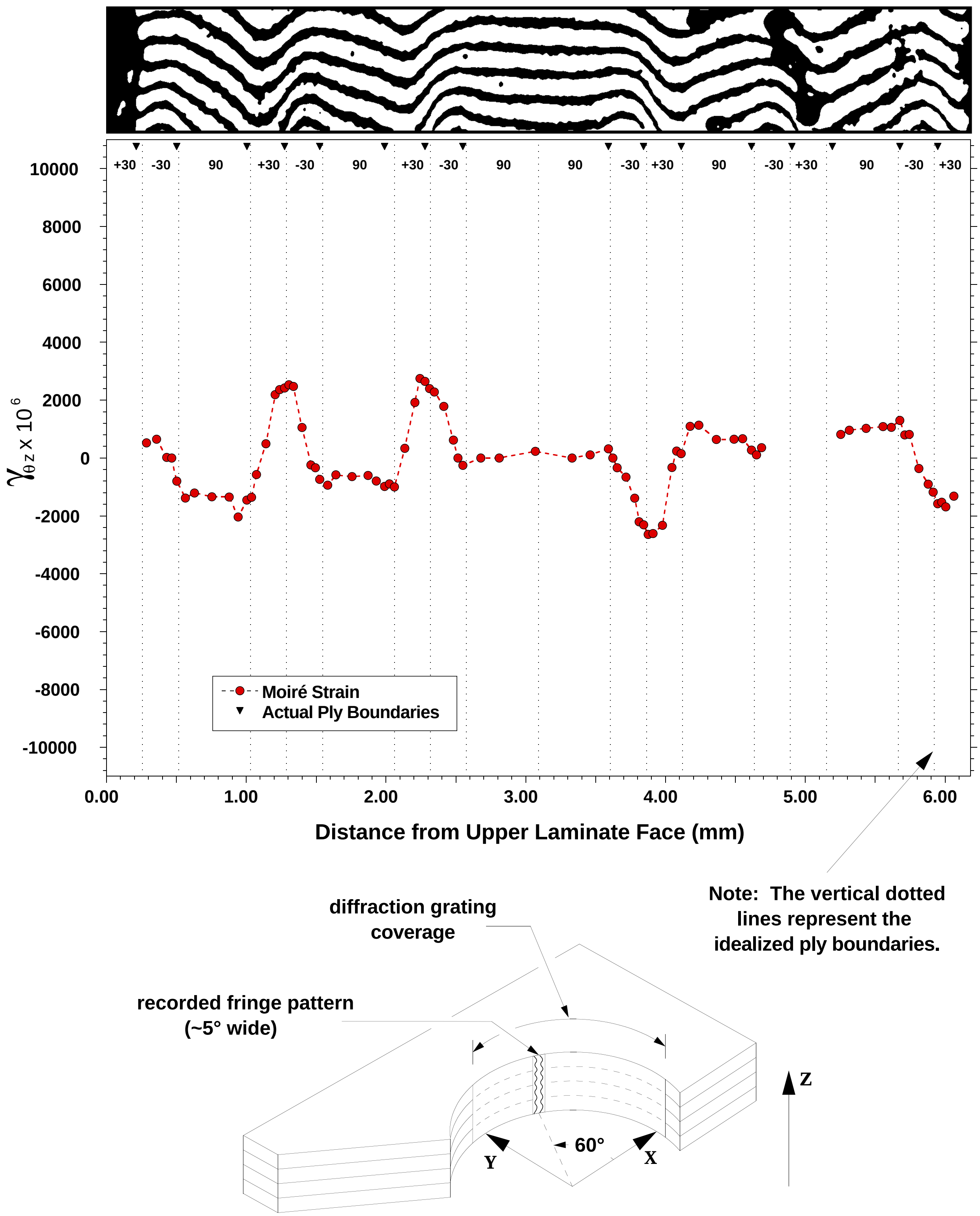

Figure 3.31: Theta-Z shear strain variation at 60° for the $[+30_2/-30_2/90_4]_{3s}$ laminate (note: shear strain calculated from U_θ pattern only).

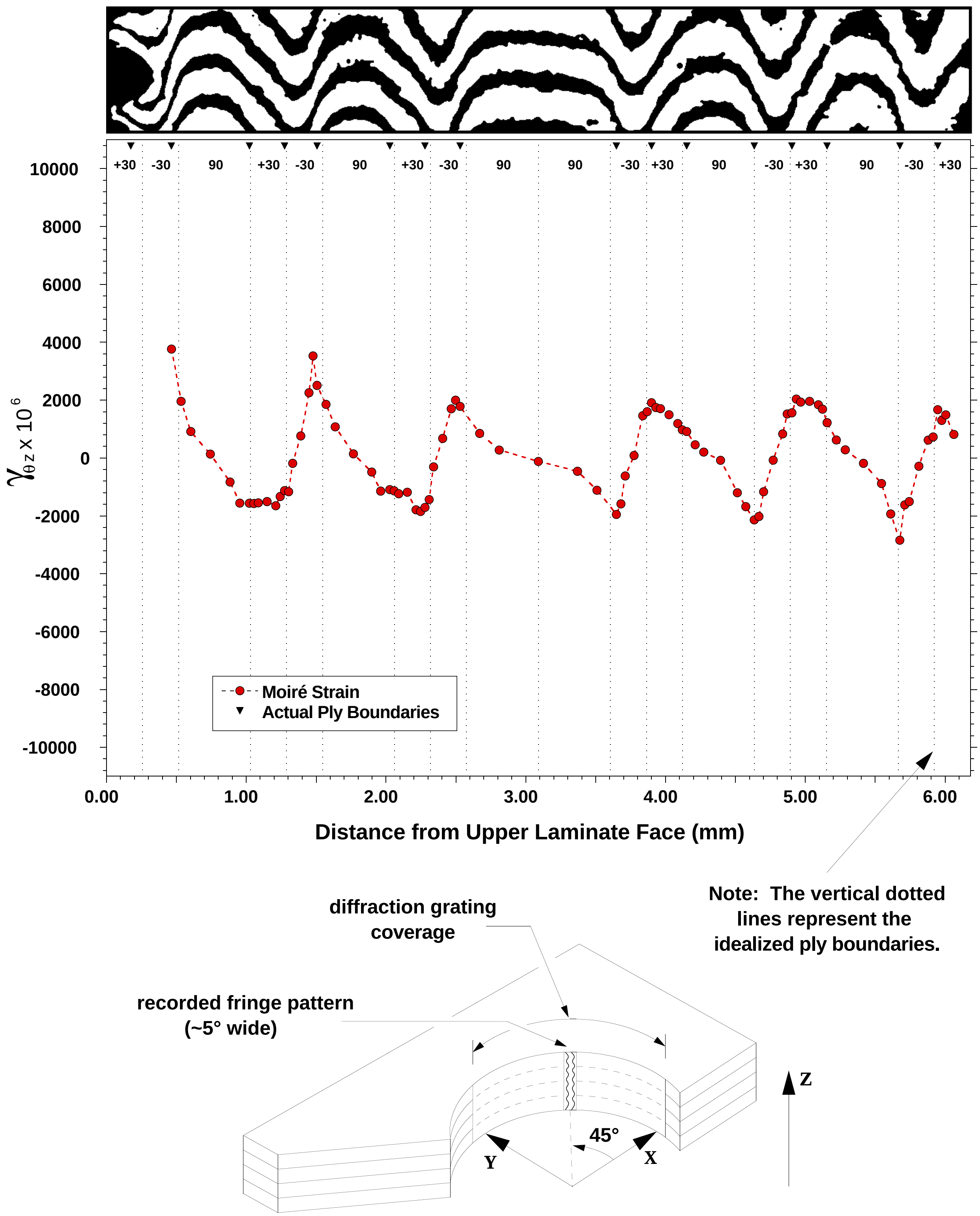

Figure 3.32: Theta-Z shear strain variation at 45° for the $[+30_2/-30_2/90_4]_{3s}$ laminate (note: shear strain calculated from U_θ pattern only).

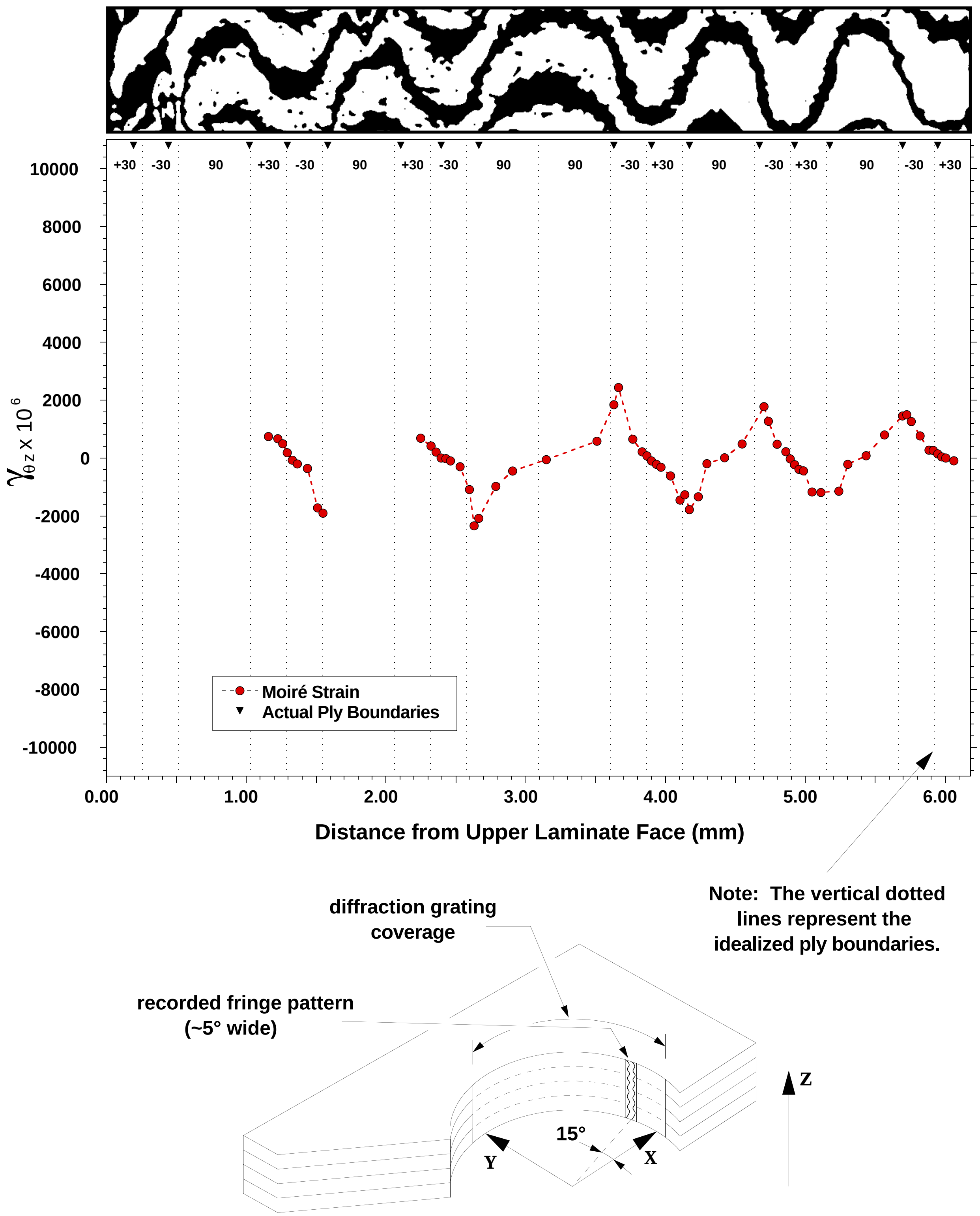

Figure 3.33: Theta-Z shear strain variation at 15° for the $[+30_2/-30_2/90_4]_{3s}$ laminate (note: shear strain calculated from U_θ pattern only).

ε_z for the $[+30°_2/-30°_2/90°_4]_{3s}$ Laminate

Results of the fringe analyses of the U_z fringe patterns for ε_z at 90°, 84°, 75°, 66°, and 60° are presented in Figures 3.34-3.38. The fringe patterns used for these analyses are shown in Figure 3.19. As mentioned in Section 2.4.2, ε_z was calculated from the fringe patterns using the tangent method described in Appendix B. ε_z is determined by $\Delta N_z/\Delta z$, which varies significantly in the fringe patterns. All plots in these figures share the same scale.

Sharp compressive minima are located around the interfaces between the +30° and -30° degree plies for Figure 3.34-3.38 with the exception that the minima are somewhat broad at the 60° location. Broad tensile maxima occur within the 90° ply groupings. In some cases, these maxima are bowl shaped with the values of ε_z near the center of the 90° plies being slightly less tensile than at the interfaces between the 90° plies and the neighboring plies.

An interesting observation is that the maxima in the 90° plies nearest the laminate surface in Figures 3.34-3.38 are nearly equivalent to the values of ε_θ at the corresponding angular locations in Figures 3.20-3.24. Values of ε_z at the 90° angular location exceed 5000 $\mu\varepsilon$ which is approximately 4.7 times the applied far-field axial strain. Also, the maximum magnitude of the compressive ε_z strains at the ±30° interface nearest the laminate mid-plane for Figures 3.34-3.36 (90°, 84°, and 75°) are approximately twice the tensile ε_θ at the corresponding angular locations in Figures 3.20-3.22. Compressive values of ε_z at the 90° angular location approach -9000 $\mu\varepsilon$ which is approximately 8.4 times, in magnitude, than the applied far-field axial strain. At the 66° and 60° locations, the maximum compressive ε_z magnitudes are approximately equivalent to the corresponding ε_θ at 66° and 60°.

A very important large-scale trend is clearly visible in Figures 3.34-3.38. The values of ε_z from the plies near the mid-plane tend to be more compressive than in equivalent plies near the laminate faces. Results such as this have not been previously documented in the literature. This result is important in the sense that the strain behavior in a given ply is not solely dependent on its immediate neighbors. It is dependant on the position of that ply within the laminate.

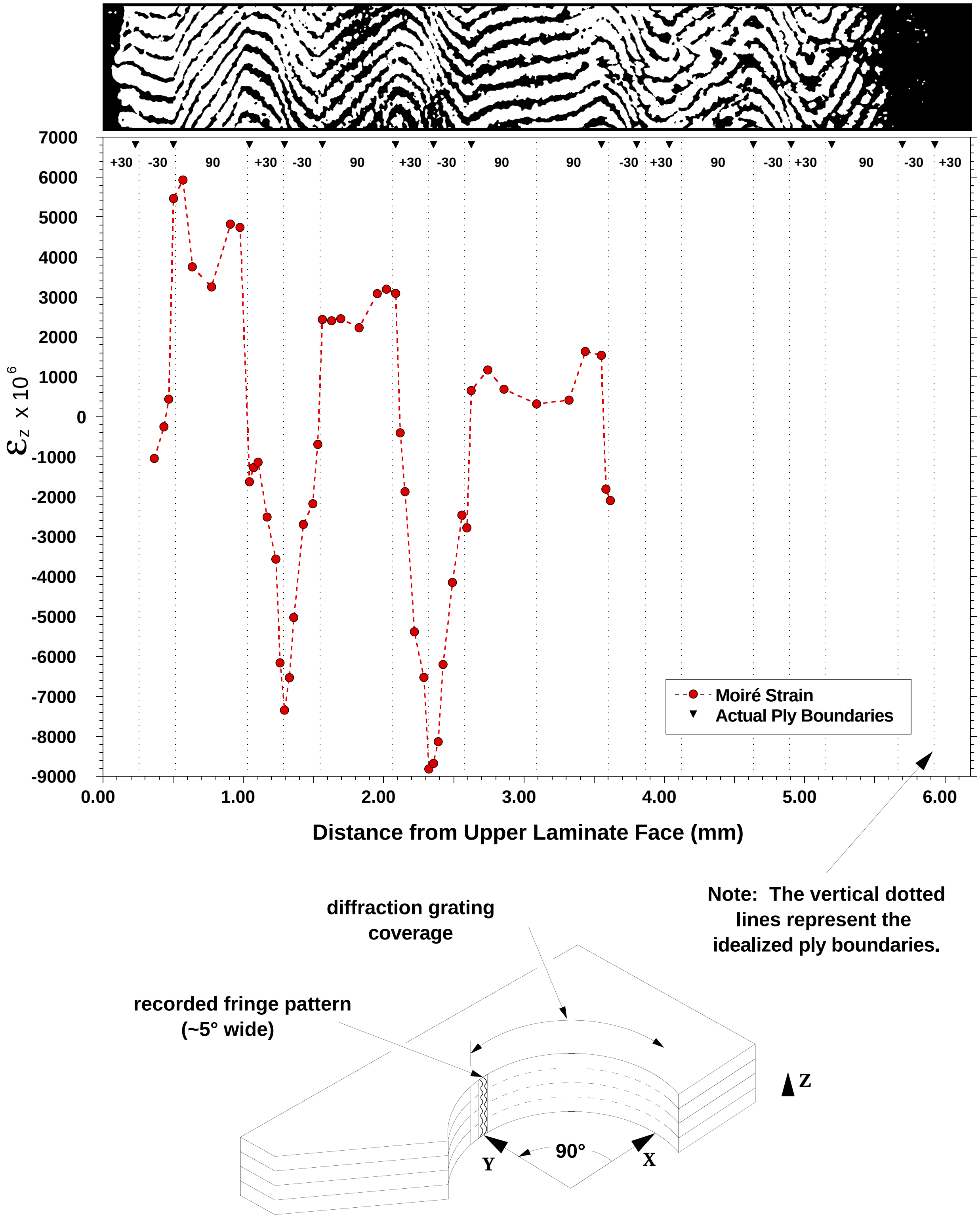

Figure 3.34: Z-direction strain variation at 90° for the $[+30_2/-30_2/90_4]_{3s}$ laminate (note: the U_z fringe pattern contains a carrier of rotation).

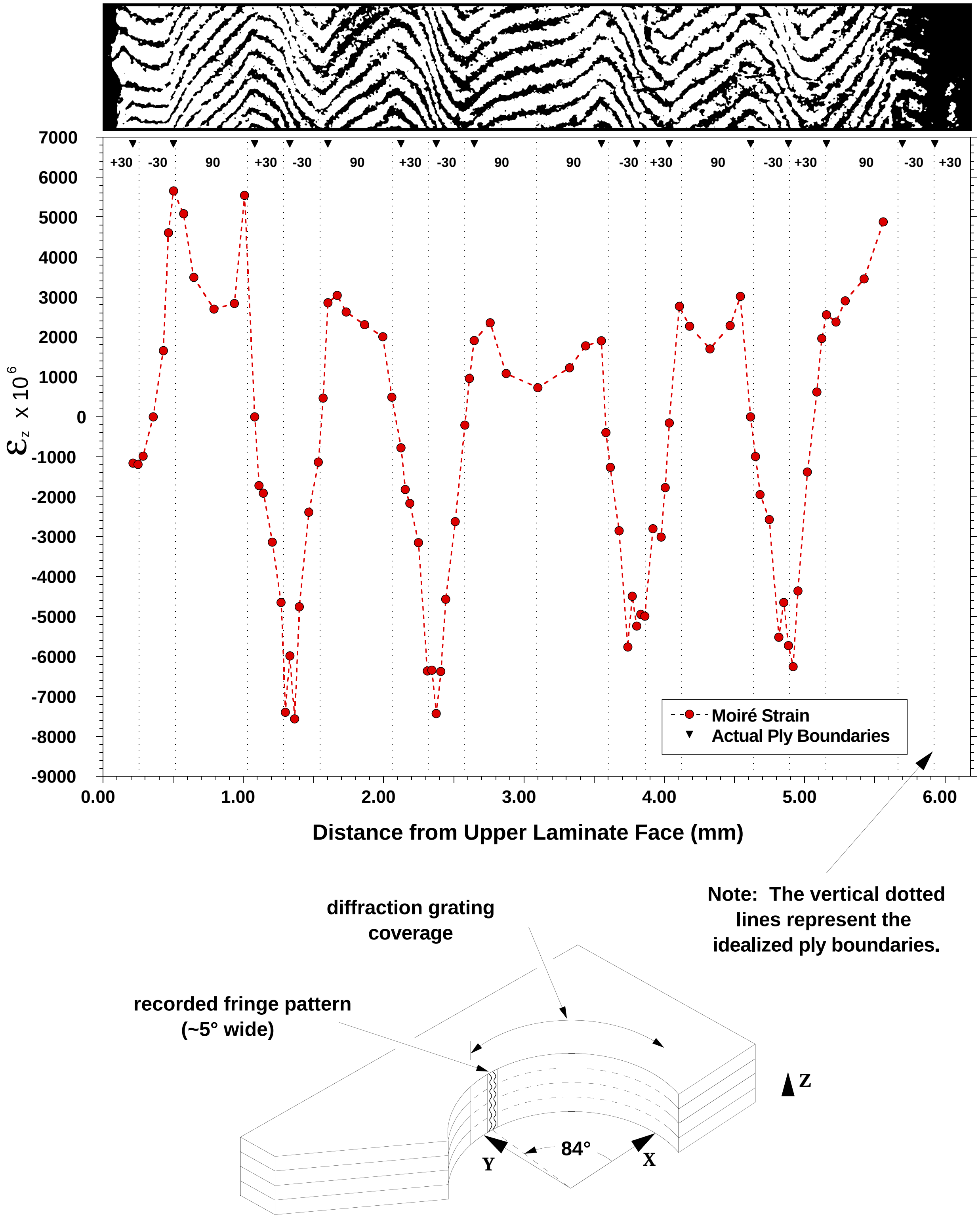

Figure 3.35: Z-direction strain variation at 84° for the $[+30_2/-30_2/90_4]_{3s}$ laminate (note: the U_z fringe pattern contains a carrier of rotation).

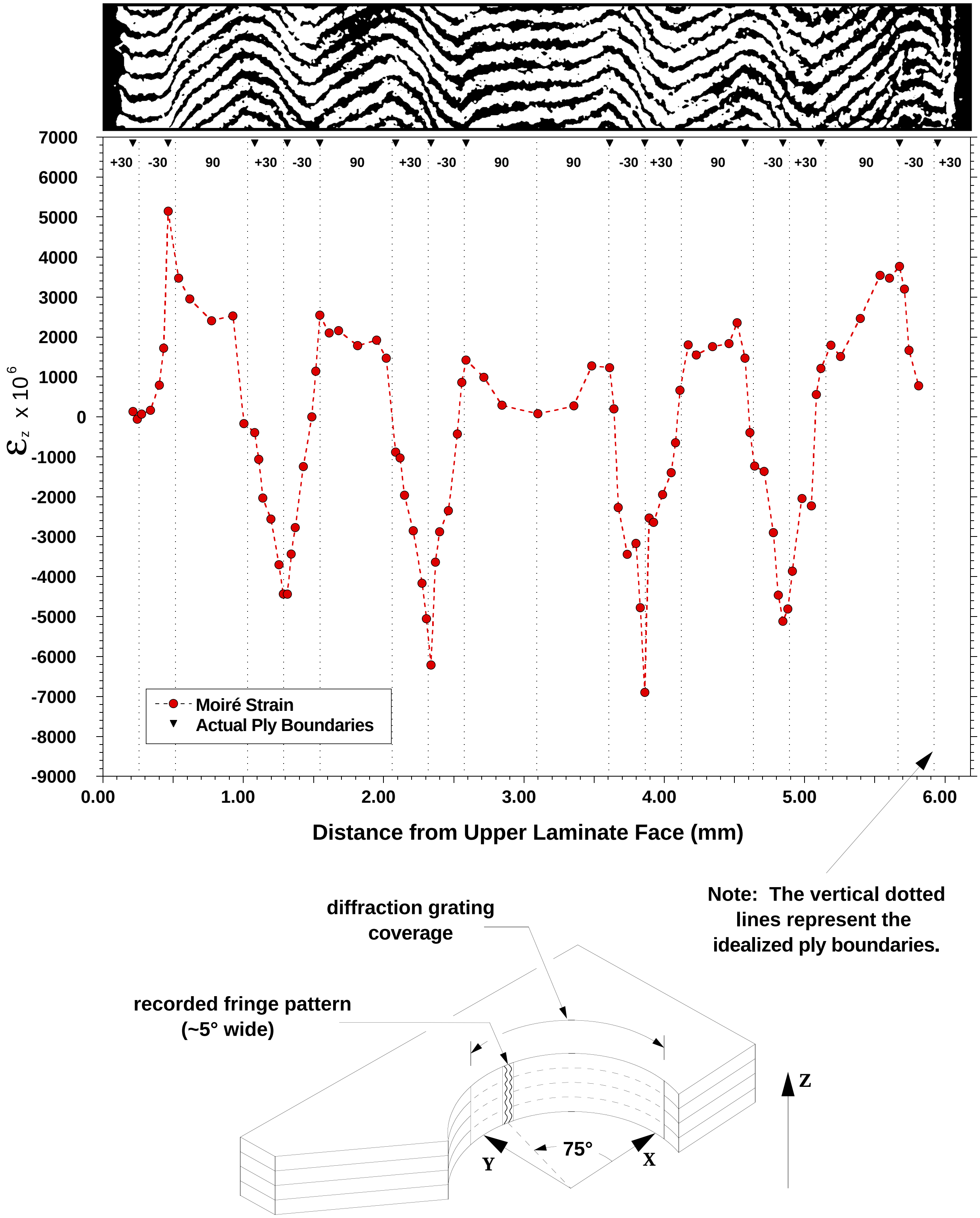

Figure 3.36: Z-direction strain variation at 75° for the $[+30_2/-30_2/90_4]_{3s}$ laminate (note: the U_z fringe pattern contains a carrier of rotation).

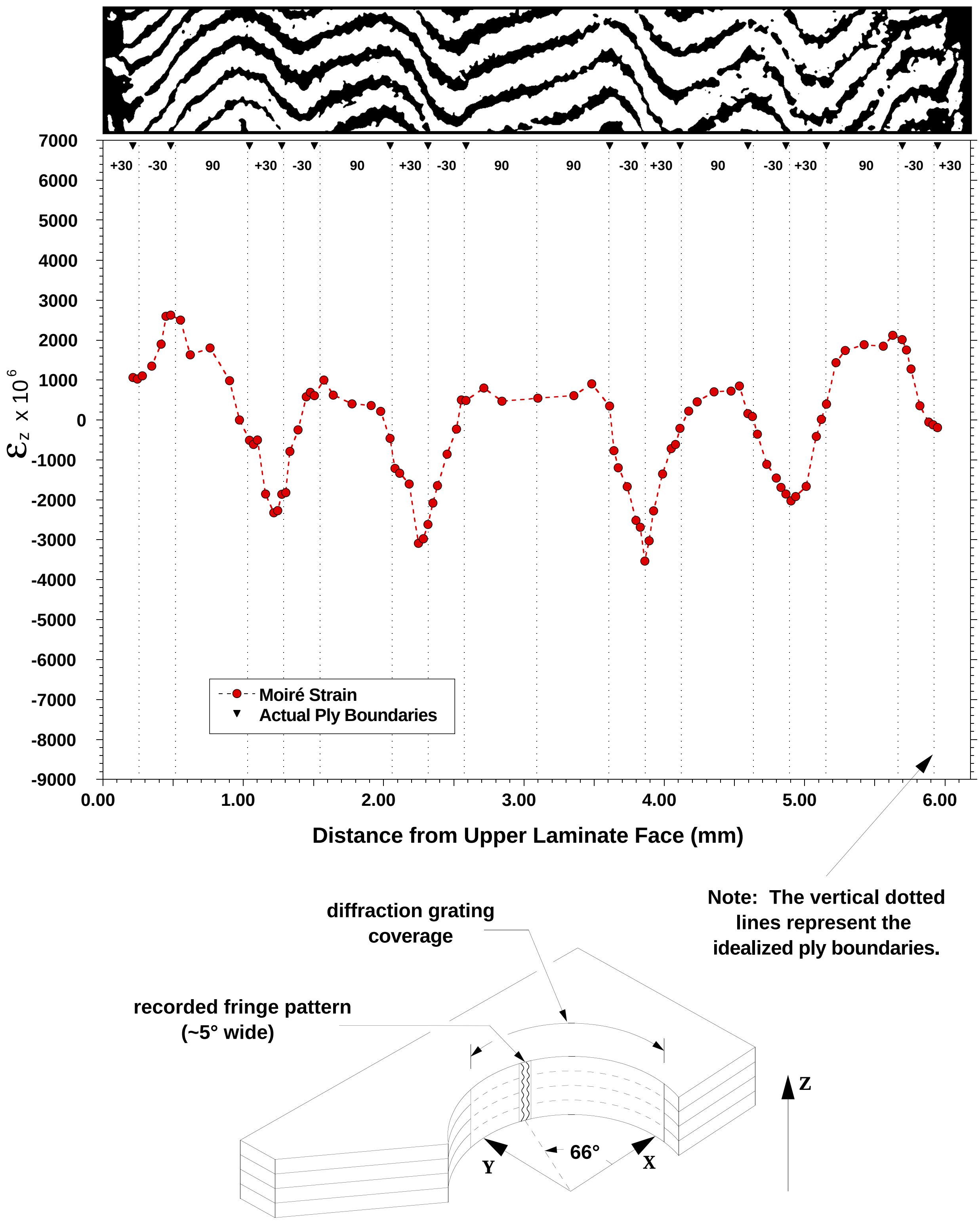

Figure 3.37: Z-direction strain variation at 66° for the $[+30_2/-30_2/90_4]_{3s}$ laminate (note: the U_z fringe pattern contains a carrier of rotation).

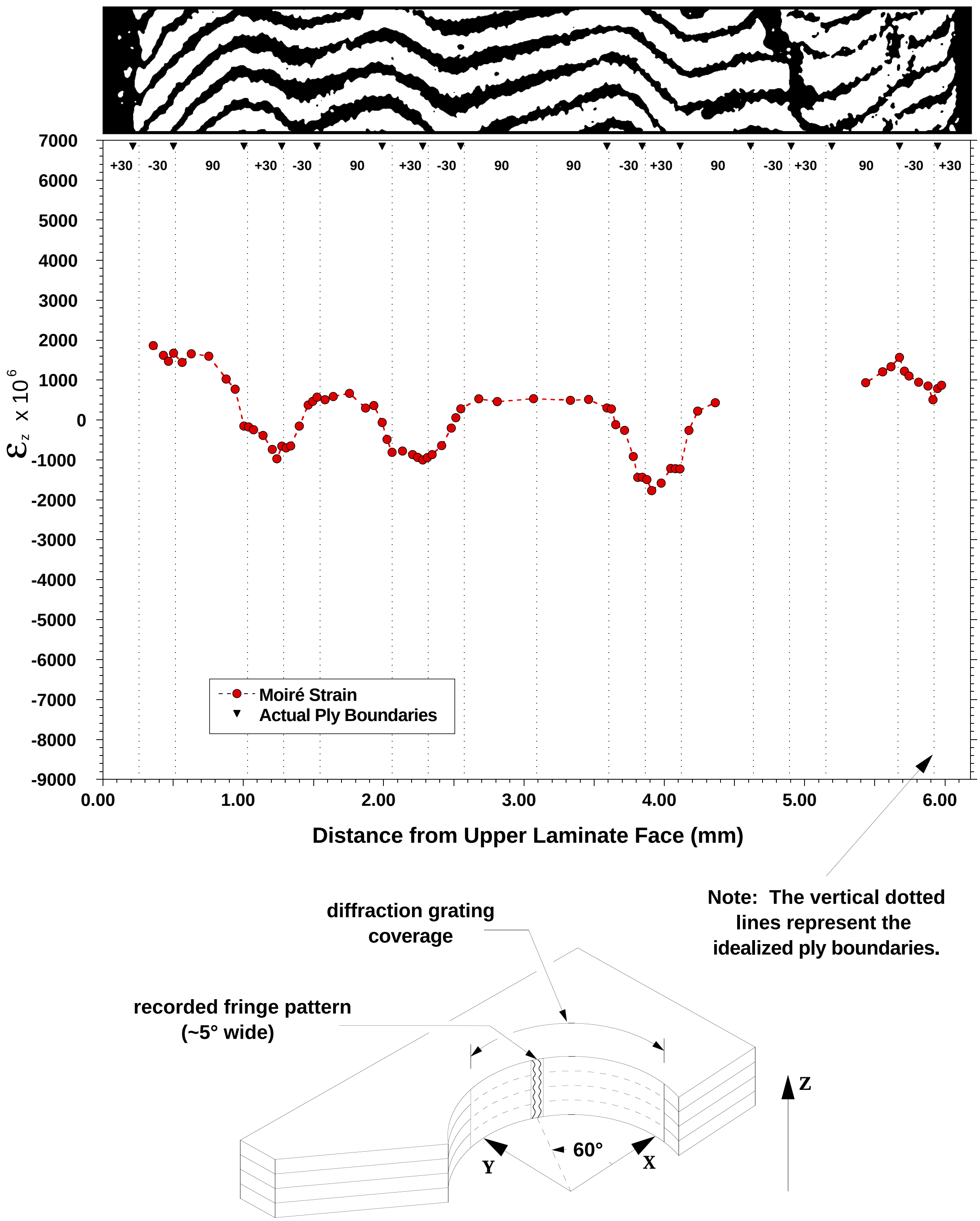

Figure 3.38: Z-direction strain variation at 60° for the $[+30_2/-30_2/90_4]_{3s}$ laminate (note: the U_z fringe pattern contains a carrier of rotation).

3.3 Discussion of Loaded Composite Results

3.3.1 Qualitative Phenomenological Discussion

The following discussion attempts to qualitatively describe the causes of the strain distribution features discussed in Section 3.2 using simple, phenomenological illustrations. Information presented in the following sections is not meant for calculating exact behavior. The intent is to provide methods for roughly determining the ply-by-ply strain behavior around the periphery of a hole in laminated composites. The ε_θ strain distribution will be discussed first. This will be followed by discussions of the distributions of $\gamma_{\theta z}$ and ε_z, respectively.

ε_θ Strain

The ply-by-ply variations in ε_θ observed in both composite specimens can be explained qualitatively through an examination of a two-dimensional solution of a tensile-loaded infinite fiber reinforced lamina with an open hole. Variations of ε_θ for the 0° through 90° angular locations for various lamina exposed to a unit far-field stress are presented in Figures 3.39. Figure 3.39a contains the distribution for a 0° lamina and for a 90° lamina. Figure 3.39b shows the variation of ε_θ for a +30° lamina, for a -30° lamina, and for a 90° lamina. These distributions were calculated using the two-dimensional solutions detailed in Greszczuk (1972). It is clear from these plots that individual laminae have different strain behavior around the periphery of a hole. If the constraint caused by neighboring plies on each ply of a multi-layered composite is reduced in the region around the hole, each ply would have a tendency to behave more like an individual lamina.

Recalling that Figures 3.6 and 3.7 showed a trend of higher tensile ε_θ in the 0° plies, it is clear from Figure 3.39a that an unconstrained 0° lamina would experience greater strain than an unconstrained 90° lamina at these angular locations. At the 45°, 60°, and 66° angular locations, Figure 3.39a shows that an unconstrained 0° lamina would experience lower tensile strain than the unconstrained 90° lamina. This same trend is visible in Figure 3.11 and to a much lesser degree in Figures 3.9 and 3.10.

Figure 3.39b shows that an unconstrained -30° ply would have significantly higher tensile ε_θ at the 60°, 66°, and 75° angular locations. This trend is also visible within Figures 3.22-3.24 (ε_θ at the 75°, 66°, and 60° locations). At the 45° angular location, an unconstrained -30° lamina would be in compression, while the 90° and +30° laminae would be in tension. In Figure 3.25, there is a hint that the -30° plies are generally less tensile than the others.

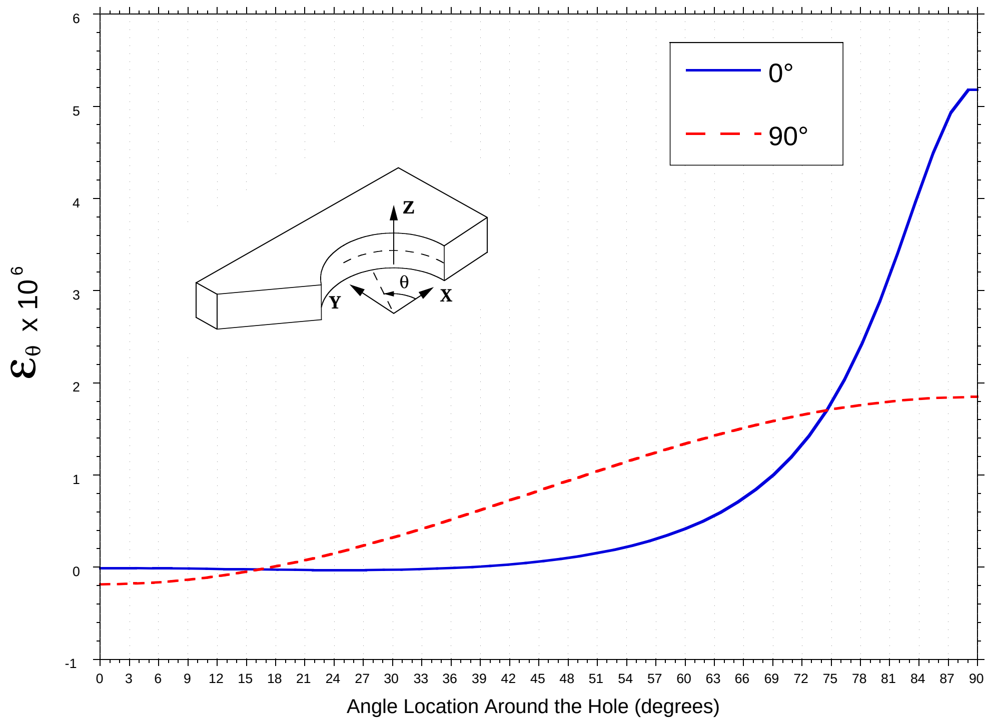

(a)

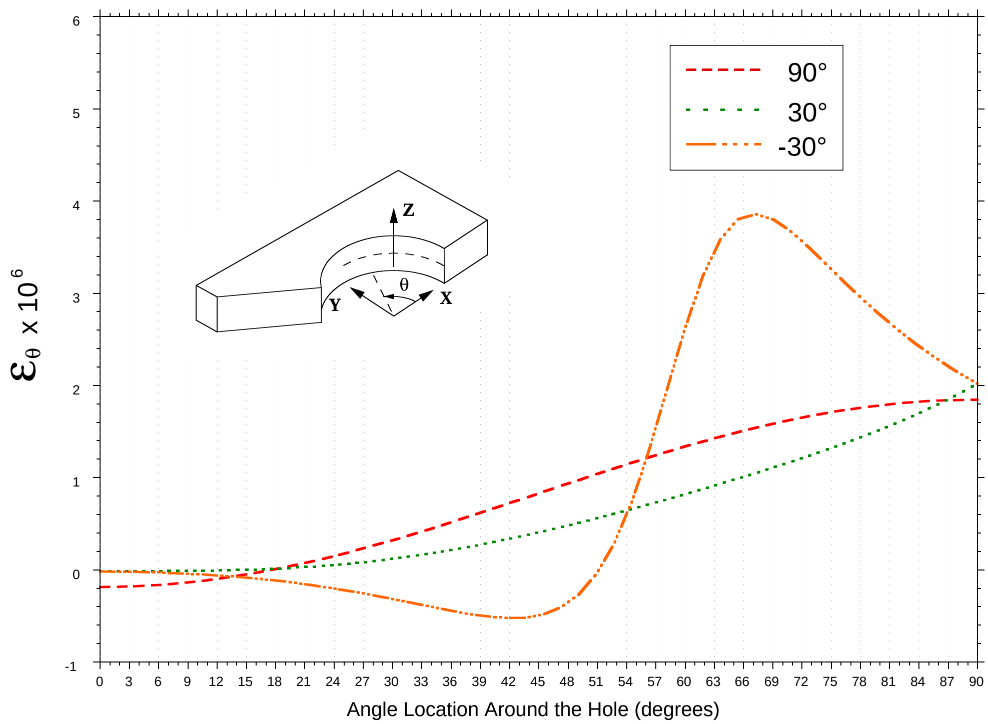

(b)

Figure 3.39: Circumferential strain variation caused by a unit far-field stress obtained from 2-D analyses of four IM7/5250-4 laminae with holes.

$\gamma_{\theta z}$ Strain

One author mentioned in Chapter 1 claimed that the free-edge effect at a given point on a curved surface will be similar to the free-edge effect on an equivalent straight edge (Ye and Yang, 1988). Figure 3.40 shows a distribution of the $\eta_{xy,x}$ term discussed in Chapter 1 for laminae fabricated with IM7/5250-4. Also contained in Figure 3.40 is a schematic of an imaginary tensile coupon cut from the $[+30°_2/-30°_2/90°_4]_{3s}$ specimen. The coupon has its long edges tangent to the hole at the 75° angular location. The lay-up of the newly cut coupon would be $[+45°_2/-15°_2/-75°_4]_{3s}$. Examining the distribution of $\eta_{xy,x}$, it is found that the +45° ply (the +30° ply in the original laminate) has an $\eta_{xy,x}$=–0.74, the -15° ply (the -30° ply in the original laminate) has an $\eta_{xy,x}$= 2.20, and the -75° ply (the 90° ply in the original laminate) has an $\eta_{xy,x}$= 0.15. Herakovich (1981) showed that the potential for interlaminar shearing between neighboring plies on a straight free edge is dependant on the difference between their respective $\eta_{xy,x}$ coefficients. Examining the $\gamma_{\theta z}$ variation at the 75° location in Figure 3.29 and using the above-listed $\eta_{xy,x}$, it is possible to explain the distribution of shear at this angular location. The $\eta_{xy,x}$ components for the +30° and -30° plies are -0.74 and 2.20, respectively. This large difference in $\eta_{xy,x}$ results in a large value of $\gamma_{\theta z}$ at the interface between these two plies. The $\eta_{xy,x}$ components for the -30° and 90° plies are 2.20 and 0.15, respectively. This somewhat smaller difference in $\eta_{xy,x}$ results in smaller values of $\gamma_{\theta z}$ at the interface between these two plies. Finally, the $\eta_{xy,x}$ components for the 90° and +30° plies are 0.15 and -0.74, respectively. This small difference between neighboring $\eta_{xy,x}$ results in a small value of $\gamma_{\theta z}$ at the interface between these two plies.

As mentioned at the beginning of Section 3.2.2, an interesting phenomenon was observed in the U_θ fringe patterns of Figure 3.17. Examination of the mid-plane region for angular locations near the 60° location shows that the central fringes are cupped toward the right or left, depending on which side of the 60° location they are located. The $\eta_{xy,x}$ term for the -30° ply (0° for a coupon cut tangent to the 60° location) is equal to zero at the 60° location. For angular locations greater than 60°, the $\eta_{xy,x}$ value for the -30° ply rapidly becomes positive; and for angular locations less than 60°, the $\eta_{xy,x}$ value rapidly becomes negative. In the vicinity of the 60° angular location, the $\eta_{xy,x}$ values for the +30° ply are always negative and change very slowly. In the region around 60°, the $\eta_{xy,x}$ values for the 90° ply are always positive and also change very slowly. The sign change in the $\eta_{xy,x}$ component of the -30° ply on either side of the 60° location causes the interesting fringe variations. For angles less than 60°, the tendency is for the -30° ply to shear in the same direction as the +30° ply and in the opposite direction from the 90° ply. For angles greater than 60°, this tendency is reversed.

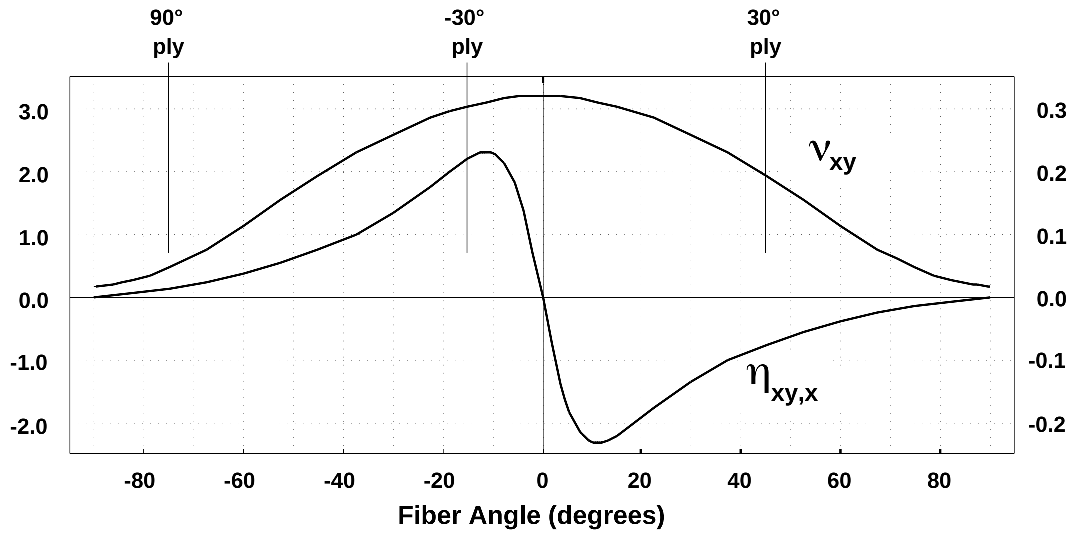

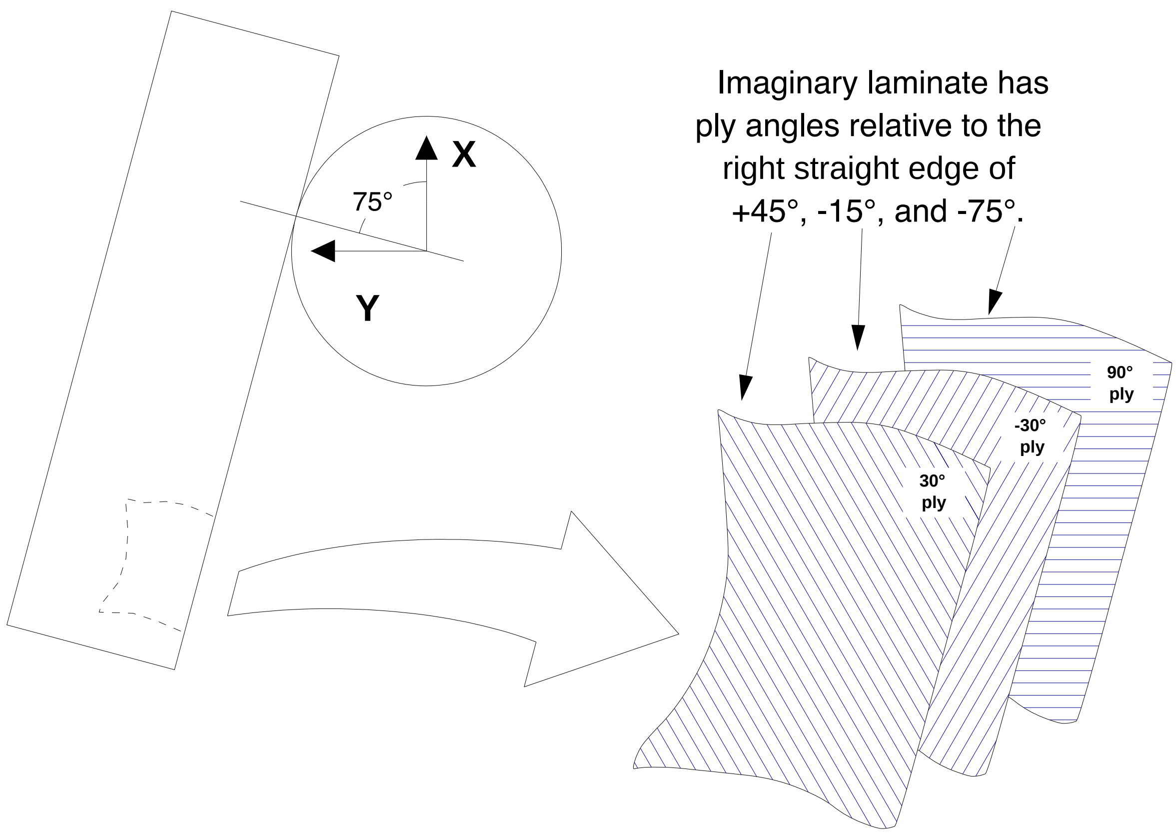

Figure 3.40: Variation of $\eta_{xy,x}$ and ν_{xy} for a lamina manufactured with IM7/5250-4. Specific points noted are for the plies of an imaginary laminate cut from the $[+30_2/-30_2/90_4]_{3s}$ laminate tangent to the hole at the 75° location.

Distributions of $\gamma_{\theta z}$ from the top surface of the laminate to the mid-plane at 56°, 58°, 60°, 62°, and 64° are shown in Figure 3.41. These data were obtained using phase-shifting analysis. The peaks located at the +30°/-30° interfaces rapidly decay as the angular location changes from 64° to 56°. The behavior at the -30°/90° interfaces changes from highly negative to positive as the angular location changes from 64° to 56°. These two trends are caused by the large magnitude and sign variation in the $\eta_{xy,x}$ term for the -30° ply. The behavior of $\gamma_{\theta z}$ in the region of the 90°/+30° interfaces remains relatively constant with angular location change. This is a result of the slowly changing nature of the $\eta_{xy,x}$ coefficients for the +30° and 90° plies.

ε_z Strain

The ply-by-ply behavior of ε_z exhibited in Figures 3.34-3.38 can be explained by again consulting Figure 3.40. This figure contains a distribution of ν_{xy} for a lamina of IM7/5250-4 material at any angle and the schematic of an imaginary tensile coupon cut from the original $[+30°_2/-30°_2/90°_4]_{3s}$ specimen, tangent to the hole at the 75° location. The lay-up of the newly cut coupon would be $[+45°_2/–15°_2/–75°_4]_{3s}$. From the distribution of ν_{xy} in Figure 3.40, it is found that the +45° ply (the +30° ply in the original laminate) has a ν_{xy}=0.19, the -15° ply (the -30° ply in the original laminate) has a ν_{xy}= 0.30, and the -75° ply (the 90° ply in the original laminate) has a ν_{xy}= 0.05. Herakovich (1981) discussed that the nature of ε_z between neighboring plies on a straight free edge is dependant on the difference between the respective ν_{xy} of each ply. Both ν_{xy} values for the +30° and -30° plies are larger than the ν_{xy} for the 90° ply. This would cause the ±30° ply groups to contract in the transverse direction more than the 90° plies. The 90° plies would be placed in a peel-like deformation state, resulting in tensile strain in the z-direction. The ±30° ply groups would, consequently, be compressed in the z-direction. The strain behavior in Figure 3.36 (ε_z for the 75° location) corresponds with this description.

As mentioned in Section 3.2.2 and visible in Figures 3.34-3.38, ε_z for the $[+30°_2/-30°_2/90°_4]_{3s}$ specimen in the outer plies is generally more tensile than in the interior plies. This behavior may be caused by a variation in the ply constraints at different locations within the laminate. The ±30° ply groupings at the laminate surface are less constrained than the ±30° ply groupings at interior locations. Compression is lower in these groupings than within the interior ±30° ply groupings, since there are no 90° plies (expanding in the z-direction) on one side of the outer ±30° ply groupings. This results in a tensile shift of ε_z in the regions near the laminate faces and a compressive shift of ε_z in the regions near the mid-plane.

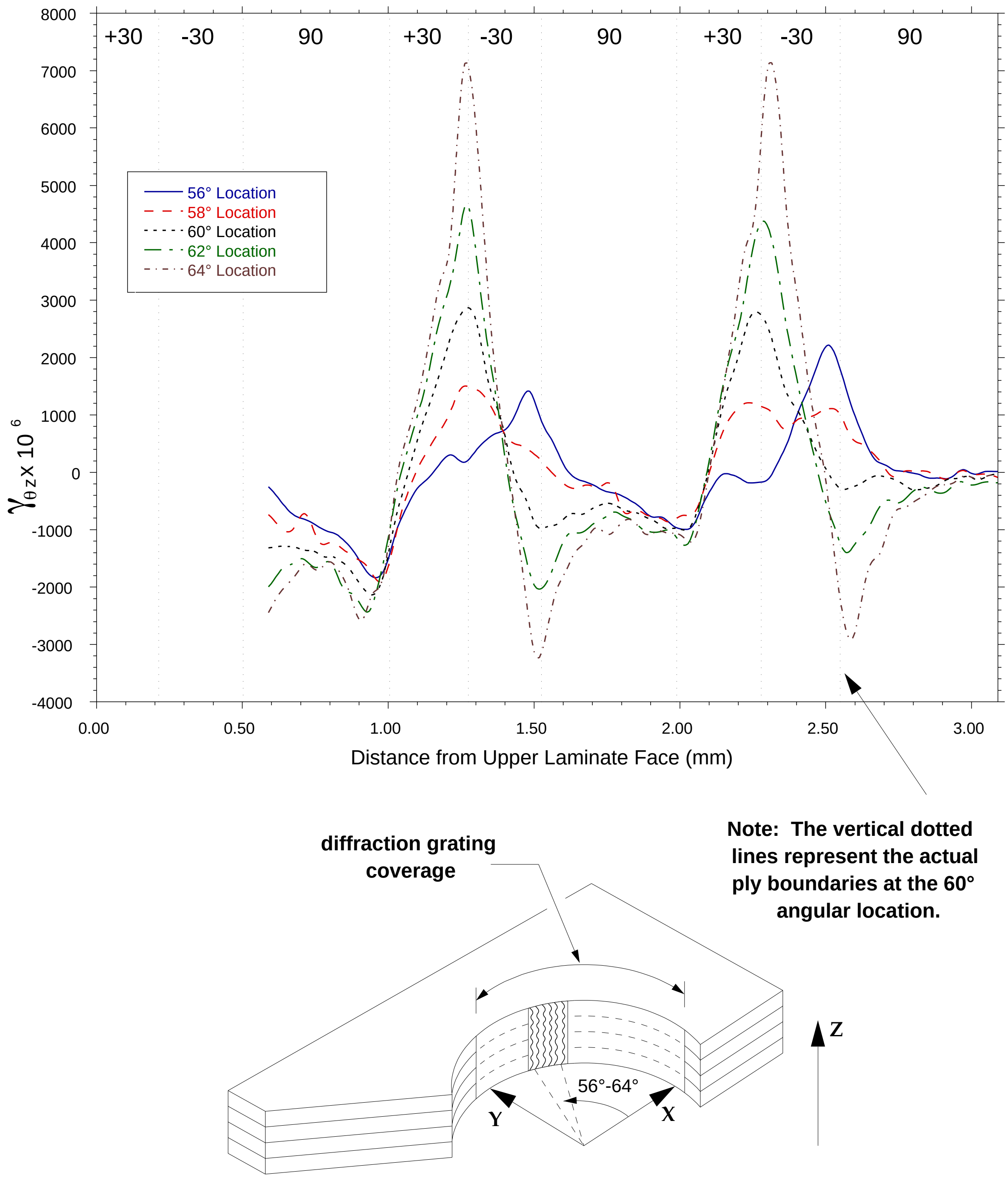

Figure 3.41: Theta-Z shear strain variations for 56°, 58°, 60°, 62°, and 64° from the $[+30_2/-30_2/90_4]_{3s}$ laminate obtained using phase-shifting moiré.

3.4 Results and Discussion of Viscoelastic Deformation

Photographs of select fringe patterns from the first post-load sector gratings replicated from both composites are presented in Figure 3.42. The U_θ fringe patterns at the 87° location from the $[+30°_2/-30°_2/90°_4]_{3s}$ specimen and at the 78° location from the $[0°_4/90°_4]_{3s}$ composite are shown. Both fringe patterns contain carriers of extension. Immediately obvious are the localized shearing deformations. These deformations occur at the locations of highest load-induced shear on both specimens.

Results from the phase-shifting analysis of the 87° region of the $[+30°_2/–30°_2/90°_4]_{3s}$ are shown in Figure 3.43. One of the digitally recorded fringe patterns from the first post-load sector grating is shown in Figure 3.43a. The contour map of U_θ displacements, after subtracting the null field information and removing a slight carrier of rotation, is presented in Figure 3.43b. The shear strain distribution, averaged over a 0.5° slice, is shown in Figure 3.43c. Calculated shear strain values are quite large. They are also of the same sign as the load-induced peak shear strains.

Photographs of the U_θ fringe patterns at the 84° location from the $[+30°_2/–30°_2/90°_4]_{3s}$ specimen and at the 78° location from the $[0°_4/90°_4]_{3s}$ composite from the second post-load sector gratings are shown in Figure 3.44. Both fringe patterns contain carriers of extension. The fringe pattern from the $[0°_4/90°_4]_{3s}$ specimen shows only very slight signs of the deformation exhibited by the fringe pattern in Figure 3.42. The U_θ fringe pattern for the 84° location from the $[+30°_2/–30°_2/90°_4]_{3s}$ specimen shows greatly reduced deformation when compared with Figure 3.42. In some areas of this fringe pattern, all evidence of shear deformation is gone. It appears that most of the observed deformation found in both specimens, shown in Figure 3.42, has crept back to the original undeformed state as shown in Figure 3.44.

Examination of the second post-load sector in the interferometer yielded some unexpected results. At angular locations where little or no deformation was observed in the first post-load sector gratings, significant but small deformation was observed in the second post-load sector gratings. These deformations again take the form of shearing deformations, but are more similar to the load-induced fringes. At this time, it is not known what caused these deformations. The specimens were stored away from heat and were not loaded again after the loading cycles discussed in Chapter 2. Replication of the second post-load sector gratings occurred at approximately the same temperatures as all other grating replications.

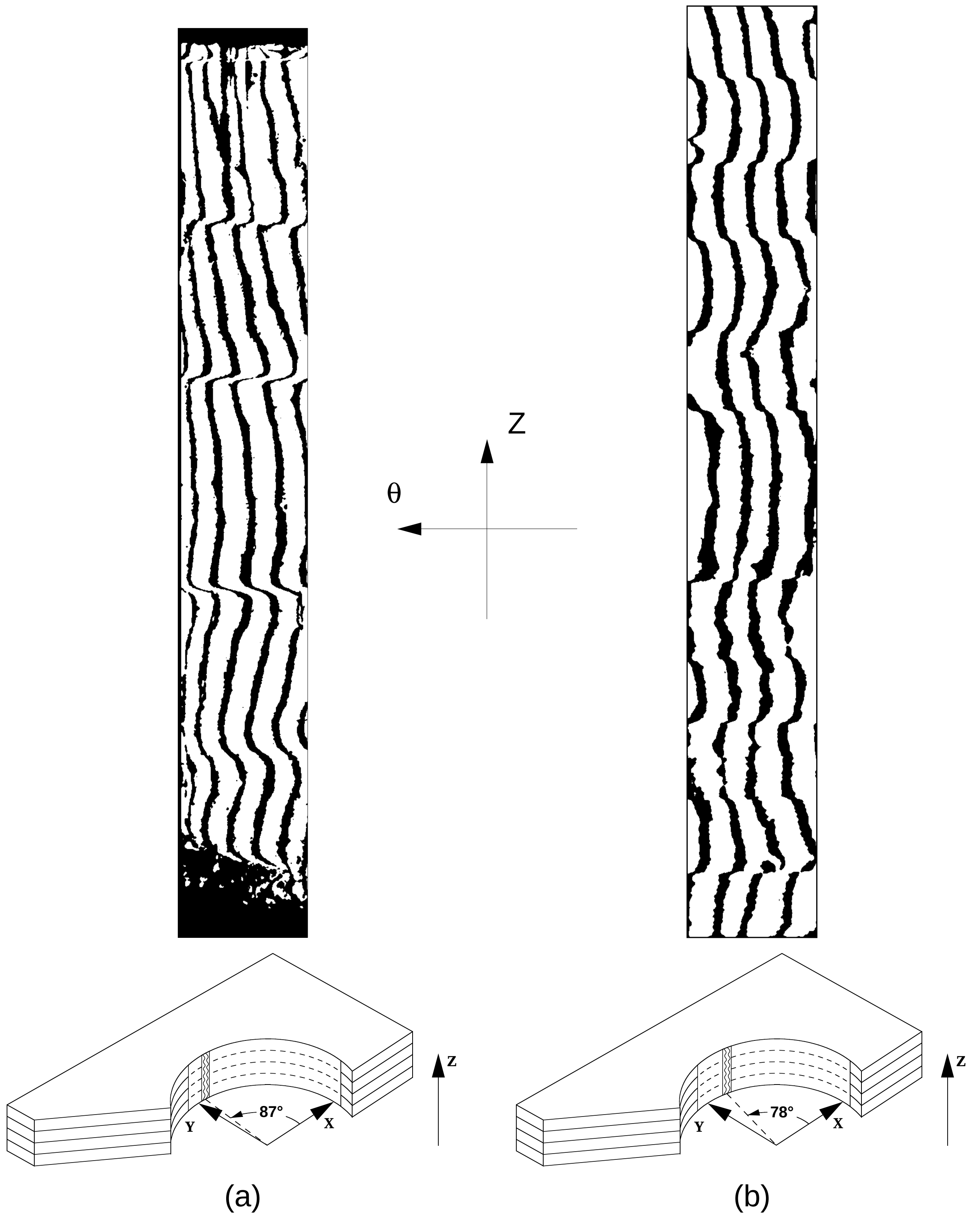

Figure 3.42: U_θ fringe patterns from the first post-load sector gratings from (a) the $[+30_2/-30_2/90_4]_{3s}$ laminate and (b) the $[0_4/90_4]_{3s}$ laminate (note: both patterns contain a carrier of extension).

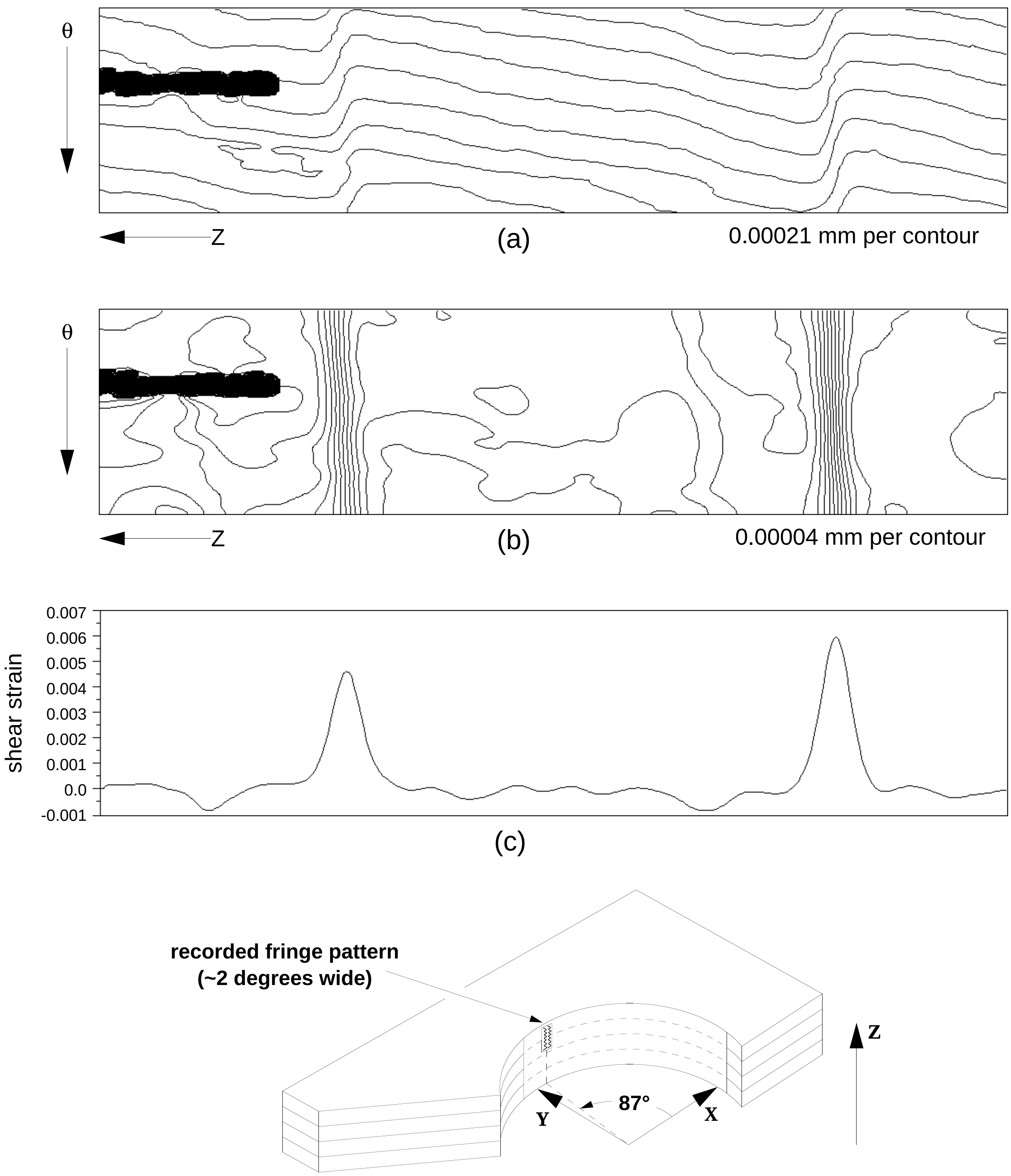

Figure 3.43: (a) ~2° portion of the U_θ contour pattern with carrier of extension from the first post-load sector from the $[+30_2/-30_2/90_4]_{3s}$ laminate at 87°. (b) U_θ after null subtraction and carrier removal. (c) Theta-Z shear strain variation averaged over bottom 0.5° of data.

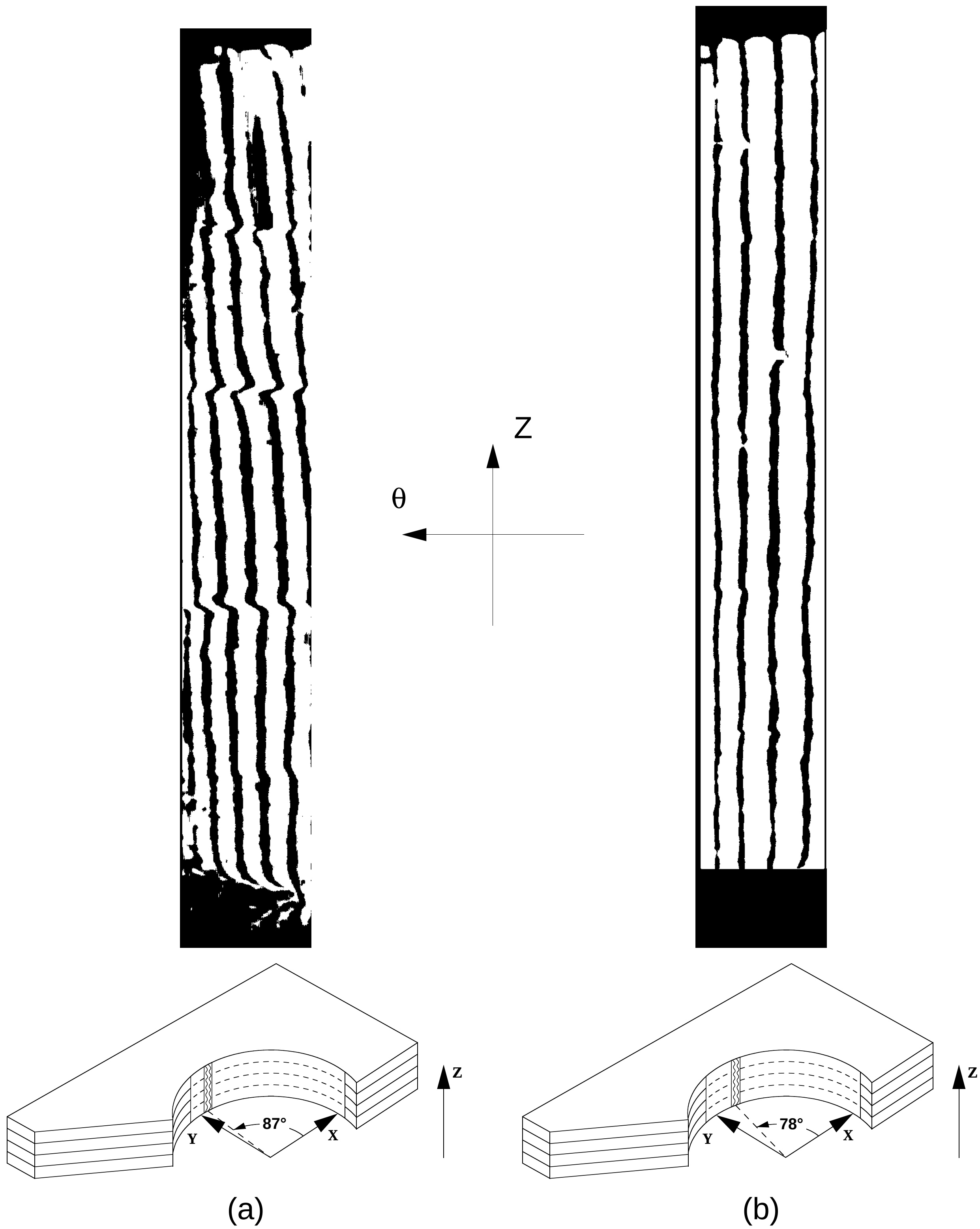

Figure 3.44: U_θ fringe patterns from the second post-load sector gratings from (a) the $[+30_2/-30_2/90_4]_{3s}$ laminate and (b) the $[0_4/90_4]_{3s}$ laminate (note: both patterns contain a carrier of extension).

One possible cause of the observed deformation is that both specimens could have absorbed significant amounts of moisture between the replication of the first and second post-load sector gratings. The response of a composite to moisture absorption, similar to the response of a composite to a temperature change, can cause significant deformation.

This unexpected deformation in the second post-load sector gratings complicates the conclusions made about the creep-out of the recorded viscoelastic deformation. It is, however, unlikely that deformations caused by moisture absorption would completely counteract the large post-load shear deformations recorded. Therefore, it is likely that these viscoelastic deformations have mostly crept out, and the specimens have nearly returned to their original state.

Further study of the source of this unexpected deformation needs to be conducted. Moisture is strongly suspected as the cause. Careful tests would be required to examine the ply-by-ply effects of moisture absorption on the strain state of a composite. Perhaps a composite could be prepared such that the original specimen grating could be applied to a pristine, thoroughly dried specimen. The changes in strain behavior with moisture absorption could then be studied using the methodologies described in Chapter 2.

It is important to note that no mysterious deformations were present in the sector grating replicated from the $[+30°_2/-30°_2/90°_4]_{3s}$ specimen just prior to the application of load. The fringe images obtained from this sector grating were nearly identical to the fringe patterns obtained from the original sector grating used to replicate a grating onto the specimen. Therefore, the load-induced deformation discussed previously is not tainted with mysterious deformations of the type found in the second post-load sector gratings.

3.5 Sources of Noise

The distributions of strain presented in the previous sections are not smooth. Accompanying the expected variations in strain are also significant amounts of noise. Some of this noise is caused by errors in the manual analyses of the fringe patterns. These types of errors are discussed in Appendix B. Other noise sources fall into two categories. Those sources that accurately represent the material behavior (not errors), and those sources that distort the actual material behavior (errors) .

There are many sources of noise that cause errors in the measurement of actual material behavior. These are primarily related to diffraction grating quality. The diffraction gratings at any step in the process can be damaged by dust or bubbles present in the replicating agent. Physical damage, such as scratches or surface contamination, can effect the accuracy of displacements measured from a diffraction grating. Too much pressure during a replicating step can also cause unwanted distortion of the diffraction grating. The methodologies presented in Chapter 2 are susceptible to these types of problems. Each of the multiple replication steps incur small amounts of grating damage (dust, bubbles, scratches, pressure distortions, etc.) which accumulate in the final replicated gratings.

Several sources of noise exist that are actually representative of the specimen deformation. Localized plastic or viscoelastic deformations could be responsible for rough looking strain distributions. Another source of noise-like actual behavior is material variability. Large-scale material inconsistencies were known to exist. Both specimens exhibited ply waviness to some degree. Small-scale variability was also documented. A fiber-reinforced laminate is not constructed from plies of homogeneous material. Local variability of fiber spacing, resin-rich zones between plies, fiber misalignment (local or global), and perhaps the individual fibers themselves could all contribute to a roughness in the fringe patterns. Figure 3.45 contains micrographs of typical distributions of fibers in one of the extra IM7/5250-4 laminates fabricated for this research. The fibers are approximately 0.005 mm (0.0002 inches) in diameter. The scale of each pixel in the scanned fringe patterns analyzed as described in Chapter 2 was approximately one-half a fiber diameter. It is unlikely, however, that features as small as one fiber contributed greatly to the roughness in the calculated strain patterns. This is because the gage lengths of 1° to 2° used in the strain analyses are on the order of 50 to 100 times the size of a fiber.

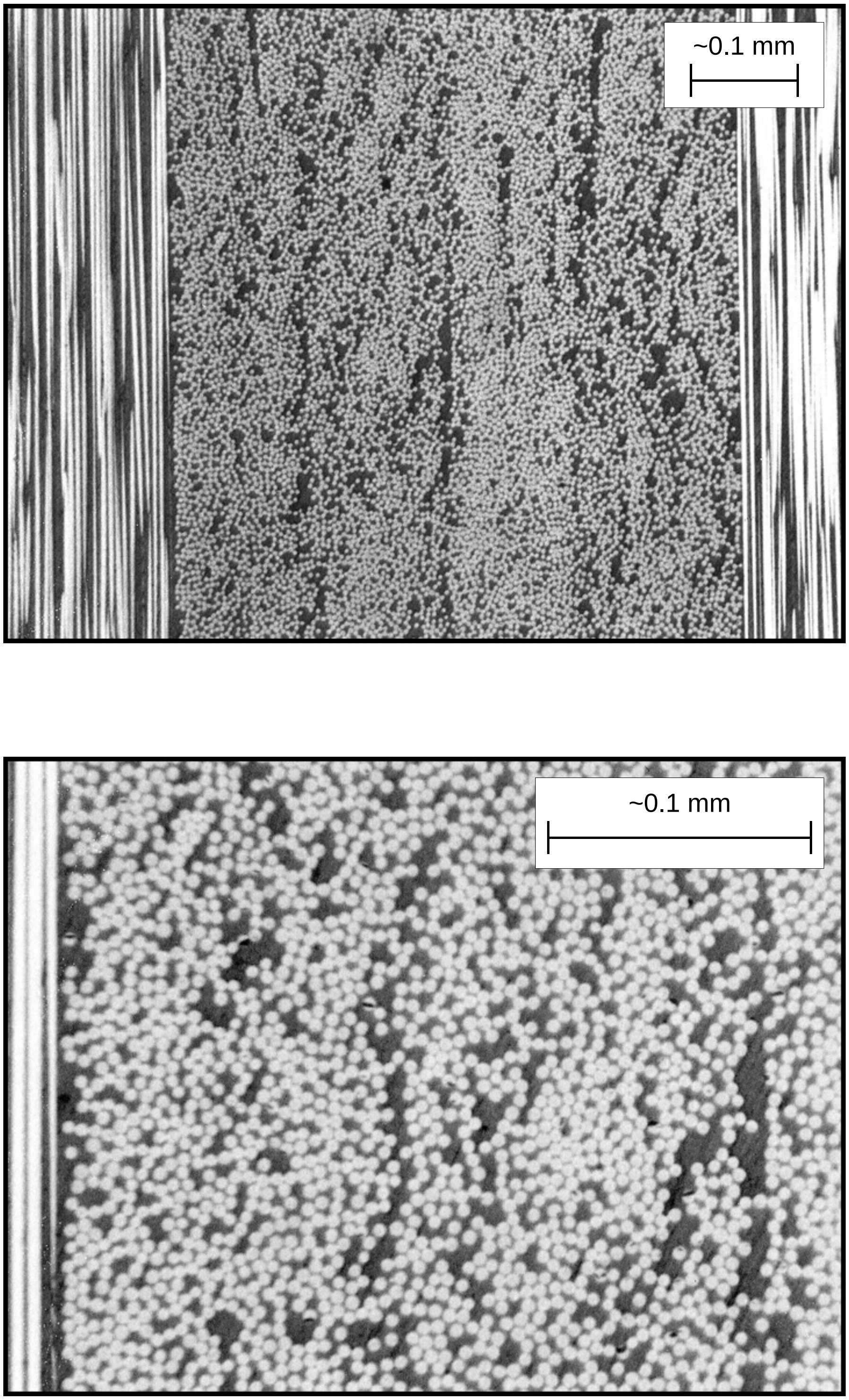

Figure 3.45: Micrographs from a typical IM7/5250-4 laminate examined in this research.

Chapter 4: Discussion of Numerical Results

4.1 SVELT Modeling

The SVELT modeling was performed by Dr. Endel Iarve of the University of Dayton Research Institute in conjunction with Wright Laboratory, Materials Directorate, in Dayton, Ohio. All SVELT results presented in this document are based on half-laminate models with symmetry conditions applied at the mid-plane. Subdivisions of the curvilinear coordinate system were introduced to build the basic spline functions. Subdivisions in ρ were concentrated toward the hole edge while subdivisions in ϕ were equally spaced around the perimeter of the hole. Although the coordinate system used by SVELT is not a cylindrical system, in the vicinity of the hole, ρ is analogous to the radial coordinate and ϕ is analogous to the θ coordinate. Figure 4.1 shows the in-plane mesh used to model the $[0°_4/90°_4]_{3s}$ and $[30°_2/\text{-}30°_2/90°_4]_{3s}$ composites studied in this research. One subdivision through the thickness of each ply grouping was used in modeling both composites. Another model of the $[30°_2/\text{-}30°_2/90°_4]_{3s}$ composite specimen used two subdivisions per ply to briefly study the effects of increased mesh density on the comparison. The two composite lay-ups were modeled with the properties of IM7/5250-4 listed in Table 2.2. Both models exactly duplicated the transverse in-plane dimensions, the idealized interlaminar dimensions, and the hole dimensions of the tested composite specimens. The modeled specimen lengths were shorter than the specimens tested with moiré interferometry. This aided in model convergence.

Data obtained from the SVELT model consisted of ε_θ, ε_z, and $\gamma_{\theta z}$ around the periphery of the hole at 1° increments. Data were distributed through each ply grouping such that 21 points were acquired for each ply. Two values of each strain component were reported at each ply interface. These were calculated using the displacement solutions from each of the neighboring plies. The load was introduced into the SVELT models through the application of a uniform end displacement. All SVELT data required scaling to match the experimental load conditions. The numerical data was scaled to match the applied far-field stress of 50 MPa for the $[30°_2/\text{-}30°_2/90°_4]_{3s}$ specimen. The numerical data for the $[0°_4/90°_4]_{3s}$ specimen was scaled to match the measured far-field strain.

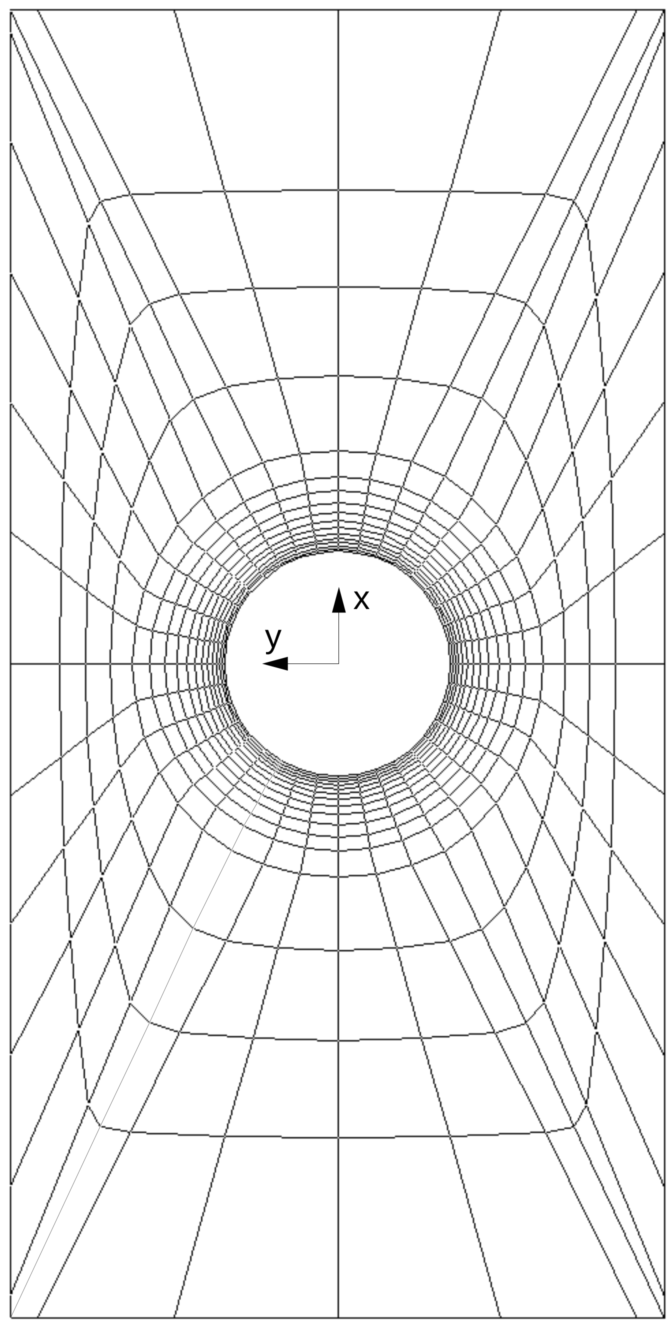

Figure 4.1: SVELT mesh used to model the $[0_4/90_4]_{3s}$ and $[+30_2/-30_2/90_4]_{3s}$ laminates.

4.2 Comparison of Moiré and SVELT Data

The SVELT data in the following sections was obtained using the mesh with only one sub-layer per ply grouping unless otherwise noted. The format of the plots are identical to the graphs presented in Chapter 3. The data ranges for a given angular location and strain component are also the same as the Chapter 3 plots.

4.2.1 Comparison of Data for the $[0°_4/90°_4]_{3s}$ Laminate

ε_θ for the $[0°_4/90°_4]_{3s}$ Laminate

The comparison of experimentally and numerically obtained ε_θ distributions for the 84°, 75°, 60°, and 45° angular locations are shown in Figures 4.2-4.5. Note that the SVELT data does not extend all the way to the laminate faces. An error in the data output routine resulted in the recording of only 12 of the 21 surface ply data points. The overall match between the SVELT and moiré data is quite close. Noise and ply waviness contribute to mismatches between the two data sets in some areas. The expected trends outlined in Section 3.3.1 and Figure 3.39a are visible in the SVELT data as well as in the moiré data. Figure 4.3 shows that SVELT does not predict large ply-by-ply variations in ε_θ at 75° as confirmed by the moiré measurements. At the 90° angular location, the analysis shows that the 0° plies experience higher tensile strain than the 90° plies. At the 60° and 45° locations, the analysis shows the opposite trend: the 90° plies experience higher tensile strain.

$\gamma_{\theta z}$ for the $[0°_4/90°_4]_{3s}$ Laminate

The comparison of experimentally and numerically obtained $\gamma_{\theta z}$ distributions for the 75°, 60°, and 45° angular locations are presented in Figures 4.6-4.8. The effects of the ply waviness found in the $[0°_4/90°_4]_{3s}$ specimen are visible as horizontal shifts in the moiré data with respect to the SVELT data. If data shift is taken into account, the match between SVELT and moiré data is very close. The only significant discrepancy between the numerical and experimental results occurs at the ply interfaces. The measured shear strain at these locations tends to be of larger magnitude than predicted by SVELT. This discrepancy may be caused by the viscoelastic shear deformation documented at these locations.

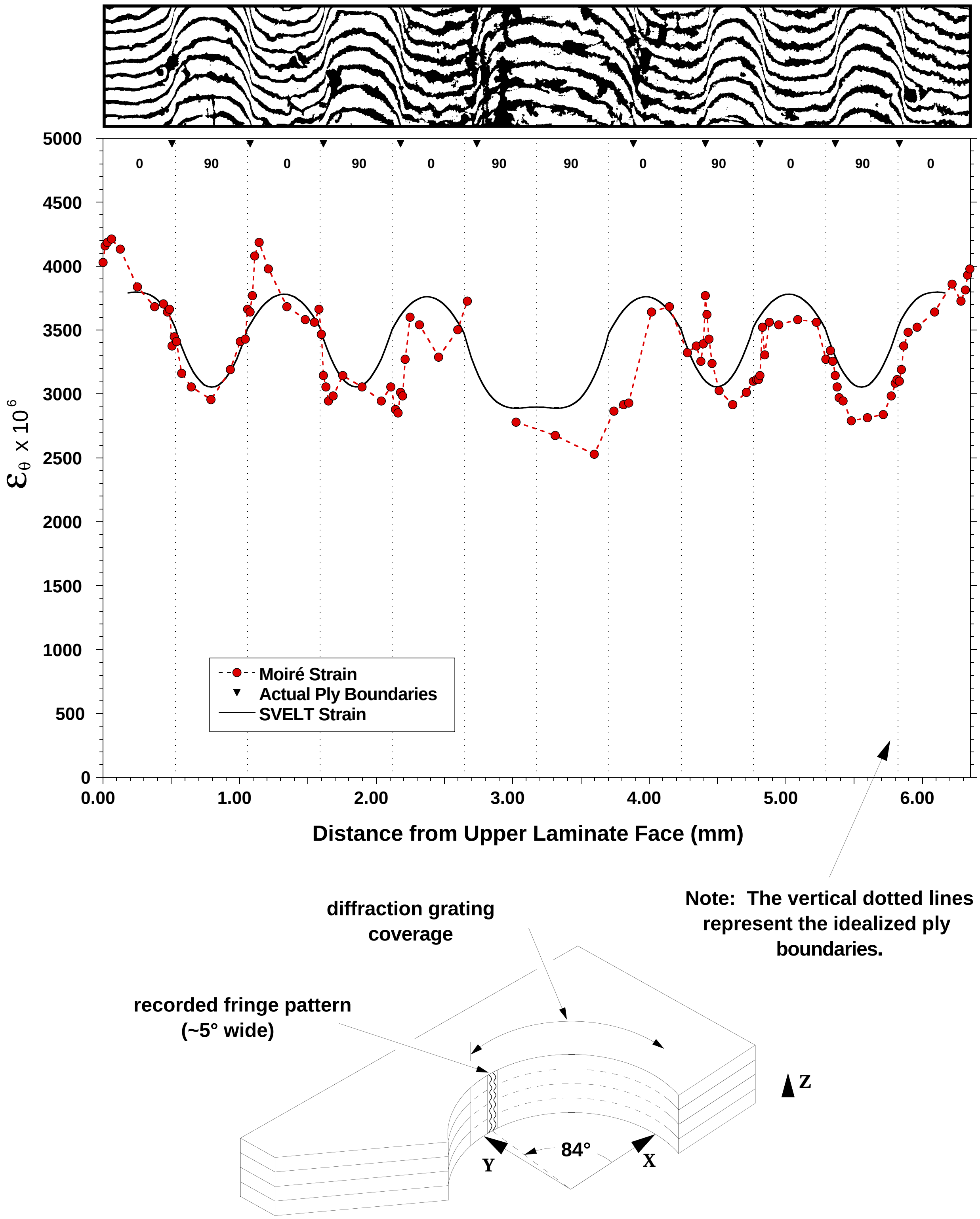

Figure 4.2: Circumferential strain comparison at 84° for the $[0_4/90_4]_{3s}$ laminate.

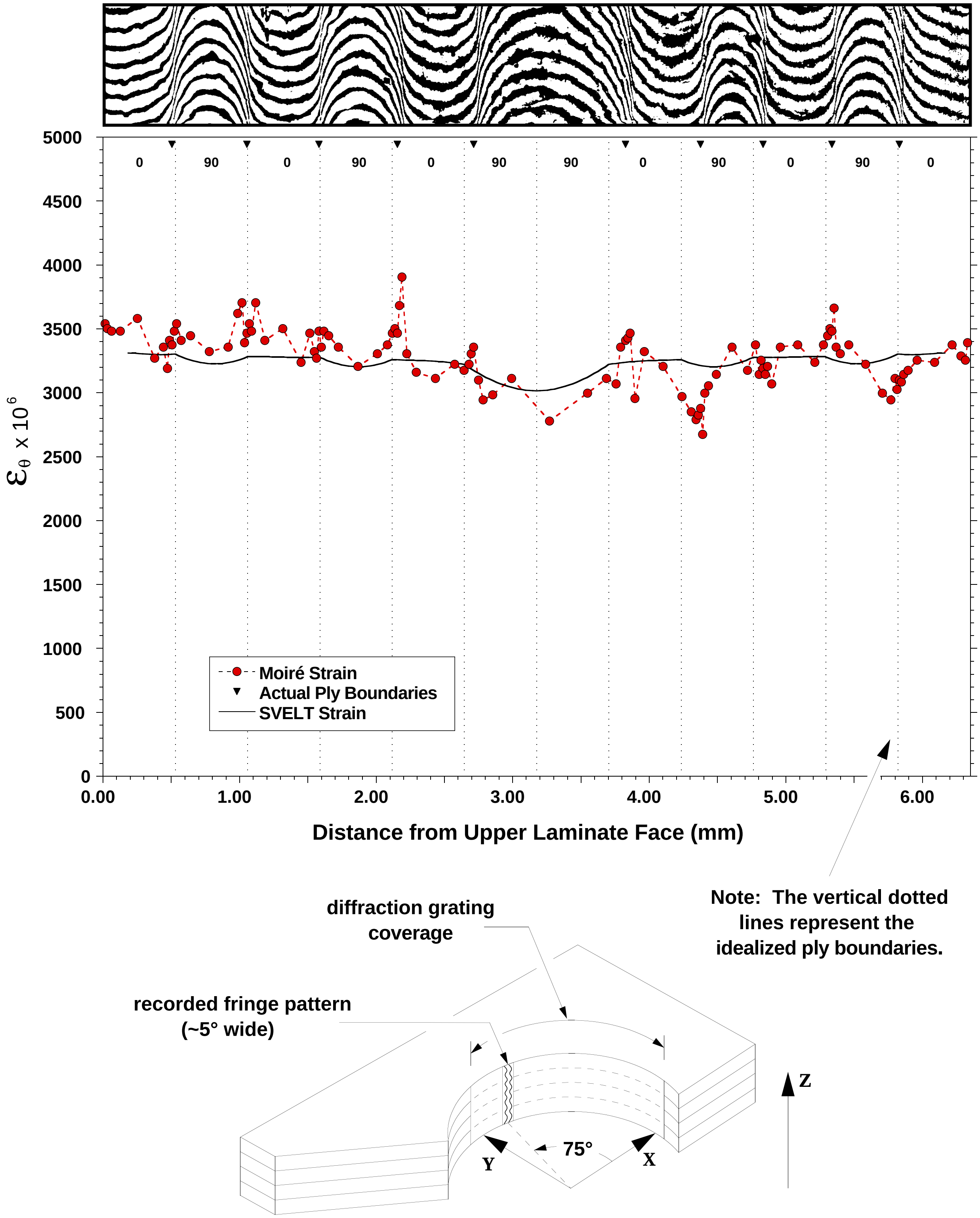

Figure 4.3: Circumferential strain comparison at 75° for the $[0_4/90_4]_{3s}$ laminate.

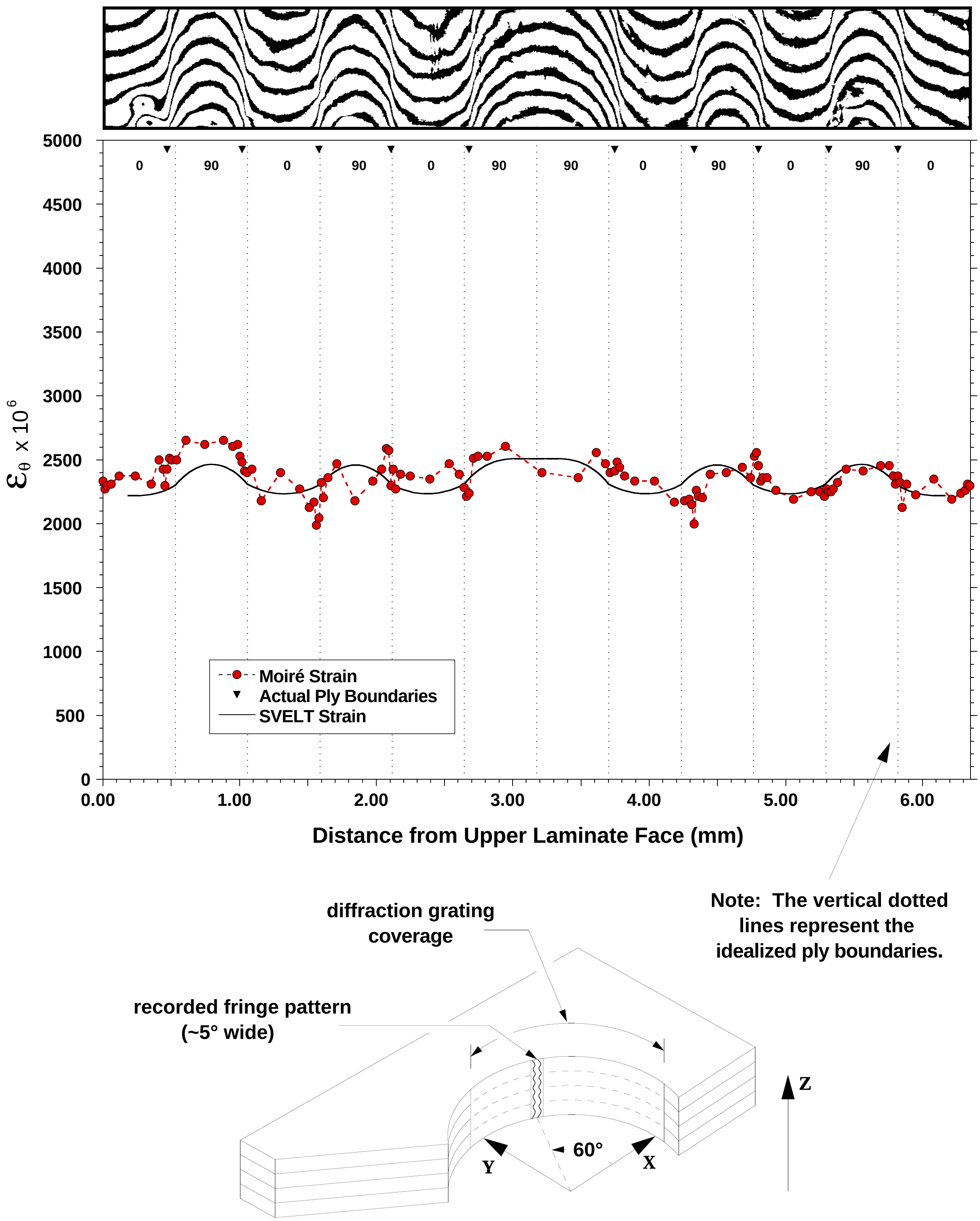

Figure 4.4: Circumferential strain comparison at 60° for the $[0_4/90_4]_{3s}$ laminate.

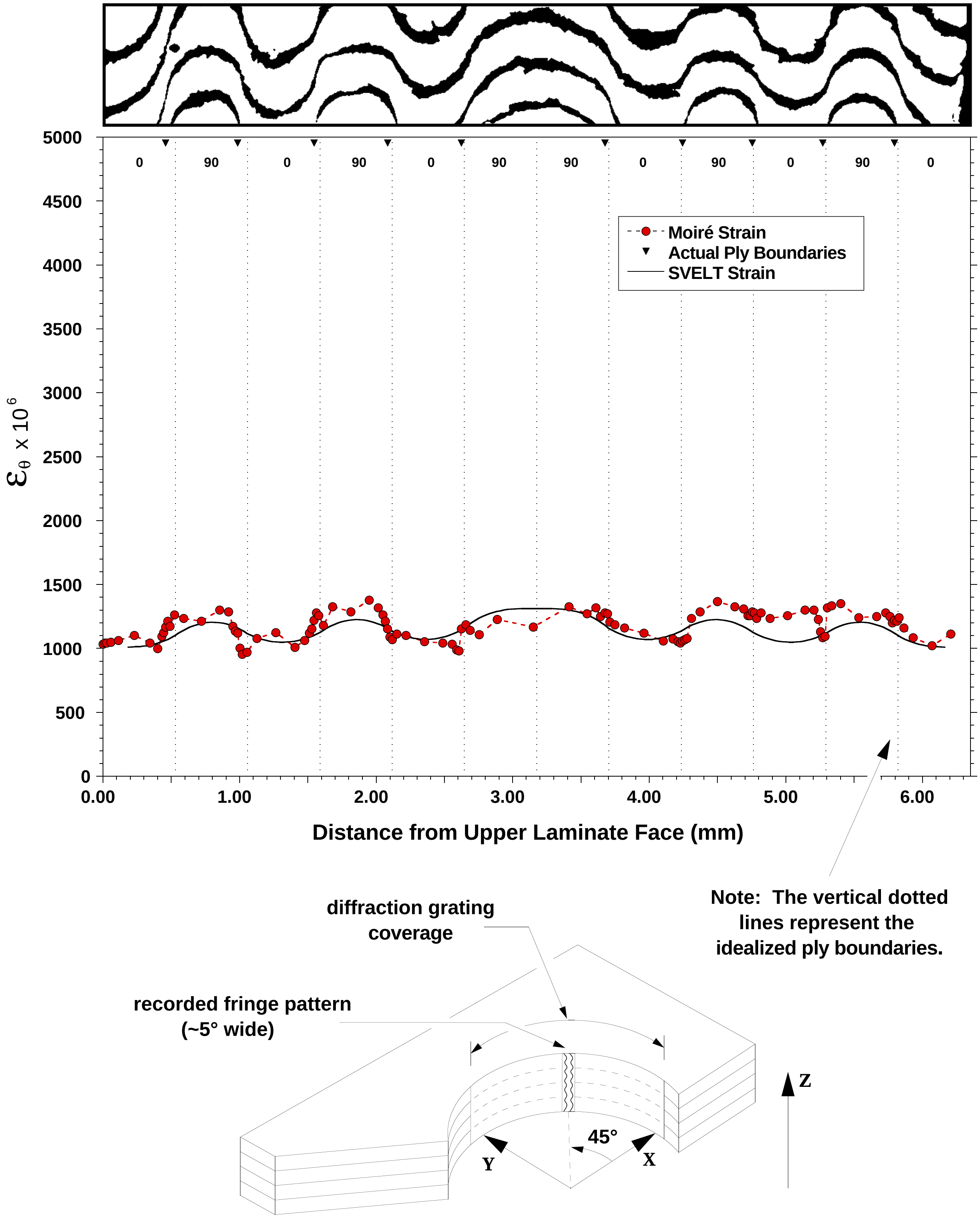

Figure 4.5: Circumferential strain comparison at 45° for the $[0_4/90_4]_{3s}$ laminate.

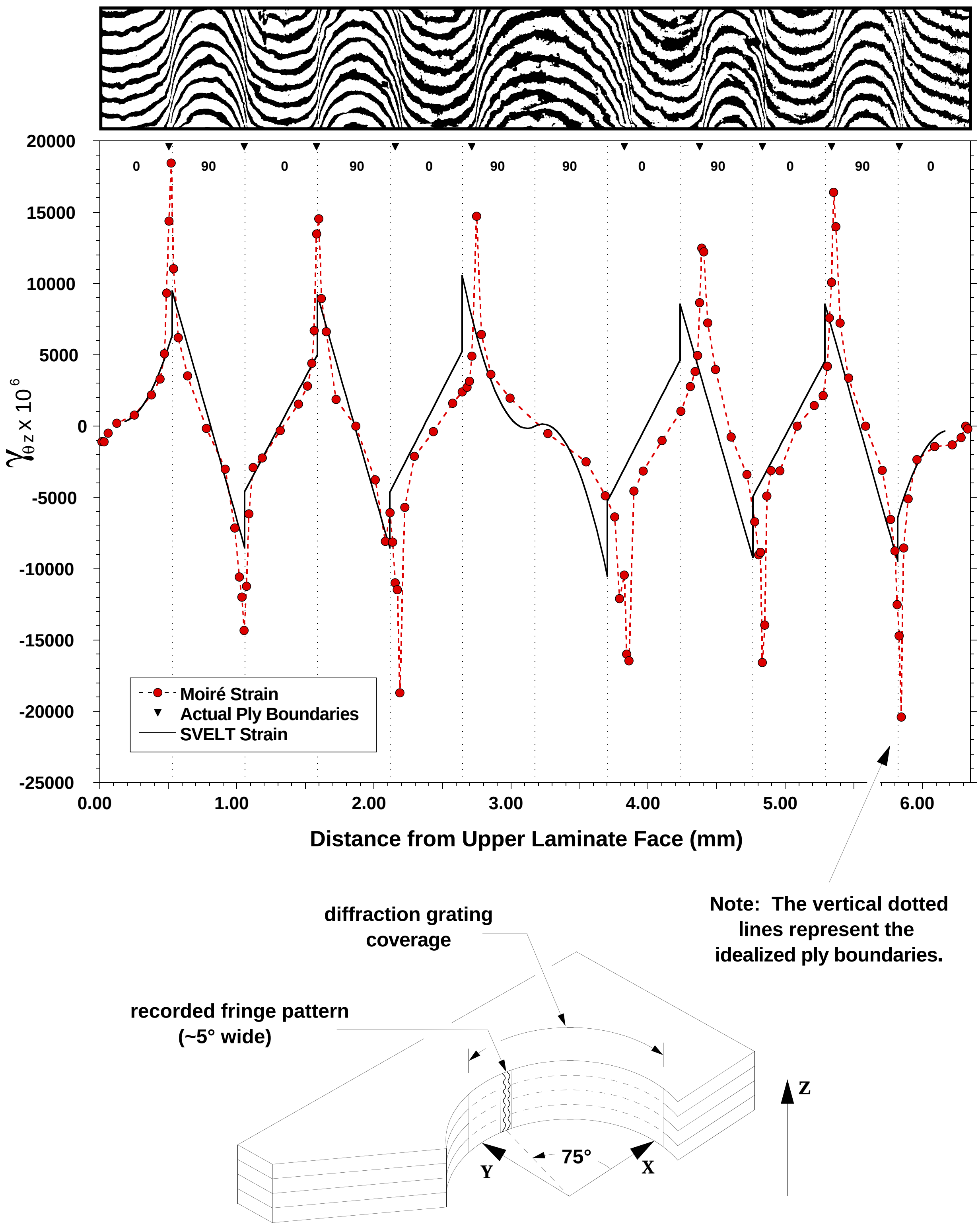

Figure 4.6: Theta-Z shear strain comparison at 75° for the $[0_4/90_4]_{3s}$ laminate (note: shear strain calculated from U_θ pattern only).

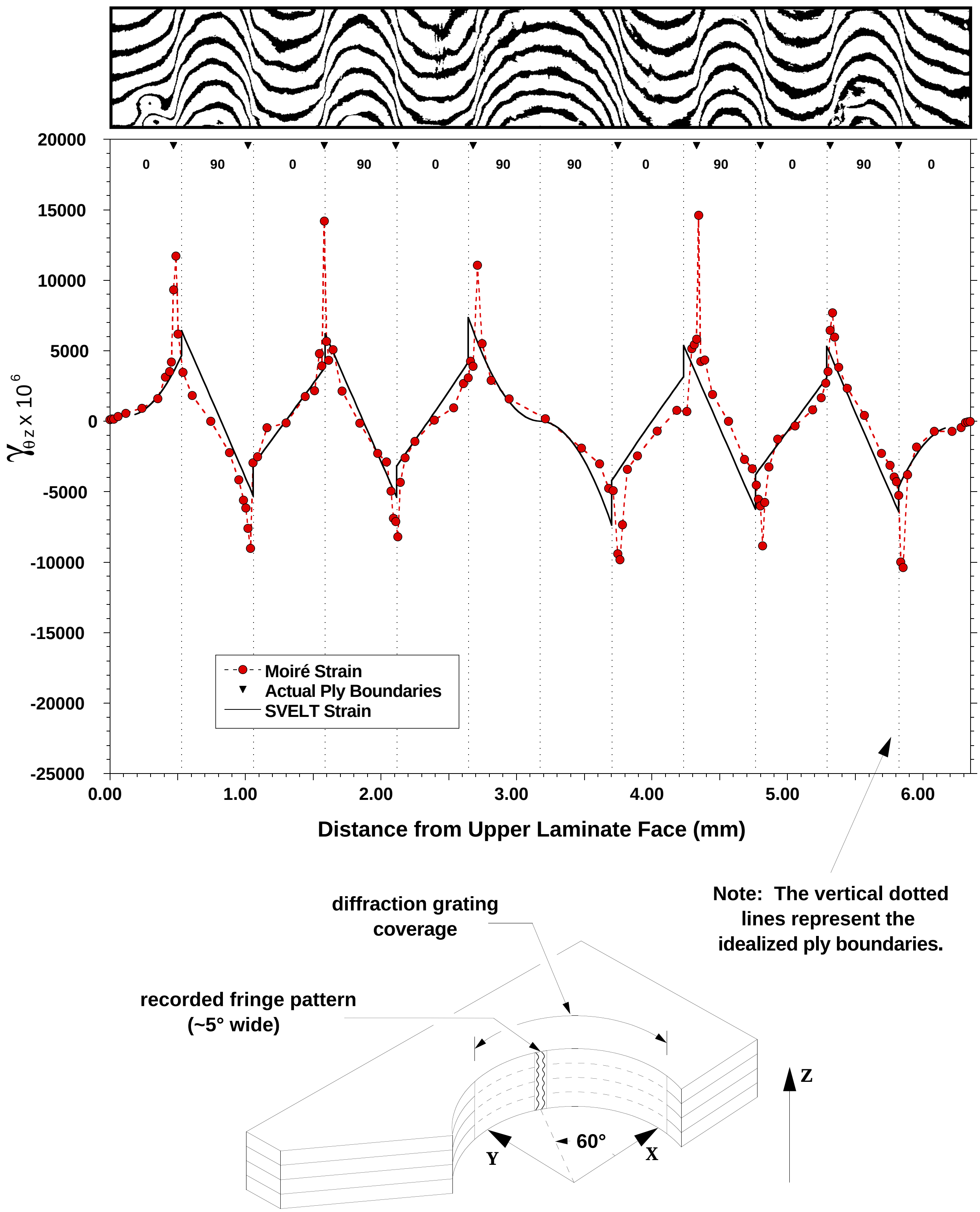

Figure 4.7: Theta-Z shear strain comparison at 60° for the $[0_4/90_4]_{3s}$ laminate (note: shear strain calculated from U_θ pattern only).

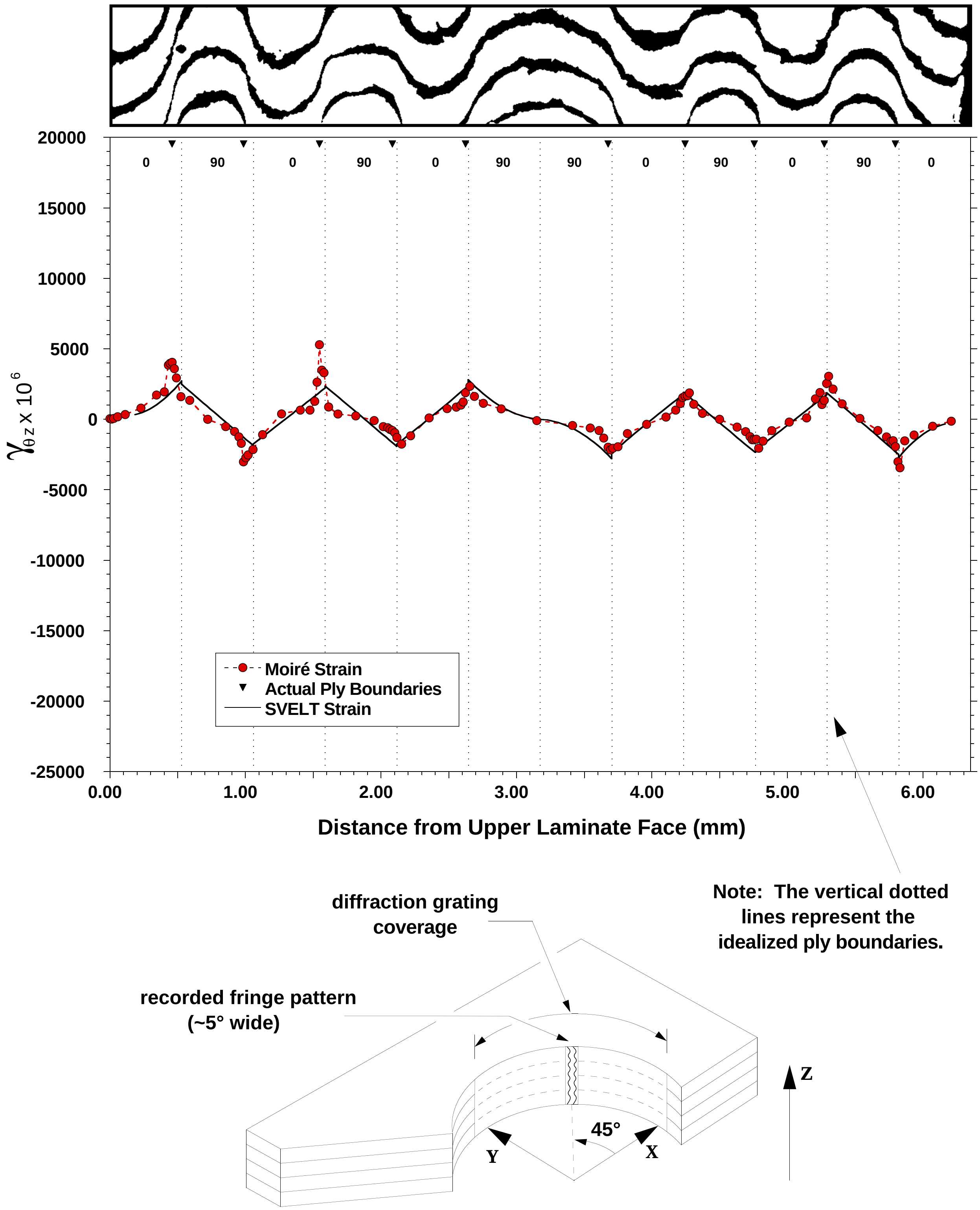

Figure 4.8: Theta-Z shear strain comparison at 45° for the $[0_4/90_4]_{3s}$ laminate (note: shear strain calculated from U_θ pattern only).

4.2.2 Comparison of Data for the $[+30°_2/-30°_2/90°_4]_{3s}$ Laminate

ε_θ for the $[+30°_2/-30°_2/90°_4]_{3s}$ Laminate

The experimentally and numerically obtained ε_θ distributions for the 84°, 75°, 66°, 60°, and 45° angular locations are compared in Figures 4.9-4.13. Note that the SVELT data presented in these charts also does not extend to the laminate faces. The SVELT predictions compare very well with the measured behavior. For the most part, the trends and the magnitudes show a close match. The expected trends, determined using Figure 3.39b, are also visible in the SVELT data. Figures 4.10-4.12 show that ε_θ in the -30° plies is more tensile than in neighboring plies. The strain in the -30° plies at the 45° angular location is shown to be slightly less tensile than in neighboring plies. Both of these results can be roughly anticipated from the behavior of tensile-loaded unconstrained laminae with holes. The slightly refined SVELT model with two sub-layers per ply grouping did not significantly change the predicted behavior of ε_θ.

$\gamma_{\theta z}$ for the $[+30°_2/-30°_2/90°_4]_{3s}$ Laminate

The comparison of experimentally and numerically obtained $\gamma_{\theta z}$ distributions for the 90°, 75°, 60°, and 15° angular locations are shown in Figures 4.14-4.17. Again, the match between the moiré and SVELT strain distributions is very close. Small details predicted by SVELT are also found in the moiré data. For example, the downward cupping of the moiré strain distributions in the 90° plies at the left of Figures 4.14 and 4.15 is mimicked accurately by the SVELT data. At the 15° angular location, the sharp details predicted by SVELT are generally not visible in the moiré strain data. This is not surprising considering the sparseness of the displacement fringe data available for analysis at this location. The general match at this location, however, is quite close. The slightly refined SVELT model did not significantly change the predicted behavior of $\gamma_{\theta z}$.

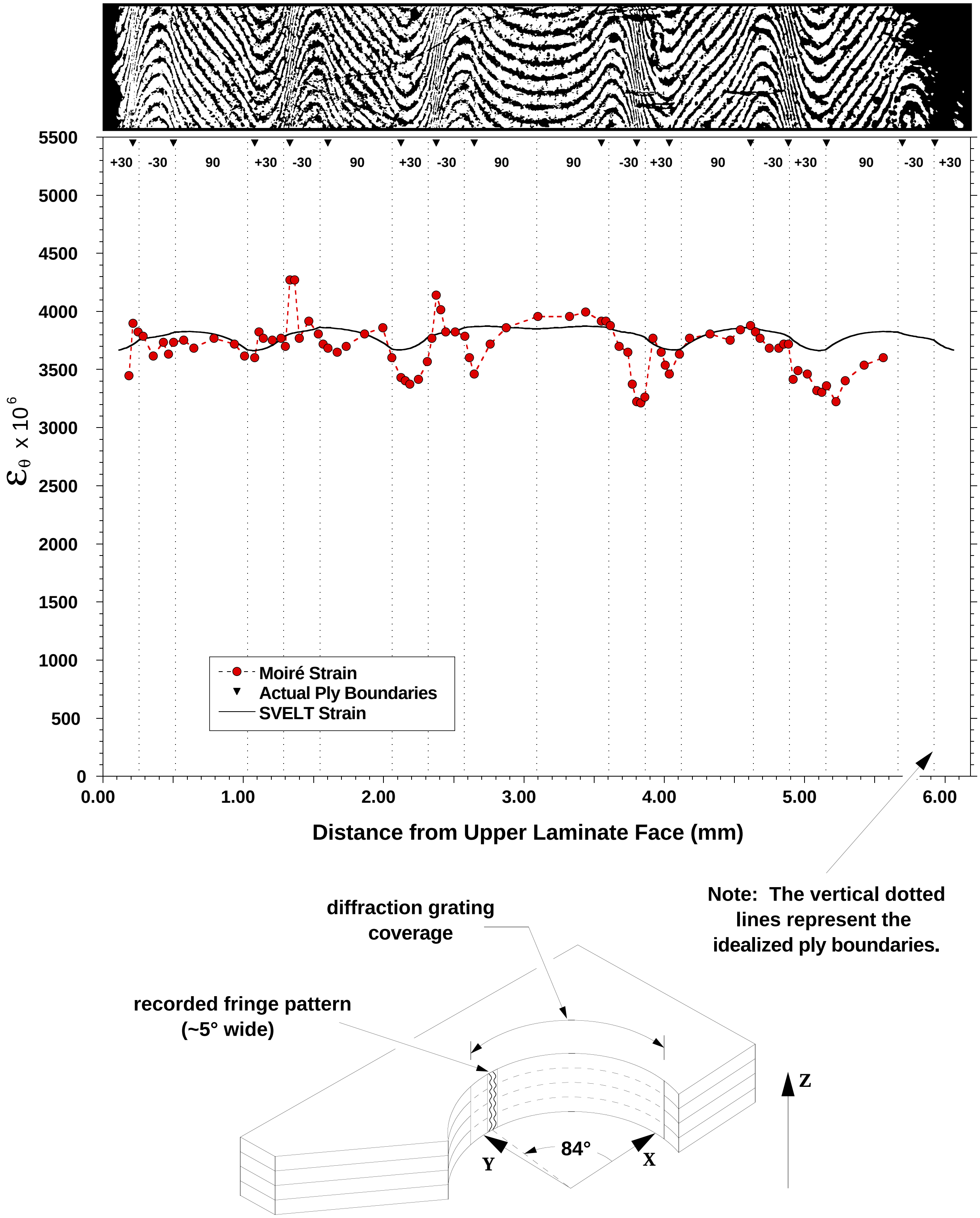

Figure 4.9: Circumferential strain comparison at 84° for the $[+30_2/-30_2/90_4]_{3s}$ laminate.

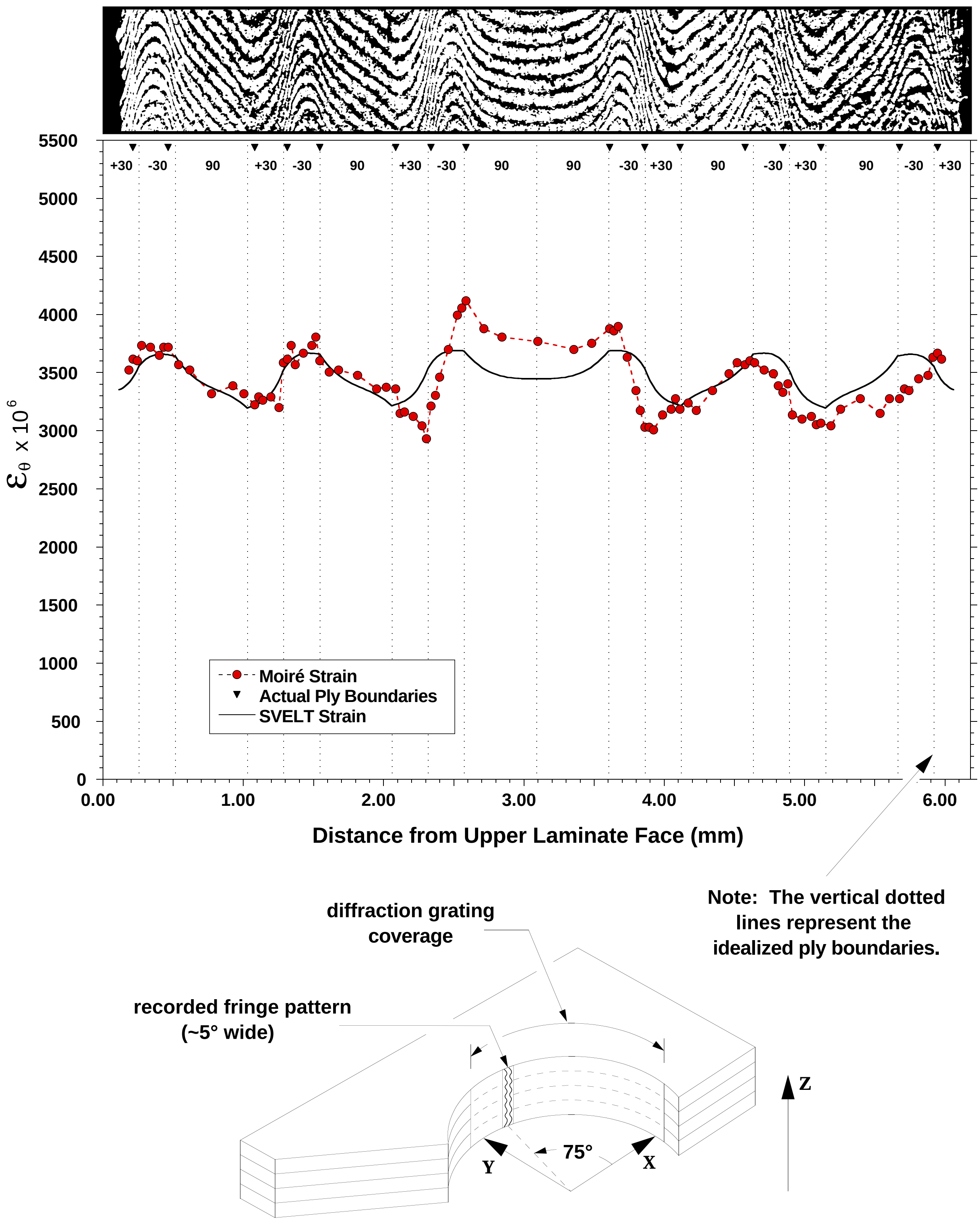

Figure 4.10: Circumferential strain comparison at 75° for the $[+30_2/-30_2/90_4]_{3s}$ laminate.

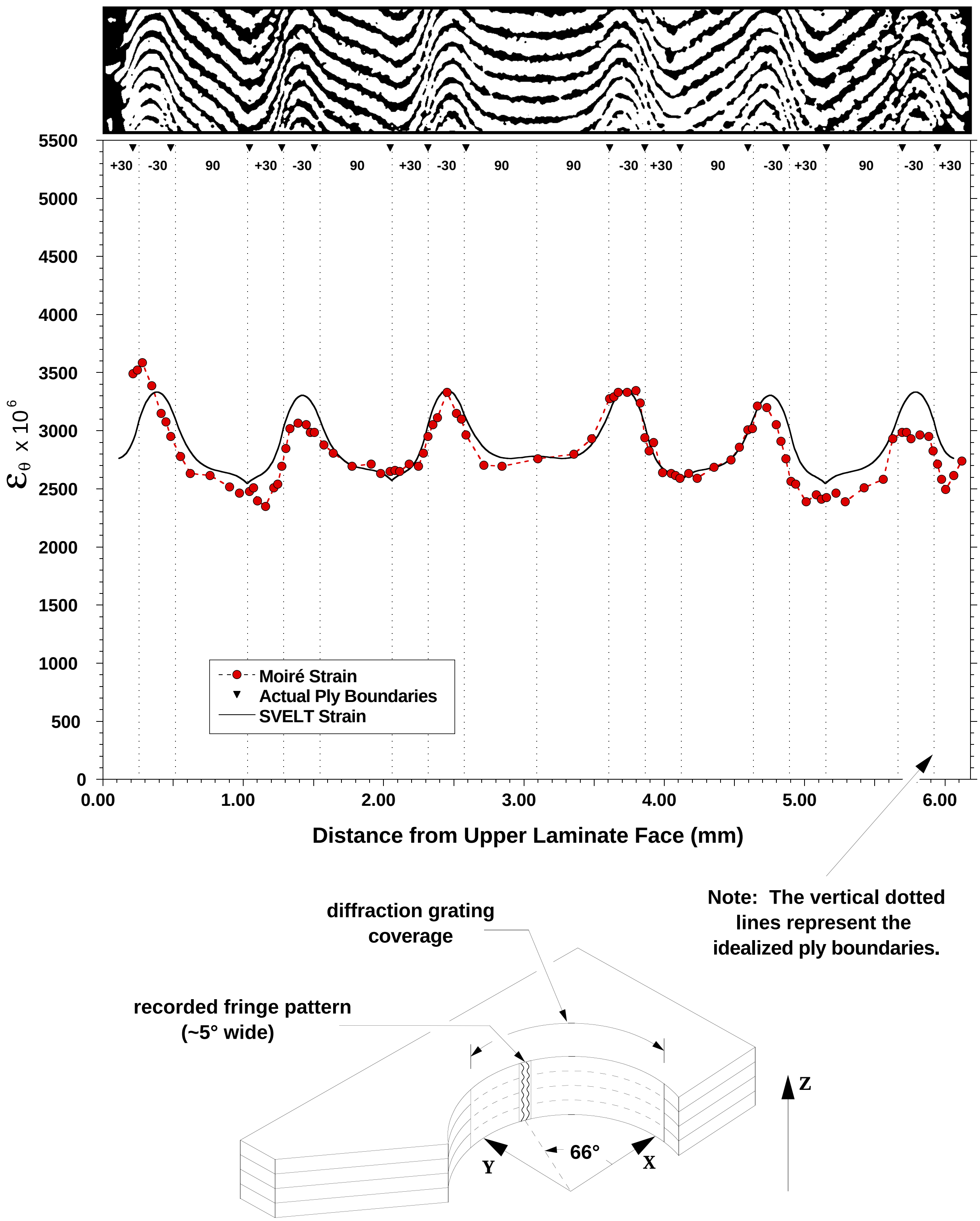

Figure 4.11: Circumferential strain comparison at 66° for the $[+30_2/-30_2/90_4]_{3s}$ laminate.

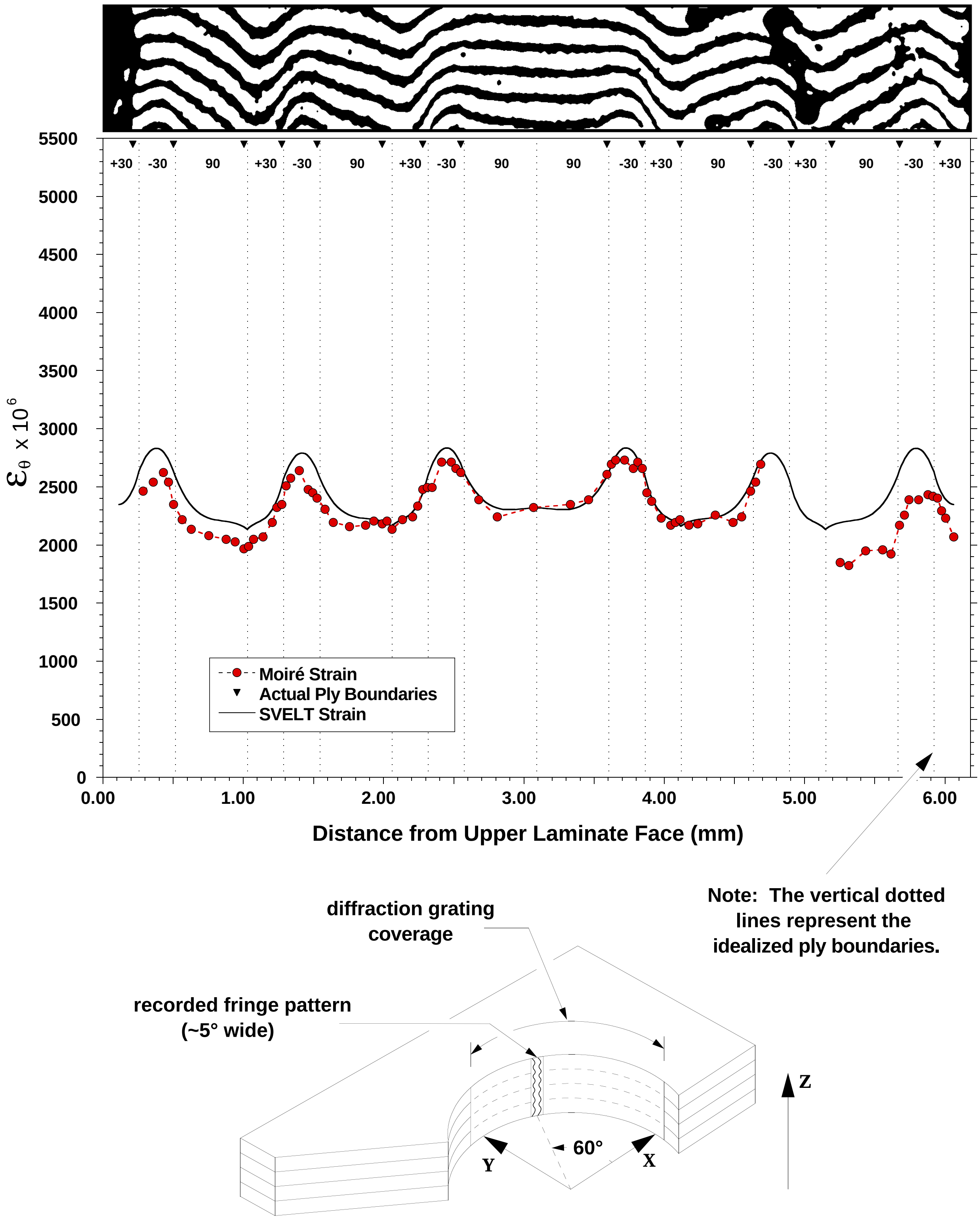

Figure 4.12: Circumferential strain comparison at 60° for the $[+30_2/-30_2/90_4]_{3s}$ laminate.

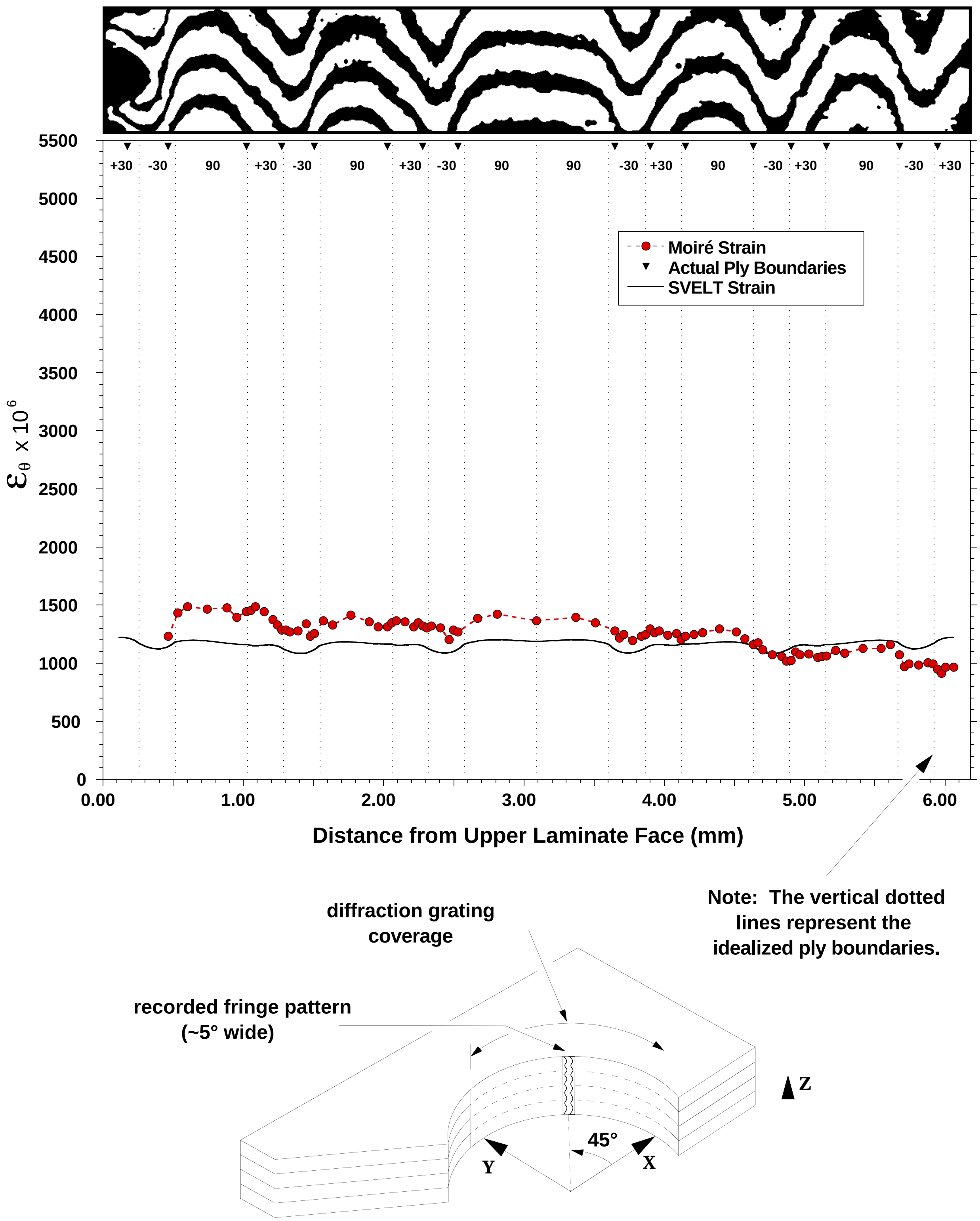

Figure 4.13: Circumferential strain comparison at 45° for the $[+30_2/-30_2/90_4]_{3s}$ laminate.

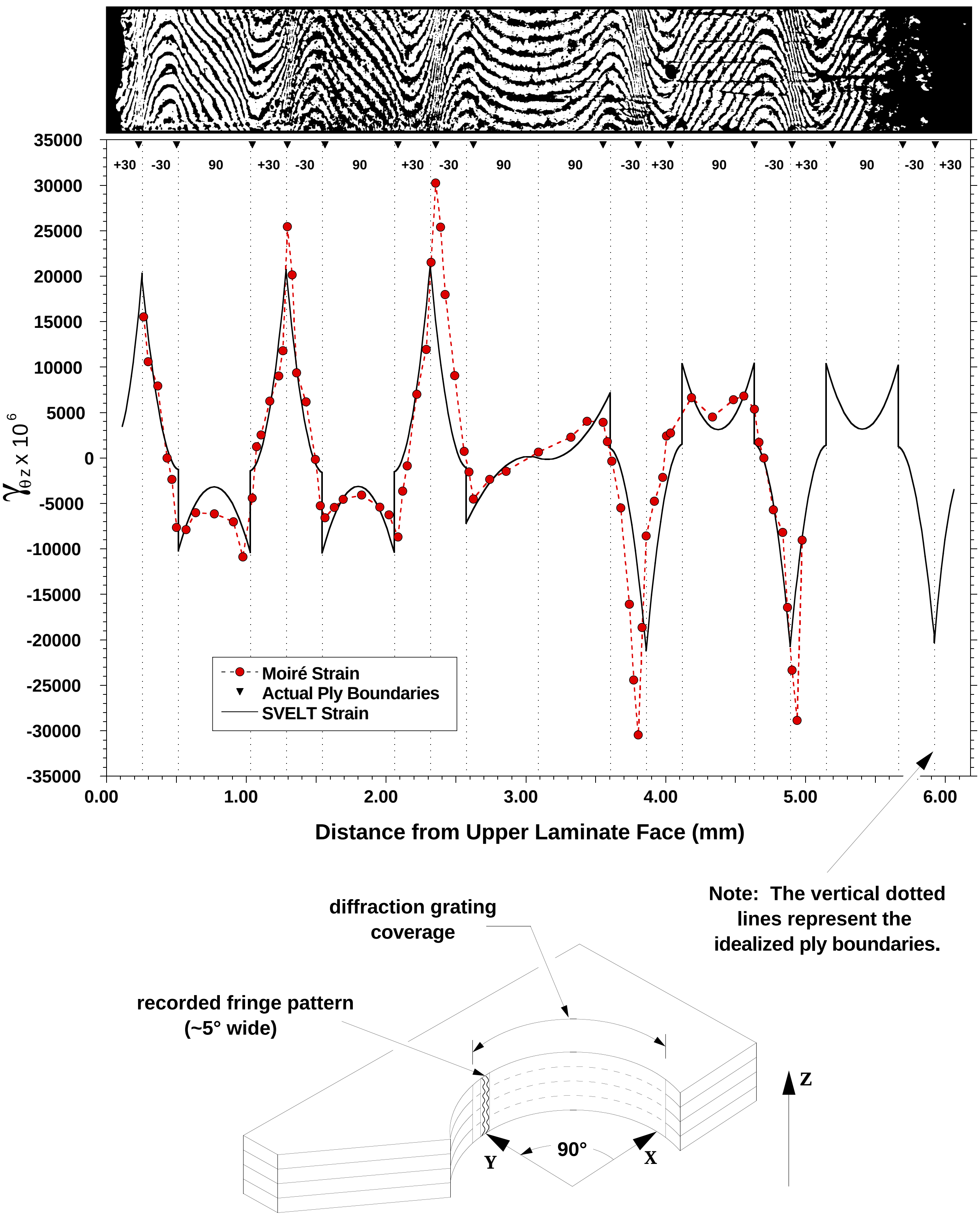

Figure 4.14: Theta-Z shear strain comparison at 90° for the $[+30_2/-30_2/90_4]_{3s}$ laminate (note: shear strain calculated from U_θ pattern only).

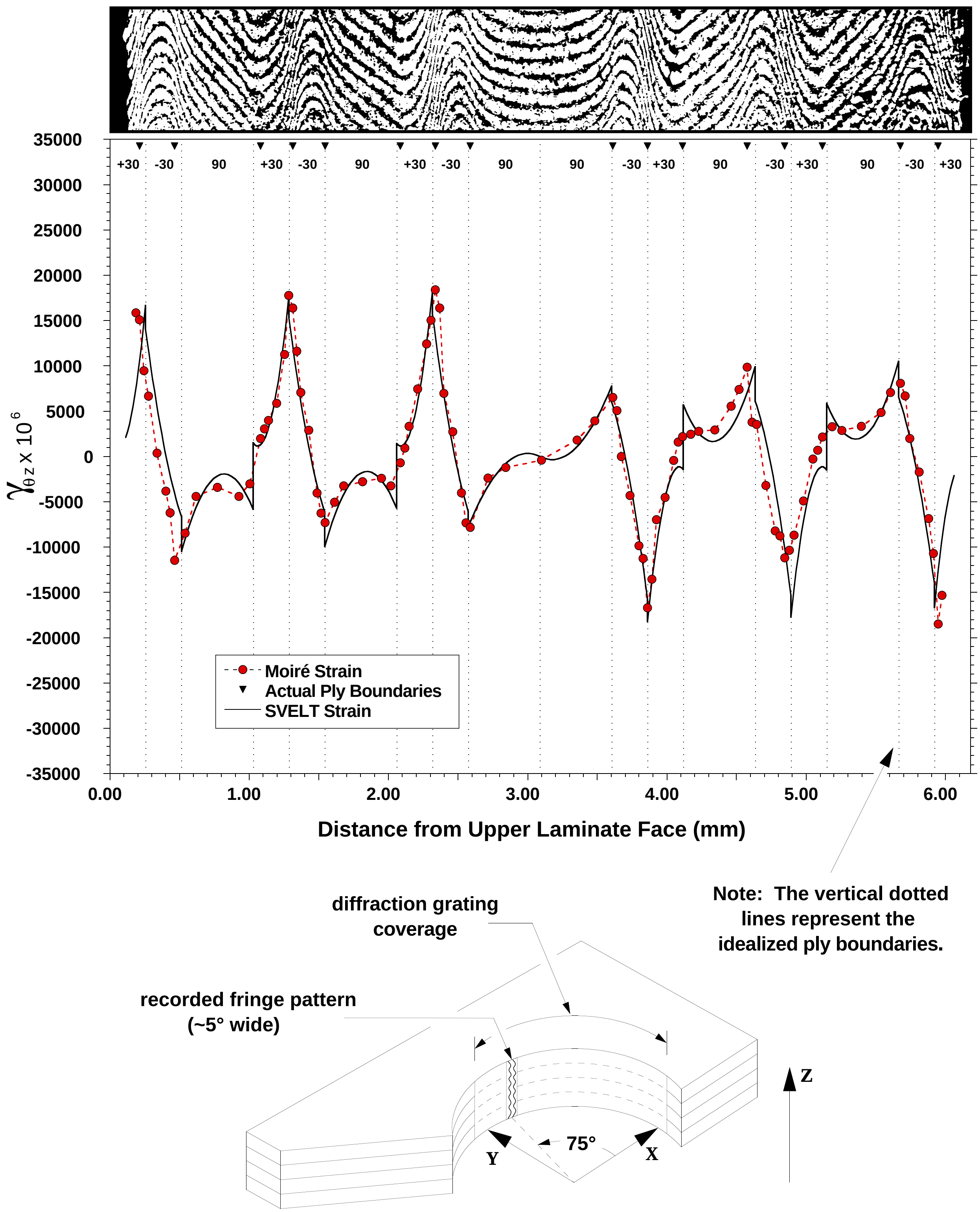

Figure 4.15: Theta-Z shear strain comparison at 75° for the $[+30_2/-30_2/90_4]_{3s}$ laminate (note: shear strain calculated from U_θ pattern only).

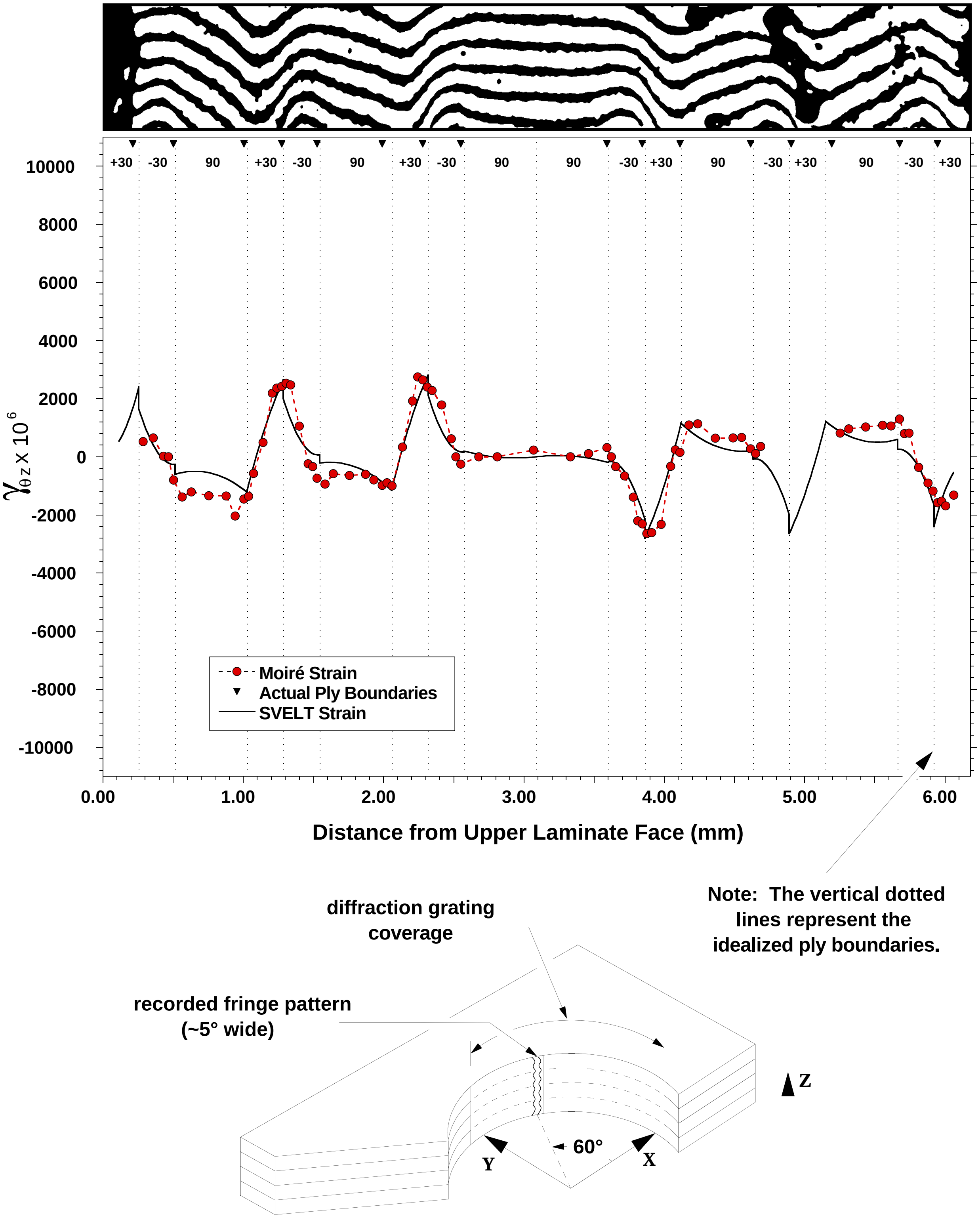

Figure 4.16: Theta-Z shear strain comparison at 60° for the $[+30_2/-30_2/90_4]_{3s}$ laminate (note: shear strain calculated from U_θ pattern only).

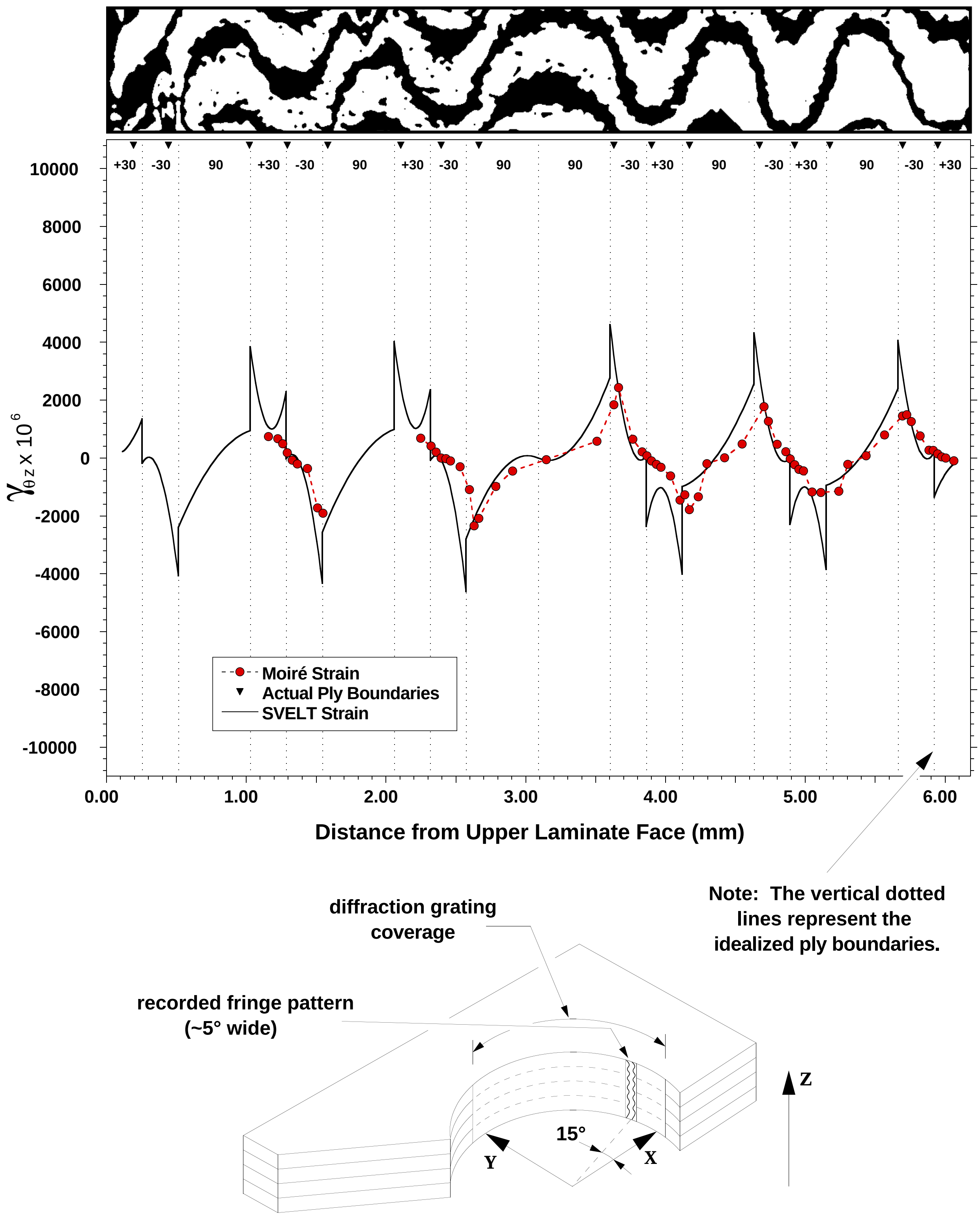

Figure 4.17: Theta-Z shear strain comparison at 15° for the $[+30_2/-30_2/90_4]_{3s}$ laminate (note: shear strain calculated from U_θ pattern only).

ε_z for the $[+30°_2/-30°_2/90°_4]_{3s}$ Laminate

The experimentally and numerically obtained ε_z distributions for the 84°, 75°, 66°, and 60° angular locations are shown in Figures 4.18-4.21. Comparison of the SVELT and moiré strain distributions shows that the trends generally match well. The magnitudes, however, do not match as closely as the other components of strain compared previously. The predicted tensile and compressive peak values of strain are lower in magnitude than those measured using moiré interferometry. The local shapes of the predicted distributions are not quite the same as the measured distributions. For example, the moiré data generally predicts the distributions of ε_z in the 90° plies to be somewhat bowl shaped as shown in Figures 4.18 and 4.19. The SVELT analysis predicts these locations to have a slightly hill shaped distribution of ε_z. The slightly refined SVELT model with two sub-layers per ply grouping tends to correct this trend as shown in the distribution of ε_z in Figure 4.22 for the 75° angular location.

The refined model, however, does not correct the magnitude discrepancy. There are possible causes of this discrepancy. The model is likely in need of further mesh refinement. Both models constructed for this research were considered to have coarse in-plane and out-of-plane meshes. Another modeling-related problem could result from the use of incorrect material constants. The out-of-plane stiffness was assumed to be the same as the in-plane transverse stiffness. If there is a significant difference in the actual and modeled out-of-plane stiffness, the resulting distributions of ε_z could differ significantly.

Interestingly, the SVELT data does predict the large-scale trend visible in the moiré data. Although not as pronounced as in the moiré data, the SVELT strain distributions do show that the outer ply groupings exhibit generally more tensile behavior than the interior ply groupings for the angular locations shown.

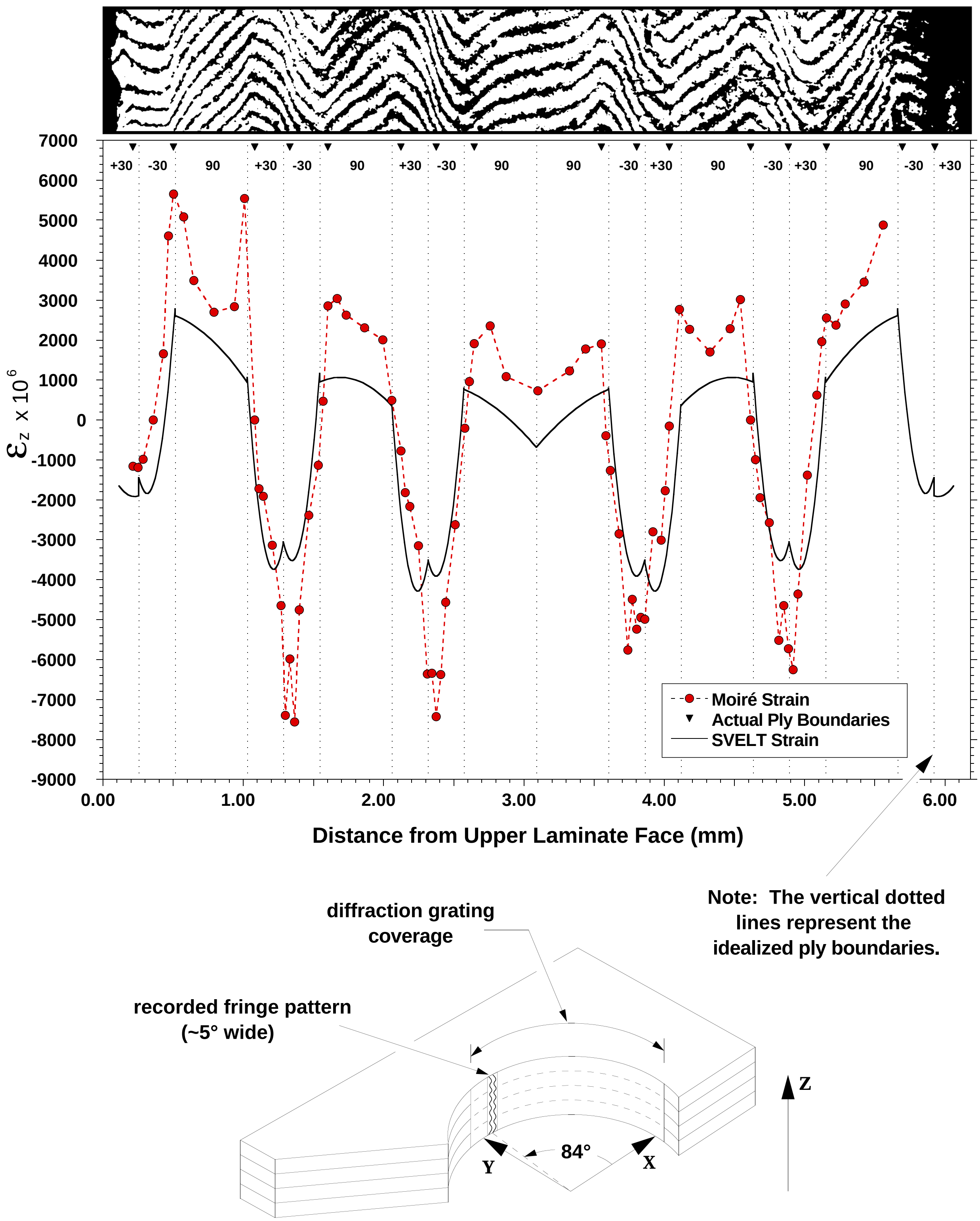

Figure 4.18: Z-direction strain comparison at 84° for the $[+30_2/-30_2/90_4]_{3s}$ laminate (note: the U_z fringe pattern contains a carrier of rotation).

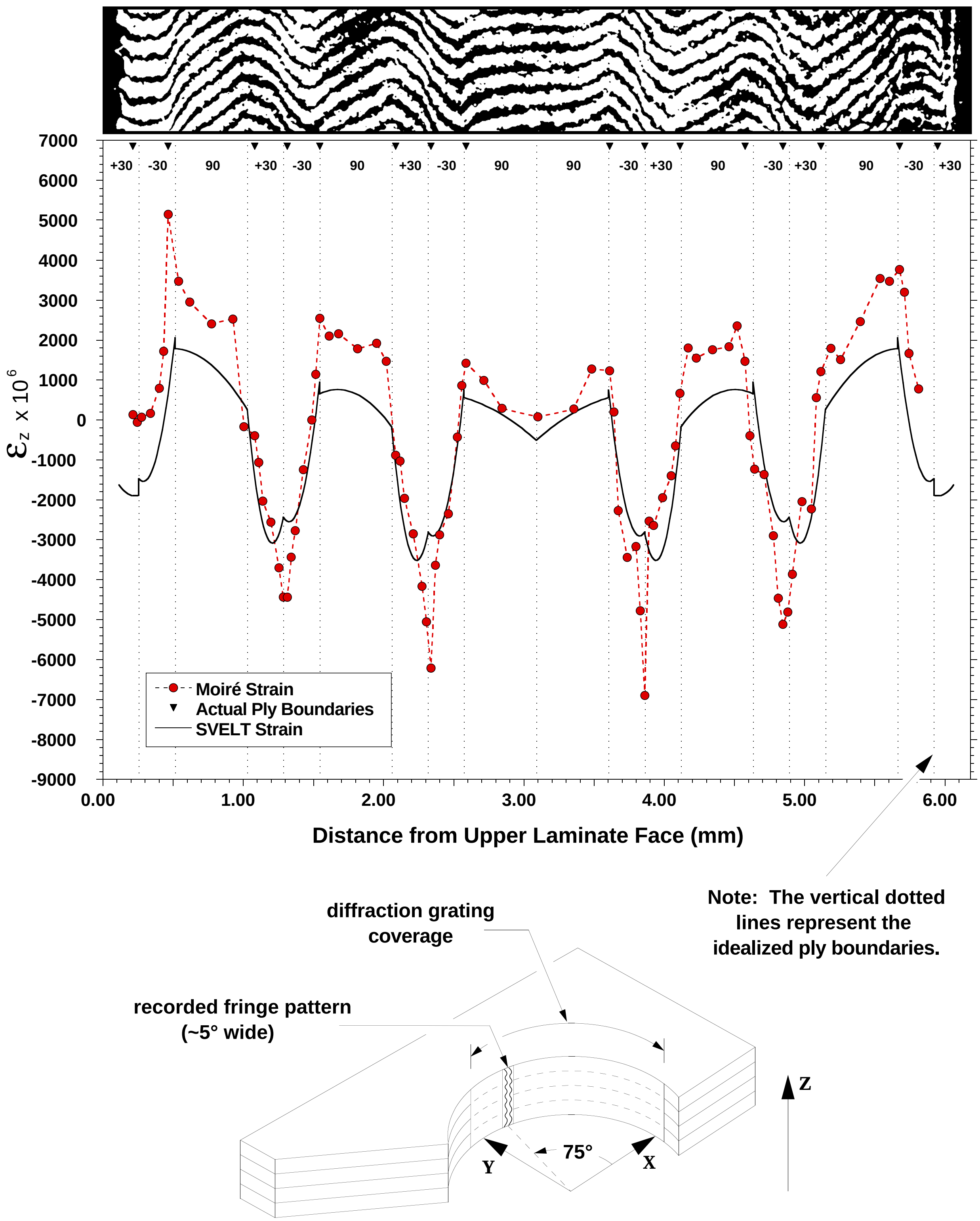

Figure 4.19: Z-direction strain comparison at 75° for the $[+30_2/-30_2/90_4]_{3s}$ laminate (note: the U_z fringe pattern contains a carrier of rotation).

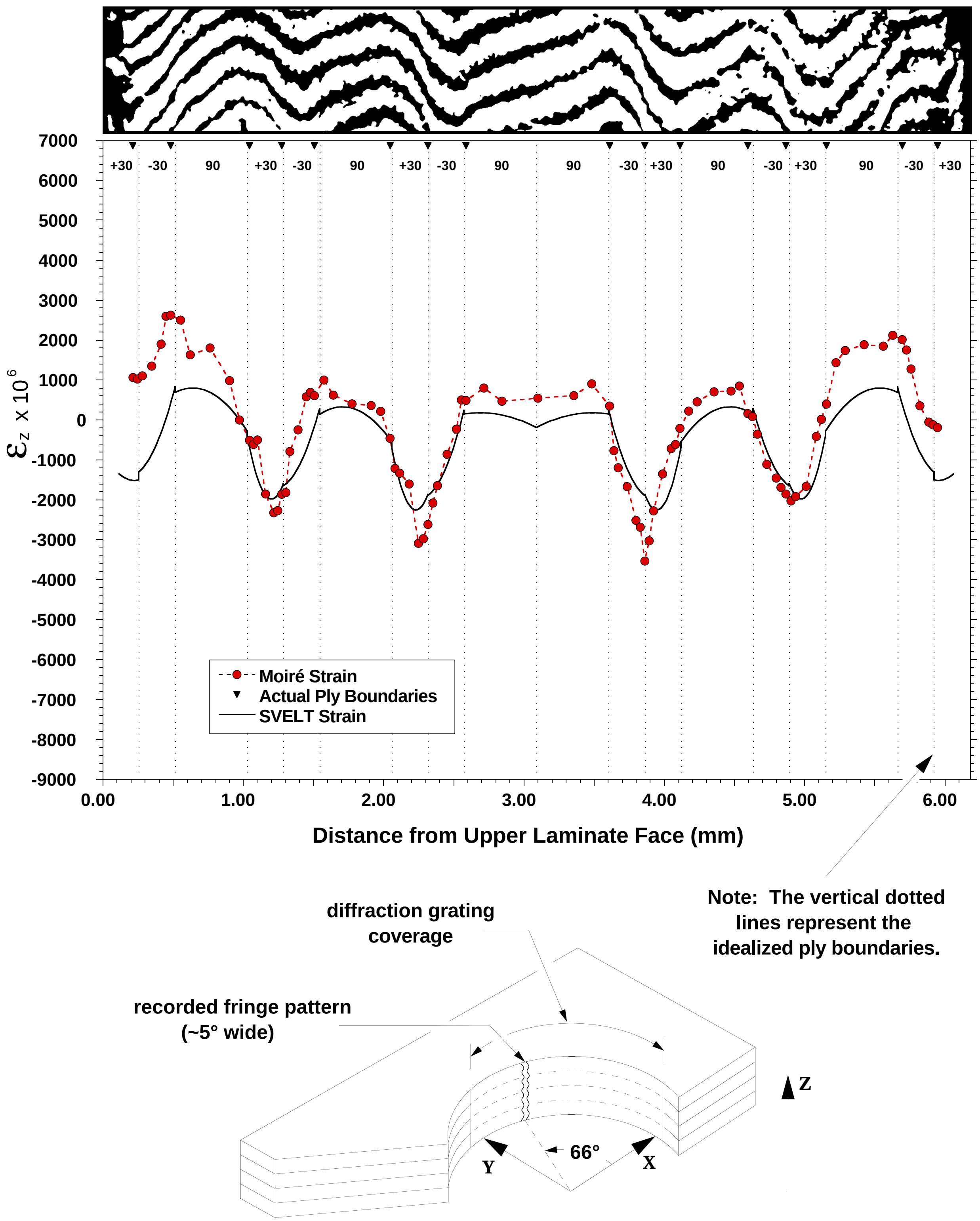

Figure 4.20: Z-direction strain comparison at 66° for the $[+30_2/-30_2/90_4]_{3s}$ laminate (note: the U_z fringe pattern contains a carrier of rotation).

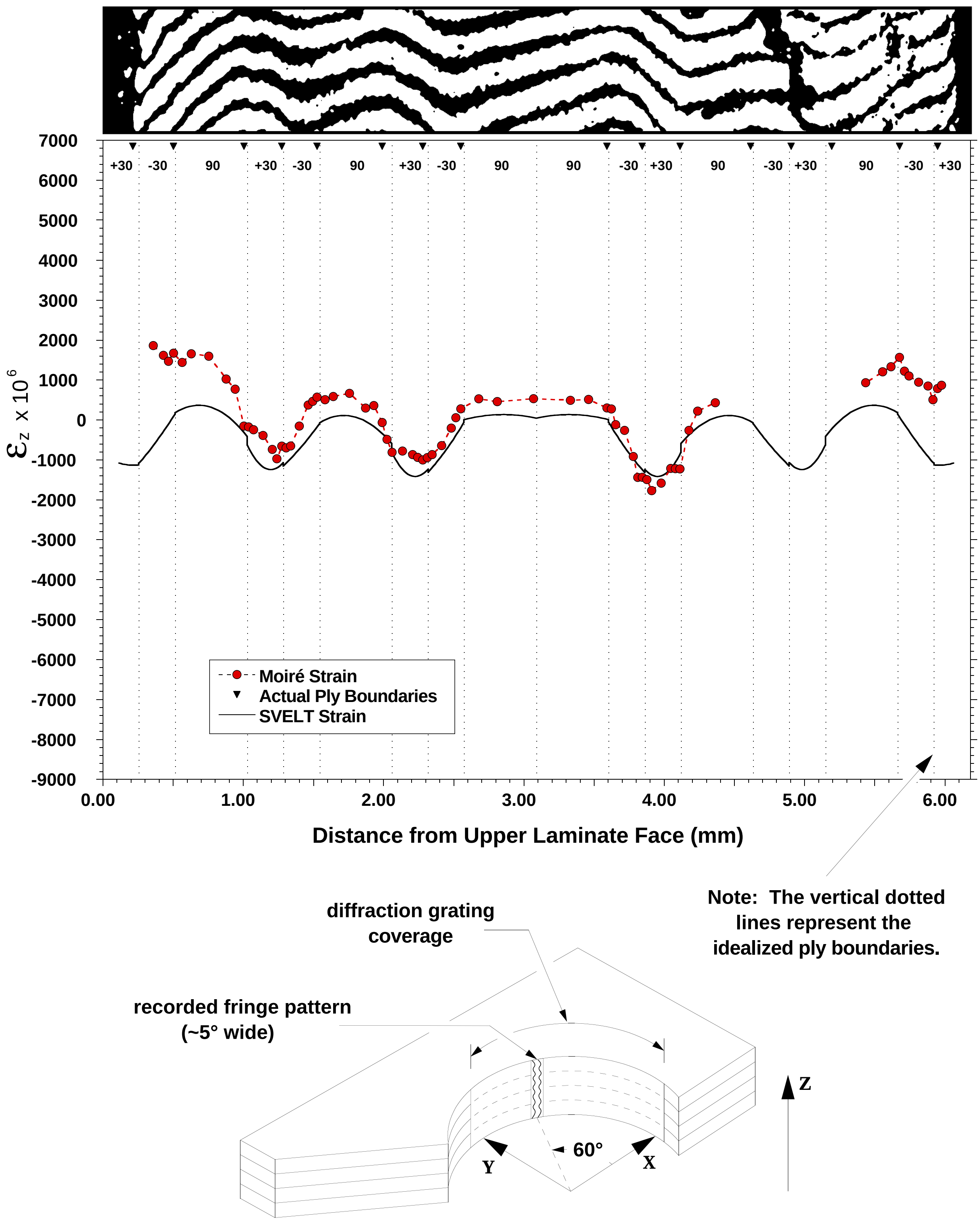

Figure 4.21: Z-direction strain comparison at 60° for the $[+30_2/-30_2/90_4]_{3s}$ laminate (note: the U_z fringe pattern contains a carrier of rotation).

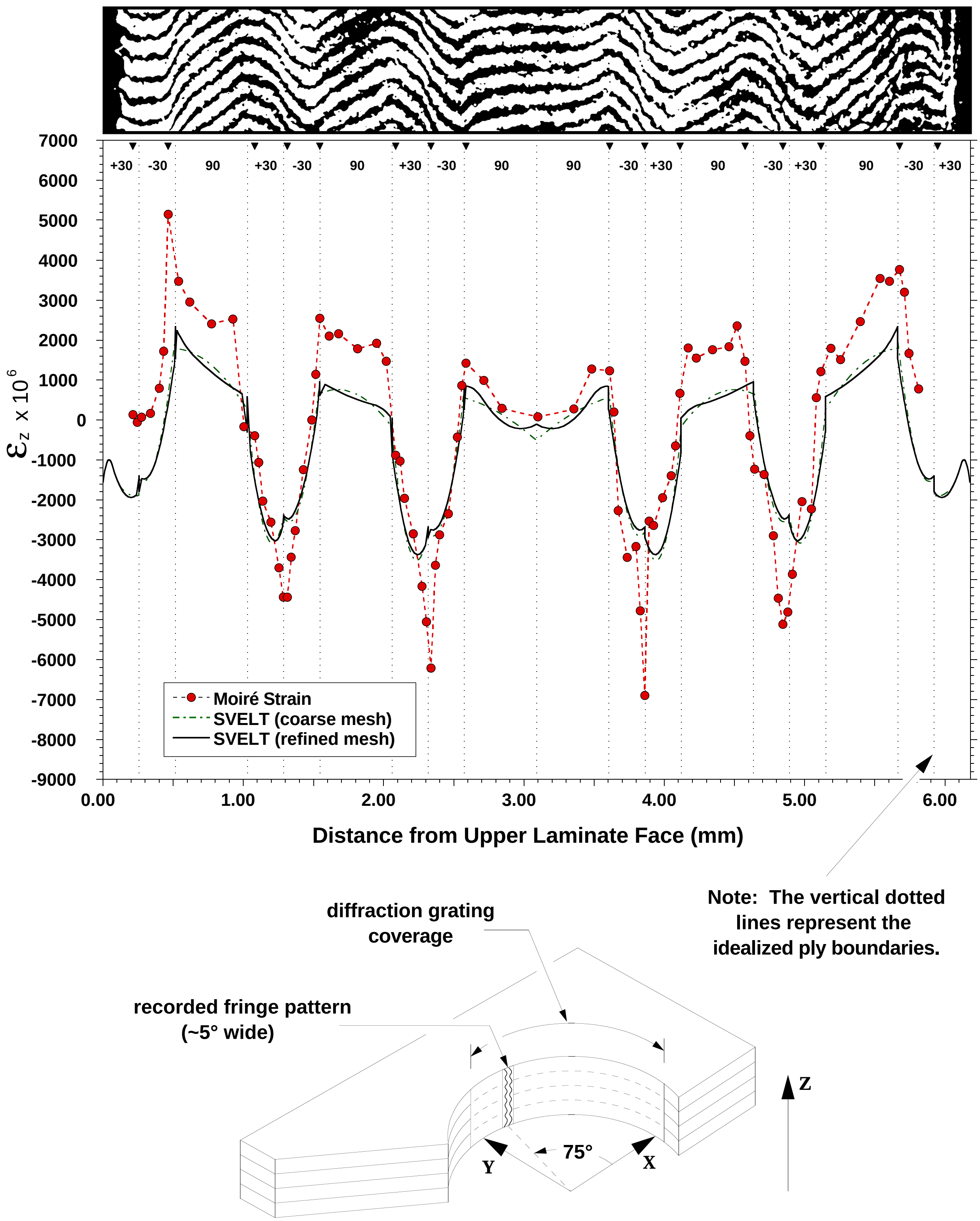

Figure 4.22: Z-direction strain comparison at 75° for the $[+30_2/-30_2/90_4]_{3s}$ laminate using two SVELT mesh refinements to obtain the numerical data (note: the U_z fringe pattern contains a carrier of rotation).

Chapter 5: Conclusions and Further Research

5.1 Conclusions

5.1.1 Summary

Moiré interferometry techniques were developed to measure the deformation on a portion of the cylindrical face of a hole in a loaded specimen. These techniques were applied to one aluminum and two composite specimens with open holes. The aluminum specimen was fabricated from 7075-T6 aluminum. Both composite specimens where fabricated from IM7/5250-4 pre-preg with ply lay-ups of $[0°_4/90°_4]_{3s}$ and $[+30°_2/-30°_2/90°_4]_{3s}$, respectively. New moiré techniques were developed and evaluated using the aluminum specimen. Distributions of displacements and strain were obtained with high confidence on a sub-ply basis at select angular locations from the composites. Measured strain behavior was complex and displayed ply-by-ply trends. Larger scale trends associated with the location of a ply with respect to the mid-plane were also documented. Viscoelastic shearing strains were observed.

The nature of the strain distributions were explained with analogy to two-dimensional lamina behavior. Analogues were made between the observed behavior and the behavior of tensile-loaded lamina at a straight edge or the behavior of tensile-loaded lamina containing open holes. The measured strains were compared with the three-dimensional analysis technique known as Spline Variational Elastic Laminate Technology (SVELT) and corroborated the usefulness of SVELT.

5.1.2 Contributions to the Experimental Technique

The main contributions of this work are three-fold. First, diffraction grating replication techniques were introduced such that the grating was applied to the specimen using a machined steel circular sector and square plate combination. Replicas of the deformed specimen diffraction grating were also produced using the same methods. Advantages of this method include the ability to carefully align the plate and sector combination with the specimen and to control the amount of pressure applied during the replication process. Another advantage with this method is that the deformed replicas of the specimen diffraction gratings are attached to a dimensionally stable steel substrate, and these gratings can be interrogated in a moiré interferometer at a later time.

The second contribution concerns the use of phase-shifting analysis in conjunction with fringe pattern recording using a CCD camera. This type of digital analysis proved extremely useful when large quantities of data were desired, such as for the 2° incremental study of $\gamma_{\theta z}$ from 56° to 64°. Phase-shifting analysis also proved essential in evaluating the viscoelastic deformation over a portion of the hole surface at 87° in the $[+30°_2/-30°_2/90°_4]_{3s}$ specimen. For analysis of the general components of strain caused by loading, however, the use of phase-shifting proved difficult to implement.

The third and most important contribution of this research is that a method of directly examining the replicated curved diffraction gratings using moiré interferometry was explored and implemented. The method of viewing discrete angular sections within an interferometer eliminates all difficulties associated with the nonuniformity of diffraction grating thickness on steel shims and the associated unknown additions to circumferential strain. Errors caused by variations in shim grating thickness or by out-of-plane rotation effects were estimated to be less than 60 $\mu\varepsilon$. The marvelous fringe pattern mosaics presented in Figures 3.4-3.5 and Figures 3.17-3.19 demonstrate how these discrete data can be used to create an almost visually continuous fringe pattern around a quadrant of a hole. Thus, changes from angular location to angular location can be easily detected and investigated. The discrete angular section method proved simple and robust to use. It was possible to determine, with high confidence, the angular location being photographed. The usefulness of applying different carriers of rotation and/or extension can be explored at the convenience of the researcher. The method holds great promise for applications involving measurements on any singly curved surface.

5.1.3 Specific Observations and Conclusions

Specific observations and conclusions associated with the accomplished research are contained in the following paragraphs.

The aluminum specimen was used to investigate and verify new moiré techniques. Experimental strain results on the flat face and cylindrical hole surface were compared with strain results from an elasticity solution. Correlation of the experimental and analytical results on the flat face and the cylindrical hole surface was very close, imparting confidence in the moiré methods developed in this research.

Variations in the ply-by-ply distributions of ε_θ at specific angular locations for both composites were documented. This behavior is contrary to the behavior of the strain on the straight edge of a composite where ε_x is constant. Similar behavior was reported in Boeman (1991). When compared with the far-field axial strain, concentrations of up to 6.0 in ε_θ were found.

It was observed in this research that the general ply-by-ply behavior of ε_θ could be estimated by examining the behavior of tensile-loaded unconstrained laminae with holes. Plies demonstrating higher strain than neighboring plies would, as unconstrained laminae, also have a correspondingly higher strain concentration. The lessening of ply constraints in the vicinity of a free edge is believed to be responsible for this behavior. That is, plies would be able to behave more like unconstrained laminae in the region near an edge than deep in the bulk composite. Also, since the laminates examined in this research were thick, the corresponding free-edge boundary layer was relatively deep.

Very large ply-by-ply variations in shear were documented in both composite specimens. Values of up to 30 times the far-field axial strain were found at the interfaces between some neighboring plies. The observed behavior was explained by comparing the $\eta_{xy,x}$ values (calculated from hypothetical laminates cut tangent to the location of interest) associated with neighboring plies. The larger the difference between $\eta_{xy,x}$ values, the larger the value of $\gamma_{\theta z}$ found at their mutual interface. As discussed in Chapter 1, many authors have suggested that γ_{xz} could be singular at a straight free edge for laminates with mismatches in $\eta_{xy,x}$. The large $\gamma_{\theta z}$ results presented in the present research support the prediction of singular behavior between plies with large mismatches in $\eta_{xy,x}$.

Amazing levels of detail were visible in the distributions of shear strain. For example, the peak values of $\gamma_{\theta z}$ were broader in the $[+30°_2/-30°_2/90°_4]_{3s}$ specimen than in the $[0°_4/90°_4]_{3s}$ specimen. Also, the phase-shifting analysis of the angular region from 56°-64° of the $[+30°_2/-30°_2/90°_4]_{3s}$ specimen revealed shear behavioral trends related to the angular position around the periphery of the hole. For these particular angular locations, it was documented that at some ply locations the shear strain remained essentially constant with changing angular position. At other locations (often only 0.1 mm away from the constant shear positions), it was found that large peaks rapidly degraded with angular position.

The large values of $\gamma_{\theta z}$ found at some of the ply interfaces is believed to be responsible for viscoelastic deformation. Large shearing deformations were observed at zero load in both previously loaded specimens. The locations of these deformations exactly corresponded with the locations of the highest recorded $\gamma_{\theta z}$. Later attempts to verify the continued existence of these deformations demonstrated that they had mostly crept back to the original undeformed state. However, mysterious small deformations, probably caused by moisture absorption, have confused any definite conclusions about the nature of the observed viscoelastic deformations. It is believed that these deformations actually were mostly temporary and that the supposed moisture-induced deformation is a separate issue.

Large variations of ε_z were observed in the $[+30°_2/-30°_2/90°_4]_{3s}$ specimen. At some locations, the compressive magnitudes of ε_z were found to be approximately twice the local values of ε_θ, and the tensile magnitudes of ε_z were found to be approximately equal to the local ε_θ values. The observed behavior was approximately explained by comparing the ν_{xy} values (calculated from hypothetical laminates cut tangent to the location of interest) associated with neighboring plies. The large values of ν_{xy} in the +30° and -30° plies, when compared with the small ν_{xy} of the 90° plies, resulted in tensile ε_z in the 90° ply groupings and compressive ε_z in the ±30° ply groupings for the angular locations examined.

A larger scale variation in the behavior of ε_z on the cylindrical surface of the hole of the $[+30°_2/-30°_2/90°_4]_{3s}$ specimen was also documented. The values of ε_z in the plies near the laminate faces were more tensile than the values of ε_z in corresponding plies near the laminate mid-plane. It is believed that the lower constraint of the outer ±30° ply groupings caused these groupings to be placed in a less compressive state than interior ±30° ply groupings. This resulted in the neighboring 90° ply groupings being subjected to greater tension than interior 90° plies.

The noisy nature of the strain distributions calculated from the fringe patterns probably resulted from a combination of things. Fringe analysis errors certainly existed. Errors caused by grating and optical problems also existed. Much of the noise, however, is believed to be an accurate measure of the true material behavior. This statement accents the highly variable nature of fiber-reinforced composites. Variations in composite materials are pronounced at many geometric scales. The composites studied in this research had variations in fiber volume fraction on a fiber level. They probably contained variations in the fiber alignment as well. Ply-level material variability was also evidenced by the easily visible ply waviness. Strains were calculated using a gage length of at least 50 times the diameter of a fiber, so it is unlikely that variations in strain around individual fibers contributed to the variability in the measured strain distributions. However, larger variations in the fiber volume or fiber alignment could have contributed to the roughness of the measured strain distributions.

The correlation between moiré strain results and SVELT strain results was very close. The match between the ε_θ and $\gamma_{\theta z}$ components of strain from both composite lay-ups was extraordinarily close in magnitude and distribution shape. Aside from reasonably low levels of noise and random differences, there appeared to be no consistently occurring difference between the actual and predicted distributions of ε_θ and $\gamma_{\theta z}$. The correlation between the moiré and SVELT strain distributions of ε_z were not as close as for the other strain components. The distribution shapes compared well, but the magnitudes predicted by SVELT were consistently lower than the moiré measurements. Possible explanations include the use of an insufficiently refined modeling mesh or the use of improper out-of-plane properties in the model. The SVELT analysis, however, did predict the large-scale variation in the distribution of ε_z discussed previously.

5.2 Recommendations for Further Research

5.2.1 Improvements in the Replication Techniques

The replication techniques used in this research could benefit from additional refinement. Of particular importance is further research into ideal replicating adhesives. For replicating to a specimen (or onto the initial shim), the ideal adhesive would need to have low viscosity, good adhesion, low shrinkage, and high hardness. It also must be able to replicate a grating without entraining bubbles. Many of the flaws in the gratings used in this research are caused by bubbles. As mentioned in Appendix A, extraordinary efforts were taken to eliminate all bubbling, but very small bubbles often appeared in the cured gratings. This was particularly true for very thin gratings.

The ideal resin for replication of the deformed specimen gratings would need to have several attributes. It would need to have low shrinkage for accurate grating replication, it would need a short cure time to minimize viscoelastic effects, and it must be coatable with a metallic coating for enhanced reflectivity. The ideal resin would also have selective adhesion. The adhesion of the resin to the machined sector must be sufficient to allow for clean separation from the specimen grating. The adhesion to the specimen grating must be sufficiently poor to allow for separation without damage. This ideal adhesive must also cure reliably. The RTV silicon rubbers used in this research did not always cure correctly, resulting in ruined tests and longer loading periods.

Another change that could result in a superior technique would be the abandonment of the square steel replication plate. Using this plate during replication of the grating to the specimen worked flawlessly. However, replicating the deformed specimen grating using RTV-615 resulted in slight tearing of the sector replica grating at the edge adjacent to the steel plate. The quality of the fringe patterns obtained from the replicas of the flat face gratings were inferior to those that could be obtained using typical moiré interferometry procedures. It is felt that the implementation of the entire replication process would be more robust if the square steel replication plate were eliminated from the procedure.

5.2.2 Additional Recommendations

Several additional areas of future research would enhance the information gained in this research. These include the following:

- A thorough study of the repeatability of these measurements is necessary to completely verify the robustness of the technique.
- An examination of the linearity or nonlinearity of the strain versus load behavior of various composites would be of great interest.
- Measurement of the strain behavior in composites up to and past failure initiation is also extremely important for the prediction of ultimate strength of a composite structure with at hole.
- An investigation into the causes of the discrepancy in the magnitudes of ε_z measured by moiré and predicted by SVELT is necessary to enhance the confidence in each technique.
- An investigation into the effects of moisture absorption on the ply-level strain state in a composite would be extremely important to the modeling and design communities. It could also answer the questions concerning the mysterious deformation documented in this research.
- A careful examination into the viscoelastic deformations observed in this research could also be of great use to the modeling and design communities.
- Research into the sources of noise mentioned previously would be invaluable. The geometric scale over which a measurement (using the techniques described in this research) was valid could possibly be determined. If required, further enhancements to the techniques could be investigated in order to improve the level of spatial resolution and displacement sensitivity.
- Averaging the recorded distributions of strain from each side of the mid-plane may address some of the noise and anomalous behavior presented in this research. An investigation into this type of averaging is recommended.

References

Altus, E., A. Rotem, and M. Shmueli, 1980, "Free-Edge Effects in Angle Ply Laminates: A New Three Dimensional Finite Difference Solution," *Journal of Composite Materials*, Vol. 14, pp. 21-30.

Asundi, A. and F. Yang, 1993, "Moire Interferometry Strain Analysis Using FFT Technique for Fiber Reinforced Composite Laminates With Hole," *ICCM/9. Composites: Properties and Applications*, Madrid, Spain, University of Zaragoza, Vol. 6, pp. 874-881.

Barboni, R., R. Carbonaro, and P. Gaudenzi, 1995, "On the use of a Multilayer Higher-Order Theory for the Stress Analysis Around a Circular Hole of Laminates Under Tension," *Composite Structures*, Vol. 32, pp. 649-658.

Boeman, R., 1991, "Interlaminar Deformations on the Cylindrical Surface of a Hole in Laminated Composites: An Experimental Study," Center for Composite Materials and Structures Report No. CCMS-91-07, Virginia Polytechnic Institute and State University.

Bogdanovich, A. and E. Iarve, 1992, "Numerical Analysis of Impact Deformation and Failure in Composite Plates," *Journal of Composite Materials*, Vol. 26, No. 4, pp. 520-545.

Bogdanovich, A. and E. Yarve, 1983, "Stress Analysis in Multilayered Beams Under Transverse Dynamic Bending," *Mechanics of Composite Materials*, Vol. 19, pp. 604-616 (translated from Russian by Consultants Bureau, New York, March, 1984).

Bogdanovich, A. and E. Yarve, 1988, "Numerical Solution of Two-Dimensional Problem of Non-Steady Deformation of Laminated Media," *Mechanics of Composite Materials*, Vol. 24, pp. 31-38 (translated from Russian by Consultants Bureau, New York, July, 1988).

Bogdanovich, A. and E. Yarve, 1989, "Numerical Analysis of the Impact Deformation of Plates Made of Composites," *Mechanics of Composite Material*s, Vol. 25, pp. 586-599 (translated from Russian by Consultants Bureau, New York, March, 1990).

Bone, D., H. Bachor, and J. Sandeman, 1986, "Fringe-Pattern Analysis Using a 2-D Fourier Transform," *Applied Optics*, Vol. 25, No. 10, pp. 1653-1660.

Carlsson, L., 1983, "Interlaminar Stresses at a Hole in a Composite Member Subjected to In-Plane Loading," *Journal of Composite Materials*, Vol. 17, pp. 238-249.

Creath, K., 1988, "Phase-Measurement Interferometry Techniques," *Progress in Optics*, Vol. 26, pp. 350-393.

Dai, F., J. McKelvie, and D. Post, 1990, "An Interpretation of Moiré Interferometry from Wavefront Interface Theory," *Optics and Lasers in Engineering*, Vol. 12, pp. 1-18.

Dally, J. and W. Riley, 1965, <u>Experimental Stress Analysis</u>, McGraw-Hill, New York.

Daniel, I., R. Rowlands, and J. Whiteside, 1974, "Effects of Material and Stacking Sequence on Behavior of Composite Plates with Holes," *Experimental Mechanics*, Vol. 14, No. 1, pp. 1-9.

Dong, S. and D. Goetschel, 1982, "Edge Effects in Laminated Composite Plates," *Journal of Applied Mechanics*, Vol. 49, pp. 129-135.

Durelli, A. and V. Parks, 1970, <u>Moiré Analysis of Strain</u>, Prentice-Hall, Englewood Cliffs, New Jersey.

El-Zein, M. and K. Reifsnider, 1990, "The Strength Prediction of Composite Laminates Containing a Circular Hole," *Journal of Composites Technology & Research*, Vol. 12, No. 1, pp. 24-30.

Folias, E., 1992, "Boundary Layer Effects of Interlaminar Stresses Adjacent to a Hole in a Laminated Composite Plate," *International Journal of Solids and Structures*, Vol. 29, No. 2, pp. 171-186.

Foye, R. and D. Baker, 1970, "Design of Orthotropic Laminates," *11th Annual AIAA Structures, Structural Dynamics, and Materials Conference*, Denver, Colorado.

Green, A. and W. Zerna, 1954, <u>Theoretical Elasticity</u>, Clarenden Press, Oxford.

Greszczuk, L., 1972, "Stress Concentrations and Failure Criteria for Orthotropic and Anisotropic Plates with Circular Openings," *Composite Materials: Testing and Design (Second Conference)*, ASTM, pp. 363-381.

Guo, Y., D. Post, and B. Han, 1992, "Thick Composites in Compression: An Experimental Study of Micromechanical Behavior and Smeared Engineering Properties," *Journal of Composite Materials*, Vol. 26, No. 13, pp. 1930-1944.

Hale, R. and D. Adams, 1996, "Influence of In-Plane Fiber Misalignment on Moiré Interferometry Results," submitted to *Journal of Composite Materials*.

Han, B., 1992, "Higher Sensitivity Moiré Interferometry for Micromechanics Studies," *Optical Engineering*, Vol. 31, No. 7, pp. 1517-1526.

Han, B., 1993, "Interferometric Methods with Enhanced Sensitivity by Optical/Digital Fringe Multiplication," *Applied Optics*, Vol. 32, No. 25, pp. 4713-4718.

Hariharan, P., B. Oreb, and T. Eiju, 1987, "Digital Phase-shifting Interferometry: A Simple Error-compensating Phase Calculation Algorithm," *Applied Optics*, Vol. 26, No. 13, pp. 2504-2506.

Herakovich, C., 1981, "On the Relationship Between Engineering Properties and Delamination of Composite Materials," *Journal of Composite Materials*, Vol. 15, pp. 336-348.

Herakovich, C., D. Post, M.B. Buczek, and R. Czarnek, 1985, "Free-Edge Strain Concentrations in Real Composite Laminates: Experimental-Theoretical Correlation," *Journal of Applied Mechanics*, Vol. 52, pp. 787-793.

Howland, R., 1930, "On the Stress in the Neighborhood of a Circular Hole in a Strip Under Tension," *Phil.Transactions of the Royal Society of London*, Vol. 229, pp. 49-86.

Huntley, J., 1989, "Noise-Immune Phase Unwrapping Algorithm," *Applied Optics*, Vol. 28, No. 15, pp. 3268-3270.

Iarve, E., 1996, "Spline Variational Three Dimensional Stress Analysis of Laminated Composite Plates with Open Holes," *International Journal of Solids and Structures*, Vol. 33, No. 14, pp. 2095-2118.

Iarve, E., D. Rose, R. Channel, and N. Pagano, 1994, "Workshop on the Use of the SVELT Model for Joint Strength Prediction," Wright Patterson AFB, Ohio.

Iarve, E. and S. Soni, 1993a, "Stress Analysis in Compression Loaded Rectangular Composite Plates Containing an Open Hole," *ICCM-9 Proceedings III*, Madrid, pp. 135-142.

Iarve, E. and S. Soni, 1993b, "Three-Dimensional Stress Analysis in Compression Loaded Laminates Containing an Open Hole," *Winter Annual Meeting of the ASME*, New Orleans, Vol. 37, pp. 117-132.

Iarve, E., 1997, Personal Communication.

Jones, R., 1975, Mechanics of Composite Materials, Hemisphere Publishing Corporation, New York.

Kassapoglou, C. and P. Lagace, 1986, "An Efficient Method for the Calculation of Interlaminar Stresses in Composite Materials," *Journal of Applied Mechanics*, Vol. 53, pp. 744-750.

Kassapoglou, C. and P. Lagace, 1987, "Closed Form Solutions for the Interlaminar Stress Field in Angle-Ply and Cross-Ply Laminates," *Journal of Composite Materials*, Vol. 21, pp. 292-308.

Kim, R. and S. Soni, 1984, "Experimental and Analytical Studies On the Onset of Delamination in Laminated Composites," *Journal of Composite Materials*, Vol. 18, pp. 70-80.

Kirsch, G., 1898, "Die Theorie der Elastizität und die Bedürfnisse der Festigkeitslehre," *Zeitschrift des Vereines Deutscher Ingenieure*, Vol. 42, No. 29, pp. 797-807.

Ko, C. and C. Lin, 1992, "Method for Calculating the Interlaminar Stress in Symmetric Laminates Containing a Circular Hole," *AIAA Journal*, Vol. 30, pp. 197-204.

Lassahn, G., P. Taylor, V. Deason, and J. Lassahn, 1994, "Multiphase Fringe Analysis with Unknown Phase Shifts," *Optical Engineering*, Vol. 33, No. 6, pp. 2039-44.

Lekhnitskii, S., 1963, Theory of Elasticity of an Anisotropic Elastic Body, Holden-Day, San Francisco.

Lekhnitskii, S., 1968, Anisotropic Plates, Gordon and Breach Science Publishers, New York.

Lin, S., 1992, "Integration and Processing of High-Resolution Moiré-interferometry Data: A Full-Field Hybrid Method for the Study of Mechanics," Ph.D. Dissertation, Virginia Polytechnic Institute and State University.

Lo, K., E. Wu, and D. Konishi, 1983, "Failure Strength of Notched Composite Laminates," *Journal of Composite Materials*, Vol. 17., pp. 384-398.

Lucking, W., S. Hoa, and T. Sankar, 1984, "The Effect of Geometry on Interlaminar Stresses of $[0/90]_S$ Composite Laminates with Circular Holes," *Journal of Composite Materials*, Vol. 17, pp. 188-198.

McKelvie, J. and C. Walker, 1978, "A Practical Multiplied Moiré-Fringe Technique," *Experimental Mechanics*, Vol. 18, No. 8, pp. 316-320.

Mollenhauer, D., 1995, "A Comparison of Experimental and Analytical Strains in the Vicinity of a Hole," Class project for ESM 5984: Scientific Visual Analysis and Multimedia, Virginia Polytechnic Institute and State University, full project available for download at ftp://ftp.sv.vt.edu/pub/projects95, summary project available at http://www.sv.vt.edu.

Nishioka, T. and S. Atluri, 1982, "Stress Analysis of Holes in Angle-Ply Laminates: An Efficient Assumed Stress "Special-Hole-Element" Approach and a Simple Estimation Method," *Computers and Structures*, Vol. 15, No. 2, pp. 135-147.

Oplinger, D., B. Parker, and F. Chiang, 1974, "Edge-Effect Studies in Fiber-Reinforced Laminates," *Experimental Mechanics*, Vol. 14, No. 9, pp. 347-354.

Pagano, N., 1974, "On the Calculation of Interlaminar Normal Stress in Composite Laminates," *Journal of Composite Materials*, Vol. 8, pp. 65-81.

Pagano, N., 1978, "Stress Fields in Composite Laminates," *International Journal of Solids and Structures*, Vol. 14, pp. 385-400.

Pagano, N. and R.B. Pipes, 1970, "The Influence of Stacking Sequence on Laminate Strength," *Journal of Composite Materials*, Vol. 5, pp. 50-57.

Pagano, N. and R.B. Pipes, 1973, "Some Observations on the Interlaminar Strength of Composite Laminates," *International Journal of Mechanical Sciences*, Vol. 15, pp. 679-688.

Perry, K. and J. McKelvie, 1993a, "A Comparison of Phase-Shifting and Fourier Methods in the Analysis of Discontinuous Fringe Patterns," *Optics and Lasers in Engineering*, Vol. 19, pp. 269-284.

Perry, K. and J. McKelvie, 1993b, "An Investigation of Delamination in Composite Materials Using Phase Shifting Moiré Interferometry," *Proceedings of the 1993 SEM "50th Anniversary" Spring Conference on Experimental Mechanics*, Dearborn, Michigan, pp. 298-307.

Pipes, R., 1972, "Solution of Certain Problems in the Theory of Elasticity for Laminated Anisotropic Systems," Ph.D. Dissertation, University of Texas, Arlington.

Pipes, R. and I. Daniel, 1971, "Moiré Analysis of the Interlaminar Shear Edge Effect in Laminated Composites," *Journal of Composite Materials*, Vol. 5, pp. 255-259.

Pipes, R. and N. Pagano, 1970, "Interlaminar Stresses in Composite Laminates Under Uniform Axial Extension," *Journal of Composite Materials*, Vol. 4, pp. 538-549.

Pipes, R. and N. Pagano, 1974, "Interlaminar Stresses in Composite Laminates - An Approximate Elasticity Solution," *Journal of Applied Mechanics*, Vol. 41, No. 3, pp. 668-672.

Plassa, M., 1969, "Effects of Elastic Instability of Thin Germanium Films," *Thin Solid Films*, Vol. 3, No. 5, pp. 305-314.

Post, D., 1996, Personal Communication.

Post, D., B. Han, and P. Ifju, 1994, High Sensitivity Moiré: Experimental Analysis for Mechanics and Materials, Springer-Verlag Inc., New York.

Pullman, D. and J. Schaff, 1996, "Three Dimensional Spline Variational and Finite Element Theory: A Comparison for a Laminate With a Circular Hole," *American Society for Composites, 11th Technical Conference on Composite Materials: Structural Design and Analysis Methods*, Atlanta.

Raju, I. and J. Crews, Jr., 1982, "Three-Dimensional Analysis of $[0/90]_s$ and $[90/0]_s$ Laminates with a Central Circular Hole," NASA-TM-83300.

Reiss, E. and S. Lock, 1961, "On the Theory of Plane Stress," *Quarterly Applied Mathematics*, Vol. 19, pp. 195-203.

Reissner, E., 1950, "On a Variational Theorem in Elasticity," *Journal of Mathematics and Physics*, Vol. 29, pp. 90.

Rowlands, R., I. Daniel, and J. Whiteside, 1973, "Stress and Failure Analysis of a Glass-Epoxy Composite Plate with a Circular Hole," *Experimental Mechanics*, Vol. 13, No. 1, pp. 31-37.

Rybicki, E. and D. Schmueser, 1978, "Effect of Stacking Sequence and Lay-Up Angle on Free-Edge Stresses Around a Hole in a Laminated Plate Under Tension," *Journal of Composite Materials*, Vol. 12, pp. 300-313.

Saeger, K., 1989, "An Efficient Semi-Analytical Method for the Calculation of Interlaminar Stresses Around Holes," Ph.D. Dissertation, Massachusett Institute of Technology.

Savin, G., 1969, Stress Concentration Around Holes, Pergamon Press, New York.

Schaff, J., D. Mollenhauer, and D. Rose, 1996, "Stress Analysis and Experimental Testing of a Structural Composite Laminate with a Hole," *American Society for Composites, 11th Technical Conference on Composite Materials: Structural Design and Analysis Methods*, Atlanta.

Serabian, S., 1991, "The Effects of Nonlinear Intralaminar Shear Behavior on the Modeling Accuracy of $[(0/90)_3,0]_s$ and $([+45/-45]_{3s}$ Pin-Loaded Laminates," *Journal of Composites Technology & Research*, Vol. 13, No. 4, pp. 236-248.

Singh, H. and J. Sirkis, 1994, "Direct Extraction of Phase Gradients from Fourier-Transform and Phase-Step Fringe Patterns," *Applied Optics*, Vol. 33, No. 22, pp. 5016-5020.

Tan, S.C. and R.Y. Kim, 1990, "Strain and Stress Concentrations in Composite Laminates Containing a Hole," *Experimental Mechanics*, Vol. 30, No. 4, pp. 345-351.

Thompson, D. and O. Griffin, Jr, 1990, "2-D to 3-D Global/Local Finite Element Analysis of Cross-Ply Composite Laminates," *Journal of Reinforced Plastics and Composites*, Vol. 9, pp. 492-502.

Tuttle, M. and D. Graesser, 1990, "Compression Creep of Graphite/Epoxy Laminates Monitored using Moiré Interferometry," *Optics and Lasers in Engineering*, Vol. 12, pp. 151-171.

Wang, A. and F. Crossman, 1977, "Some New Results on Edge Effect in Symmetric Composite Laminates," *Journal of Composite Materials*, Vol. 11, pp. 92-106.

Wang, S. and I. Choi, 1982a, "Boundary Layer Effects in Composite Laminates: Part 1 – Free-Edge Stress Singularities," *Journal of Applied Mechanics*, Vol. 49, pp. 541-548.

Wang, S. and I. Choi, 1982b, "Boundary Layer Effects in Composite Laminates: Part 2 – Free-Edge Stress Solutions and Basic Characteristics," *Journal of Applied Mechanics*, Vol. 49, pp. 549-560.

Whitcomb, J., I. Raju, and J. Goree, 1982, "Reliability of the Finite Element Method for Calculating Free-Edge Stresses in Composite Laminates," *Computers & Structures*, Vol. 15, No. 1, pp. 23-37.

Whitney, J., I. Daniel, and R. Pipes, 1984, Experimental Mechanics of Fiber Reinforced Composites Materials, The Society for Experimental Mechanics, Brookfield Center, Connecticut.

Whitney, J. and R. Nuismer, 1974, "Stress Fracture Criteria for Laminated Composites Containing Stress Concentrations," *Journal of Composite Materials*, Vol. 8, No. 2, pp. 253-265.

Whitney, J. and C. Sun, 1973, "A Higher Order Theory for Extensional Motion of Laminated Composites," *Journal of Sound and Vibration*, Vol. 30, p.85.

Ye, L. and B. Yang, 1988, "A Boundary Layer Approach to Interlaminar Stresses in Composite Laminates with Curved Edges," *Journal of Reinforced Plastics and Composites*, Vol. 7, pp. 179-198.

Yen, W. and C. Hwu, 1993, "Interlaminar Stresses Around Hole Boundaries of Composite Laminates Subjected to In-plane Loading," *Composite Structures*, Vol. 24, No. 4, pp. 299-310.

Appendix A: Grating Replication Procedure

This section contains the replication procedure used in this research. Slight modifications were made as experience was gained, so the procedure is somewhat flexible. A print-out of this procedure was generally followed during the replication process, with each step being mentally or physically checked off when completed. The procedures listed below assume a working knowledge of the basic practices of moiré interferometry as described in Post *et al.* (1994).

A.1: Grating onto a Shim (from Flat Grating)

(1) Select and label a shim. Measure the thickness of the shim using a digital micrometer stage (a few locations should be adequate) to verify that the shim is of constant thickness.

(2) Clean a shim with acetone. Make a few marks on the back side of the shim to identify the replication area.

(3) Clean a 12.7 mm (0.500 inch) gage block (or equivalent) that will be used as a pressure plate. The gage block used in the present research was 34.9 mm (1.375 inches) long and 12.7 mm (0.5 inches) wide. Coat it with a Teflon release agent.

(4) Prepare a grating mold with an evaporation deposited coating of aluminum, a coating of Kodak Photo Flo (dry for at least 24 hours), and another coating of aluminum. This will allow for clean separation. Attach a long alignment fence (or two small fences) in the manner described in Post *et al.* (1994). This will allow the grating to be aligned properly with the edges of the shim. Make absolutely sure that the area chosen to replicate the grating over has no dust or other blemish that would effect the thickness of the grating.

(5) Heat the oven to 50°C and place the shim, grating, and gage block in the oven. Preheated surfaces were intended to prevent bubble evolution. This was only partially successful.

(6) Pour components of the replication resin into plastic cups. For this step, the commercial casting resin, Envirotex Lite, was used. Use only a little, since eventually only enough to fill a test-tube will be used. Vacuum debulk for 20 to 40 minutes under high vacuum.

(7) Pour equal parts of the debulked resin (or the proper mixing ratio if Evirotex Lite is not used) into a test tube, mix very thoroughly with a spatula (try not to entrain bubbles), and centrifuge for 5 minutes. Pour off most of the adhesive and vacuum debulk the remainder.

(8) Remove the grating from the oven and pour a very narrow strip of adhesive onto the grating in the region near but not where the shim will eventually be positioned. Place a paper mat below the grating over the work surface so that the grating does not cool too much.

(9) Take the shim out of the oven and carefully settle it onto the strip of adhesive. Place the gage block onto the center of the shim between the marks made in Step 2. Gently slide the shim against the alignment fences, being sure to drag enough adhesive with the assembly.

(10) Center the grating and shim assembly under the pressure application apparatus and screw the micrometer down until the tip just touches the gage block. The pressure application apparatus is simply a micrometer held vertically by a frame. Turn the micrometer 0.1 mm (0.004 inch) at most. The amount of required micrometer deflection is, of course, dependant on the compliance of the pressure application apparatus. The required force is small. Carefully clean up any excess epoxy with cotton swabs.

(11) When cured (at least 12 hours), carefully separate the assembly. Post-cure the grating for several hours at ~65°C. Mark the front of the grating with scratches at the periphery of the good grating area (the part of the grating under the pressure block). Any epoxy on the back surface of the shim or flashing on the edge of the shim can be scraped off or sanded lightly with 600 grit sandpaper. An optional step is to measure the thickness of the grating using a digital micrometer stage. This step will damage the grating under the hemispherical micrometer head.

A.2: Grating onto a Replication Plate

(1) Clean the replication plate thoroughly with acetone. Place cellophane tape over the two central holes (an alignment pin hole and the screw hole to attach the plate to the sector) on the back of the replication plate. This prevents the replication epoxy from wicking far into the holes. Preheat the plate to 50°C.

(2) Follow the same adhesive mixing procedure as in Section A.1. Pour a pool of adhesive in the center of the grating exactly where the center of the plate will be placed. Settle the plate onto the pool, put a weight on it, and clean the edges with cotton swabs. Two different resins were tried: PC-10C and Envirotex Lite. The PC-10C was chosen since it tended to be harder when cured than the Envirotex Lite.

(3) When the epoxy is cured, drill and ream the epoxy out of the central holes before separating. Separate and blow off any dust. Any epoxy flashing on the edges can be removed by sanding, and the two central holes can be cleared by reaming.

(4) Coat with Photo Flo and aluminum as described in Section A.1, Step 4.

A.3: Grating onto a Replication Sector

(1) Coat the shim/grating with Photo Flo solution and aluminize.

(2) Prepare the sector by lightly sanding to remove any burrs or surface blemishes. Clean with acetone.

(3) Prepare the replicating apparatus as pictured in Figure 2.2. Clean the translation stage and the spacer. Coat the translation stage and spacer with a release agent. Attach the sector as shown in Figure 2.2. Place the rubber band in the correct location such that the shim is contacted in the center of the overlapping area between shim and sector. Practice with a spare shim and make sure that the rubber band location bends the shim around the sector without any twisting. Use a hair drier to gently heat the translation stage, the sector, and the surrounding area.

(4) Preheat the oven to 50°C and place the shim with grating into the oven.

(5) Mix the adhesive according to the instructions in Section A.1. Pour a thin strip onto the shim over the region where the sector will contact the shim. Start the pouring away from the region of interest. Clean up any excess adhesive outside the region of interest with cotton swabs. Two different resins were tried: PC-10C and Envirotex Lite. The PC-10C was chosen since it tended to be harder when cured than the Envirotex Lite.

(6) Slowly push the sector and translation stage into the shim. Continue pushing the translation stage until the proper location is reached and then lock the translation stage in place. The proper location is when the shim is tangent at the ends of the circular sector. Carefully clean excess adhesive. Allow 12 hours for cure.

(7) Remove the translation stage lock and slowly move the translation stage away from the rubber band (the shim will automatically separate from the sector). Post-cure the sector for several hours at 65°C. Sand any remaining epoxy flashing with 600 grit sandpaper.

(8) Evaluate the sector grating in the interferometer.

(9) Coat with Photo Flo and aluminum again as usual.

A.4: Grating onto a Specimen

(1) Clean the specimen with acetone.

(2) Place the replication plate from Section A.2 into the alignment frame shown in Figure 2.5. Make sure it is aligned properly for the angular area of desired moiré measurements. Gently slide the sector prepared in Section A.3 onto the alignment pin while placing a bolt through the sector and plate bolt hole. Carefully tighten the sector screw and then remove the alignment pin (this is very important). This will help prevent the possibility of the sector being permanently attached to the plate if epoxy wicks under the sector. Place the specimen and the alignment frame into a 50°C oven. The specimen might be too long for this, but prop open the door and allow the specimen to project out of the oven.

(3) Mix the adhesive as described in Section A.1 (in this case, PC-10C was used). Remove the specimen and alignment frame from the oven, and pour the adhesive over the plate around the sector. This replication step is performed with the specimen horizontally oriented. Pool a bit more adhesive in front of the face of the sector.

(4) Carefully lower the specimen over the alignment frame assembly, pushing the adhesive toward the sector. Push the specimen in an axial direction to properly engage the sector with the 0° area of the specimen. Slightly tighten the transverse pressure screws. Swing the interlaminar pressure plate into place and slightly tighten its screws. Continue to alternate tightening the two sets of pressure screws while applying occasional axial force to the specimen. Do not over tighten the transverse pressure screws as this will ruin the grating in the 90° region of the specimen.

(5) While horizontal, clean the excess epoxy from the sector area with cotton balls and swabs. Turn the alignment frame to a vertical orientation by clamping one of the end tabs in a table vise. Clean the excess epoxy from the backside of the specimen. Continue cleaning the excess epoxy from the front and back thoroughly for about 45 minutes. Let cure at least 24 hours.

(6) Remove the specimen from the vise and orient horizontally. Separate the replication plate from the specimen by first loosening the transverse pressure screws. Then remove the screw attaching the sector to the replication plate (place a pin in the alignment pin hole to help prevent torsional forces from damaging the sector and hole grating). Remove the interlaminar pressure plate and put specimen removal screws into place (only one screw was used and was located at the corner nearest the sector face).

(7) Apply pressure with this screw (distributed on an aluminum plate) such that the crack front will approach the face of the sector. This seemed to work quite well for separating the replication plate from the specimen while leaving the sector attached to the specimen.

(8) Clamp the protruding portion of the sector in a vise. Attach a C-clamp onto the specimen as shown in Figure A.1. Gently tap the C-clamp with the plastic handle of a screwdriver until the specimen separates. Remove the C-clamp and recover the sector from the vise.

(9) Visually examine the gratings on the flat face of the specimen and the cylindrical surface of the hole. Also pay special attention to the interface between the grating on the face and on the hole surface.

A.5: Grating from a Loaded Specimen

(1) Clean a sector that does not have a grating on it. Coat the bottom with aluminum, Photo Flo, and aluminum in the same manner as described in Section A.1. This will prevent the silicon rubber from sticking to the underside of the sector. Lightly sand the sector face with 600 grit sandpaper and carefully dust with pressurized air.

(2) Clean a new replication plate and the prepared sector with acetone. Do not clean the aluminized bottom surface of the sector, just the cylindrical face. Prime with SS4155 using a lens cleaning tissue to spread the liquid (avoid getting any SS4155 on the bottom surfaces of the sector--this will help prevent the adhesion of the sector to the plate). Let dry one hour at room temperature.

(3) Place replication plate and sector assembly in the alignment frame. Be sure to align the sector correctly and to remove the alignment pin.

(4) Mix the RTV-615 and vacuum debulk for 20 to 30 minutes.

(5) Pour the silicon rubber resin onto the replication plate around the sector. Pool a little more in front of the sector face.

(6) Bring the alignment frame assembly up to the loaded specimen (oriented vertically in the testing machine) and press the assembly onto the specimen. Be careful not to scrape the sides of the hole with the sector. When an adequate amount of silicon rubber has been forced through the hole around the sector, settle the assembly against the side of the hole.

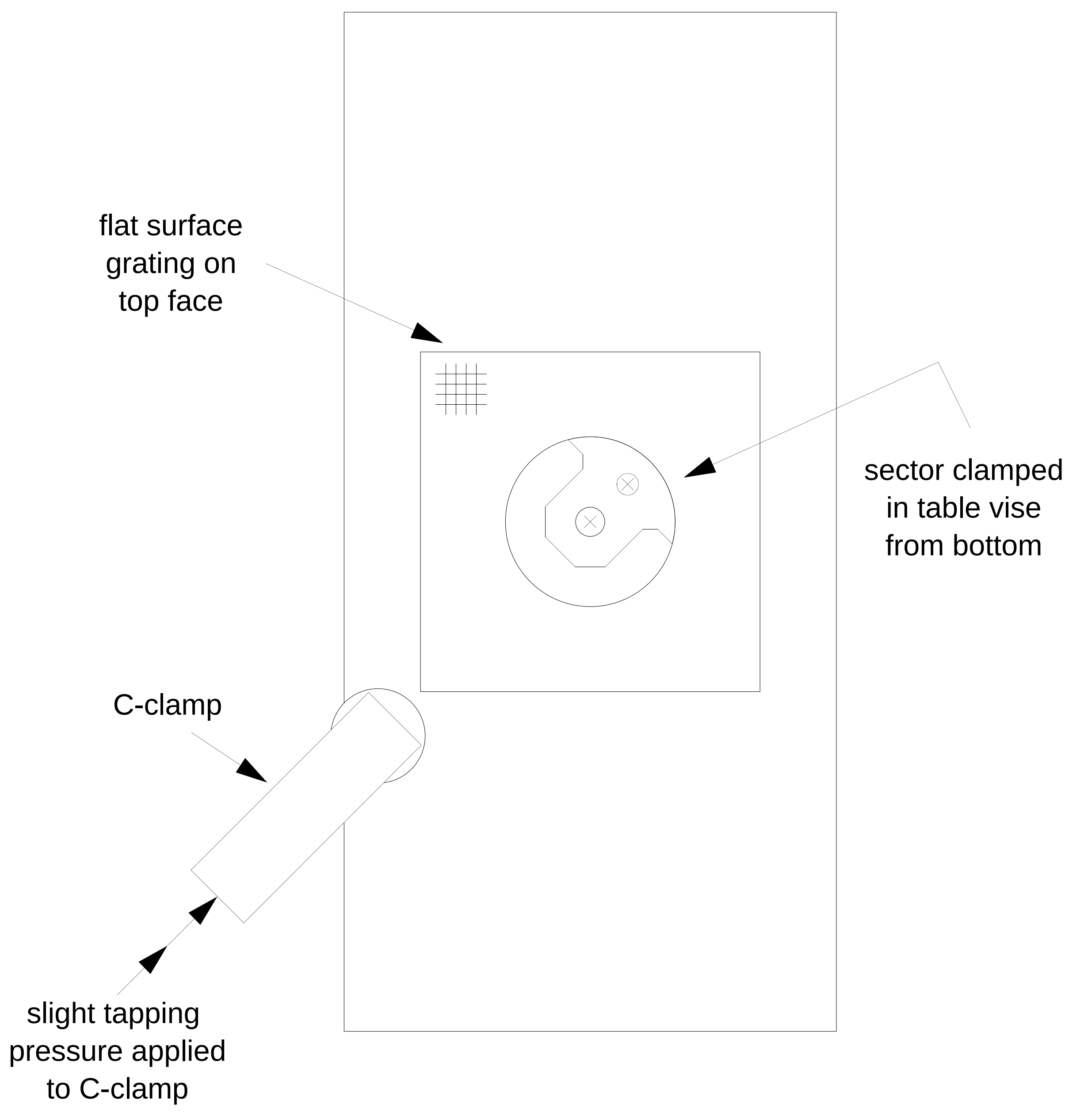

Figure A.1: Removal of the original sector from the specimen during the process of replicating a grating onto a specimen.

(7) Swing the interlaminar pressure plate into place. Slightly tighten the interlaminar pressure screws. Very slightly tighten the transverse pressure screws. Continue to alternate tightening the two sets of pressure screws. The vertical orientation of the specimen (cylindrical grating portion toward the bottom) in the testing frame will allow the alignment frame to settle into the adhesive in the axial direction. Do not over tighten the transverse pressure screws as this will ruin the grating in the 90° region of the specimen. Clean up excess silicon rubber and verify the alignment of the replication frame with respect to the specimen.

(8) Clean the edges more thoroughly with cotton and a relatively sharp instrument (something like a dental tool). Clean the excess material from the specimen face by using cotton swabs slightly dampened with alcohol. Clean periodically for at least two hours (perhaps even three hours). Allow to cure at least 18 hours.

(9) Separate using the same methods as described in Steps 6 and 7 of Section A.4 except apply pressure such that the crack front approaches the open side of the hole first. It is believed that this will allow the silicon rubber to start a tear at the interface between the sector and the plate more effectively than having the crack approach from the sector face. Remove the sector from the specimen by bolting a screw into the bolt hole. Gently apply pressure to the screw until separation occurs. Cotton placed between the sector and the opposite face of the hole will shield the composite from the impact of the sector separation.

(10) Post-cure the plate and sector at 100°C for 24 hours. Vacuum deposit a very thin layer of gold onto the faces of these gratings.

Appendix B: Extracting Strain from Displacements

B.1: Overview of Fringe Analysis Methods

There are many methods for determining strain from a displacement field. Most of these described below are still in current use. The simplest (and often the best) methods are a local finite difference method (referred to as the finite-increment method) and a slope determination from a plot of displacement versus coordinate. The local finite-increment method measures the distance in the desired coordinate direction between two or more fringes as shown in Figure B.1. The standard linear strain displacement equations, Equation 1.7, can be modified to produce the following equations suitable for determining strain in this situation.

$$\varepsilon_{xx} = \frac{1}{f}\frac{\Delta N_x}{\Delta x}, \quad \varepsilon_{yy} = \frac{1}{f}\frac{\Delta N_y}{\Delta y}, \quad \gamma_{xy} = \frac{1}{f}\left(\frac{\Delta N_y}{\Delta x} + \frac{\Delta N_x}{\Delta y}\right) \tag{B.1}$$

ΔN_x and ΔN_y are the change in fringe order, Δx and Δy are the change in coordinate, and f is the virtual reference grating frequency. The slope determination method simply plots the variation of displacement with respect to a coordinate direction. Figure B.2 shows a schematic of this method where a curve is fitted to the data and the slope (strain) is determined at any x coordinate.

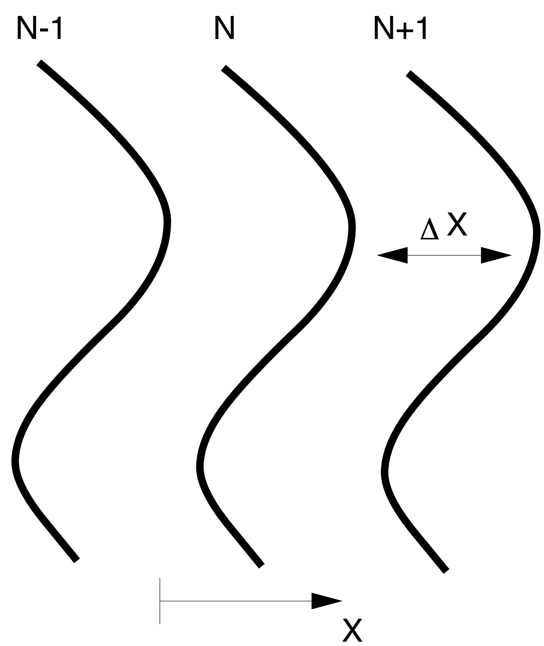

Figure B.1: Schematic of the finite-increment method.

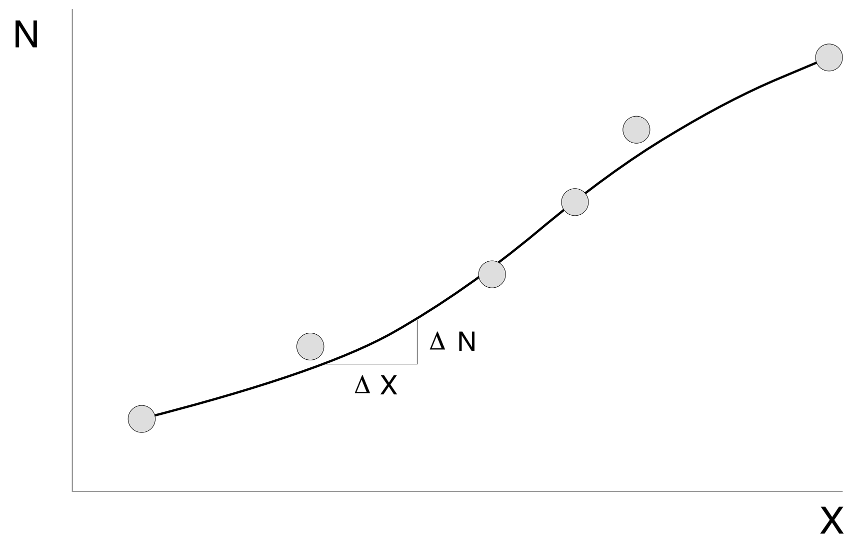

Figure B.2: Schematic of the slope method.

Another method for extracting strain from displacement patterns is mechanical differentiation. Superimposing two identical displacement patterns and then offsetting one slightly produces a geometric moiré effect where the fringe orders are proportional to strain. The component of strain depicted is determined by the direction of the offset. Its magnitude per fringe is dependant on the amount of offset. Shear must be determined from two patterns representing each of the cross derivative terms.

Fringe vectors can be used to determine strain in situations where other methods fail. This method is often known as the tangent method. Figure B.3 shows a fringe vector, F_x, broken into its components, F_{xy} and F_{xx} (for this example, the displacement field is the x-displacement field). Figure B.4 shows a situation where using fringe vectors is appropriate. In this hypothetical fringe pattern, the fringe gradient in the x-direction is difficult to determine. The fringe gradient in the y-direction, however, is easily obtained. Using the relationships in Equations B.2 and B.3, strain in the x-direction can be calculated by measuring the angle ϕ at the desired location.

$$\varepsilon_{xx} = \frac{1}{f} F_{xx} \quad , \quad \varepsilon_{yy} = \frac{1}{f} F_{yy} \quad , \quad \gamma_{xy} = \frac{1}{f}\left(F_{xy} + F_{yx}\right) \qquad \text{(B.2)}$$

$$F_{xy} = F_{xx} \tan(\phi) \qquad \text{(B.3)}$$

The hypothetical fringe pattern shown in Figure B.4 is similar to the zones of high shear documented in the composites studied in this research; except in this case, the high strain zone is the normal strain instead of the shear strain.

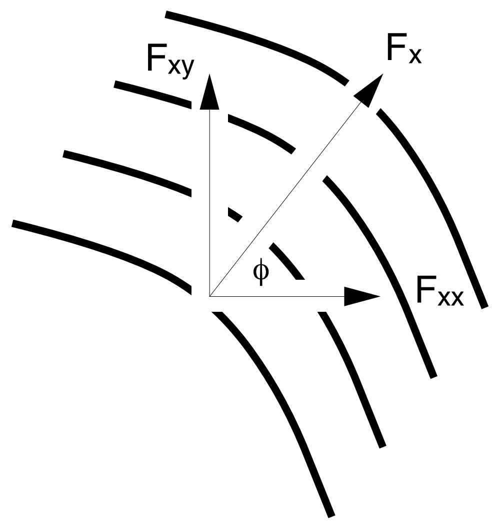

Figure B.3: Schematic of fringe vectors.

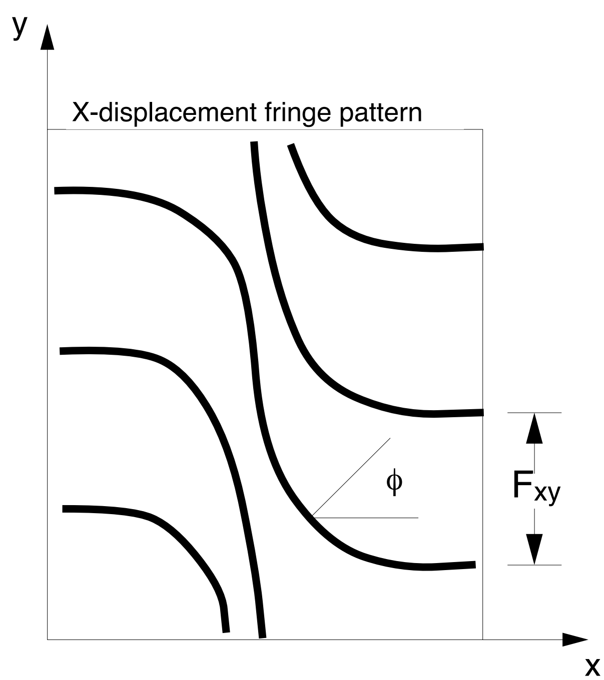

Figure B.4: Schematic of the tangent method.

The previously described methods of extracting strains from displacement patterns are applicable only along a line or at a point. Recent efforts have focused on extracting strains from an entire two-dimensional field of displacements. Lin (1992) developed a method where displacement fringes were digitized and inserted into the mesh of a finite element model (FEM). The FEM package was then used to calculate strains. Tuttle and Graesser (1990) examined a scanned image of a fringe pattern. They determined the fringe centers on a row-by-row and column-by-column basis. Strains were obtained by numerically differentiating along rows and columns.

Two methods have recently become popular in digitally determining the point-by-point displacements using moiré interferometry. The phase-shifting (quasi heterodyne) and Fourier transform (spatial heterodyne) methods take fringe data and convert it directly into displacement data (Creath, 1988; Lassahn, *et al.,* 1994; Perry and McKelvie, 1993a; Perry and McKelvie, 1993b; Singh and Sirkis, 1994). Thus a matrix of digital displacement data can be manipulated to produce strains. Two methods have been used to determine strains from these data. Simple numerical differentiation works well; but due to the noisy nature of the data, smoothing must be implemented before or after differentiation (Mollenhauer, 1995). Surface fitting also has been used either on a global basis or a local basis to determine the strains (Perry and McKelvie, 1993a).

A relatively new method of determining strains has been presented by Singh and Sirkis (1994). In this method, fringe patterns are first obtained digitally and then the phase distribution is calculated using Fourier transforms or phase-shifting interferometry. One of the drawbacks of either technique is that obtaining the displacement field requires a complicated procedure of eliminating a $-\pi$ to π ambiguity in the phase data. Singh and Sirkis (1994) avoid this problem by going directly to strains from the phase data. Displacements can be recovered through integration.

B.2: Discussion of Fringe Analysis Errors

Errors caused by mistakes during the manual analysis of fringe patterns are certainly a possibility. The two manual analysis techniques used in this research (the finite-increment and tangent methods) are not immune to analysis errors. Unfortunately, assigning plus or minus error to the calculated strain is not routine. If an error in the geometric length measurement is made in the finite-increment method, for example, the resulting error in strain shows a nonlinear dependance upon the value of the measured strain.

Figure B.5a shows a plot of this situation. All data were calculated using typical values of strain and scale appropriate for comparison with the strain data presented in Chapter 3. Within this figure, the correct strain is plotted along with the magnitude of strain error caused by the average of ±2 "pixel" errors in the fringe center measurement. The fringe patterns analyzed in this project were digitally scanned into a computer and a graphics program used for the analyses, thus, the reference to "pixels," which are regularly spaced intensity data points in the fringe image. From this figure, it is clear that the magnitude of the error increases as the calculated strain values increase. The relative error is small, however. It is always less than 250 με for strains less than 5,000 με (5% error).

Figure B.5b shows a similar graph for the case of a ±1° measurement error when using the tangent method. Again all data were calculated using typical values of strain and scale appropriate for comparison with the strain data presented in Chapter 3. The results are very similar to the case for the finite-increment method. The relative error increases with increasing strain, and errors are always less than 250 $\mu\varepsilon$ for strains less than 5,000 $\mu\varepsilon$. Unfortunately, the tangent term in Equation B.2 rapidly approaches infinity as the measured tangent angle approaches 90°. This causes the relative error to increase dramatically for higher strains and a given angular measurement error. For example, errors over 10,000 $\mu\varepsilon$ are possible for the maximum shear calculated in this research (35,000 me). The majority of shear values recorded for the $[+30°_2/-30°_2/90°_4]_{3s}$ specimen are below 10,000 $\mu\varepsilon$ in value. The level of error corresponding with this strain value is less than 1,000 $\mu\varepsilon$ (10% error). The majority of shear strain values measured from the $[0°_4/90°_4]_{3s}$ specimen were below 5,000 $\mu\varepsilon$ and the corresponding 250 $\mu\varepsilon$ error.

The errors caused by manual analysis of fringes are not systematic. They would manifest themselves as random noise. The errors for the majority of strain measurements are small. Most are less than 250 $\mu\varepsilon$. However, the tangent method can yield significant analysis errors when strains are large. The majority of shear data measured in this study were below 10,000 $\mu\varepsilon$ which represents a level of strain that would produce a 10% error for a ±1° error in measurement angle.

However, determining the fringe centers using the finite-increment method was typically more reliable than ±2 pixels. The tangent angle was increasingly easy to measure as the level of shear increased, since the fringes tended to get narrower and better defined. As a result of this, both estimates of measurement error (±2 pixel and ±1°) are believed to be conservative, and the levels of error discussed above are quite conservative.

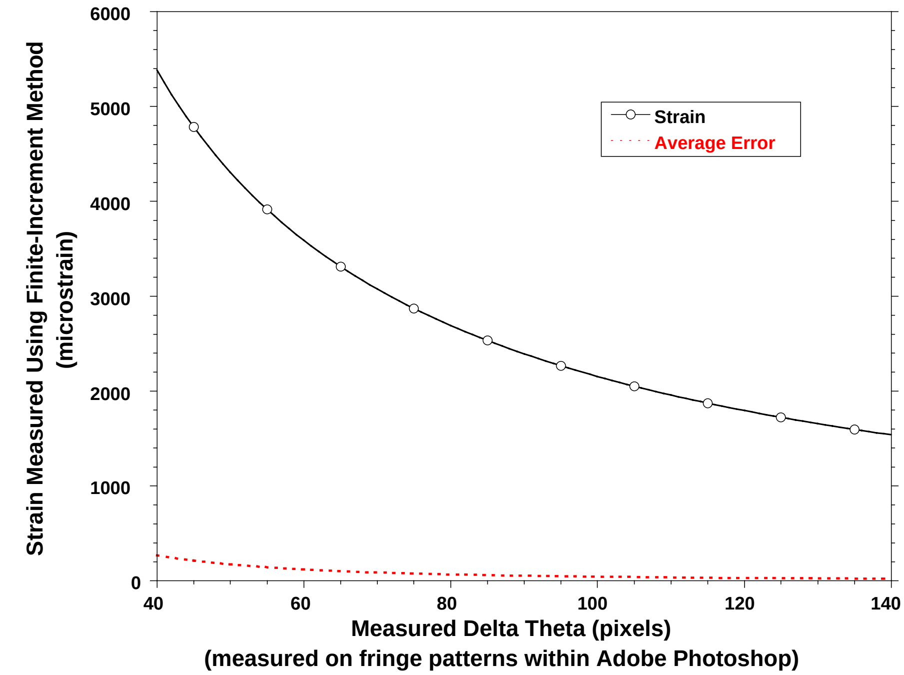

(a)

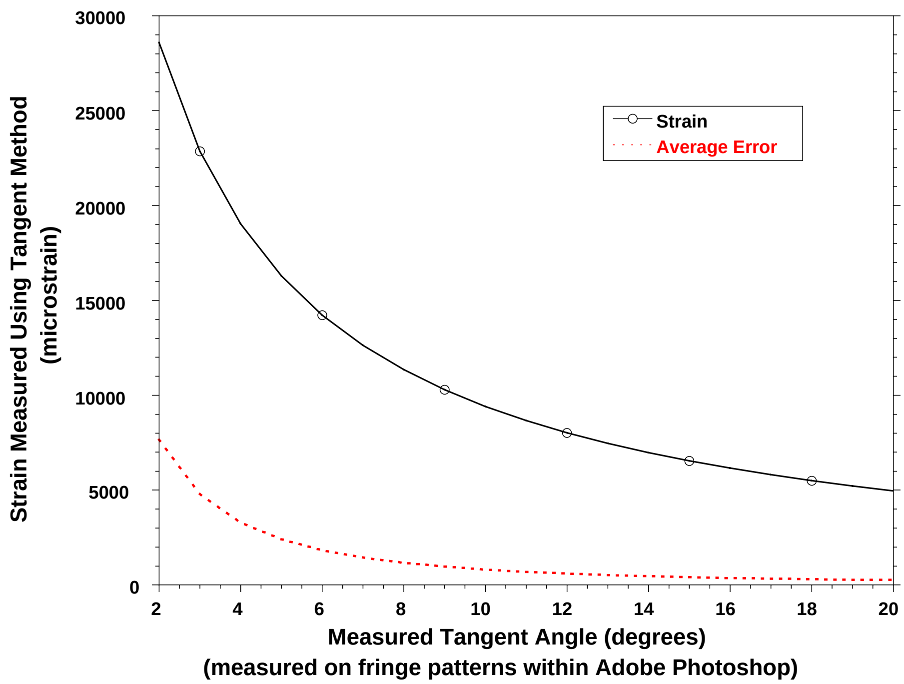

(b)

Figure B.5: Strain error caused by analysis measurement errors: (a) ±2-pixels using the finite-increment method; (b) ±1° using the tangent method.

Vita

David Hilton Mollenhauer was born near Yellow Springs, Ohio, on March 25, 1967. His parents moved to College Station, Texas, when he was 5 years old. David completed his public education in College Station.

He attended Texas A&M University and earned a Bachelor of Science degree in Aerospace Engineering in May 1990. While attending college, David had approximately one year of Cooperative Education work at the NASA Johnson Space Center in Houston, Texas. At NASA, he worked at the Propulsion and Power Division, the Crew and Thermal Systems Division, and the Advanced Programs Office. Also while at Texas A&M, David worked on a NASA Jet Propulsion Laboratory materials testing program conducted at the university. This work involved the post-impact buckling response of laminated composite plates.

In August 1990, David was hired by the United States Air Force and entered into civilian employment under the Air Force's Palace Knight program. In May 1992, he completed his Masters of Science degree in Engineering Mechanics at the Virginia Polytechnic Institute and State University (VPI&SU). His research at VPI&SU focused on modeling and measuring the strain in a plate caused by the deformation of a piezoceramic patch bonded to the plate.

Upon completion of the Masters degree, David began work at the Materials Directorate of the Air Force's Wright Laboratory in Dayton, Ohio. At the Materials Directorate, he was responsible for setting up a moiré interferometry laboratory. David's projects included examination of residual strains in high temperature woven fiber-reinforced composites, measurement of strains in composites with molded holes, and correlation of surface strains in the vicinity of a hole with numerical results.

In August 1994, David returned to VPI&SU to start work on a Doctorate in Engineering Mechanics. Upon completion of the requirements for the Ph.D. in 1997, he returned to the Materials Directorate in Dayton, Ohio, where he is currently a civilian employee.